Transactions of the ASME, Journal of Heat Transfer (ISSN 0022-1481) is published monthly by The American Society of Mechanical Engineers, Three Park Avenue, New York, NY 10016. Periodicals postage paid at New York, NY and additional mailing offices. POSTMASTER: Send address changes to Transactions of the ASME, Journal of Heat Transfer, c/o THE AMERICAN SOCIETY OF MECHANICAL ENGINEERS, 22 Law Drive, Box 2300, Fairfield, NJ 07007-2300. **CHANGES OF ADDRESS** must be received at Society headquarters seven weeks before they are to be effective. Please send old label and new address. **STATEMENT from By-Laws.** The Society shall not be responsible for statements or opinions advanced in papers or ... printed in its publications (B7.1, Para. 3).

Journal of Heat Transfer

Published Monthly by ASME

VOLUME 130 • NUMBER 3 • MARCH 2008

RESEARCH PAPERS

TECHNICAL BRIEFS

(Contents continued on inside back cover)

This journal is printed on acid-free paper, which exceeds the ANSI Z39.48-1992 specification for permanence of paper and library materials. ♾™
♻ 85% recycled content, including 10% post-consumer fibers.

The ASME Journal of Heat Transfer is abstracted and indexed in the following:

Applied Science and Technology Index, Chemical Abstracts, Chemical Engineering and Biotechnology Abstracts (Electronic equivalent of Process and Chemical Engineering), Civil Engineering Abstracts, Compendex (The electronic equivalent of Engineering Index), Corrosion Abstracts, Current Contents, E & P Health, Safety, and Environment, Ei EncompassLit, Engineered Materials Abstracts, Engineering Index, Enviroline (The electronic equivalent of Environment Abstracts), Environment Abstracts, Environmental Engineering Abstracts, Environmental Science and Pollution Management, Fluidex, Fuel and Energy Abstracts, Index to Scientific Reviews, INSPEC, International Building Services Abstracts, Mechanical & Transportation Engineering Abstracts, Mechanical Engineering Abstracts, METADEX (The electronic equivalent of Metals Abstracts and Alloys Index), Petroleum Abstracts, Process and Chemical Engineering, Referativnyi Zhurnal, Science Citation Index, SciSearch (The electronic equivalent of Science Citation Index), Theoretical Chemical Engineering

Intermediate Scaling of Turbulent Momentum and Heat Transfer in a Transitional Rough Channel

Abu Seena
Department of Mechanical Engineering,
Korea Advanced Institute of Science and Technology,
Daejeon, 305-701 Korea
e-mail: abuseena@kaist.ac.kr

Noor Afzal
Department of Mechanical Engineering,
Aligarh University,
Aligarh 202 002, India
e-mail: noor.afzal@yahoo.com

The properties of the mean momentum and thermal balance in fully developed turbulent channel flow on transitional rough surface have been explored by method of matched asymptotic expansions. Available high quality data support a dynamically relevant three-layer description that is a departure from two-layer traditional description of turbulent wall flows. The scaling properties of the intermediate layer are determined. The analysis shows the existence of an intermediate layer, with its own characteristic of mesolayer scaling, between the traditional inner and outer layers. Our predictions of the peak values of the Reynolds shear stress and Reynolds heat flux and their locations in the intermediate layer are well supported by the experimental and direct numerical simulation (DNS) data. The inflectional surface roughness data in a turbulent channel flow provide strong support to our proposed universal log law in the intermediate layer, that is, explicitly independent transitional surface roughness. There is no universality of scalings in traditional variables and different expressions are needed for various types of roughness, as suggested, for example, with inflectional type roughness, Colebrook–Moody monotonic roughness, etc. In traditional variables, the roughness scale for inflectional roughness is supported very well by experimental and DNS data. The higher order effects are also presented, which show the implications of the low Reynolds-number flows, where the intermediate layer provides the uniformly valid solutions in terms of generalized logarithmic laws for the velocity and the temperature distributions.
[DOI: 10.1115/1.2804945]

Keywords: thermal convection, intermediate layer, mesolayer, wall roughness, universal relations, generalized log laws, turbulent channel flow

1 Introduction

The convective heat transfer from surfaces beneath a flowing turbulent fluid is especially important in large number of technological applications as rate of this heat transfer is significantly augmented relative to the laminar flow condition [1,2]. Despite the importance of the Reynolds shear stress and Reynolds heat flux relative to momentum and energy transport, the proper scaling remains an open question [3,4]. Challenges limiting progress relate to the scarcity of high quality data sets that also span a useful Reynolds-number range. Interestingly, neither inner nor outer normalizations are successful in the vicinity of the peak in the Reynolds-stress and Reynolds heat flux profiles. The present effort explicitly addresses this issue.

In the classical, two-layer, description overall, the vast majority of Reynolds-stress data reported in the literature is shown under either inner or outer normalization. Inner normalization utilizes the friction velocity $u_\tau=(\tau_w/\rho)^{1/2}$ and the kinematic viscosity ν. Outer normalization utilizes the channel half-height or boundary-layer thickness δ. It is shown by Afzal [5–7] that along with the outer and inner scales, δ and ν/u_τ, respectively, an intermediate layer mesoscale $(\nu u_\tau/\delta)^{1/2}$ is fundamental to the description of the mean flow. The mesolayer also play a significant role in the scaling of the period of turbulent bursts in a channel (Afzal [8]). The normalization of the Reynolds stress has described the existence of the scaling of a third layer. Afzal [5,6] has revealed an alternative physical/theoretical framework for describing the structure of wall-bounded flows. This framework includes a structure for such flows that differs considerably from the nearly universally accepted sub-, buffer, logarithmic, and wake layer structures. From theoretical reasoning, the scaling provides the Reynolds-stress profile, and the velocity profile, near the location of its peak of Reynolds shear stress. Afzal has presented a strong evidence that a mesolayer exists, and estimated its characteristic length scale to be in agreement with experimental data.

It is well known that traditional inner and outer layers arose from pioneering observations of data by Prandtl and Karman. The inability of the two-layer approximation to capture the experimental features completely is well known (Refs. [6,9,10]). The two-layer model is far from being exact and could be easily bettered by introducing further intermediate models. In fact, the traditional two-layer approximation is merely an approximation that was introduced to pick out the main features of the flow. It is shown here that adding an intermediate layer will provide a further better result, and one may hope that fact adding more intermediate layers will provide even better results. As we are dealing with open Reynolds mean momentum equations without any closure model, it is not possible to find out all the necessary substantive intermediate layers in the sense the method of matched asymptotic expansions. Thus, the observations from data would play a very crucial role in a decision if any of the intermediate layer or called mesolayer is a substantive layer, in addition to traditional inner and outer layers. The mesolayer scale is the geometric mean of the traditional inner and outer scales. The velocity profile in the mesolayer scale provides the half-velocity defect law (Ref. [7]) where mesolayer velocity $U_m=U_c/2$, where U_c is the velocity on the axis of the channel. The implications of the mesolayer scale on higher order effects have been investigated that are supported by the data (shown in our figures) that clearly indicate that there is scope for improvement.

Wei et al. [9,10] have observed that the existence and scaling of

Contributed by the Heat Transfer Division of ASME for publication in the JOURNAL OF HEAT TRANSFER. Manuscript received September 17, 2006; final manuscript received September 12, 2007; published online March 6, 2008. Review conducted by Sai C. Lau.

a third layer in momentum balance were first found by Afzal [6]. The mesolayer scaling is shown analytically to have the same legitimacy as the inner and outer scalings, in the sense that the mesolayer necessarily exists, by reasoning as valid as any theoretical basis for the traditional scalings. Wei et al. [11] also attempted thermal mesoscale $\sigma=\sqrt{(T_w-T_c)/(T_\tau \mathrm{Pr} R_\tau)}$ as a Peclet number dependent parameter associated with the maximum normalized nondimensional temperature difference. Wei et al. [11] in their Fig 6(*b*) proposed $\sigma=\sqrt{1.35}(\mathrm{Pr}R_\tau)^{-1/4}$ from data of Abe and Kawamura and Iwamoto et al. The classical overlapping regions of inner and outer scalings are described by Afzal and Yajnik [3] and Kader and Yaglom [4] where $(T_w-T_c)/T_\tau=k_t^{-1}\ln R_\tau+C_t$ and consequently $\sigma\sim(\mathrm{Pr}R_\tau)^{-1/2}\sqrt{\ln R_\tau}$. Consequently, the thermal mesoscale $\sigma=\sqrt{(T_w-T_c)/(T_\tau \mathrm{Pr} R_\tau)}$ proposed by Wei et al. [11] is not analogous to their momentum mesolayer scale $\epsilon=R_\tau^{-1/2}$ [5,6,9,10]. In present work, our thermal intermediate layer scale is $\sigma=(\mathrm{Pr}R_\tau)^{-1/2}$, in analogy with momentum intermediate layer scale $\epsilon=R_\tau^{-1/2}$ [5,6].

The present work deals with an alternate variables (Afzal and Seena [12]), the surface roughness potential $\phi=\exp(k\Delta U_+)$, connected with ΔU_+ the traditional roughness function of Clauser [13] for a turbulent boundary layer, in terms of the transitional roughness inner variable $\zeta=Z_+/\phi$ and the roughness friction Reynolds number $R_\phi=R_\tau/\phi$, where the velocity and Reynolds stresses have been universal expressions that are explicity independent of transitional wall roughness. The intermediate layers in a turbulent boundary layer are analyzed in terms of alternate variables of Afzal and Seena [12], where the velocity profiles and friction factor predictions are universal relations that are explicitly independent of wall roughness but implicitly depend on roughness potential ϕ. The extensive experimental data provide good support to universal log laws for the velocity profile and the friction factor on transitional rough wall boundary layers. Millikan [14] was first to propose the two-layer asymptotic theory. For transitional rough and fully smooth pipes in the wall region, he adopted the smooth wall variable Z_+ and for fully rough pipes he used the inner wall variable Z/h. Millikan [14] proposed the log law, where the prefactor is the Karman constant (a universal number) and the additive term B_T depends on wall roughness and represents a shift of the velocity profile in the overlap region. For fully rough walls, the additive intercept B_F also has a universal value that differs from the fully smooth wall value B. Clauser [13] simplified the matter and represented $B_T=B-\Delta U_+$ for a rough wall by defining a roughness function ΔU_+ due to transitional wall roughness in addition to smooth wall log law. The roughness function ΔU_+ is a useful descriptor of the surface roughness effects on mean velocity distribution in the inner region. It physically represents the roughness dominated shift in the velocity profile from the log law of a smooth wall. For $\Delta U_+>0$, the shift is downwards due to increase of the drag and $\Delta U_+<0$ the shift is upwards due to reduction of the drag of the rough surface. The normal coordinate is $Z=y+\epsilon_r$, where ϵ_r is the origin of the normal coordinate on the rough surface, caused by irregular protrusions of the hydraulic roughness of height h. It is a particular level between the protrusion bases and heads, which automatically satisfies the constraints $0<\epsilon_r<h$ and $\epsilon_r=0$ for smooth surface.

The present work deals with estimation of the mesoscale corrections for thermal boundary layer over the tradition two-layer theory and its implications of temperature distribution and Reynolds heat flux in fully developed turbulent channel flow with transitional surface roughness. The paper provides an accounting of the relative dominance of the three (inner, outer, and meso) layers in the thermal boundary layer. A fairly complete qualitative and order-of-magnitude quantitative picture emerges for large Peclet numbers. An analysis is given for fully developed thermal transport with constant heat flux supplied at the boundary. The analysis proceeds from the averaged heat equation for fully developed thermal transport and utilizes various scaling by method of matched asymptotic expansions for a fully developed turbulent channel flow with transitional surface roughness. The paper provides an accounting of the relative dominance of the three terms in that averaged thermal transport equation. The results show a clear decomposition of the turbulent layer into zones, each with its characteristic transport mechanisms. The higher order effects also presented in Appendix show the implications of the low Reynolds-number flows, where the intermediate layer provides the uniformly valid solutions in terms of generalized logarithmic laws for the velocity and the temperature distributions.

2 Analysis of Reynolds Momentum and Energy Equations

The Reynolds equation of mean motion in fully developed channel flow is

$$\nu\frac{\partial^2 u}{\partial y^2}+\frac{\partial \tau}{\rho\partial y}=\frac{\partial p}{\rho\partial x} \tag{1}$$

Here $u(y)$ is the axial velocity, y is the normal coordinate, $\tau=-\rho\langle u'v'\rangle$ is the Reynolds shear stress, and $u_\tau=\sqrt{\tau_w/\rho}$ is the friction velocity where τ_w is the skin friction, ρ is the fluid density, and ν is the molecular kinematic viscosity of fluid. The boundary conditions on the wall and axis of symmetry are $y=0$, $u=\tau=0$ and $y=\delta$, $u-U_c=\tau=0$.

The thermal Reynolds equation of temperature profile in fully developed channel flow is

$$\frac{\nu}{\mathrm{Pr}}\frac{\partial^2 T}{\partial y^2}+\frac{\partial \tau_t}{\rho\partial y}=u\frac{\partial T}{\partial x} \tag{2}$$

Here $T(y)$ is the temperature, y is the normal coordinate, $\tau_t=-\rho\langle v't'\rangle$ is the appropriate thermal Reynolds stress, $\mathrm{Pr}=\nu/\alpha$ is molecular Prandtl number, $T_\tau=-q_w/(\rho C_p u_\tau)$ is the friction temperature, q_w is the wall heat flux, and α is molecular thermal diffusivity. The boundary conditions on the wall and axis of symmetry are $y=0$, $T-T_w=\tau_t=0$ and $y=\delta_t$, $T-T_c=\tau_t=0$. An integral on Reynolds momentum and thermal equations (1) and (3) across the channel gives

$$\frac{\partial p}{\rho\partial x}=-\frac{\tau_w}{\rho\delta}=-\frac{u_\tau^2}{\delta} \tag{3a}$$

$$\frac{\partial T}{\partial x}=\frac{q_w}{\rho C_P\delta U_b}=-\frac{u_\tau T_\tau}{\delta U_b} \tag{3b}$$

The shear stress $\tau_w/\rho=\nu(du/dy)_w$ and wall heat transfer rate $q_w/\rho C_p=-\mathrm{Pr}^{-1}\nu(dT/dy)_w$. The skin friction $C_f=2\tau_w/(\rho U_c^2)$ and Stanton number $\mathrm{St}=u_\tau T_\tau/[U_c(T_W-T_c)]$.

The Reynolds mean momentum and energy equations in the channel flow become

$$\nu\frac{du}{dy}+\frac{\tau}{\rho}=u_\tau^2\left(1-\frac{y}{\delta}\right) \tag{4}$$

$$\frac{\nu}{\mathrm{Pr}}\frac{dT}{dy}+\frac{\tau_t}{\rho}=-u_\tau T_\tau\left(1-\frac{1}{\delta}\int_0^y\frac{u}{U_b}dy\right) \tag{5}$$

In transitional rough pipes, the present work deals with the alternate four new scales, the inner wall transitional roughness variable ζ, associated with a particular roughness level, the roughness scale ϕ connected with roughness function ΔU_+, the roughness friction Reynolds number R_ϕ (based on roughness friction velocity), and roughness Reynolds number Re_ϕ (based on roughness average velocity) where the mean turbulent flow is universal, little above the roughness sublayer. The flow does not explicity depend on the pipes roughness. Based on alternate rough wall variables, the inner variables are defined as

$$\zeta = \frac{Z_+}{\phi}, \quad Z_+ = \frac{Zu_\tau}{\nu}, \quad Z = y + \epsilon_r \tag{6}$$

The normal coordinate $Z=y+\epsilon_r$, where ϵ_r is the origin of the normal coordinate located below the top of the roughness element, caused by irregular protrusions of the hydraulic roughness of height h. It is a particular level between the protrusion bases and heads, which automatically satisfies the constraints $0<\epsilon_r<h$ and $\epsilon_r=0$ for smooth surface. The roughness friction Reynolds number R_ϕ and roughness Reynolds number Re_ϕ are

$$R_\phi = \frac{R_\tau}{\phi}, \quad \mathrm{Re}_\phi = \frac{\mathrm{Re}}{\phi} \tag{7}$$

where $R_\tau=u_\tau\delta/\nu$ is the roughness Reynolds number and $\mathrm{Re}=U_b d/\nu$ based on pipe diameter $d=2\delta$ and average velocity U_b. The two Reynolds numbers are connected by the relation $R_\phi=\mathrm{Re}_\phi\sqrt{C_f/2}$. Extensive analysis of data shows that the roughness scale ϕ is connected with roughness function ΔU_+, as given below

$$U_+ = \frac{1}{k}\ln\phi \tag{8}$$

The overall description of turbulent shear flow has been in terms of three separate length scales (inner wall, outer, and meso- or intermediate layers) at large Reynolds numbers. The scale of the meso- or intermediate layer is the geometric mean of inner and outer scales. The inner, outer, and mesolayer variables and corresponding Reynolds equation (1) become the following:

Inner wall layer,

$$u = u_\tau f(\zeta,R_\phi), \quad \tau = \rho u_\tau^2 g(\zeta,R_\phi), \quad \zeta = \frac{Z_+}{\phi} \tag{9}$$

$$T = T_w + T_\tau f_t(\zeta,R_\phi), \quad \tau_t = \rho C_p u_\tau T_\tau g_t(\zeta,R_\phi) \tag{10}$$

$$\frac{df}{\phi d\zeta} + g = 1 - R_\phi^{-1}\zeta, \quad \frac{df_t}{\phi \mathrm{Pr} d\zeta} + g_t = 1 - R_\phi^{-1}\frac{u_\tau}{U_b}\int_0^\zeta f d\zeta \tag{11}$$

Outer defect layer,

$$u = U_c - u_\tau F(Y,R_\phi), \quad \tau = \rho u_\tau^2 G(Y,R_\phi), \quad Y = \frac{Z}{\delta} \tag{12}$$

$$T = T_c - T_\tau F_t(Y,R_\phi), \quad \tau_t = \rho C_P u_\tau T_\tau G_t(Y,R_\phi), \tag{13}$$

$$G = 1 - Y + \frac{R_\phi^{-1}}{\phi}\frac{dF}{dY}, \quad G_t = 1 - \frac{U_c}{U_b}Y + \frac{u_\tau}{U_b}\int_0^Y F dY + \frac{R_\phi^{-1}}{\phi \mathrm{Pr}}\frac{dF_t}{dY} \tag{14}$$

The matching of two layers in the overlap region for large Reynolds numbers $R_\phi\to\infty$ through Izakson–Millikan–Kolmogorov hypotheses (Afzal [15]) giving the functional equations for velocity and temperature profiles as described below.

$$f(\zeta) = \frac{U_c}{u_\tau} - F(Y), \quad \zeta\frac{df}{d\zeta} = Y\frac{dF}{dY} \tag{15}$$

$$f_t(\zeta) = \frac{T_c - T_w}{T_\tau} - F_t(Y), \quad \zeta\frac{df_t}{d\zeta} = Y\frac{dF_t}{dY} \tag{16}$$

The uniformly valid solution for velocity profile and friction factor becomes

$$\frac{u}{u_\tau} = \frac{1}{k}\ln\zeta + B + \frac{\Pi}{k}W(Y) \tag{17a}$$

$$\frac{U_c - u}{u_\tau} = -\frac{1}{k}\ln Y + \frac{\Pi}{k}[W(1) - W(Y)] \tag{17b}$$

$$\frac{U_c}{u_\tau} = \frac{1}{k}\ln R_\phi + B + D \tag{18}$$

where $W(Y)$ is the momentum wake function. The velocity profile (17*a*) for fully smooth surface yields Coles [16] wall-wake composite relation. The Reynolds shear stress results are

$$\frac{\tau}{\tau_w} = 1 - \frac{1}{\phi k\zeta} \tag{19a}$$

$$\frac{\tau}{\tau_w} = 1 - Y \tag{19b}$$

The uniformly valid solution for temperature profile and friction temperature becomes

$$\frac{T - T_w}{T_\tau} = \frac{1}{k_t}\ln\zeta + B_t + \frac{\Pi}{k}W_t(Y) \tag{20a}$$

$$\frac{T_c - T}{T_\tau} = -\frac{1}{k_t}\ln Y + \frac{\Pi_t}{k_t}[W_t(1) - W_t(Y)] \tag{20b}$$

$$\frac{T_c - T_w}{T_\tau} = \frac{1}{k_t}\ln R_\phi + B_t + D_t \tag{21}$$

where $W_t(Y)$ is the thermal wake function. The Reynolds heat flux results are

$$\frac{\tau_t}{q_w} = 1 - \frac{1}{\phi k_t \mathrm{Pr}\zeta} \tag{22a}$$

$$\frac{\tau_t}{q_w} = 1 - \frac{U_c}{U_b}Y \tag{22b}$$

The elimination of $\ln R_\phi$ term from relations (18) and (21) may be expressed as an alternate relation

$$\frac{2\mathrm{St}}{C_f} = \frac{k_t}{k}\left[1 + \left\{(B_t + D_t)\frac{k_t}{k} - (B + D)\right\}\sqrt{\frac{C_f}{2}}\right]^{-1} \tag{23}$$

where St is the Stanton number and C_f is skin friction coefficient. For large Reynolds numbers $\mathrm{Re}\to\infty$, skin friction coefficient $C_f\to 0$ and relation (23) yield $2\mathrm{St}/C_f=k_t/k$. If Prandtl number $\mathrm{Pr}=1$ the solution implies $k_t=k$ and we get $2\mathrm{St}/C_f=1$ the Reynolds analogy [17] between the momentum and heat transfer for turbulent flow in transitional rough channel.

3 Intermediate Layer

The intermediate (mesolayer) variable is (Afzal [5–8])

$$\eta = \sqrt{\zeta Y} = YR_\phi^{1/2} = \zeta/R_\phi^{1/2} \tag{24}$$

The velocity and Reynolds shear stress relations are

$$u = U_m - u_\tau\mathcal{F}(\eta,R_\phi) \tag{25a}$$

$$\tau = \rho u_\tau^2[1 - R_\phi^{-1/2}\mathcal{G}(\eta,R_\phi)] \tag{25b}$$

and the temperature and thermal Reynolds heat flux relations are

$$T = T_m - T_\tau\mathcal{F}_t(\eta,R_\phi) \tag{26a}$$

$$\tau_t = \rho C_p u_\tau T_\tau[1 - R_\phi^{-1/2}\mathcal{G}_t(\eta,R_\phi)] \tag{26b}$$

The Reynolds mean momentum and energy equations (4) and (5) become

$$\frac{d\mathcal{F}}{\phi d\eta} + \mathcal{G} = \eta \tag{27a}$$

$$\frac{d\mathcal{F}_t}{\phi \mathrm{Pr} d\eta} + \mathcal{G}_t = \frac{U_m}{U_b}\eta - \frac{u_\tau}{U_b}\int_0^\eta \mathcal{F} d\eta \tag{27b}$$

The matching of three layers would have two overlap regions. Overlap 1 region is between outer layer and intermediate layer and Overlap 2 region is between intermediate layer and inner layer. In each overlap region, the matching may be carried out for large Reynolds numbers $R_\phi \to \infty$ giving the functional equations for velocity and temperature profiles. On the other hand, the addition of relations (17*a*) and (17*b*) leads to velocity distribution in the intermediate layer variable η as where uniformly valid velocity profile becomes

$$\frac{u - U_m}{u_\tau} = \frac{1}{k} \ln \eta + \frac{1}{2}(B - D) + \frac{\Pi}{2k} W(Y) \tag{28}$$

where $U_m = U_c/2$ is the characteristic intermediate layer velocity. Based on relation (28), the Reynolds momentum equation (27*a*) gives Reynolds shear stress in the intermediate layer as

$$\frac{\tau}{\tau_w} = 1 - R_\phi^{-1/2}\left(\eta + \frac{1}{k\phi\eta}\right) + R_\phi^{-1}\frac{\Pi}{2\phi k}\frac{dW}{dY} \tag{29}$$

The above relations, in the intermediate layer, become

$$\frac{u - U_m}{u_\tau} = \frac{1}{k} \ln \eta + \frac{1}{2}(B - D) \tag{30}$$

$$\tau_+ = 1 - R_\phi^{-1/2}\left(\eta + \frac{1}{k\phi\eta}\right) \tag{31}$$

where $\tau_+ = \tau/\tau_w$. The Reynolds-stress maxima $\eta_{\max}$ and maximum value $\tau_{\max}$ are

$$\eta_{vm} = \frac{1}{\sqrt{k\phi}} \tag{32a}$$

$$\frac{\tau_m}{\tau_w} = 1 - \frac{2}{\sqrt{\phi k R_\phi}} \tag{32b}$$

In terms of wall variables, these results may be expressed as given below

$$Z_{+vm} = \sqrt{\frac{R_\tau}{k}} \tag{33a}$$

$$\frac{\tau_m}{\tau_w} = 1 - \frac{2}{\sqrt{kR_\tau}} \tag{33b}$$

The addition of relations (20*a*) and (20*b*) gives temperature distribution in intermediate layer variable η as where uniformly valid temperature profile becomes

$$\frac{T - T_m}{T_\tau} = \frac{1}{k_t} \ln \eta + \frac{1}{2}(B_t - D_t) + \frac{\Pi_t}{2k_t} W_t(Y) \tag{34}$$

where $T_m = (T_c + T_w)/2$ is the characteristic intermediate layer temperature. Based on relation (34), the Reynolds thermal equation (28) gives Reynolds hear flux in the intermediate layer as

$$\frac{\tau_t}{q_w} = 1 - R_\phi^{-1/2}\left(\frac{u_c}{U}M(\eta) + \frac{u_c}{2U}\eta + \frac{1}{k_t\phi \mathrm{Pr}\,\eta}\right) + R_\phi^{-1}\frac{\Pi_t}{2\phi k_t \mathrm{Pr}}\frac{dW_t}{dY} \tag{35}$$

where $M(\eta) = \int_0^\eta \mathcal{F} d\eta$. The temperature profile and thermal Reynolds stress become

$$\frac{T - T_m}{T_\tau} = \frac{1}{k_t} \ln \eta + \frac{1}{2}(B_t - D_t) \tag{36}$$

$$\tau_{t+} = 1 - R_\phi^{-1/2}\left(\frac{1}{\phi k_t \mathrm{Pr}\,\eta} + \frac{U_c}{2U_b}\eta\right) \tag{37}$$

where $\tau_{t+} = \tau/q_w$. The thermal Reynolds-stress maxima η_{tm} and maximum value τ_{tm} are

$$\eta_{\mathrm{tm}} = \sqrt{\frac{2U_b/U_c}{\phi k_t \mathrm{Pr}}} \tag{38a}$$

$$\frac{\tau_{\mathrm{tm}}}{q_w} = 1 - \sqrt{\frac{2U_c/U_b}{\phi k_t \mathrm{Pr} R_\tau}} \tag{38b}$$

In terms of wall variables, the result (38*a*) becomes

$$Z_{+\mathrm{tm}}\mathrm{Pr} = \sqrt{\frac{2U_b}{U_c}\frac{\mathrm{Pr}R_\tau}{k_t}} \tag{39}$$

4 Results and Discussion

In present work, a simple expression for roughness scale ϕ is proposed (Afzal and Seena [12])

$$\phi = 1 + \chi h_+ \exp\left(-\frac{j}{h_+}\right) \tag{40a}$$

$$\Delta U_+ = \frac{1}{k} \ln \phi \tag{40b}$$

where $\chi = \exp[k(B - B_F)]$, B and B_F, respectively, are the additive constants in inner log law velocity profiles for fully smooth wall and fully rough wall, $j \neq 0$ is a free parameter. The particular value $j = 0$ corresponds to Colebrook [18] monotonic commercial roughness. The roughness scale ϕ relation (40*a*) for parameter $j \neq 0$ has a point of inflection at origin $h_+ = 0$. The choice $j = 11$ for inflectional roughness (sand grain data of Nikuradse [19] compares well with the data. Further, the exponential function in the relation (40*a*) approaches unity and zero, respectively, $h_+ \to \infty$ and $h_+ \to 0$, that maintain, for example, the friction factor expression of the Nikuradse [19] for fully rough pipes and Prandtl [20] for fully smooth pipes.

The intermediate layer or the mesolayer scale

$$\Delta = \sqrt{\frac{\nu\delta}{\phi u_\tau}} \tag{41a}$$

$$\frac{\Delta}{\delta} = R_\phi^{-1/2} \tag{41b}$$

is fundamental for description of the mean flow. The present analysis shows that the velocity distribution (30) in the intermediate layer is governed by half-velocity defect law $(u - U_m)/u_\tau$ versus η, where $U_m = U_c/2$ and for fully smooth surface $\phi = 1$ and intermediate layer variable $\eta = \xi$. The half-velocity defect profiles $(u - U_m)/u_\tau$ versus ξ are shown in Figs. 1(*a*), 2(*a*), and 3(*a*) from fully smooth channel direct numerical simulation (DNS) data of Iwamoto et al. [21] for $R_\tau = 109.4$, 150.5, 297.9, 395.8, and 642.5, Abe et al. [22,23] for $R_\tau = 180$, 395, 640, and 1020, and Hoyas and Jimenez [24] for $R_\tau = 186$, 550, 930, and 2003. Our mesolayer prediction (30), marked by a solid line in the same figures, is supported by the DNS data. The location $\eta_{1/2}$ from relation (37) where mesolayer convection/advection velocity is $U_m = U_c/2$ yields

$$\eta_{1/2} = \exp(-kC), \quad \zeta_{+1/2} = \exp(-kC)\sqrt{R_\phi} \tag{42}$$

The data on fully smooth surface ($\phi = 1$) analyzed by Afzal [5–7] predicted $y_{+1/2} = 0.44\sqrt{R_\tau}$ for fully developed turbulent pipe flow and $y_{+1/2} = 0.75\sqrt{R_\tau}$ for turbulent boundary layer.

The Reynolds shear stress in the intermediate layer variables $(\tau_+ - 1)\sqrt{R_\phi}$ versus η is predicted by the relation (31). In fully smooth wall variables, the Reynolds shear stress $(\tau_+ - 1)\sqrt{R_\tau}$ versus ξ in the intermediate layer are shown in Figs. 1(*b*), 2(*b*), and 3(*b*) from DNS data of Iwamoto et al. [21] for $R_\tau = 109.4$, 150.5, 297.9, 395.8, and 642.5, Abe et al. [22,23] for $R_\tau = 180$, 395, 640, and 1020, and Hoyas and Jimenez [24] for $R_\tau = 186$, 550, 930, and

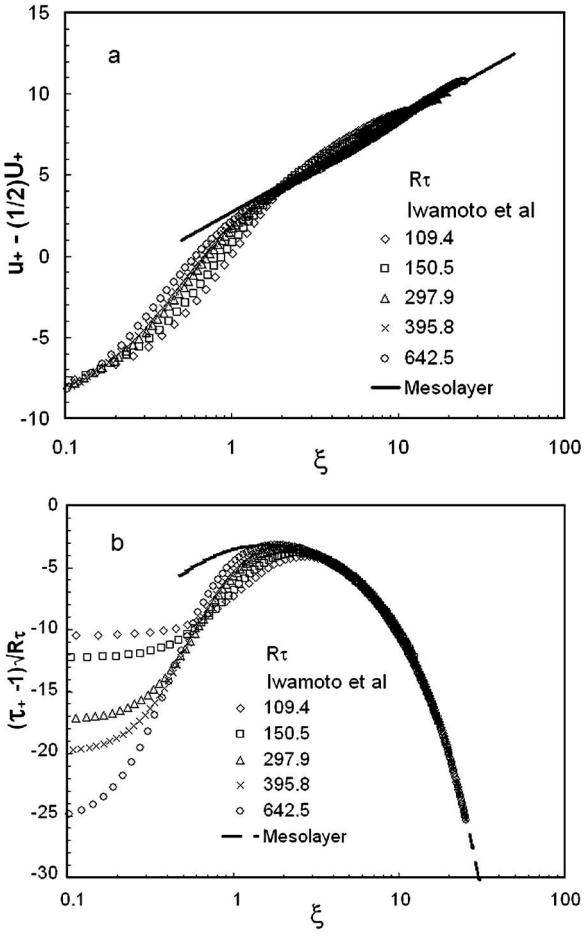

Fig. 1 The comparison of fully smooth channel DNS data of Iwamoto et al. [21] with the intermediate layer theory. (*a*) Half-defect ($U_m=U_c/2$) velocity profile data and our prediction Eq. (30). (*b*) Reynolds shear stress data and our prediction (31).

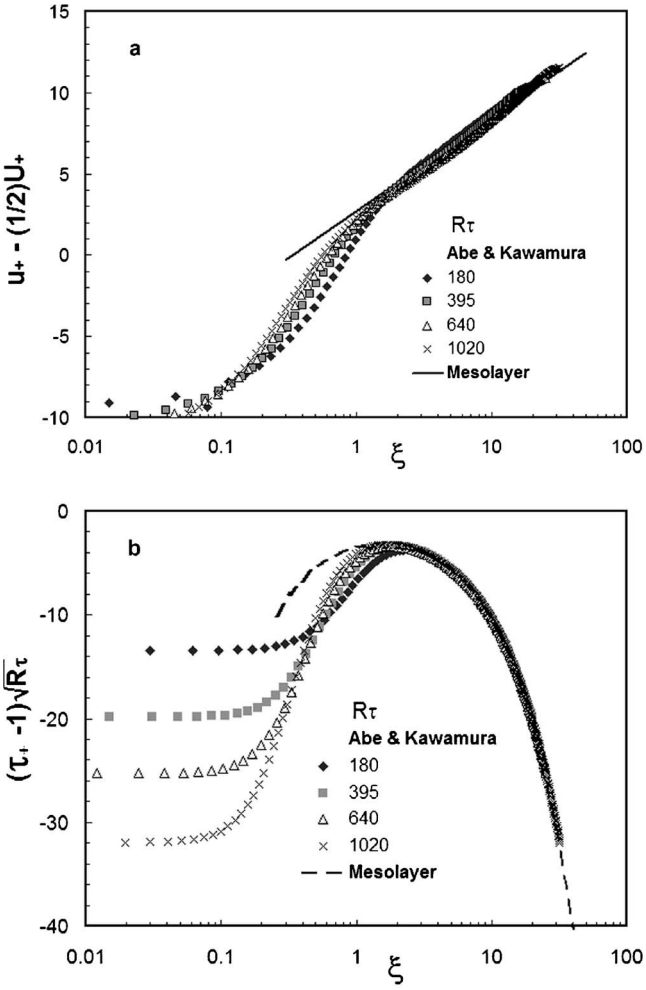

Fig. 2 The comparison of fully smooth channel DNS data of Abe et al. [22] with the intermediate layer theory. (*a*) Half-defect ($U_m=U_c/2$) velocity profile data and our prediction Eq. (30). (*b*) Reynolds shear steers data and our prediction (31).

2000. Our prediction (31) for Reynolds shear stress that is marked by dashed lines in same figures compares well with DNS data for $\eta>2$.

The Reynolds shear stress maximum value and its location are given by the relations (39) in the intermediate layer variables. In the wall layer variables, the relations (33*a*) and (33*b*) give the location and magnitude of the maxima of Reynolds shear stress, which are explicitly independent of transitional surface roughness. However, the functions Z_{+m} and R_τ depend on roughness through normal coordinate $Z=y+\epsilon_r$, where the origin ϵ_t is located below the top of the roughness element, caused by irregular protrusions of the hydraulic roughness of height h. Consequently, effect of surface roughness is to shift the origin of normal coordinate for the velocity distribution and Reynolds shear stress. For fully smooth surface $\epsilon_r=0$, the location and magnitude of maxima of Reynolds shear stress relations (33*a*) and (33*b*) yield

$$y_{+vm}=\sqrt{\frac{R_\tau}{k}} \tag{43a}$$

$$\frac{\tau_m}{\tau_w}=1-\frac{2}{\sqrt{kR_\tau}} \tag{43b}$$

These relations were first given by Afzal [5,6], where $k=0.4$ predicted $y_{+\max}/\sqrt{R_\tau}=1.58$ and with $k=0.39$ giving $y_{+\max}/\sqrt{R_\tau}=1.60$, whereas experimental data predicted 1.85 (Afzal [5,6]) and 1.87 (Long and Chen [25]). The Reynolds shear stress maximum $\tau_{+\max}$ and location $y_{+\max}$ are shown in Figs. 4(*a*) and 4(*b*) from fully smooth pipe and channel data from experimental of Zanoun [26], DNS data of Iwamoto et al. [21], Abe et al. [22,23], Hoyas and Jimenez [24], and Moser et al. [27]. These data are in very good agreement with our prediction (43*a*) and (43*b*), and for $R_\tau \leqslant 1000$ the little departure of the data may be taken as a higher order effect.

The machine honed surface transitional super pipe data of Shockling [28] for roughness $\delta/h=7190$ and $0.1\leqslant h_+\leqslant 45$ is analyzed here in the intermediate layer. These data in the inner and outer variables have been analyzed by Afzal and Seena [12] where for roughness scale ϕ their prediction (40*a*) and (40*b*) with $j=11$ compare very well with the inflectional roughness of Shockling [28] and $j=0$ corresponds to Colebrook [18] monotonic roughness. In terms of half-velocity defect $U_m=U_c/2$, the intermediate layer velocity distribution in the variables $(u-U_m)/u_\tau$ versus ξ is shown in Fig. 5(*a*). The data shift their locations with change of roughness parameter h_+ for a prescribed δ/h. The half-velocity defect in mesolayer $(u-U_m)/u_\tau$ versus η, as shown in Fig. 5(*b*), is universal, explicitly independent of transitional surface roughness. The universality of our prediction (30) for half-velocity defect mesolayer velocity, based on roughness scale (40*a*) and (40*b*) with $j=11$, is supported very well by the data.

The temperature distribution in the mesolayer layer is governed by half-temperature defect law (34), where $T_m=(T_w+T_c)/2$ and is supported by DNS data of Abe et al. for $R_\tau=180$, 395, 640 and

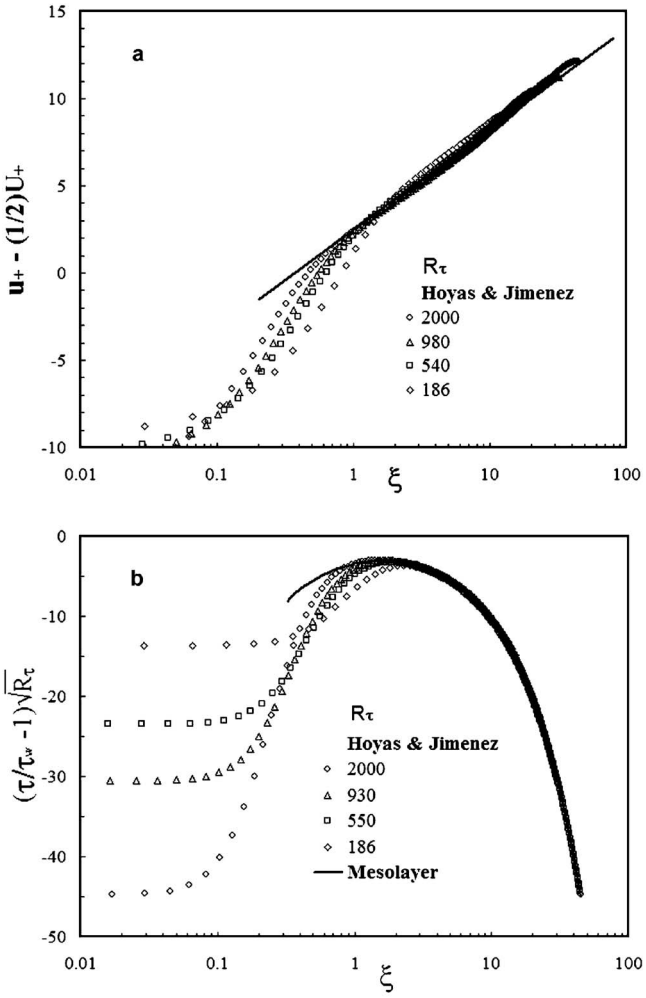

Fig. 3 The comparison of fully smooth channel DNS data of Hoyas and Jimenez [24] with the intermediate layer theory. (*a*) Half-defect ($U_m = U_c/2$) velocity profile data and our prediction Eq. (30). (*b*) Reynolds shear steers data and our prediction (31).

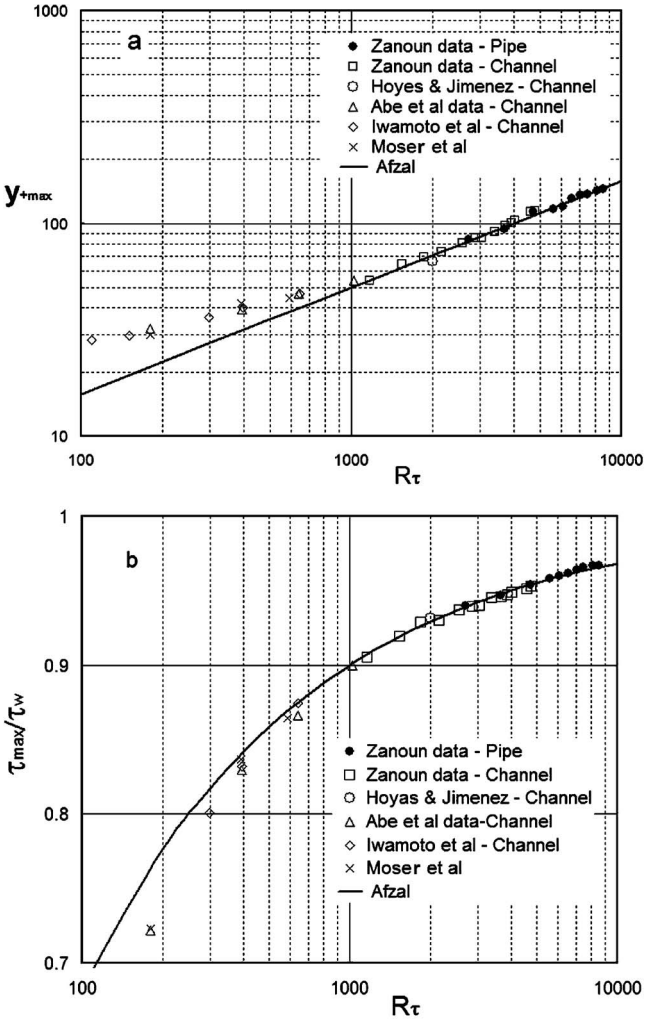

Fig. 4 Comparison of the maxima of the Reynolds shear stress (*a*) Location y_{+max} (*b*) Maximum value τ_{max}/τ_w with fully smooth ($\phi=1$) pipe and channel data of Zanoun [26], channel DNS data of Iwamoto et al. [21], Abe et al. [22,23], Hoyas and Jiemenz [24], and Moser et al. [27].

1020 shown in Fig. 6(*a*), where our prediction (34) is marked by a solid line. In the mesolayer, the Reynolds heat flux is shown in Fig. 6(*b*) from DNS data of Abe et al. for $R_\tau=180$, 395, 640 and 1120. Our prediction of Reynolds heat flux stress (37) also shown in the same figure compares well with DNS data for $\eta>2$. For fully smooth surface $\epsilon_r=0$, the location and magnitude of maxima of Reynolds heat stress from (38*a*) and (38*b*) are

$$y_{+\mathrm{tm}}\mathrm{Pr} = \sqrt{\frac{2U_b}{U_c}\frac{\mathrm{Pr}R_\tau}{k_t}} \tag{44a}$$

$$\frac{\tau_{\mathrm{tm}}}{q_w} = 1 - \sqrt{\frac{2U_c/U_b}{\phi k_t \mathrm{Pr}R_\tau}} \tag{44b}$$

The location and magnitude of Reynolds heat flux maxima are shown in Figs. 7(*a*) and 7(*b*) from DNS data of Abe et al. for $R_\tau=180$, 395, 640 and 1020. The present prediction (44*a*) and (44*b*) also shown in the same figures is supported very well by the data.

The location of the mean velocity U_{m1} at the peak of Reynolds shear stress with respect to outer velocity from data in boundary layer, channel, and pipe by Wooldridge and Muzzy [29] and Simpson [30] reported $U_{m1}/U_c=0.60$ and 0.63, respectively, which is nearly the same as $U_m/U_c=2/3$ (Afzal [6]) in mesolayer.

The location of the mean temperature T_{m1} at the peak of Reynolds heat flux with respect to excess of outer temperature over wall temperature in the thermal boundary layer. From data of Iwamoto et al. for Iwamoto et al. [21] for $R_\tau=109.4$, 150.5, 297.9, 395.8, and 642.5, Abe et al. [22,23] for $R_\tau=180$, 395, 640, and 1020 and Hoyas and Jimenez [24] for $R_\tau=186$, 550, 930, and 2000 are shown in Fig. 8. The figure implies that the large Reynolds-number asymptotes for mesolayer velocity and mesolayer temperature

$$\frac{U_{mR}}{U_c} = \frac{2}{3} \tag{45a}$$

$$\frac{T_{mR} - T_w}{T_c - T_w} = \frac{2}{3} \tag{45b}$$

are of order unity, but less than one.

The extension of Izakson–Millikan argument for moderately large Reynolds numbers demanded the order of the higher order effect. Further, for lower Reynolds numbers it is not known to what order the Izakson [31] and Millikan [14] argument is valid. Afzal [15] postulated that in fully developed turbulent flow in a pipe or channel, the higher order effect is of order R_ϕ^{-1} and the additional terms $1/y_+$ to inner log law and Y to outer log law arise

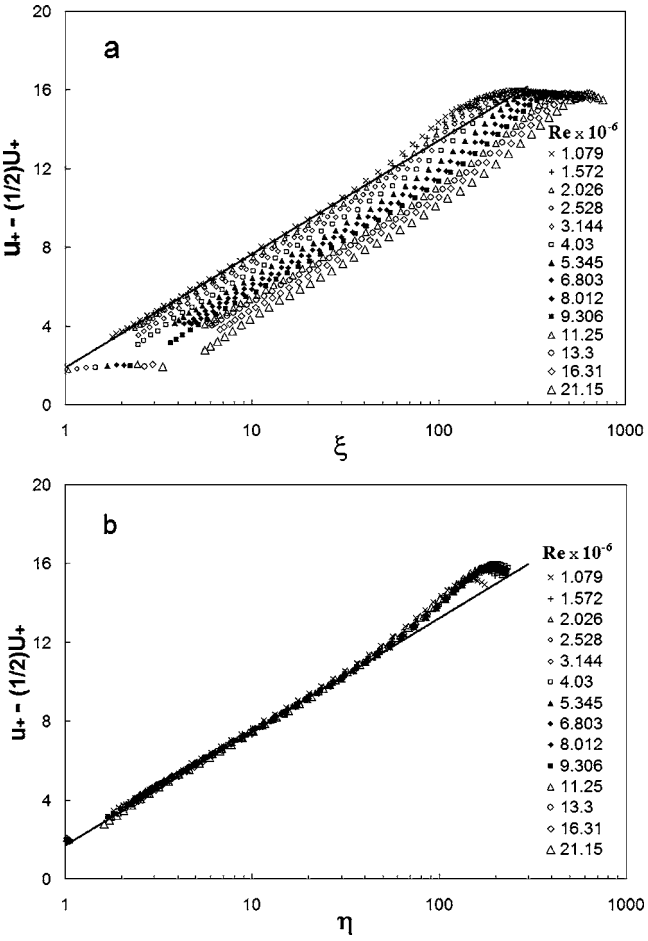

Fig. 5 Half-defect ($U_m=U_c/2$) velocity profile data in the intermediate layer for transitional rough surface for Shockling [28] for machined honed pipe roughness. (*a*) Nonuniversal behavior in traditional mesolayer variables $(u-U_m)/2$ versus ξ. (*b*) Our universal intermediate layer half-defect law $(u-U_m)/2$ versus η. Predictions based on roughness scale (47) with $j=11$.

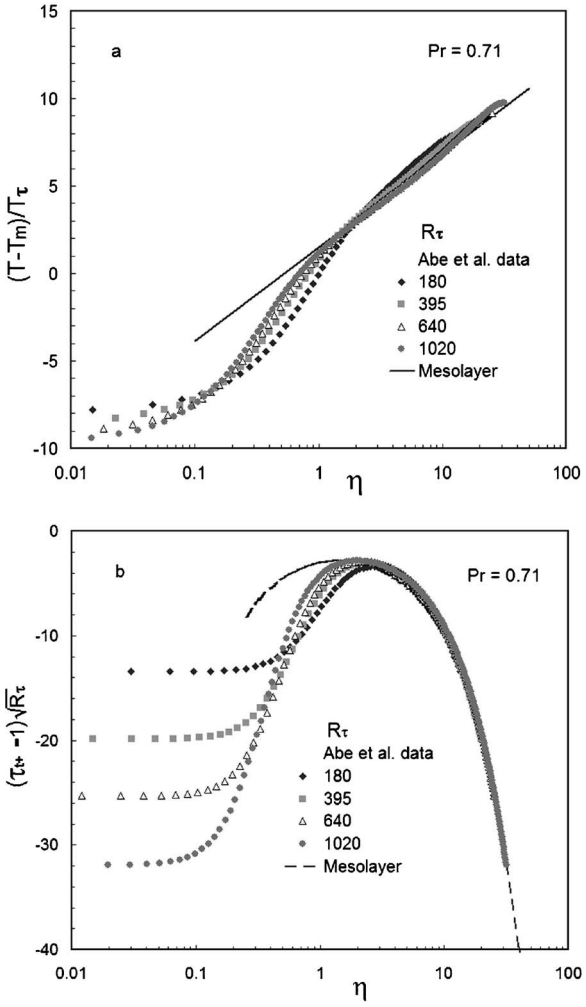

Fig. 6 The comparison of the fully smooth channel ($\phi=1$, $\eta=\xi$) DNS data of Abe et al. [22,23] with the intermediate layer thermal convection theory. (*a*) Half-defect $[T_m=(T_w+T_c)/2]$ temperature profile data and our prediction Eq. (36). (*b*) Reynolds heat flux profile data and our prediction (37).

in lowest order log law solutions. It can be shown that in the intermediate layer ($\eta=y_+/\sqrt{R_\phi}=\sqrt{R_\phi}Y$) the velocity profile may be obtained from the addition of the inner and outer layer expansions of Afzal [15]. The velocity profile in terms of generalized logarithmic law provided from the intermediate layer solution, following Afzal [15], becomes (Afzal [32])

$$u_+ = A_0 \ln \zeta + B_0 + \frac{B_{0,1}}{\zeta} + D_{0,1}Y + \frac{B_{0,2}}{\zeta^2} + D_{0,2}Y^2 + \cdots \quad (46)$$

where A_0, B_0, $B_{0,1}$, $D_{0,1}$, and $B_{0,2}$ are the constants independent of the Reynolds number. In a manner analogous to Eq. (46) the temperature profile as the generalized logarithmic law from intermediate layer becomes

$$\frac{T-T_w}{T_\tau} = A_{t0} \ln \zeta + B_{t0} + \frac{B_{t0,1}}{\zeta} + D_{t0,1}Y + \frac{D_{t0,1}}{\zeta^2} + D_{t0,2}Y^2 + \cdots \quad (47)$$

where A_{t0}, B_{t0}, $D_{t0,1}$, $D_{t0,1}$, and $D_{t0,2}$ are the constants independent of Reynolds number.

From mesolayer theory, Afzal [5,6] found that the higher order effects are of order $R_\phi^{-1/2}$ and the additional terms $1/\sqrt{y_+}$ to inner log law and $\sqrt{Y}$ to outer log law arise in lowest order log law solutions, and the alternate generalized logarithmic law for velocity distribution yields

$$u_+ = A_0 \ln \zeta + B_0 + \frac{B_{0,1/2}}{\sqrt{\zeta}} + b_{0,1/2}\sqrt{Y} + \frac{B_{0,1}}{\zeta} + b_{0,1}Y + \cdots \quad (48)$$

Likewise, for temperature distribution the alternate generalized logarithmic law is

$$\frac{T-T_w}{T_\tau} = A_{t0} \ln \zeta + B_{t0} + \frac{B_{t0,1/2}}{\sqrt{\zeta}} + D_{t0,1/2}\sqrt{Y} + \frac{B_{t0,1}}{\zeta} + D_{t0,1}Y + \cdots \quad (49)$$

It can also be shown that the generalized logarithmic law of velocity temperature distributions are also valid for moderately large Reynolds numbers provided various coefficients of powers of ζ and Y terms and the constants of the additive terms are regarded as a function ϵ, the inverse of roughness friction Reynolds number (Afzal [32]).

The intermediate layer velocity distribution, in terms of velocity U_{mR} at the maxima of Reynolds shear stress, may be expressed in nondimensional form as

$$\frac{u-U_{mR}}{u_\tau} = J(\eta) \quad (50a)$$

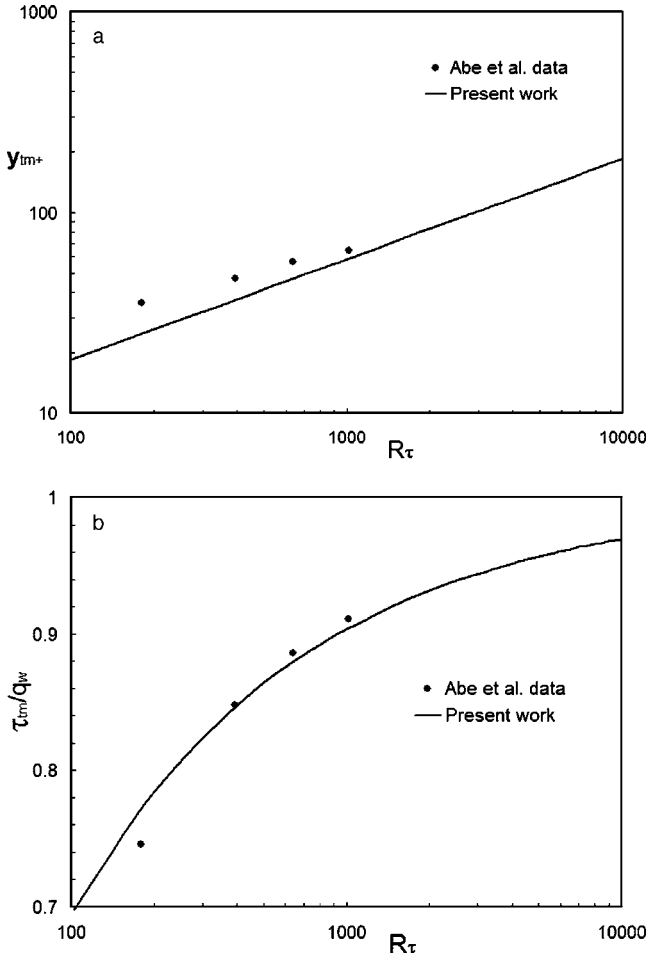

Fig. 7 Comparison of our predictions with the peak of the Reynolds heat flux with DNS data of Abe et al. [22,23] fully smooth channel. (*a*) Location y_{+tm}; (*b*) Maximum value τ_{tm}/q_w.

$$\frac{u - U_{mR}}{u_\tau} = J_1(\eta - \eta_m) \tag{50b}$$

where for fully smooth surface $\eta = \xi$ and $\eta_m = \xi_m$. The intermediate velocity profile $(u - U_{m1})/u_\tau$ versus ξ for fully smooth channel

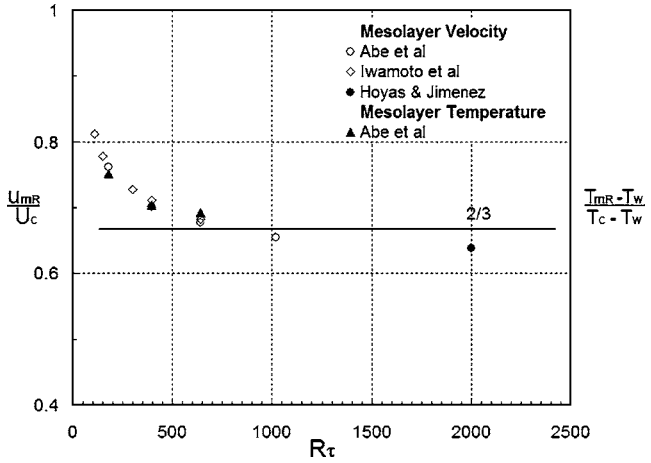

Fig. 8 Comparison of the intermediate layer velocity U_{mR} and intermediate layer temperature T_{mR} at the points of maximum Reynolds shear stress and Reynolds heat flux with fully smooth channel DNS data by Iwamoto et al. [21], Abe et al. [22,23], and Hoyas and Jiemenez [24]. Present proposal: —— 2/3 asymptote for large Reynolds numbers.

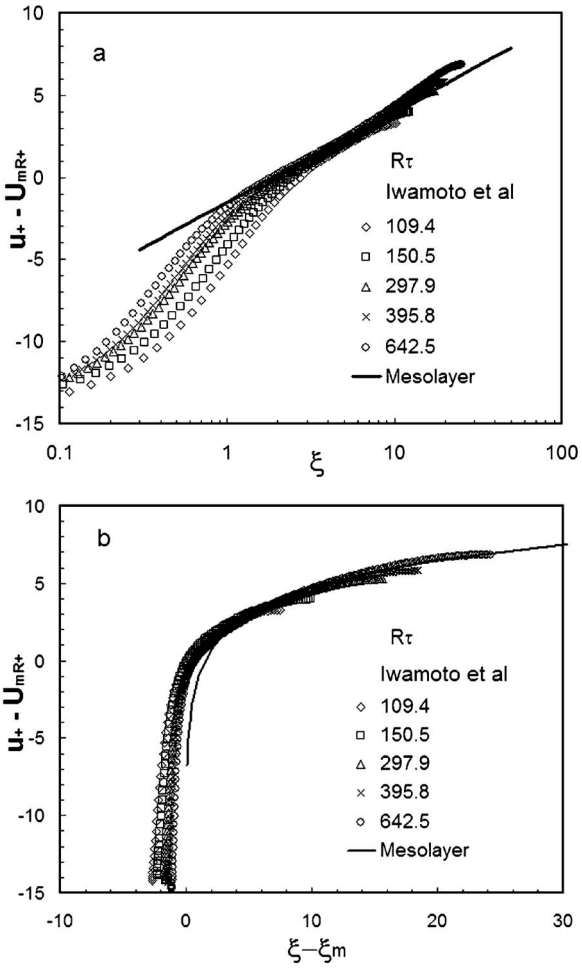

Fig. 9 Velocity distribution $(u - U_{m1})/u_\tau$ in the intermediate layer from smooth channel DNS data of Iwamoto et al. [21], where the velocity U_{m1} is estimated at maxima of Reynolds shear stress. (*a*) Intermediate layer variable ξ. (*b*) Alternate intermediate layer variable $\xi - \xi_m$ from maxima in Reynolds shear stress. (—) Intermediate layer log region for velocity distribution.

from DNS data of Iwamoto et al. [21] for $R_\tau = 109.4$, 150.5, 297.9, 395.8, and 642.5 are shown in Figs. 9(*a*) and 9(*b*). The data of Abe et al. [22,23] for $R_\tau = 180$, 395, 640, and 1020 and Hoyas and Jimenez [24] data for $R_\tau = 2003$ are shown in Figs. 10(*a*) and 10(*b*). A line marked, in each of these figures, shows logarithmic behavior in the intermediate velocity distribution.

The mesolayer temperature distribution, in terms of temperature T_{mR} at the maxima of Reynolds heat flux, may be expressed in nondimensional form as

$$\frac{T - T_{mR}}{T_\tau} = K(\eta) \tag{51a}$$

$$\frac{T - T_{mR}}{T_\tau} = K_1(\eta - \eta_{tm}) \tag{51b}$$

For fully smooth surface $\eta_t = \xi_t$ and $\eta_{tm} = \xi_{tm}$. The mesolayer profile profile $(T - T_{mR})/T_\tau$ versus ξ for fully smooth channel from DNS data of Abe et al. [22,23] for $R_\tau = 180$, 395 and 640 shown in Figs. 11(*a*) and 11(*b*). A line marked, in each of these figures, shows logarithmic behavior in the mesolayer temperature distribution.

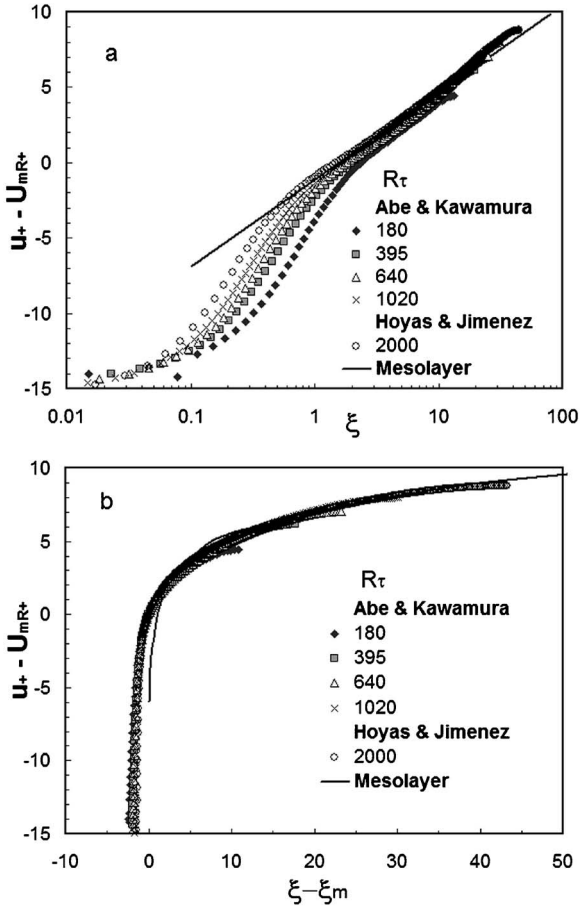

Fig. 10 Velocity distribution $(u-U_{mR})/u_\tau$ data in the intermediate layer from smooth channel DNS data of Abe et al. [22] and Hoyas and Jimenez [24], where the velocity U_{mR} is estimated at maxima of Reynolds shear stress. (*a*) Intermediate layer variable ξ. (*b*) Alternate intermediate layer variable $\xi-\xi_m$ from maxima in Reynolds shear stress. (—) Intermediate layer log region for velocity distribution.

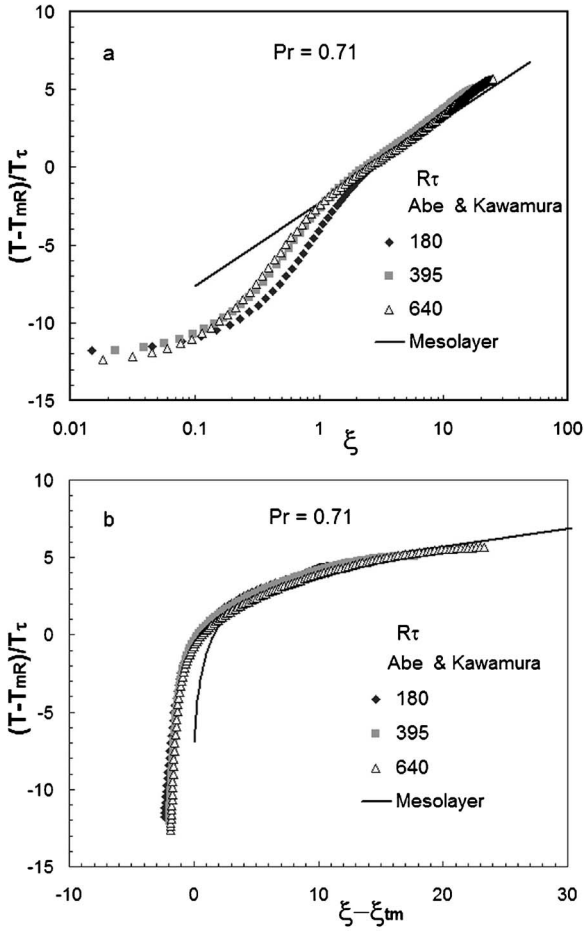

Fig. 11 Temperature distribution $(T-T_{mR})/T_\tau$ in the intermediate layer from smooth channel DNS data of Abe et al. [22], where the temperature T_{mR} is estimated at maxima of Reynolds heat flux. (*a*) Intermediate layer variable ξ. (*b*) Alternate intermediate layer variable $\xi-\xi_{tm}$ from maxima in Reynolds shear stress. (—) Intermediate layer log region for temperature distribution.

5 Conclusions

The analysis deals with four alternates: the inner wall transitional roughness variable $\zeta=Z_+/\phi$, associated with a particular roughness level, defined by roughness scale ϕ connected with roughness function ΔU_+, the roughness friction Reynolds number R_ϕ (based on roughness friction velocity), and roughness Reynolds number Re_ϕ (based on roughness average velocity) where the mean turbulent flow, little above the roughness sublayer, does not depend on transitional roughness.

The traditional two-layer approximation is merely an approximation that was introduced to pick out the main features of the flow. It is shown here that adding an intermediate layer will provide a further better result, and one may hope that fact adding more intermediate layers will provide even better results. As we are dealing with open Reynolds mean momentum equations without any closure model, it is not possible to find out all the necessary substantive intermediate layers in the sense the method of matched asymptotic expansions. Thus, the observations from data show that the intermediate layer plays a crucial role. The higher order effects in the intermediate layer provide uniformly valid solution in terms of generalized logarithmic laws for the velocity and temperature distributions.

An intermediate layer, between the inner and outer layers, has been proposed for thermal turbulent boundary layer in a transitional surface roughness of the channel. The mesolayer velocity is $U_m=U_c/2$ and mesolayer temperature is $T_m=(T_w+T_c)/2$. In the intermediate layer, the velocity distribution is given by half-defect velocity law and temperature distribution by half temperature detect law that is explicitly independent of surface roughness.

Our predictions for the Reynolds shear stress and Reynolds heat flux profiles compare well with data in the intermediate layer. The peak value and location of the Reynolds shear stress and Reynolds heat flux profiles also compare well with data for large Reynolds numbers.

The data in the intermediate layer provide strong support to our proposed log laws as the universal relations that are explicitly independent transitional surface roughness. There is no universality of scaling in traditional variables and different expressions are needed for various types of roughness, as suggested, for example, with inflectional type roughness, monotonic Colebrook–Moody roughness, etc. In traditional variables, the roughness scale for inflectional type roughness is supported very well by experimental data.

Acknowledgment

N.A. is thankful to the All India Council of Technical Education, New Delhi for the support of this work.

References

[1] Incropera, F. P., and DeWitt, D. P., 1985, *Introduction to Heat Transfer*, 1st ed., Wiley, New York.

[2] Kays, W. M., and Crawford, M., 1983, *Convective Heat and Mass Transfer*, 3rd ed., McGraw-Hill, New York.

[3] Afzal, N., and Yajnik, K., 1971, "Asymptotic Theory of Heat Transfer in Two Dimensional Turbulent Boundary Layers," Z. Angew. Math. Phys., **22**, pp. 863–865.

[4] Kader, B. A., and Yaglom, A. M., 1972, "Heat and Mass Transfer Laws for Fully Turbulent Wall Flows," Int. J. Heat Mass Transfer, **15**, pp. 2329–2351.

[5] Afzal, N., 1982, "A Sub-Boundary Layer With a Two Dimensional Turbulent Boundary Layer," J. Mec. Theor. Appl., **1**, pp. 963–973.

[6] Afzal, N., 1982, "Fully Developed Turbulent Flow in a Pipe: An Intermediate Layer," Arch. Appl. Mech., **53**, pp. 355–377.

[7] Afzal, N., 1984, "The Mesolayer Theory of Turbulent Flows," AIAA J., **22**, pp. 437–439.

[8] Afzal, N., 1984, "Period Between Bursting in Turbulent Shear Flow: Intermediate Scaling," Curr. Sci., **53**(12), pp. 640–642.

[9] Wei, T., Fife, P., Klewicki, J., and McMurtry, P., 2005, "Properties of the Mean Momentum Balance in Turbulent Boundary Layer, Pipe and Channel Flows," J. Fluid Mech., **522**, pp. 303–327.

[10] Wei, T., Fife, P., and Klewicki, J., 2007, "On Scaling the Mean Momentum Balance and its Solutions in Turbulent Couette–Poiseuille," J. Fluid Mech., **573**, pp. 371–398.

[11] Wei, T., Fife, P., Klewicki, J., and McMurtry, P., 2005, "Scaling Heat Transfer in Fully Developed Turbulent Channel Flows," Int. J. Heat Mass Transfer, **48**, pp. 5284–5296.

[12] Afzal, N., and Seena, A., 2007, "Alternate Scales for Turbulent Flow in Transitional Rough Pipes: Universal Log Laws," ASME Trans. J. Fluids Eng., **129**, pp. 80–90.

[13] Clauser, F. H., 1956, "The Turbulent Boundary Layer," *Advances in Applied Mechanics*, Vol. 4, Academic, New York, pp. 2–52.

[14] Millikan, C. B., 1939, "A Critical Discussion of Turbulent Flows in Channels and Circular Tubes," *Proceedings of the Fifth International Congress on Applied Mechanics*, J. P. den Hartog and H. Peters, eds., Wiley, New York/ Chapman and Hall, London, pp. 386–392.

[15] Afzal, N., 1976, "Millikan Argument at Moderately Large Reynolds Numbers," Phys. Fluids, **19**, pp. 600–602.

[16] Coles, D., 1956, "The Law of the Wake in the Turbulent Boundary Layer," J. Fluid Mech., **1**, pp. 191–226.

[17] Karman, V. T., 1939, "The Analogy Between Skin Friction and Heat Transfer," Trans. ASME, **61**, pp. 705–710.

[18] Colebrook, C. F., 1939, "Turbulent Flow in Pipes With Particular Reference to the Transition Region Between the Smooth and Rough Pipe Laws," J. Inst. Civ. Engr. London, **11**, pp. 133–156.

[19] Nikuradse, J., 1933, "Laws of Flow in Rough Pipe," VDI, Forchungsheft N-361, English translation NACA TM 1292.

[20] Prandtl, L., 1935, "The Mechanics of Viscous Fluids," *Aerodynamic Theory*, Vol. 3, W. F. Durand, ed., California Institute of Technology, Pasadena, pp. 34–208.

[21] Iwamoto, K., Suzuki, Y., and Kasagi, N., 2002, "Reynolds Numbers Effects on wall Turbulence: Towards Effective Feed Back Control," Int. J. Heat Fluid Flow, **177**, pp. 678–689.

[22] Abe, H., Kawamura, H., and Matsuo, Y., 2004, "Surface Heat-Flux Fluctuations in a Turbulent Channel up to R_τ=1020 With Pr=0.025 and 0.71," Int. J. Heat Fluid Flow, **25**, pp. 404–419.

[23] Abe, H., and Kawamura, H., 2002, "A Study of Turbulence Thermal Structure in a Channel Flow Through DNS up to R_τ=640 With Pr=0.025 and 0.71," *Proceedings of the Ninth Turbulence Conference*, pp. 399–402.

[24] Hoyas, S., and Jimenez, J., 2006, "Scaling of the Velocity Fluctuations in Turbulent Channels up to Re=2003," Phys. Fluids, **18**, p. 011702.

[25] Long, R. R., and Chen, T. C., 1981, "Experimental Evidence of the Existence of the Mesolayer in Turbulent Systems," J. Fluid Mech., **105**, pp. 19–59.

[26] Zanoun, E. S., 2003, "Answer to Some Open Questions in Wall-bounded Laminar and Turbulent Flows," Doctor-Ingeniur, University of Erlangen-Nurnberg, Germany.

[27] Moser, R. D., Kim, J., and Mansour, N. N., 1999, "Direct Numerical Simulation of Turbulent Channel Flow up to Re_τ=590," Phys. Fluids, **11**, pp. 943–945.

[28] Shockling, M. A., 2005, "Turbulent Flow in Rough Pipe," MSE thesis, Princeton University, Princeton, NJ.

[29] Wooldridge, C. E., and Muzzy, E. J., 1966, "Boundary Layer Turbulence Measurements With Mass Addition and Combustion," AIAA J., **4**, pp. 2009–2016.

[30] Simpson, R. L., 1970, "Characteristics of Turbulent Boundary Layers at Low Reynolds Numbers With and Without Transpiration," J. Fluid Mech., **42**, pp. 769–802.

[31] Izakson, A. A., 1937, "On Formula for the Velocity Distribution Near Walls," Tech. Phys, USSR, **4**, pp. 155–159.

[32] Afzal, N., 2008, "Generalized Logarithmic Laws for the Velocity and Temperature Profiles in a Turbulent Pipe and Channel Flows," unpublished.

Experimental and Numerical Study of One, Two, and Three Embedded Needle Cryoprobes Simultaneously Operated by High Pressure Argon Gas

Z. Magalov

A. Shitzer
e-mail: mersasa@tx.technion.ac.il

D. Degani

Department of Mechanical Engineering,
Technion, Israel Institute of Technology,
Haifa 32000, Israel

One, two, and three needle cryoprobes, 1.47 mm *outside diameter, simultaneously and uniformly operated by high pressure argon gas, were tested in a gel simulating the thermal properties of biological tissues. The probes were inserted into the same depth in the gel through two parallel templates with holes drilled on a* 5×5 mm^2 *mesh. The temperature of the active segment of the probe was monitored by a single soldered thermocouple (TC). Temperatures in the gel were monitored by K-type TC strings in the radial, and in the downward and upward axial directions. The phase-change problem in the gel was solved by* ANSYS7.0, *based on the enthalpy method. Calculated and measured results compared reasonably well with the most deviations observed in the upward axial direction. Results of this study may be summarized as follows: (a) Due to the cylindrical structure of the probe, the advancement of the frozen fronts was more pronounced in the upward axial and the radial directions than in the downward direction. (b) The farthest placement of the two probes* (10 mm) *yielded the largest volumes enclosed by the isothermal contours. (c) In the tightest two placement configurations of the three probes, the* -40°C *fronts of all frozen lumps have joined together even after* 1 min *of operation, while in the less tight configurations, joining occurred later. (d) In multiprobe applications and for a given duration of application, there exists a certain placement configuration that will produce the maximal volume of any temperature-specific frozen lump. The computational tool presented in this study could assist the surgeon in the preplanning of cryosurgical procedures and thus reduce uncertainties and enhance its success rate.*
[DOI: 10.1115/1.2804943]

Keywords: cryosurgery, multicryoprobes, ablation ratio, frozen volumes, lethal temperatures

Introduction

Cryosurgery is a medical technique involving the application of cryotemperatures for destroying undesired tissues [1]. It was in use as early as in the mid-19th century when James Arnott, an English physician, used salt-ice mixtures to treat malignant tissues [2]. The so-called "modern era" of cryosurgery was initiated in 1961, when Irving Cooper, an American neurosurgeon, developed a cryosurgical system [3]. In this system liquid nitrogen was used in a heat conducting metal tube the closed end of which was brought into contact with the treated tissue.

Cryosurgical destruction of biological tissues may be achieved by either one of the following processes: immediate and delayed. The immediate process involves direct destruction of cells while the delayed one invokes postapplication damage due to the destruction of blood vessels and/or a delayed immune system response. The immediate destruction process is dominated by the formation of intracellular ice obtained at high cooling rates or the osmotic drying of the cells due to the appearance of extracellular ice at low cooling rates. These processes were reviewed by Gage and Baust [4] and more recently by Hoffman and Bischof [5].

The key advantages of this technique are as follows: (a) invasion of the tissue is minimal, (b) the application is localized, (c) minimal loss of blood is involved, (d) it possesses unaesthetic capabilities, (e) duration of the application is short, (f) the procedure is repeatable, (g) it requires minimal hospitalization or may even be applied ambulatorily, (h) it incurs minimal cost, and, (i) in certain cases, it may invoke the immune system. In spite of these advantages, the cryosurgical technique is still finding limited applications, mainly in urology [6] and in dermatology [7]. The reason for this lack of wider popularity stems mainly from the uncertainty in the final outcome of the procedure and the inability to ensure complete freezing of the entire target tumor in a short application due to the latter's irregular shape.

The simultaneous application of multiprobes, in combination with modern imaging techniques, e.g., ultrasound, computerized tomography (CT) and magnetic resonance imaging (MRI), have alleviated these hindrances to a certain extent and have extended the use of cryosurgery in the treatment of prostate and liver cancer [1,6]. These imaging techniques, however, are incapable of acquiring detailed temperature distributions inside the frozen area. Ultrasound, which is the most commonly applied imaging technique in cryosurgery, has its own limitations. Among these is the opaqueness of the frozen phase (ice) to sound waves. Thus, obtaining detailed, three-dimensional temperature distribution data beyond the frozen front by ultrasound is not possible. Currently,

Contributed by the Heat Transfer Division of ASME for publication in the JOURNAL OF HEAT TRANSFER. Manuscript received September 15, 2006; final manuscript received June 18, 2007; published online March 6, 2008. Review conducted by Jay M. Khodadadi.

even the more expensive and complex CT or MRI imaging techniques are incapable of providing temperature details inside the frozen region.

An effective cryosurgical treatment, particularly of malignant tissues, requires that optimal destruction conditions be achieved throughout the entire volume of the tumor, including a predetermined margin for certainty. It is known that different types of cells exhibit different sensitivities to freezing but, in general, the lower is the temperature achieved, the higher is the rate of destruction. In the treatment of cancer, a sufficiently low temperature should be ensured so as to effect complete destruction. Mazur [8] defines the critical temperature for cell destruction within the range of $-5\,^{\circ}\mathrm{C}$ to $-50\,^{\circ}\mathrm{C}$. Intracellular ice forms in prostate cells at temperatures below $-40\,^{\circ}\mathrm{C}$ [9], which, therefore, serves as a target temperature in this application. Other investigators suggest that even higher temperatures, e.g., $-20\,^{\circ}\mathrm{C}$, may be lethal to the cells [10]. The cooling rate maintained at the freezing front has also been cited as a factor that determines the survival of the frozen tissue [11].

It follows from the above discussion that precise and detailed knowledge of the temperature field that develops during the freezing process is essential to the surgeon. Such information may be obtained by solving the dynamic heat transfer problem. The problem to be solved, referred to as the Stefan problem, is nonlinear mainly due to the removal of the heat of fusion liberated at the moving front separating the two phases. In tissues, unlike pure substances, e.g., pure water, phase-change transition occurs over a temperature range, which further complicates the analysis. Analytical solutions to this problem are few [12–14] as are those involving phase-change in biological tissue [15–17]. Consequently, investigators employ numerical solution techniques, e.g., the front tracking method [18] or the enthalpy method [19,20]. The application of multiprobes in tissuelike substances was analyzed by Keanini and Rubinsky [21] who presented a general technique for optimizing cryosurgical procedures. Rabin and Stahovich [22] and Rabin et al. [23] have introduced cryoheaters as a means of controlling the extent of the multiprobes' frozen region in order to protect certain tissue regions from destruction during the cryosurgical process. No experimental results were presented in any of these latter studies.

Rewcastle et al. [24] analyzed the ice ball formation using an axisymmetric, finite difference model around a single cryoprobe. Model predictions were compared to measured data and were found to conform to within $\pm 5\,^{\circ}\mathrm{C}$. Jankun et al. [25] developed an interactive software simulation package (CRYOSIM) for cryoablation of the prostate by liquid nitrogen operated cryoprobes. The model is based on a finite difference numerical technique. Acquired ultrasound data are used to online adjustment of model parameters and in the prediction of the temporal variations of the isothermal surfaces in the prostate. The package facilitates the simulation and tracking of the "therapeutic temperature" in the prostate. Baissalov et al. discussed a semiempirical treatment planning model for optimization of multiprobes [26]. They developed a finite element procedure to analyze the 3D heat transfer problem in a model of the prostate. Predicted locations of the frozen front were compared to x-ray readings to within ± 2 mm. The optimization procedure was demonstrated by simulating the placement of six cryoprobes at equal radial distances in a medium around a central urethral warmer. Rewcastle et al. [27] presented a 3D finite difference analysis of ice ball formation for one, three, and five cryoprobes. Results of the 3.4 mm diameter argon-operated probes, with 30 mm long active segments, yielded good comparisons to experimental data in gelatin. The authors defined an "ablation ratio" as the percentage volume of a certain temperature, which is considered ablative, or lethal, to the tissue, relative to the volume of the total frozen volume. The value of this ratio for their three-probe configuration was calculated at 0.21. Wan et al. [28] presented a finite element model of multiprobe cryosurgery of the prostate, which was based on a variational principle.

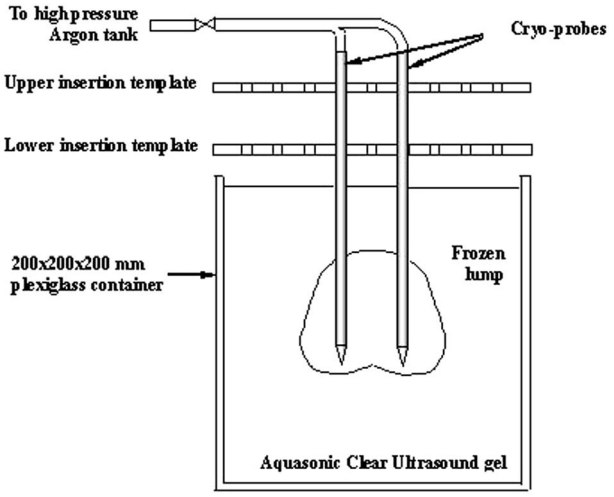

Fig. 1 Schematic drawing of the experimental setup showing two embedded cryoprobes

Model results were verified by comparison to an analytical solution of an idealized problem and to experimental data obtained for a single probe. The case of six-probe symmetric positioning in the prostate was simulated and 2D quadrant results were demonstrated. The authors define a "freezing exposure index," which relates the combined effect of freezing temperature and the duration the tissue is held at this temperature, as the index of damage caused to the tissue.

The purpose of the present study is to analyze the dynamics of the temperature field developing during the phase-change heat transfer problem in a tissue-simulating medium (gel) due to the simultaneous operation of up to three needle cryoprobes. The probes are embedded in the gel in a number of different configurations that are dictated by the insertion templates. The problem is solved numerically by ANSYS 7.0 using the enthalpy method. Experiments were conducted with high pressure argon-operated cryoprobes [29] and data were compared to the numerical results.

Experiments

Experiments were conducted in a separate study at Galil Medical facilities [29] with the needlelike cryoprobe(s) embedded in Aquasonic Clear ultrasound gel (Parker Laboratories, Inc.), as depicted in Fig. 1. The gel was contained in a Plexiglass container the sides of which measured 0.2 m. The 1.47 mm o.d. SEEDNET® cryoprobes were inserted into the gel to a depth of 50 mm. The length of the thermally active segment at the tip of the probe was reported at 15 mm, while the remainder of the probe's shaft was assumed to be insulated. Probe insertions were done through two horizontally parallel templates, each consisting of an array of 1.5 mm holes drilled on a 5×5 mm^2 mesh to ensure parallel and precise positioning of the probes. The cryoprobes were operated by high pressure argon gas (Joule-Thompson effect) with a constantly regulated inlet pressure of 24.1 MPa (3500 psi (gauge)). The volumetric flow rate of argon to each probe was about 12 sl/m (standard liters per minute).

The surface temperature of the thermally active segment of each cryoprobe was monitored at one point by a type-K thermocouple (TC) that was soldered onto the probe surface, 5 mm from the tip (see Fig. 2). Temperatures in the phase changing gel were continuously monitored by 22 type-K TCs arranged along strings of 2 mm spaced junctions. These TC strings were placed in the gel at three locations, as illustrated in Fig. 2 (single probe application):

(a) Radial location (eight junctions), perpendicular to the probe surface outward, with the first TC placed at 5 mm

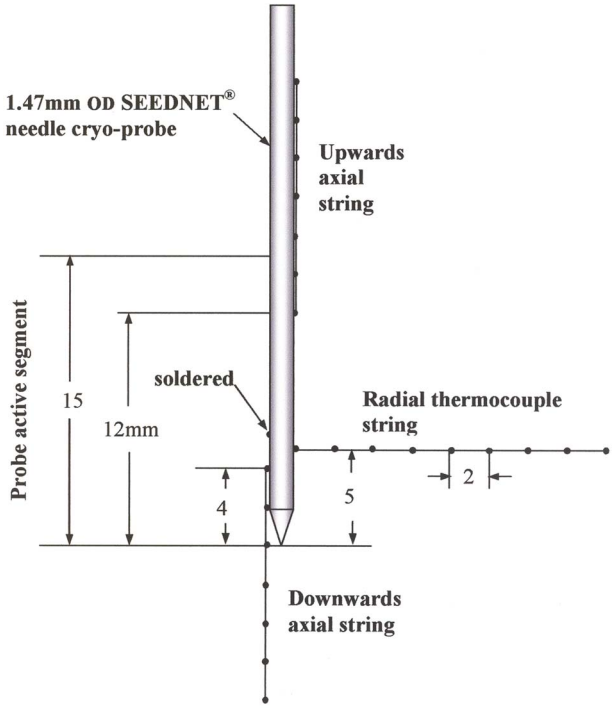

Fig. 2 Schematic drawing of the placement of the TCs for a single cryoprobe embedded in the gel. Dimensions are in mm.

above the tip of the probe, barely touching its surface. Rewcastle et al. [24] have used four TCs radially.

(b) Lower axial location (seven junctions) pointing downward and away from the tip of the probe, with the first and second TC junctions barely touching the lower part of the shaft of the probe at 4 mm and 2 mm above the tip, respectively, and the third coinciding with the plane perpendicular to the tip of the probe.

(c) Upper axial location (seven junctions) pointing upward toward the base of the cryoprobe and barely touching its shaft with the first TC placed at a point 12 mm above its tip. Rewcastle et al. [24] have used a total of four TCs in the axial direction.

Three separate sets of experiments were performed with one, two, and three cryoprobes. In all experiments the probes were inserted into the same 50 mm depth in the gel and were operated simultaneously and uniformly. In the two-probe experiments, the centerlines of the probes were placed 5 mm, 7.07 mm (on a diagonal between template holes), and 10 mm apart, as determined by the insertion templates. The three-probe experiments included four triangular configurations, as shown in Fig. 3. All experiments were run for about 12 min and began after the temperature of the gel had stabilized and became uniform. Measurements obtained with the three probes were omitted from the analysis due to uncertainties in the results.

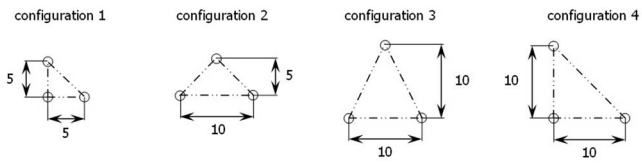

Fig. 3 Placement configurations for the three-probe experiments. Dimensions are in mm.

Table 1 Thermal properties of the phase-changing gel

Density ρ (kg/m^3)	1000
Specific heat of the frozen region (kJ/m^3 K)	3.6
Specific heat of the unfrozen region (kJ/m^3 K)	1.8
Thermal conductivity of the frozen region (W/m K)	1.6
Thermal conductivity of the unfrozen region (W/m K)	0.5
Latent heat ρL (MJ/m^3)	230
Medium initial temperature (°C)	18

Analysis

The heat transfer problem in a phase-changing medium is governed by the heat equation

$$\frac{\partial H}{\partial t} = \nabla \cdot (k \nabla T) \tag{1}$$

where t is the time, k is the thermal conductivity, T is the temperature, and H is the volumetric enthalpy,

$$H = \int_{T_{\text{ref}}}^{T} \rho c_p dT \tag{2}$$

where ρ is the density and c_p is the specific heat at constant pressure.

Equations (1) and (2) are solved numerically, subject to the following assumptions:

(a) Phase transition occurs over an extended temperature range of $-1\,^\circ$C to $-8\,^\circ$C [30].

(b) The thermal conductivities in both the frozen and unfrozen regions of the medium are constant, with a different value in each region, and vary linearly in the phase transition range [31].

(c) The specific heats in both the frozen and unfrozen regions of the medium are constant, with a different value in each region. In the phase transition range it is equal to the average value of the two regions with the addition of the latent heat of fusion [32].

Table 1 lists the thermal properties of the medium that were used in the analysis.

The cases considered were those of either one, two, or three simultaneously and uniformly operated cryoprobes. In all cases the cryoprobes were assumed to be inserted into the same 50 mm depth in the gel, as was done in the experiments, with the active segment fully engulfed by the gel. The remainder length of the probe's shaft was assumed to be insulated. All cases were analyzed by the enthalpy method and solved by a commercial finite element package, ANSYS 7.0. Postprocessing of the data was done by specifically written codes in MATLAB 6.5. Each of these cases was analyzed separately and is presented below.

One-Probe Application. Due to its geometry, the one-probe application may be solved as a two-dimensional, axisymmetric problem. The boundary conditions for this geometry are shown in Fig. 4. Along section EF=15 mm, the time variable temperature shown in Fig. 5, which approximates the temperature variations measured by the TC that was soldered onto the probe, is imposed. The remaining sections on this side are assumed to be adiabatic: AF=100 mm, due to symmetry, and ED=85 mm, with a half probe diameter offset, due to its contact with the insulated portion of the probe. The top free surface of the gel, section DC, is assumed to be insulated. At the remaining sections, AB=100 mm, DC=99.25 mm, and BC=200 mm, a constant temperature of 18 °C is assumed, equal to the initial condition in the gel (Table 1). The lengths of these latter sections were determined iteratively to ensure that the temperatures in the vicinity of the boundaries remain unchanged, as required by the boundary conditions.

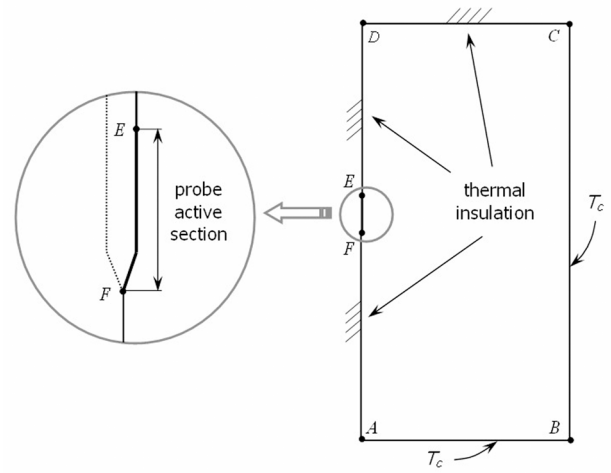

Fig. 4 Schematic drawing of the numerical solution domain for the one-probe application

The finite element meshing of the problem was done by ANSYS using linear triangular elements (PLANE55). The entire solution domain was divided into three regions to achieve fine meshing in areas adjacent to the probe, as shown in Fig. 6. Altogether, 8262 linear triangular elements with 4267 nodes, each with one degree of freedom of temperature, were used. Typical running times for analyzing 30 min of probe application, on a Pentium 4, 2.4 GHz computer, were about 15 min.

Two-Probe Applications. The two-probe application is a three-dimensional problem which is more complex than the axisymmetrical one-probe case, and thus requires more computational resources. Selection of the numerical solution domain for this case was done in a manner similar to the previous one. This resulted in a 200 mm long cubic computational domain. This domain ensures the satisfaction of the assumed constant temperature boundary conditions on the sides and bottom surface of the cube, as verified by iterations. The upper surface, through which the probes are inserted into the gel, is assumed to be thermally insulated. On the active section of the cryoprobe, the temperature variations that were measured by a single soldered TC in a separate study at Galil Medical [29] were applied (similar to Fig. 5).

The computational domain was divided into linear, four node

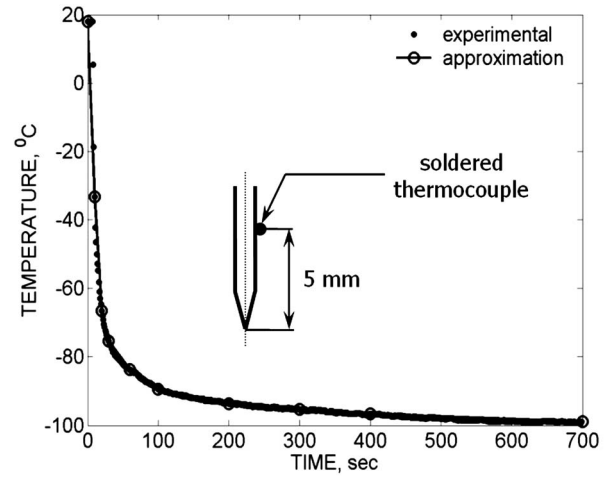

Fig. 5 Temperature variations measured by the TC soldered onto the surface of the cryoprobe 5 mm above its tip. Circles designate the numerical approximations of the measured data.

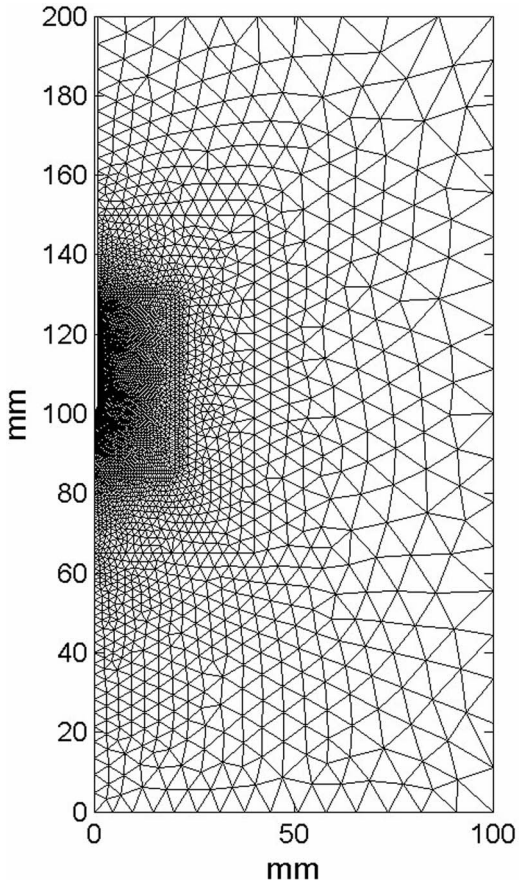

Fig. 6 Finite element mesh for the two- and three-probe applications

tetrahedral elements (SOLID70), each node with one degree of freedom of temperature. The total numbers of elements and nodes that were used in the computations, with different mesh densities as in the one-probe case, are listed in Table 2. Typical running times for analyzing 30 min of probe application on a Pentium 4, 2.4 GHz computer were about 6–7 h.

Three-Probe Applications. The three-probe problem is treated similarly to the two-probe case. Four basic insertion configurations were studied, as dictated by the insertion templates, Fig. 3. The computational domain of a 200 mm cube chosen for these cases is identical to the one used for the two-probe applications. The inclusion of an additional probe required longer computational times and a larger number of tetrahedral elements, as listed in Table 3 for all studied configurations. Typical running times for analyzing 30 min of probe application on a Pentium 4, 2.4 GHz computer were about 6–8 h.

Testing of the Numerical Code

The results of the numerical code were tested against two simple cases for which analytical solutions are available in the literature. The first case was of a long hollow cylinder exchanging

Table 2 Number of elements and nodes in the numerical model for the two-probe applications

Distance between probe centers (mm)	5	7.07	10
Number of elements	122,724	142,469	156,631
Number of nodes	21,460	24,749	27,123

Table 3 Number of elements and nodes in the numerical model for various configurations of the three-probe applications

Probe placement configuration, Fig. 3	1	2	3	4
Number of elements	113,056	147,315	207,491	180,221
Number of nodes	19,679	25,403	35,393	30,926

heat by convection with a surrounding medium at both its internal and external surfaces. This case was chosen to test the handling of axisymmetrical problems by ANSYS as in the one-probe application. The solution for this case is given by Ozisik [33]. The numerical model consisted of 567 two-dimensional linear elements (PLANE55). Values were calculated for 400 s at five equally spaced points in the cylindrical wall. The analytical solution included the first 50 elements in the series for comparison purposes. Comparison of results of all cases showed excellent conformity with a maximal deviation of about 0.4% [34].

The second test case was that of the phase-change problem of a semi-infinite pure liquid, initially at the solidification temperature, for which an analytical solution is given by Ozisik [35]. The numerical model consisted of 1374 two-dimensional triangular ele-

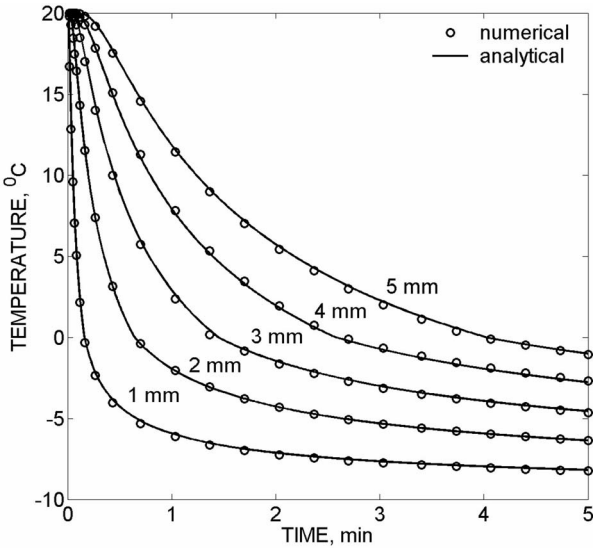

Fig. 7 Comparison of the analytical and numerical solutions for the half-space solidification problem after 5 min at 1–5 mm distances from the surface. Assumed solidification temperature range is ±0.5°C (numerical model only).

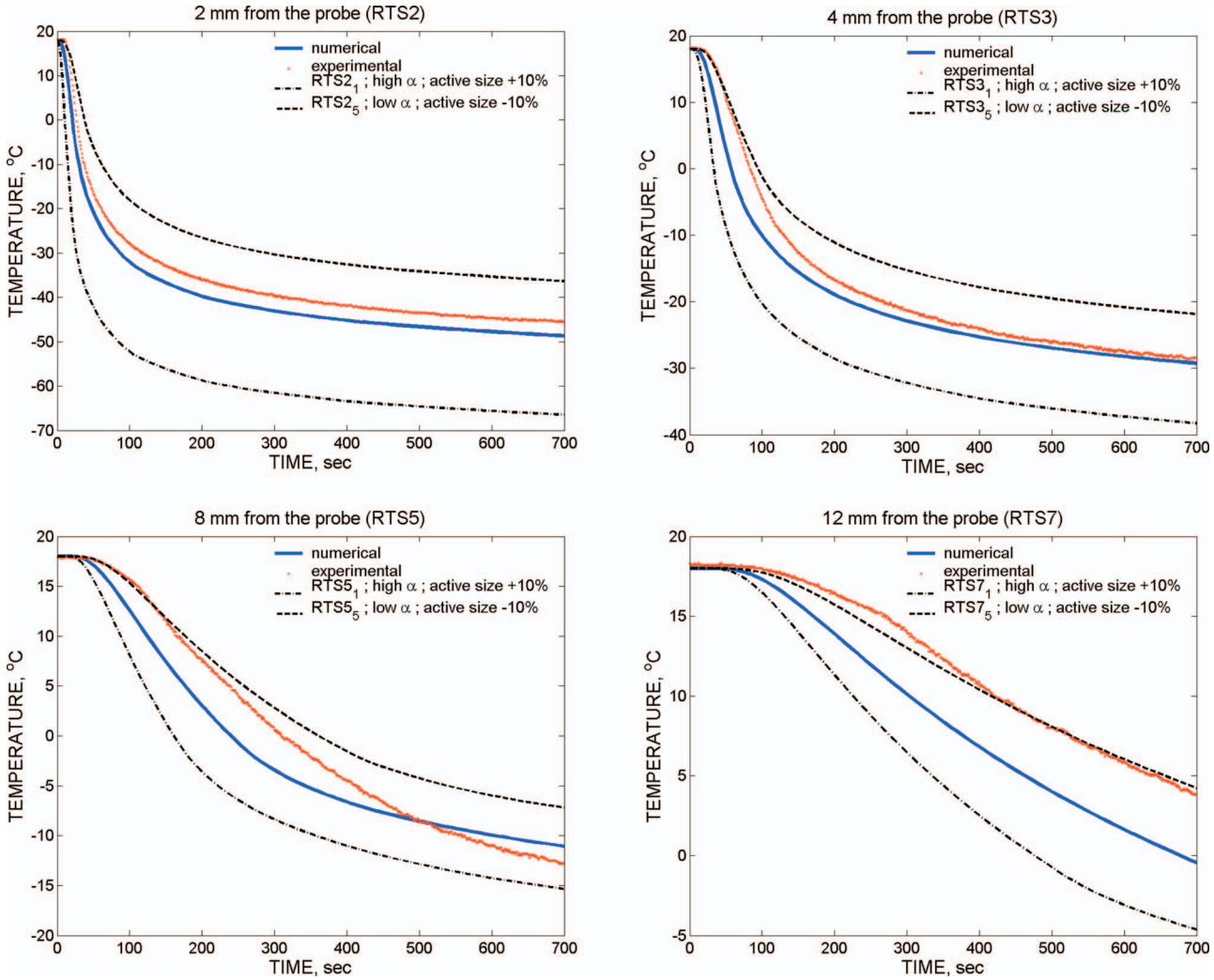

Fig. 8 Comparison of the experimental and numerical results for one-probe application in the radial direction. Upper and lower bounds are for ±10% uncertainties in the thermal diffusivity and length of the thermally active segment of the probe and ±1 mm in the positions of the TCs.

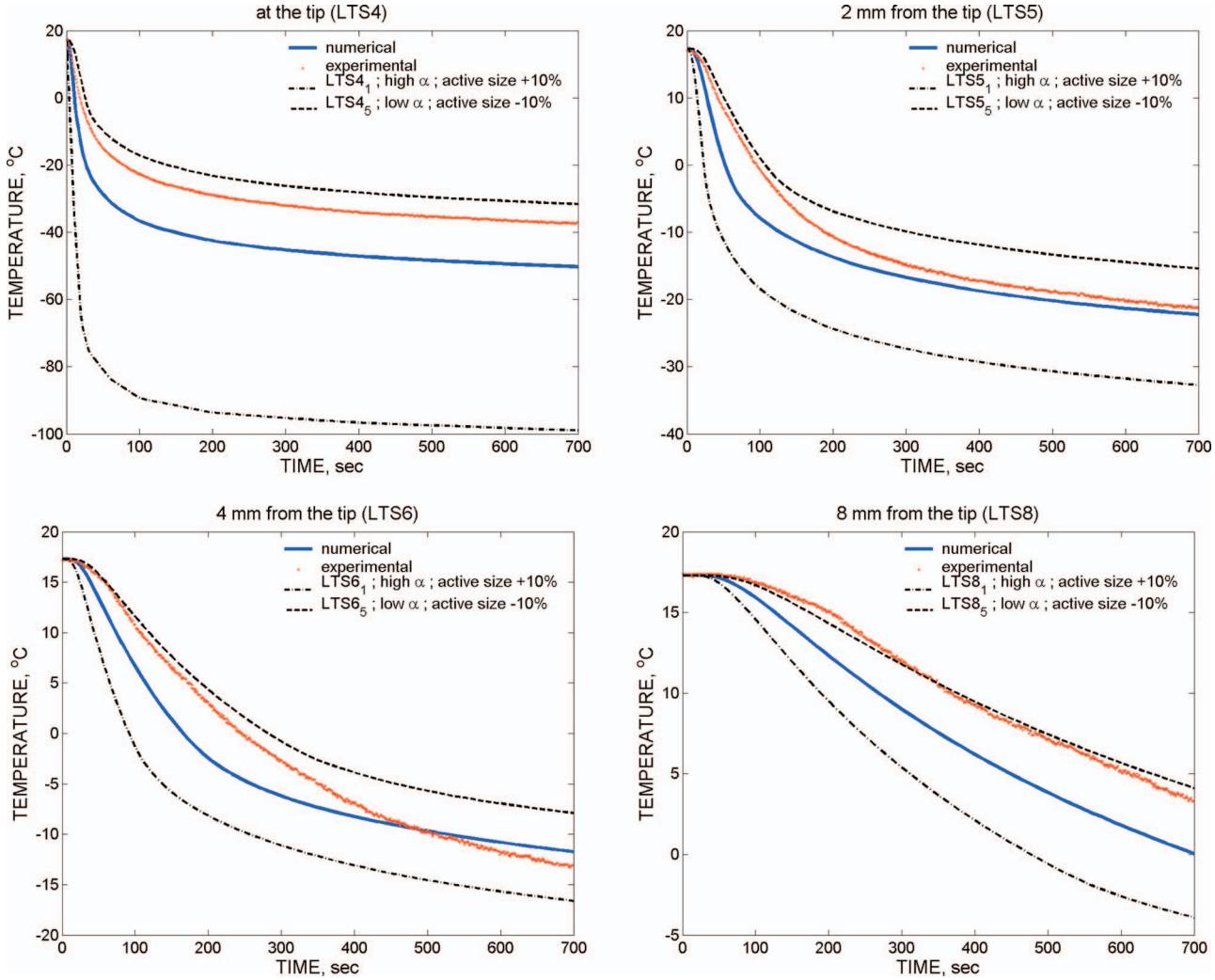

Fig. 9 Comparison of the experimental and numerical results for one-probe application in the downward axial direction. Upper and lower bounds are for ±10% uncertainties in the thermal diffusivity and length of the thermally active segment of the probe and ±1 mm in the positions of the TCs.

ments (PLANE55) with variable mesh densities. Since ANSYS does not treat directly the solidification of pure substances, which solidify at a single temperature, a phase-change temperature range needed to be specified. Four different temperature ranges were assumed around the solidification temperature: ±5°C, ±3°C, ±1°C, and ±0.5°C. Figure 7 shows comparison of results calculated for 5 min, at 1–5 mm distances from the external surface for the smallest assumed temperature range. This range yielded the best conformity of results, as is to be expected, with a maximal deviation of about 0.9% [34].

Results and Discussion

The numerical model was run for the one-, two-, and three-probe cases. In all cases studied, the temperature variations that were measured by the TCs that were soldered onto the probes' surfaces, e.g., Fig. 3, were assumed to uniformly apply over the entire active segment of the probe (along section EF of the numerical model, Fig. 4), due to lack of other data. The measured data were approximated numerically and were applied as the time-varying temperature boundary condition in the numerical solution of Eq. (1).

One-Probe Application. Temperature variations in the gel, calculated by the thermophysical values listed in Table 1, were compared to data measured by the TC strings in the radial and axial directions [29,34] and are shown in Figs. 8–10. Figure 8 refers to 2 mm, 4 mm, 8 mm, and 12 mm radial distances from the probe surface. Figure 9 compares values for 0 mm (tip), 2 mm, 4 mm, and 8 mm in the gel in the lower axial direction, downward from the probe tip. Figure 10 shows results for 18 mm, 20 mm, 22 mm, and 24 mm in the gel in the upper axial direction from the probe tip, along the assumed insulated part of the probe. As a general rule, conformity of results was better the closer the compared points were to the probe's shaft (radial) or to the probe's tip (axial). At certain locations in the gel, conformity worsened as the time of application increased. Moreover, at other points, e.g., at an 8 mm radial distance from the probe surface and at 4 mm downward from the tip of the probe, there were even crossovers of the results. Nevertheless, a close inspection of the differences between the experimental and calculated results, noting the temperature scales of each of these figures, reveals that most maximal differences are within the range of ±(4–5)°C. These results compare favorably with the ±5°C reported by Rewcastle et al. [24]. In certain cases, the differences are larger, within the range of ±(8–12)°C. Rewcastle et al. [27] estimated temperature measurement errors of ±(2.5–13)°C due to TC positioning errors alone, which depend on the local temperature gradients in the medium.

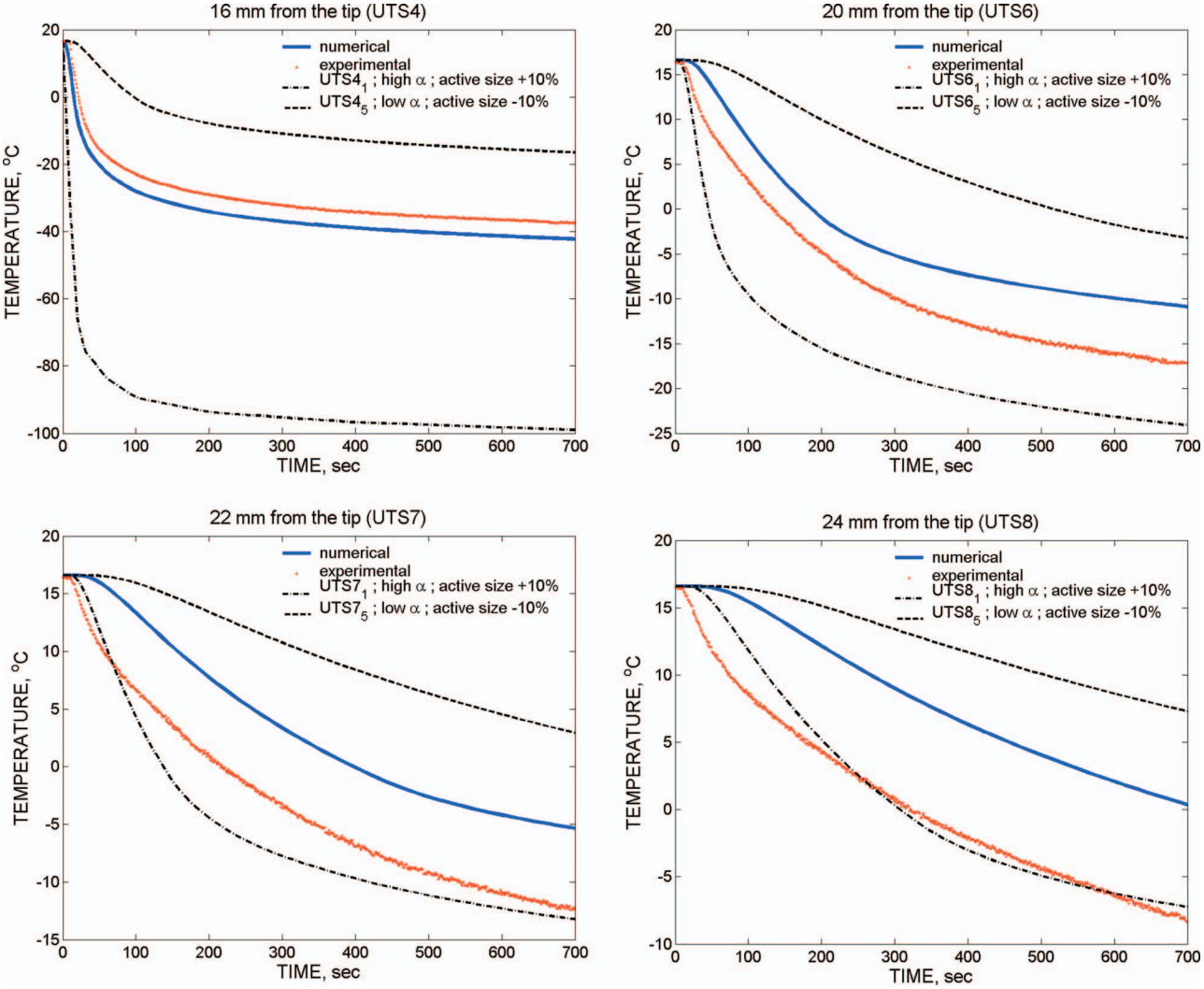

Fig. 10 Comparison of the experimental and numerical results for one-probe application in the upward axial direction. Upper and lower bounds are for ±10% uncertainties in the thermal diffusivity and length of the thermally active segment of the probe and ±1 mm in the positions of the TCs.

Certain factors may have contributed to these observed differences between the measured and calculated results:

(a) Approximation of the boundary conditions on the active segment of the probe. As noted above, the temperature along this segment was assumed to vary uniformly according to the temperature that was measured by the single TC that was soldered onto the probe surface at a point 5 mm above its tip. Due to the internal structure of the probe, it is reasonable to expect that the temperature along and around its active segment may not have been uniform. Such detailed information, however, was not available from the present experiments.
(b) Errors due to the numerical approximation of the measured data on the probe surface.
(c) Uncertainty in the actual length of the active segment of the probe. In the present study this length was assumed to extend for 15 mm, beginning at the tip, whereas the actual length could be somewhat different.
(d) Uncertainties in the exact positioning of the measuring TC junctions in the gel that may not be recording temperatures at the assumed locations, Rewcastle et al. [27].
(e) The presence of the TC strings as heat conducting elements in the gel in the vicinity of the measured points [24,27].
(f) Uncertainties in the thermophysical properties of the gel.
(g) Numerical errors due to the coarser mesh densities at locations farther from the probe surface.

A parametric study of these factors singled out the uniform boundary condition assumed along the active segment of the probe, point (a) above, as the most influencing factor [34]. However, since no additional data were available to systematically modify this boundary condition, we chose to study the effects of uncertainties in three other parameters, as follows:

(a) ±10% change in the length of the thermally active segment of the probe (point (c) above),
(b) ±1 mm change in the positioning of the TCs in the gel (point (d) above) [27]. Eight points, evenly spaced on a 1 mm radius circle around the nominal location, were included in the analysis, as shown in Fig. 11, and
(c) ±10% change in the thermal diffusivity of the gel ($k/\rho c$, point (f) above).

The effects of these parameters were studied separately. However,

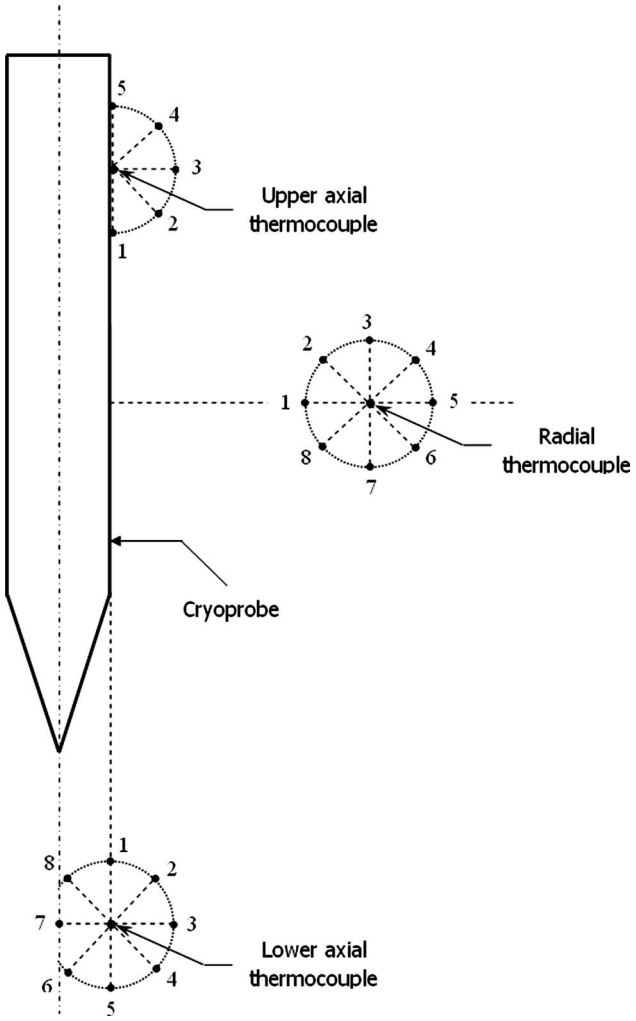

Fig. 11 Schematic of the assumed uncertainties in the radial, and upper and lower axial locations of the TCs. Circles' radii are 1 mm.

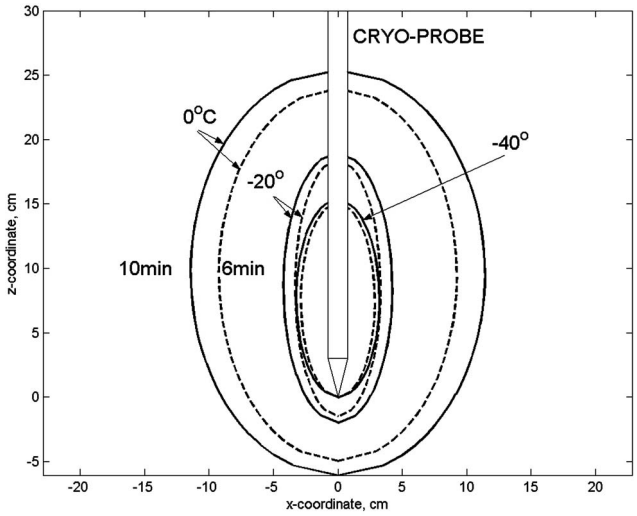

Fig. 12 Ellipsoidal approximations of measured data of isothermal contours in the frozen gel after 6 min and 10 min of a single-probe application

and with a view to conserve printing space, their effects were combined to yield upper and lower bound curves for each of the cases presented in Figs. 8–10. It is seen that the inclusion of these combined uncertainties in the computations produced temperature ranges that enclose most of the experimental results for each corresponding point in the gel.

Figure 12 shows ellipsoidal approximations of measured temperatures in the gel for a single probe application. Plotting was based on the assumption that the isothermal surfaces could be approximated by ellipsoids. One of the time-dependent principal axes of the ellipsoids was determined by the radial distances of the respective temperatures from the probe centerline. The other axis was determined by the difference between the readings of the downward and upward axial TC strings. Data of the 0°C, −20°C, and −40°C isothermal contours are plotted in Fig. 12 for 6 min and 10 min of operation of the probe. It is seen that the frozen front, represented in this study by the 0°C isothermal surface, advanced much beyond the volumes occupied by the lower two isotherms, as is to be expected. Furthermore, the subsequent advancement of the −40°C ellipsoids is significantly slower than those of both the 0°C and −20°C isothermal contours. For the

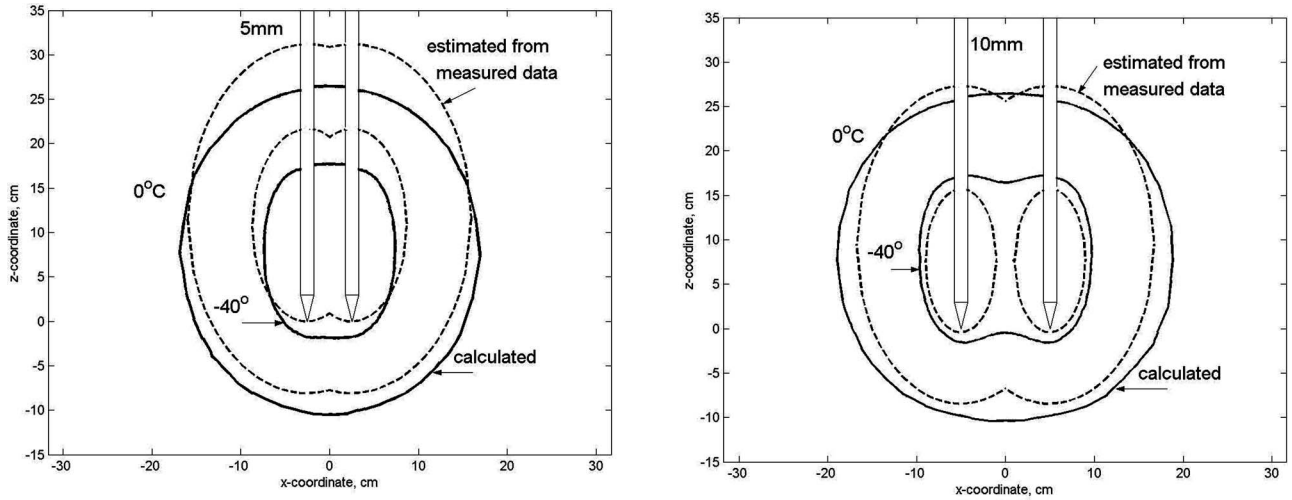

Fig. 13 Measured and calculated side cross-sectional views of 0°C and −40°C isothermal contours for two probes positioned 5 mm and 10 mm apart after 10 min of operation

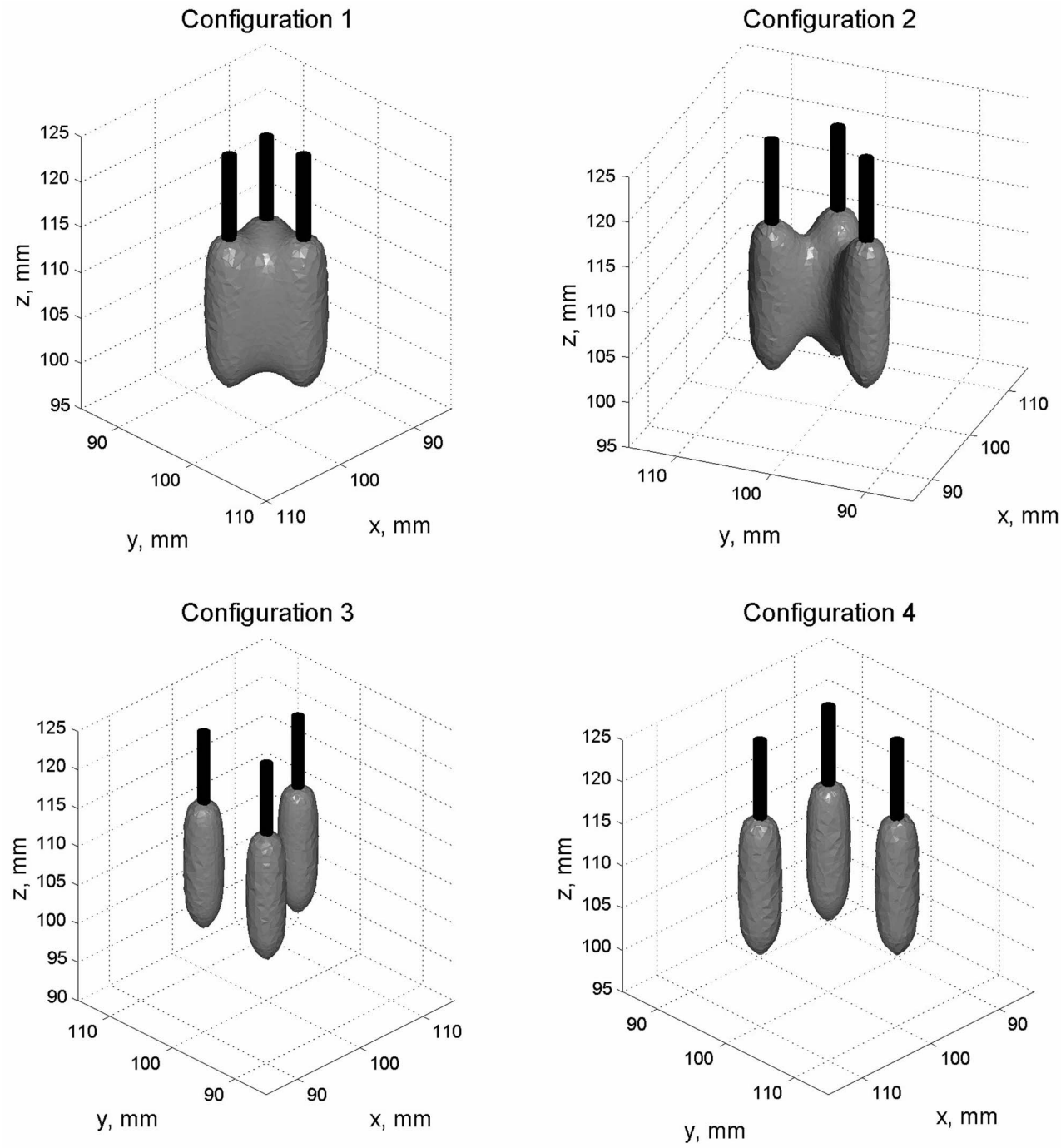

Fig. 14 Calculated −40°C isothermal 3D fronts for the four configurations of the three-probe applications after 1 min of operation

conditions of this study and due to the cylindrical structure of the cryoprobe, advancement of all shown fronts seems to favor the upward axial direction over the downward one. Front advancement in all directions is temperature dependent; the higher the temperature, the higher is the rate of growth of the volume enclosed therein.

Two-Probe Applications. Figure 13 compares side cross sections of the ellipsoidal approximations of measured data and calculated results for the 0°C and −40°C isothermal contours after 10 min of operation of the two probes that were placed 5 mm and 10 mm apart. It is clearly seen that the farther the placement of the probes, the larger are the volumes enclosed by these isothermal contours. For the probes that are placed 5 mm apart, the experimentally approximated data show a faster advancement in the upward axial direction over the calculated ones. This result is similar to the one obtained for a single probe (see Fig. 12) and most likely reflects the uncertainties associated with the boundary condition and other parameters, as discussed above. When the probes are placed 10 mm apart, calculated and experimentally approximated results come much closer together. One notable dif-

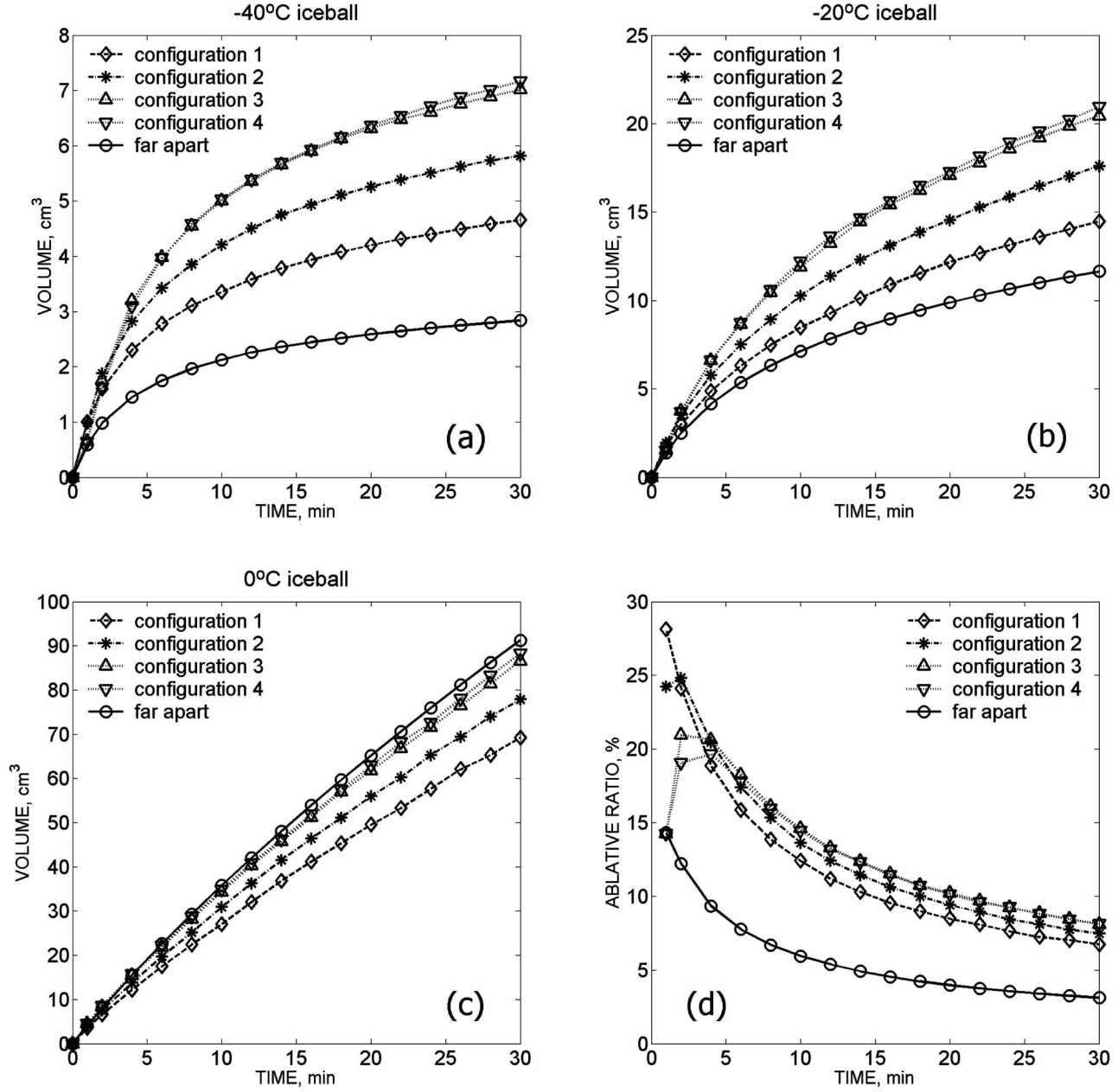

Fig. 15 Frozen volume variations obtained by three cryoprobes for different placement configurations: Volumes enclosed by the (*a*) −40°C, (*b*) −20°C, and (*c*) −0°C isothermal surfaces, respectively. (*d*) Percentages of the volumes enclosed by the −40°C isothermal surface relative to the total frozen volume (0°C isotherm).

ference for this case is in the behavior of the contours of the −40°C isotherms. It is seen that the measured two fronts of this isotherm, each emanating from either probe, have not joined together even after 10 min of application. The calculated data, on the other hand, show a uniformly connected volume for this duration of application.

Three-Probe Applications. Figure 14 presents three-dimensional calculation renderings for the four assumed placement configurations of three-probe applications. Shown are the volumes of the −40°C frozen lumps generated by each of these configurations after 1 min of application. It is seen that with the tightest placements of the probes, Configurations 1 and 2 (see Fig. 3), the fronts of all lumps have joined together even after 1 min of operation, reflecting the strong synergistic effect of the probes. In Configurations 3 and 4, in which the probes are placed wider apart from each other, the frozen lumps still remain separated after 1 min of operation and join into a continuous lump only later.

Calculated volume variations for 30 min of application and for all placement configurations of the three probes are summarized in Fig. 15. Also shown for comparison purposes are the additive volumes of three single probes that were assumed to be placed sufficiently far apart and, therefore, did not interact thermally with each other. Results are shown separately for three isothermal surfaces: (a) −40°C, (b) −20°C, and (c) 0°C (assumed to represent the frozen front). Figure 15(*d*) shows the percentage volumes enclosed by the −40°C surfaces relative to those of the frozen fronts, termed the "ablative ratio" by Rewcastle et al. [27]. One interesting result is apparent from this figure: the largest frozen front (0°C) volumes are obtained by the noninteracting probes that are placed far apart from each other. The exact opposite applies to the lower isothermal surfaces (−40 and −20°C): the smallest volumes are generated by the far-apart placed three

probes.

This phenomenon is governed by the placement strategy of the probes. Two limiting placement strategies are possible: packing all the probes together or placing them far apart from each other so as to eliminate all thermal interactions among them. Between these two limiting cases, the temperature-specific frozen volumes produced by the probes that are placed far apart will always be larger. This is because packing of the probes close together neutralizes most of the heat transfer capabilities of the touching and closely packed surfaces of the probes. However, when starting with "packed" probes and gradually moving them farther apart from each other, the inner volumes enclosed by the probes will increase. This will create an inner space in which synergistic effects among the probes will be dominant. Once this inner volume has been fully occupied by a certain isothermal surface, heat transfer in outward pointing directions will be enhanced, thus creating larger frozen volumes of the indicated isotherm. For a certain time of application, the combined inner and outer volumes would surpass that produced by the far-apart placed probes. Further moving of the probes apart would eventually obtain a maximal, temperature-specific, frozen volume. This volume will subsequently become smaller if the probes are moved farther apart and, in the limit, will approach that produced by the far-apart placed probes.

It follows that, in both Figs. 15(*a*) and 15(*b*), representing the lower two isothermal volumes, each of these placement configurations produced frozen volumes that are larger than those that were produced by the far-apart probes. When the frozen front volume is considered, Fig. 15(*c*), it is apparent that neither of the studied placement configurations lies in this region and, thus, the largest volumes are those generated by the far-apart probes.

It is also seen in Fig. 15 that the tighter is the placement of the probes, Configurations 1 and 2, the smaller is the volume occupied by each of the isothermal surfaces. Differences between the relatively larger volumes produced by the wider-spaced Configurations 3 and 4, are hardly distinguishable due to the geometrical similarity in their placement configuration. The trends indicated by both Figs. 15(*a*) and 15(*b*) suggest that, for each isothermal surface, there is a certain placement configuration, not necessarily one of those considered in this study, that would produce the maximal volume for those surfaces for a given duration of application. These "optimal" placement configurations are not identical and depend on the target, or "therapeutic" [25], temperature. Beyond this specific optimal placement configuration, increasing the distances among the three probes would produce progressively smaller isothermal volumes approaching, in the limit, the volume produced by the far-apart three probes. In summary, it could be stated that, relative to the 0°C volumes, the present placement configurations may be considered as "densely spaced," whereas they are "widely spaced" relative to both the −20°C and −40°C volumes.

Conclusion

Application of needlelike cryosurgical probes has been tested in gel whose thermal properties simulated biological tissues. Results were compared to calculations performed by a commercially available finite element package (ANSYS7.0). The accuracy of this package in handling nonlinear phase-change problems was verified by comparison to two simple analytical solutions. The main purpose of the present study is to analyze the dynamics of the temperature field developing during the phase-change heat transfer problem in a tissue-simulating medium (gel) due to the simultaneous operation of up to three embedded needlelike cryoprobes. The analysis provided an essential means for the preplanning stages of cryosurgical procedures. An important yield, as demonstrated in this article, is the pretesting of various probes' placements and insertion depths in the target tissue. Different, not necessarily uniform, modes of operation of the cryoprobes could also be examined. This could assist the physician in determining the number and locations of the probes to be inserted, the duration of their operation, and the expected spatial distributions and temporal variations of the temperature fields in the treated area. Such information is currently not readily available leading, among other things, to trial-and-error-based practices, which usually result in considerable uncertainties.

In the present study, up to three probes, in different insertion configurations to the same depth in the phase-changing medium, were considered. In all cases, the probes were assumed to be operated uniformly and followed a temperature forcing function that approximated that measured by a single TC that was soldered onto the probe's shaft. This assumption, dictated by the lack of other more detailed data, appeared to be one of the main sources of deviations between measured and calculated results in the gel. In future studies additional details of the actual temperature forcing function on the probe should be obtained. Future studies would also be expanded to include multiprobe applications with a variety of insertion modes, not necessarily limited by a uniform mesh of insertion holes, as in the present study. Different insertion depths and nonuniform operations of the probes should also be considered.

Acknowledgment

This study was supported in part by the James (Jimmy) H. Belfer Chair in Mechanical Engineering, Technion, Israel Institute of Technology. Experiments were performed by Dr. Nir Berzak of Galil Medical, Israel.

References

[1] Onik, G., 1996, "Cryosurgery," Crit. Rev. Oncol. Hematol., **23**, pp. 1–24.
[2] Rubinsky, B., and Onik, G., 1991, "Cryosurgery: Advances in the Application of Low Temperatures to Medicine," Int. J. Refrig., **14**, pp. 190–199.
[3] Shepherd, J., and Dawber, R. P. R., 1982, "The Historical and Scientific Basis of Cryosurgery," Clin. Exp. Dermatol., **7**, pp. 321–328.
[4] Gage, A., and Baust, J., 1998, "Mechanisms of Tissue Injury in Cryosurgery," Cryobiology, **37**, pp. 171–186.
[5] Hoffmann, N. E., and Bischof, J. C., 2002, "The Cryobiology of Cryosurgical Injury," Urology, **60**, pp. 40–49.
[6] Gage, A. A., and Huben, R. P., 2000, "Cryosurgical Ablation of the Prostate," Semin Urol. Oncol., **5**, pp. 11–19.
[7] Zouboulis, C. C., 1998, "Cryosurgery in Dermatology," Eur. J. Dermatol., **8**, pp. 466–474.
[8] Mazur, P., 1968, "Physical-Chemical Factors Underlying Cell Injury in Cryosurgical Freezing," *Cryosurgery*, R. Rand, A. Rinfret, and H. von Leden, eds., Thomas, Springfield, IL, pp. 32–51.
[9] Saliken, J. C., Donnelly, B. J., and Rewcastle, J. C., 2002, "The Evolution and State of Modern Technology for Prostate Cryosurgery," Urology, **60**, pp. 26–33.
[10] Zisman, A., Pantuck, A. J., Cohen, J. K., and Belldegrun, A. S., 2001, "Prostate Cryoablation Using Direct Transperineal Placement of Ultrathin Probes Through a 17-Gauge Brachytherapy Template—Technique and Preliminary Results," Urology, **58**, pp. 988–993.
[11] Orpwood, R. D., 1981, "Biophysical and Engineering Aspects of Cryosurgery," Phys. Med. Biol., **26**, pp. 555–575.
[12] Stefan, J., 1891, "Uber die Theorie des Eisbildung, Insbesondere uber die Eisbildung im Polarmeere," Ann. Phys. Chem., **42**(2), pp. 269–286.
[13] Neumann, F., 1912, "Lectures Given in the 1860's," *Die Partiellen Differential-Gleichungen der Mthematischen Physik*, 5th ed., H. Weber, ed., Friedrich Vieweg und Sohn, Braunschweig, Vol. 2, pp. 117–121.
[14] Ozisik, M. N., and Uzzell, J. C., 1979, "Exact Solution for Freezing in Cylindrical Symmetry With Extended Freezing Temperature Range," ASME J. Heat Transfer, **101**, pp. 331–334.
[15] Rubinsky, B., and Shitzer, A., 1976, "Analysis of a Stefan-Like Problem in a Biological Tissue Around a Cryosurgical Probe," ASME J. Heat Transfer, **98**, pp. 514–519.
[16] Trezek, G. J., 1985, "Thermal Analysis for Cryosurgery," *Heat Transfer in Medicine and Biology: Analysis and Applications*, A. Shitzer and R. C. Eberhart, eds., Plenum, New York, pp. 239–259.
[17] Rabin, Y., and Shitzer, A., 1995, "Exact Solution for the Inverse Stefan Problem in Non-Ideal Biological Tissues," ASME J. Heat Transfer, **117**, pp. 425–431.
[18] Weill, A., Shitzer, A., and Bar-Yoseph, P., 1993, "Finite Elements Analysis of the Temperature Field Around Two Adjacent Cryoprobes," ASME J. Biomech. Eng., **115**, pp. 374–379.
[19] Shamsundar, N., and Sparrow, E. M., 1975, "Analysis of Multidimensional Conduction Phase Change Problem Via the Enthalpy Method," ASME J. Heat Transfer, **97**, pp. 333–340.
[20] Dalhuijsen, A. J., and Segal, A., 1986, "Comparison of Finite Element Tech-

niques for Solidification Problems," Int. J. Numer. Methods Eng., **23**, pp. 1807–1829.
[21] Keanini, R. G., and Rubinsky, B., 1992, "Optimization of Multiprobe Cryosurgery," ASME J. Heat Transfer, **114**, pp. 796–801.
[22] Rabin, Y., and Stahovich, T. F., 2003, "Cryoheater as a Means of Cryosurgery Control," Phys. Med. Biol., **48**, pp. 619–632.
[23] Rabin, Y., Lung, D. C., and Stahovich, T. F., 2004, "Computerized Planning of Cryosurgery Using Cryoprobes and Cryocatheters," Technol. Cancer Res. Treat., **3**(3), pp. 229–243.
[24] Rewcastle, J. C., Sandison, G. A., Hahn, L. J., Saliken, J. C., McKinnon, J. G., and Donnelley, B. J., 1998, "A Model for the Time-Dependent Thermal Distribution Within an Iceball Surrounding a Cryoprobe," Phys. Med. Biol., **43**, pp. 3519–3534.
[25] Jankun, M., Kelly, T. J., Zaim, A., Young, K., Keck, R. W., Selman, S. H., and Jankun, J., 1999, "Computer Model for Cryosurgery of the Prostate," Comput. Aided Surg., **4**, pp. 193–199.
[26] Baissalov, R., Sandison, G. A., Donnelley, B. J., Saliken, J. C., McKinnon, J. G., Muldrew, K., and Rewcastle, J. C., 2000, "A Semi-Empirical Planning Model for Optimization of Multiprobe Cryosurgery," Phys. Med. Biol., **45**, pp. 1085–1098.
[27] Rewcastle, J. C., Sandison, G. A., Muldrew, K., Saliken, J. C., and Donnelley, B. J., 2001, "A Model for the Time Dependent Three-Dimensional Thermal Distribution Within Iceballs Surrounding Multiple Cryoprobes," Med. Phys., **28**(6), pp. 1125–1137.
[28] Wan, R., Liu, Z., Muldrew, K., and Rewcastle, J. C., 2003, "A Finite Element Model for Ice Ball Evolution in a Multiprobe Cryosurgery," Comput. Methods Biomech. Biomed. Eng., **6**(3), pp. 197–208.
[29] Galil-Medical Ltd., private communication.
[30] Rabin, Y., and Shitzer, A., 1998, "Numerical Solution of the Multidimensional Freezing Problem During Cryosurgery," ASME J. Biomech. Eng., **120**, pp. 32–37.
[31] Comini, G., and Del Guidice, S., 1976, "Thermal Aspects of Cryosurgery," ASME J. Heat Transfer, **98**, pp. 543–549.
[32] Bonacina, C., Comini, G., Fasano, A., and Primicerio, M., 1974, "On the Estimation of Thermophysical Properties in Nonlinear Heat Conduction Problems," Int. J. Heat Mass Transfer, **17**, pp. 861–867.
[33] Ozisik, M. N., 1968, *Boundary Value Problems of Heat Conduction*, International Textbook, Scranton, PA.
[34] Magalov, Z., 2005, "Investigation of the Temperature Field Developed by Simultaneously Operating Cryosurgical Probes Embedded in a Phase-Changing Medium," M.S. thesis, Technion, Israel Institute of Technology, Haifa, Israel.
[35] Ozisik, M. N., 1993, *Heat Conduction*, Wiley, New York, pp. 392–436.

Finite Element Simulation on Natural Convection Flow in a Triangular Enclosure Due to Uniform and Nonuniform Bottom Heating

S. Roy
Department of Mathematics,
Indian Institute of Technology Madras,
Chennai-600036, India
e-mail: sjroy@iitm.ac.in

Tanmay Basak[1]
e-mail: tanmay@iitm.ac.in

Ch. Thirumalesha

Department of Chemical Engineering,
Indian Institute of Technology Madras,
Chennai-600036, India

Ch. Murali Krishna
Department of Mathematics,
Indian Institute of Technology Madras,
Chennai-600036, India

A penalty finite element analysis with biquadratic elements has been carried out to investigate natural convection flows within an isosceles triangular enclosure with an aspect ratio of 0.5. Two cases of thermal boundary conditions are considered with uniform and nonuniform heating of bottom wall. The numerical solution of the problem is illustrated for Rayleigh numbers (Ra), $10^3 \leqslant Ra \leqslant 10^5$ *and Prandtl numbers (Pr),* $0.026 \leqslant Pr \leqslant 1000$*. In general, the intensity of circulation is found to be larger for nonuniform heating at a specific Pr and Ra. Multiple circulation cells are found to occur at the central and corner regimes of the bottom wall for a small Prandtl number regime (Pr* $=0.026-0.07$*). As a result, the oscillatory distribution of the local Nusselt number or heat transfer rate is seen. In contrast, the intensity of primary circulation is found to be stronger, and secondary circulation is completely absent for a high Prandtl number regime (Pr=0.7–1000). Based on overall heat transfer rates, it is found that the average Nusselt number for the bottom wall is* $\sqrt{2}$ *times that of the inclined wall, which is well, matched in two cases, verifying the thermal equilibrium of the system. The correlations are proposed for the average Nusselt number in terms of the Rayleigh number for a convection dominant region with higher Prandtl numbers (Pr=0.7 and 10).* [DOI: 10.1115/1.2804934]

Keywords: penalty finite element method, natural convection, triangular enclosure, nonuniform heating

1 Introduction

Natural convection in triangular enclosures has received considerable attention for various applications, such as energy related applications (thermal insulation of buildings using air gaps, solar energy collectors, furnaces, fire control in buildings, etc. [1,2]), geophysical applications (differential heating and cooling in lakes and estuaries, pollutant diffusion in sea, natural convection in reservoir sidearms, etc. [3]), and material processing applications (food processing and glass melt processing, etc. [4,5]).

The theoretical and experimental studies on natural convection in a triangular enclosure were first reported for attic spaces. Poulikakos and Bejan [6] studied fluid dynamics in an attic space. Their study was divided into three parts. In the first part, the flow and temperature fields in the cavity were determined by asymptotic analysis. The second part deals with the transient behavior of the attic fluid based on scaling analysis. In the last part, transient numerical studies were carried out to verify theoretical predictions. Their work [6] also established that the single-cell circulation pattern is stable with respect to Benard stability for fluid layers heated from below. Poulikakos and Bejan [7] also carried out experimental studies on natural convection in a triangular enclosure. The experimental studies were based on a cooled upper wall and a heated bottom wall in an attic space. Their results showed that the Nusselt number strongly depends on the Rayleigh number.

A significant number of earlier studies on natural convection in triangular enclosures was based on the steady states and stability of flow fields. Karyakin et al. [8] investigated convection patterns in isosceles triangle enclosures. Finite difference method was used for solving the Navier–Stokes equations, and it was found that maximum values of steady state fields may correspond to damping oscillations around the steady state values. Holtzman et al. [9] described laminar natural convection in isosceles triangular enclosures heated from below and symmetrically cooled from above. They concluded that the geometric plane of a symmetry is not a plane of symmetry for flow. They also found that the pitchfork bifurcation occurs at a critical Grashof number (Gr) for various aspect ratios, and it was also shown that the symmetric solutions are unstable to finite perturbations. Salmun [10,11] presented convection patterns with stability analysis in a triangular domain. Their numerical predictions were also supported by experimental observations. Recently, Ridouane and Campo [12] carried out a numerical investigation on transient laminar thermal convection of air confined in an isosceles triangular cavity heated from the base and symmetrically cooled from the upper inclined walls. They found that above a critical Grashof number, an asymmetrical solution exhibiting a pitchfork bifurcation arises and eventually becomes steady.

A few studies on flow and thermal investigations in triangular enclosures were also carried for various applications. Akinsete and Coleman [13] studied the laminar natural convection in right-triangular enclosures. They used finite difference technique to find

[1]Corresponding author.

Contributed by the Heat Transfer Division of ASME for publication in the JOURNAL OF HEAT TRANSFER. Manuscript received July 19, 2006; final manuscript received August 30, 2007; published online March 6, 2008. Review conducted by Jay M. Khodadadi.

out steady state solutions for various height-base ratios (H/B) ($0.625 \leq H/B \leq 1.0$) and Grashof numbers ($800 \leq Gr \leq 6.4 \times 10^4$). It has been found that a considerable proportion of the heat transfer across the base wall of the region takes place near the intersection of the base and hypotenuse. Asan and Namli [14] carried out studies on laminar natural convection in a pitched roof of a triangular cross section for summer day boundary conditions. They used a control volume integration solution technique based on stream function-vorticity formulation. The steady state solutions are obtained up to $Ra = 10^6$ and height-base ratio (H/B) of $0.125 \leq H/B \leq 1$. The results showed that the height-base ratio has influence on the temperature and flow fields. In another study, Asan and Namli [15] also studied the same problem for winter day boundary conditions. They also found that the height-base ratio (H/B) has profound influence on temperature and velocity fields.

Recently, Ridouane et al. [16] studied natural convection patterns in right-angled triangular cavities with heated vertical sides and cooled hypotenuses. The motivation of their study is based on an application in the miniaturization of electronic packaging severely constrained by space and/or weight. Numerical results were reported for the velocity field, the temperature field, and the mean convective coefficient along the heated vertical wall. For purposes of engineering design, an average Nusselt number versus height correlation equation was also constructed. Ridouane et al. [17] also carried out numerical investigations on the laminar natural convection of air confined to an isosceles triangular cavity for both summer and winter boundary conditions. The numerical predictions of velocity, temperature, and mean wall heat fluxes agree well with the experimental measurements.

The focus of earlier works is primarily on the influence of the flow field on the heat transfer process due to natural convection in triangular enclosures, and very few works mentioned about heat transfer rates up to a limited extent. The efficient heating process with uniform and nonuniform heat sources with the detailed analysis of local and average Nusselt numbers as functions of Prandtl number and Rayleigh number in a triangular enclosure is not yet reported to date. The prime objective of this article is to investigate the circulation and temperature distribution with the detailed analysis of heat transfer rate in a triangular enclosure with uniformly and nonuniformly heated bottom plate and cooled side walls. The motivation of this study is to analyze the situation where boundary conditions resemble winter day boundary conditions, where the outside temperature is cold and the inside temperature is sustained hot via any heating system. This study may also be useful to analyze the differential heating of materials with cold vertical walls. The analysis has been carried out for various materials with a range of Prandtl numbers (Pr) e.g., molten metals ($Pr = 0.026 - 0.004$), gases ($Pr = 0.7 - 1$), water ($Pr = 1.7 - 13.7$), oils ($Pr = 50 - 10^5$), etc., whereas earlier literatures primarily involve air and water only. The boundary conditions due to uniform heating correspond to jump discontinuities at corner points, and similar boundary conditions were also used in earlier works on natural convection in a square cavity [18,19]. The boundary condition due to nonuniform heating has been represented by sinusoidal distribution of temperature, and this type of boundary condition is particularly useful for processing molten glass [4].

The geometry of the triangular enclosure with boundary conditions is shown in Fig. 1. In the current study, we have used the Galerkin finite element method with a penalty parameter to solve the nonlinear coupled partial differential equations governing flow and temperature fields for both uniform and nonuniform heating of the bottom wall. Nonorthogonal grid generation has been done with isoparametric mapping [20,21]. An overview on grid generation using isoparametric mapping is given in the Appendix. The Galerkin finite element with isoparametric mapping has been used for the first time as an automatically generated grid in a pseudosquare domain makes the method robust for any complex geometry. Numerical results are obtained to display the circulation and temperature distribution within the triangle and the heat transfer rate for both the walls in terms of local and average Nusselt numbers. Local and average Nusselt numbers have been evaluated using biquadratic basis functions. The heat transfer effects were illustrated based on two cases: case I, uniformly heated bottom wall, and Case II, nonuniformly heated bottom wall.

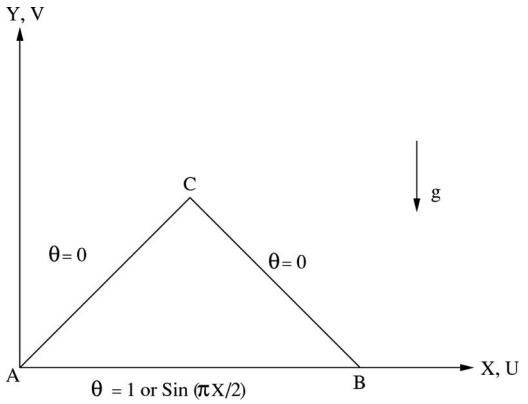

Fig. 1 Schematic diagram of the physical system

2 Governing Equations

The fluid properties are assumed to be constant, except the density variation, which was determined according to the Boussinesq approximation. It is used in the field of buoyancy driven flow. It states that density differences are sufficiently small to be neglected, except with the term multiplied by g (acceleration due to gravity). The essence of the Boussinesq approximation is that the difference in inertia is neglected, but gravity is sufficiently strong to make the specific weight appreciably different between two liquids. The governing equations for steady natural convection flow using conservation of mass, momentum, and energy can be written as

$$\frac{\partial u}{\partial x} + \frac{\partial v}{\partial y} = 0 \tag{1}$$

$$u\frac{\partial u}{\partial x} + v\frac{\partial u}{\partial y} = -\frac{1}{\rho}\frac{\partial p}{\partial x} + \nu\left(\frac{\partial^2 u}{\partial x^2} + \frac{\partial^2 u}{\partial y^2}\right) \tag{2}$$

$$u\frac{\partial v}{\partial x} + v\frac{\partial v}{\partial y} = -\frac{1}{\rho}\frac{\partial p}{\partial y} + \nu\left(\frac{\partial^2 v}{\partial x^2} + \frac{\partial^2 v}{\partial y^2}\right) + g\beta(T - T_c) \tag{3}$$

$$u\frac{\partial T}{\partial x} + v\frac{\partial T}{\partial y} = \alpha\left(\frac{\partial^2 T}{\partial x^2} + \frac{\partial^2 T}{\partial y^2}\right) \tag{4}$$

The boundary conditions are as follows:

$$u(x,0) = 0 = v(x,0) \quad T(x,0) = T_h$$

$$\text{or } T_c + (T_h - T_c)\sin\left(\frac{\pi x}{2L}\right) \quad \text{for } y = 0 \quad \forall\, 0 \leq x \leq 2L$$

$$u(x,y) = 0 = v(x,y) \quad T(x,y) = T_c \text{ (at the left inclined wall)}$$

$$y = x \quad \forall\, 0 \leq x \leq L$$

$$u(x,y) = 0 = v(x,y) \quad T(x,y) = T_c \text{ (at the right inclined wall)}$$

$$y = 2L - x \quad \forall\, L \leq x \leq 2L$$

Here, x and y are the distances measured along the horizontal and vertical directions, respectively; u and v are the velocity components in the x and y directions, respectively; T denotes the temperature; p is the pressure, and ρ is the density; T_h and T_c are the temperatures at hot bottom wall and cold inclined walls, respec-

tively; L is the height of the triangular enclosure with an aspect ratio of 0.5.

Using the following change of variables:

$$X=\frac{x}{L} \quad Y=\frac{y}{L} \quad U=\frac{uL}{\alpha} \quad V=\frac{vL}{\alpha} \quad \theta=\frac{T-T_c}{T_h-T_c}$$

$$P=\frac{pL^2}{\rho\alpha^2} \quad \mathrm{Pr}=\frac{\nu}{\alpha} \quad \mathrm{Ra}=\frac{g\beta(T_h-T_c)L^3\mathrm{Pr}}{\nu^2} \tag{5}$$

the governing equations (Eqs. (1)–(4)) reduce to nondimensional form,

$$\frac{\partial U}{\partial X}+\frac{\partial V}{\partial Y}=0 \tag{6}$$

$$U\frac{\partial U}{\partial X}+V\frac{\partial U}{\partial Y}=-\frac{\partial P}{\partial X}+\mathrm{Pr}\left(\frac{\partial^2 U}{\partial X^2}+\frac{\partial^2 U}{\partial Y^2}\right) \tag{7}$$

$$U\frac{\partial V}{\partial X}+V\frac{\partial V}{\partial Y}=-\frac{\partial P}{\partial Y}+\mathrm{Pr}\left(\frac{\partial^2 V}{\partial X^2}+\frac{\partial^2 V}{\partial Y^2}\right)+\mathrm{Ra}\,\mathrm{Pr}\theta \tag{8}$$

$$U\frac{\partial \theta}{\partial X}+V\frac{\partial \theta}{\partial Y}=\frac{\partial^2 \theta}{\partial X^2}+\frac{\partial^2 \theta}{\partial Y^2} \tag{9}$$

The transformed boundary conditions become (see Fig. 1)

$$U(X,0)=0=V(X,0) \quad \theta(X,0)=1 \quad \text{or } \sin\left(\frac{\pi X}{2}\right) \text{ on } AB$$
$$\forall\, 0\leqslant X\leqslant 2$$
$$U(X,Y)=0=V(X,Y) \quad \theta(X,Y)=0 \quad \text{on } AC \quad Y=X$$
$$\forall\, 0\leqslant X\leqslant 1$$
$$U(X,Y)=0=V(X,Y) \quad \theta(X,Y)=0 \quad \text{on } BC \quad Y=2-X$$
$$\forall\, 1\leqslant X\leqslant 2 \tag{10}$$

Here, X and Y are dimensionless coordinates varying along horizontal and vertical directions, respectively; U and V are dimensionless velocity components in the X and Y directions, respectively; θ is the dimensionless temperature; P is the dimensionless pressure; Ra and Pr are Rayleigh and Prandtl numbers, respectively.

3 Solution Procedure and Postprocessing

The momentum and energy balance equations (Eqs. (7)–(9)) are solved using the Galerkin finite element method. The continuity equation (Eq. (6)) is used as a constraint to enforce mass conservation, and this constraint may be used to obtain the pressure distribution. In order to solve Eqs. (7)–(9), we use the penalty finite element method, where the pressure P is eliminated by a penalty parameter γ and the incompressibility criteria given by Eq. (6), which results in

$$P=-\gamma\left(\frac{\partial U}{\partial X}+\frac{\partial V}{\partial Y}\right) \tag{11}$$

The continuity equation (Eq. (6)) is automatically satisfied for large values of γ. A typical value of γ that yields consistent solutions is 10^7. Using Eq. (11), the momentum balance (Eqs. (7) and (8)) reduces to

$$U\frac{\partial U}{\partial X}+V\frac{\partial U}{\partial Y}=\gamma\frac{\partial}{\partial X}\left(\frac{\partial U}{\partial X}+\frac{\partial V}{\partial Y}\right)+\mathrm{Pr}\left(\frac{\partial^2 U}{\partial X^2}+\frac{\partial^2 U}{\partial Y^2}\right) \tag{12}$$

$$U\frac{\partial V}{\partial X}+V\frac{\partial V}{\partial Y}=\gamma\frac{\partial}{\partial Y}\left(\frac{\partial U}{\partial X}+\frac{\partial V}{\partial Y}\right)+\mathrm{Pr}\left(\frac{\partial^2 V}{\partial X^2}+\frac{\partial^2 V}{\partial Y^2}\right)+\mathrm{Ra}\,\mathrm{Pr}\theta \tag{13}$$

The system of Eqs. (9), (12), and (13) with boundary conditions is solved by using the Galerkin finite element method [20]. Since the solution procedure is explained in earlier works [18,19], the detailed description in not included in this paper.

The flow circulation is represented by a stream function (ψ), which is evaluated using the relationship between the stream function (ψ) and the velocity components [22]: $U=\partial\psi/\partial Y$ and $V=-\partial\psi/\partial X$. It may be noted that the positive sign of ψ represents an anticlockwise circulation and the clockwise circulation is represented by the negative sign of ψ. The no-slip condition is valid at all boundaries as there is no cross flow; hence, $\psi=0$ is used for the boundaries. The stream functions are also evaluated via the finite element method with the biquadratic basis functions for the dependent variable as discussed in earlier works [18,19].

The heat transfer rate in terms of the local Nusselt number (Nu) is defined by

$$\mathrm{Nu}=-\frac{\partial\theta}{\partial n} \tag{14}$$

where n denotes the normal direction on a plane. The local Nusselt number on a surface contains a normal derivative, as shown in Eq. (14), and normal derivatives are evaluated using the biquadratic basis set in ξ-η domain (see Fig. 2; [19]),

$$\mathrm{Nu}_b=-\sum_{i=1}^{9}\theta_i\frac{\partial\Phi_i}{\partial Y} \tag{15}$$

$$\mathrm{Nu}_l=\sum_{i=1}^{9}\theta_i\left(-\frac{1}{\sqrt{2}}\frac{\partial\Phi_i}{\partial X}+\frac{1}{\sqrt{2}}\frac{\partial\Phi_i}{\partial Y}\right) \tag{16}$$

and

$$\mathrm{Nu}_r=\sum_{i=1}^{9}\theta_i\left(\frac{1}{\sqrt{2}}\frac{\partial\Phi_i}{\partial X}+\frac{1}{\sqrt{2}}\frac{\partial\Phi_i}{\partial Y}\right) \tag{17}$$

The average Nusselt numbers at the bottom and side walls are

$$\overline{\mathrm{Nu}_b}=\frac{\int_0^2 \mathrm{Nu}_b dX}{X|_0^2}=\frac{1}{2}\int_0^2 \mathrm{Nu}_b dX \tag{18}$$

$$\overline{\mathrm{Nu}_l}=\frac{\int_0^{\sqrt{2}} \mathrm{Nu}_l dS}{S|_0^{\sqrt{2}}}=\frac{1}{\sqrt{2}}\int_0^{\sqrt{2}} \mathrm{Nu}_l dS \tag{19}$$

and

$$\overline{\mathrm{Nu}_r}=\frac{\int_0^{\sqrt{2}} \mathrm{Nu}_r dS}{S|_0^{\sqrt{2}}}=\frac{1}{\sqrt{2}}\int_0^{\sqrt{2}} \mathrm{Nu}_r dS \tag{20}$$

Here, dS denotes the elemental length along inclined sides of the triangular cavity.

4 Results and Discussions

4.1 Numerical Tests. The computational domain in ξ-η coordinates (see Fig. 2(a)) consists of biquadratic elements. Note that the computational grid in the triangular domain is generated via mapping the triangular domain into a square domain in the ξ-η coordinate system, as discussed in the Appendix. The biquadratic

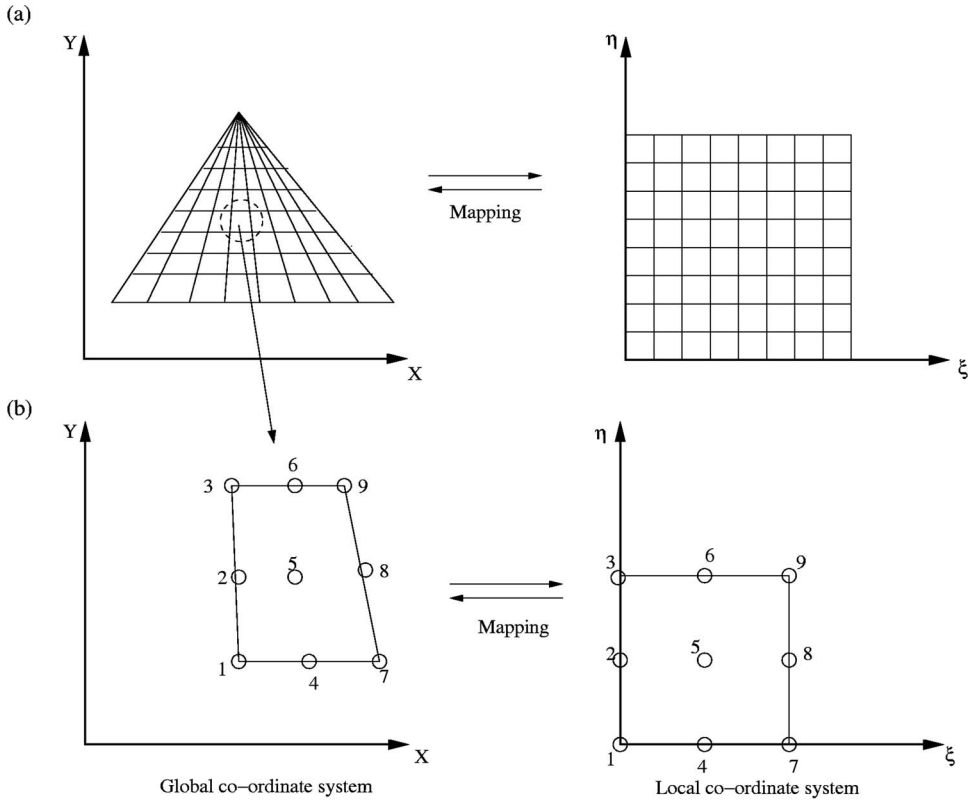

Fig. 2 (*a*) The mapping of a triangular domain to a square domain in the ξ-η coordinate system and (*b*) the mapping of an individual element to a single element in the ξ-η coordinate system

elements with a lesser number of nodes smoothly capture the nonlinear variations of the field variables, which are in contrast with finite difference/finite volume solutions available in the literature [15,23].

The jump discontinuities in Dirichlet-type wall boundary conditions at the corner points (see Fig. 1) correspond to computational singularities. In particular, the singularity at the corner nodes of the bottom wall needs special attention. The grid size dependent effect of the temperature discontinuity at the corner points on the local (and the overall) Nusselt numbers tends to increase as the mesh spacing at the corner is reduced. One way for handling the problem assumes the average temperature of the two walls at the corner and keeping the adjacent grid nodes at the respective wall temperatures as suggested by Ganzarolli and Milanez [24]. This procedure is still grid dependent unless a sufficiently refined mesh is implemented. Once any corner formed by the intersection of two differently heated boundary walls is assumed at the average temperature of the adjacent walls, the optimal grid size obtained for each configuration corresponds to the mesh spacing over which further grid refinements lead to grid invariant results in both heat transfer rates and flow fields. Similar observations were also reported by Corcione [25].

It may be noted that a Gaussian quadrature based finite element method provides the smooth solutions at the interior domain including the corner regions as the evaluation of residuals depends on interior Gauss points, and thus the effect of singularity at corner nodes is less pronounced in the final solution. In general, the Nusselt numbers for finite difference/finite volume based methods are calculated at any surface using some interpolation functions, which are now avoided in the current work. The present finite element approach offers a special advantage on the evaluation of local Nusselt number at the left, right, and bottom walls as the element basis functions are used to evaluate the heat flux [18,19].

In order to assess the accuracy of our numerical procedure, we have tested our algorithm based on the grid size 49×49 in the ξ-η domain (Fig. 2) for an isosceles triangular enclosure with cold inclined walls and hot bottom wall. The results show a similar trend as that given in the work of Asan and Namli [15]. The exact comparison between current simulation results and the results of the earlier work [15] is not shown here as the contour plots of the earlier work [15] do not possess numerical values. The accuracy of the results is further verified for domains with 24×24 and 26×26 elements, and it is observed that the results differ within 1%. Further, as a verification of the thermal equilibrium of the present steady state system, numerical values of the average Nusselt numbers on the bottom and inclined walls are compared, and it is found that the average Nusselt number of the bottom wall ($\bar{\mathrm{Nu}}_b$) is nearly $\sqrt{2}$ times the average Nusselt number of the inclined wall ($\bar{\mathrm{Nu}}_l$) as the length of the inclined wall is $\sqrt{2}$. It may be noted that the average Nusselt numbers of the bottom wall are 6.4, 6.6, and 6.6 for 20×20, 24×24, and 26×26 elements, respectively, for $\mathrm{Pr}=0.026$ and $\mathrm{Ra}=10^5$. This specific case is chosen to validate the presence of multiple circulation, and further tests are carried out to examine the stability of multiple circulation via small perturbation with asymmetric boundary conditions. For all computations, we have used 24×24 biquadratic elements or 49×49 grid points, and residual norms are restricted within 10^{-6}. The errors in average Nusselt numbers are found within 1–2% at the thermal equilibrium.

Simulation studies are performed for the Rayleigh number varying within 10^3–10^5 for a fixed Prandtl number, while the plots are obtained for Prandtl numbers $\mathrm{Pr}=0.0026$–1000. Local and average Nusselt numbers are also evaluated for specific cases. The comparative study was made for uniform and nonuniform heating of the bottom walls. In order to have a clear understand-

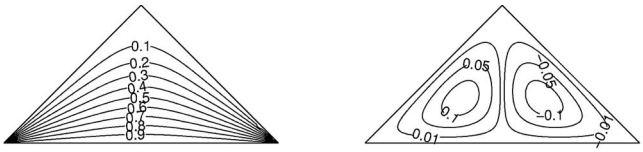

Fig. 3 Temperature and stream function contours for a uniformly heated bottom wall, $\theta(X,0)=1$, and cooled inclined walls, $\theta(X,Y)=0$, with $Ra=10^3$ and $Pr=0.026$ (Case I). Clockwise and anticlockwise flows are shown with negative and positive signs of stream function, respectively.

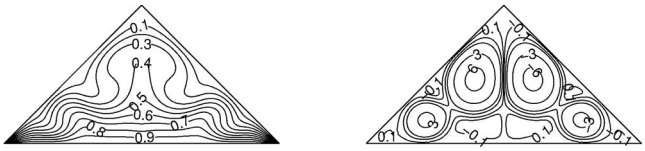

Fig. 7 Temperature and stream function contours for a uniformly heated bottom wall, $\theta(X,0)=1$, and cooled inclined walls, $\theta(X,Y)=0$, with $Ra=10^5$ and $Pr=0.026$ (Case I). Clockwise and anticlockwise flows are shown with negative and positive signs of stream function, respectively.

ing, the results are categorized into various sections. For the brevity of the paper, only the most important results are presented in the following sections.

4.2 Uniform Heating of Bottom Wall (Case I). Figures 3–9 display the effects of Ra ($Ra=10^3-10^5$) and Pr ($Pr=0.026-1000$) when the bottom wall is uniformly heated while the inclined walls are maintained at constant cold temperature. The fluid near the bottom portion of the enclosure is hotter than the fluid near the cold inclined walls, and hence the fluid near the bottom wall has a lower density than that near the inclined cold walls. Thus, the fluid near the center of the bottom wall moves upward, while the relatively heavy fluid near the cold inclined walls moves downward along the cold walls. Figure 3 shows that isotherms emerge normally from the line of symmetry toward the intersection of the inclined walls and the horizontal bottom wall. Two oppositely rotating circulation cells are present in the enclosure, and eyes of vortices are located at the center of each half of the cross section. It is observed that the left half of the axis of symmetry gives an anticlockwise circulation, whereas the right half of the axis of symmetry gives a clockwise circulation pattern. Results indicate that at a low Rayleigh number ($Ra=10^3$), the isotherm lines are smooth and monotonic as, shown for $Pr=0.026$ in Fig. 3. The magnitudes of the stream function contours are very small. This also verifies that at low Ra, the heat transfer is mostly due to conduction.

At $Ra=5\times10^3$ and $Pr=0.026$, the temperature contours with $\theta\geq0.2$ start to get deformed toward the bottom wall (Fig. 4). The presence of significant convection is also exhibited in the temperature contours, which get pushed toward the central portion of the bottom wall. The role of convection on heat transfer effects will be illustrated later via a local Nusselt number versus Rayleigh number plot. The critical Rayleigh number (for this case: $Ra=5\times10^3$) may be obtained from asymptotes of the average Nusselt number versus Rayleigh number plot, as discussed later. As the Rayleigh number increases to 10^4 for $Pr=0.026$, isotherms are more compressed near the corners of the bottom wall (see Fig. 5). This is due to the fact that the secondary circulation at the corners of the bottom wall causes the cold fluid to accelerate toward the hot bottom wall. These secondary vortices push the eye of the primary vortices slightly toward the axis of symmetry, as seen in Fig. 5. As the Rayleigh number increases to 4×10^4, secondary circulation become stronger (see Fig. 6). Therefore, more cold fluid moves toward the hot bottom wall resulting in sharp stretching at the middle of temperature contours near the cold wall. As Ra increases further for $Pr=0.026$, secondary circulation will also appear near the center of the bottom wall. This secondary circulation moves more hot fluid to the top and that results in a shift of eyes of primary vortices. Due to the larger circulation of hot fluid to the upward direction, the temperature contours with $\theta\geq0.5$

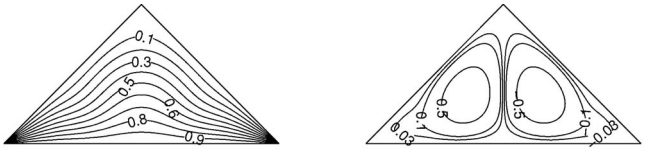

Fig. 4 Temperature and stream function contours for a uniformly heated bottom wall, $\theta(X,0)=1$, and cooled inclined walls, $\theta(X,Y)=0$, with $Ra=5\times10^3$ and $Pr=0.026$ (Case I). Clockwise and anticlockwise flows are shown with negative and positive signs of stream function, respectively.

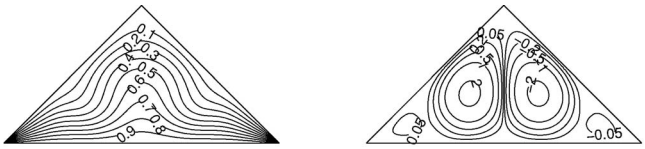

Fig. 5 Temperature and stream function contours for a uniformly heated bottom wall, $\theta(X,0)=1$, and cooled inclined walls, $\theta(X,Y)=0$, with $Ra=10^4$ and $Pr=0.026$ (Case I). Clockwise and anticlockwise flows are shown with negative and positive signs of stream function, respectively.

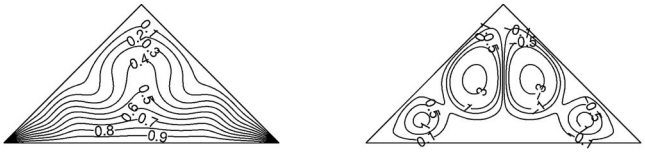

Fig. 6 Temperature and stream function contours for a uniformly heated bottom wall, $\theta(X,0)=1$, and cooled inclined walls, $\theta(X,Y)=0$, with $Ra=4\times10^4$ and $Pr=0.026$ (Case I). Clockwise and anticlockwise flows are shown with negative and positive signs of stream function, respectively.

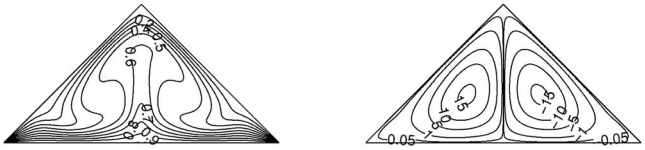

Fig. 8 Temperature and stream function contours for a uniformly heated bottom wall, $\theta(X,0)=1$, and cooled inclined walls, $\theta(X,Y)=0$, with $Ra=10^5$ and $Pr=0.7$ (Case I). Clockwise and anticlockwise flows are shown with negative and positive signs of stream function, respectively.

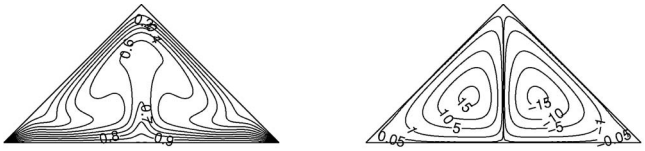

Fig. 9 Temperature and stream function contours for a uniformly heated bottom wall, $\theta(X,0)=1$, and cooled inclined walls, $\theta(X,Y)=0$, with $Ra=10^5$ and $Pr=1000$ (Case I). Clockwise and anticlockwise flows are shown with negative and positive signs of stream function, respectively.

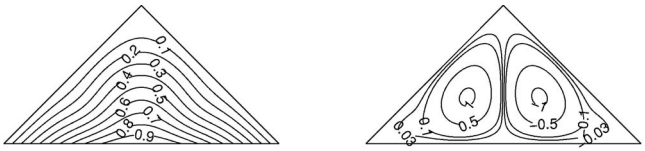

Fig. 10 Temperature and stream function contours for nonuniformly heated bottom walls, $\theta(X,0)=\sin(\pi X/2)$, and cooled inclined walls, $\theta(X,Y)=0$, with $Ra=5\times10^3$ and $Pr=0.026$ (Case II). Clockwise and anticlockwise flows are shown with negative and positive signs of stream function, respectively.

condensed in a very small regime near the bottom wall for $Ra=10^5$, as seen in Fig. 7. The additional secondary circulation near the inclined walls reduces the thermal gradient at the middle portion of the inclined walls.

As Pr increases from 0.026 to 0.7, the strength of primary circulation increases, as seen in Fig. 8, and the secondary circulation disappears. At $Ra=10^5$ and Pr=0.7, the circulation near the central regime is stronger and larger cold fluid moves toward the bottom wall. Consequently, the bottom portion of temperature contours with $\theta\geqslant0.2$ starts to get stretched toward the bottom wall due to an increase in temperature gradient. Comparative studies on Figs. 8 and 9 show that as Pr increases from 0.7 to 1000, the values of stream function and isotherms in the core cavity increase. The similar qualitative features of the stream function and isotherms are also found for Pr=10 and Pr=100 (figures not shown). It is interesting to note that the greater circulation due to higher Pr leads to an elliptical stream function deformed toward the corner portions of the bottom wall. In addition, the stream functions, except those at the central regime, are almost triangular, indicating higher intensity of flows.

4.3 Nonuniform Heating of Bottom Wall (Case II). Figures 10–12 illustrate the stream function and isotherm contours for various values of Pr=0.026–0.7 with $Ra=10^3-10^5$ when the bottom wall is nonuniformly heated. As seen in Figs. 3–9, uniform heating of bottom wall causes a finite discontinuity in Dirichlet-type boundary conditions for the temperature distribution at both edges of the bottom wall. In contrast, the nonuniform heating removes the singularity at the edges of the bottom wall and provides a smooth temperature distribution in the entire enclosure. Similar to the uniform heating case, the isotherm lines are almost

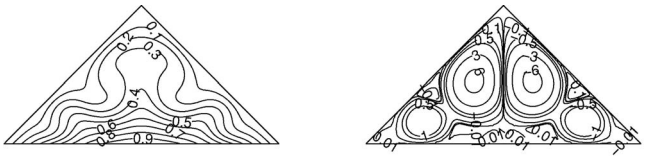

Fig. 11 Temperature and stream function contours for nonuniformly heated bottom walls, $\theta(X,0)=\sin(\pi X/2)$, and cooled inclined walls, $\theta(X,Y)=0$, with $Ra=10^5$ and $Pr=0.026$ (Case II). Clockwise and anticlockwise flows are shown with negative and positive signs of stream function, respectively.

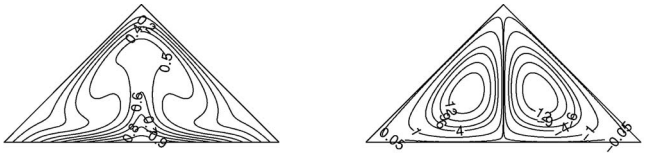

Fig. 12 Temperature and stream function contours for nonuniformly heated bottom walls, $\theta(X,0)=\sin(\pi X/2)$, and cooled inclined walls, $\theta(X,Y)=0$, with $Ra=10^5$ and $Pr=0.7$ (Case II). Clockwise and anticlockwise flows are shown with negative and positive signs of stream function, respectively.

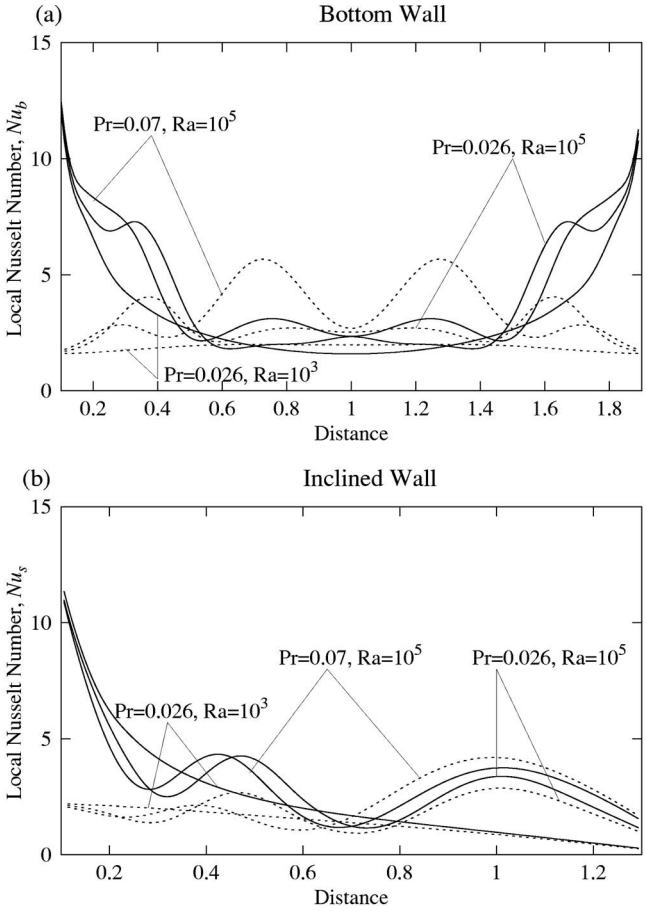

Fig. 13 Variation of the local Nusselt number with distance for low Pr at the (*a*) bottom wall and (*b*) inclined wall for uniformly (—) and nonuniformly (---) heated bottom walls and cold isothermal inclined walls.

smooth and parallel, and the magnitude of the stream function is very small at the smaller Rayleigh number regime (figure not shown). The conduction dominant heat transfer is observed up to $Ra=5\times10^3$ for Pr=0.026, which corresponds to Fig. 10. At the critical Rayleigh number ($Ra=5\times10^3$), the isotherms with $\theta\geqslant0.2$ start to get pushed toward the bottom wall due to a stronger flow of cold fluid to the bottom wall. As the thermal gradient at the central regime is larger than that with uniform heating, the intensity of circulation is stronger, resulting in larger values of stream functions at the center compared to the uniform heating case.

At $Ra=10^5$ and Pr=0.026, the circulation pattern is qualitatively similar to the uniform heating case with the identical situation (Fig. 11). Due to nonuniform heating of the bottom wall, the heating rate near the corners of the wall is generally lower, which induces less buoyancy effect, resulting in less thermal gradient near the corners. On the other hand, the thermal gradient is large near the central regime of the bottom wall. This results in a larger primary circulation and a weaker secondary circulation compared to that with the uniform heating case. Similar to the uniform heating case, many secondary circulation cells are found near the corners at the bottom wall and the middle portion of inclined walls. Also, similar to the uniform heating case, a higher Prandtl number suppresses the secondary circulation for a nonuniform heating of the bottom wall, as can be seen in Fig. 12.

4.4 Heat Transfer Rates: Local Nusselt Numbers

*4.4.1 Small Prandtl Numbers (*Pr=0.026 *and 0.07).* Figures 13(*a*) and 13(*b*) display the effects of Ra and Pr on the local

Nusselt number at the heated bottom wall and cold inclined walls, respectively. In the case of uniform heating of the bottom wall (see Fig. 13(*a*)) due to discontinuity present in the temperature boundary condition at the edges of the bottom wall, the heat transfer rate is very high at these corners, and it reduces toward the middle of the bottom wall as the compression of thermal contours is minimum at the middle due to less thermal gradient. At the inclined wall (see Fig. 13(*b*)), the heat transfer rate is maximum at the bottom edge and minimum at the top edge for all Rayleigh numbers. As Ra increases from 10^3 to 10^5, oscillations in heat transfer rate or local Nusselt number are seen near the corners and at the central regime of the bottom wall due to secondary circulation. The oscillations in heat transfer rates are also observed for the inclined walls. Due to stronger circulation near the central regime, the thermal gradient is less near the center of the inclined wall, whereas due to less mixing, the thermal gradient is large at the distance of 0.5 and 1 along the inclined wall. Common to a high Rayleigh number is the wavy distribution of a local Nusselt number due to secondary circulation.

In the case of nonuniform heating (see Fig. 13(*a*)), the local Nusselt number is almost constant for $\mathrm{Ra}=10^3$ throughout the bottom wall due to a uniform thermal gradient at the bottom wall. As Ra increases from 10^3 to 10^5, there is a large thermal gradient at $X=0.7$ and $X=1.3$, and this results in the maximum local heat transfer rate (Nu) at $X=0.7$ and $X=1.3$, approximately. It is interesting to note that the greater circulation at the central regime reduces the intensity of the secondary circulation near the center of the bottom wall, resulting in a larger thermal gradient for nonuniform heating. Thus, the nonuniform heating strategy produces a sinusoidal type of local heat transfer rate with its minimum value at the edges of the bottom wall. At the inclined wall (see Fig. 13(*b*)), the local Nusselt number curve shows a monotonic decrease from the bottom edge to the top edge of the inclined wall with its maximum value at the bottom edge of the inclined wall for $\mathrm{Ra}=10^3$. At a higher Rayleigh number, the local Nusselt number distribution is wavy in nature due to the secondary circulation similar to the uniform heating case.

*4.4.2 High Prandtl Numbers (*Pr=0.7 *and 10).* Figures 14(*a*) and 14(*b*) display the effects of Ra and Pr on the local Nusselt number at the heated bottom wall and cold inclined walls for Pr =0.7 and 10. Due to the presence of singularities at the edges of the bottom wall for the uniform heating case, the local heat transfer rates at the edges of the bottom wall are maximum and the values are minimum at the center of the bottom wall (Fig. 14(*a*)). For the case of nonuniform heating, the local Nusselt number at the bottom wall is maximum at $X=0.6$ and $X=1.4$ and produces a sinusoidal type of heat transfer rates for higher Ra($\sim 10^5$) (Fig. 14(*a*)). At higher Pr, the secondary circulation is absent and the primary circulation with larger intensity enhances thermal mixing, and this reduces the thermal gradient. Therefore, the less heat transfer rate is observed at the center of the bottom wall for both uniform and nonuniform heating cases.

Similar to Fig. 13(*b*), the local heat transfer rates at the inclined walls have maximum values at the bottom edge and decrease toward the top edge for small Ra. At a higher Rayleigh number, the local Nusselt number at the inclined wall has a minima at a distance of 0.25–0.4 along the inclined wall, and afterward the local Nusselt number increases up to a distance of 1.1. This is due to a large thermal gradient, which further results in large compression of thermal contours near the bottom and top corner points for both the uniform and nonuniform heating cases. In contrast, the local Nusselt number have more wavy distributions for smaller Prandtl numbers (Pr=0.026–0.07), as seen in Fig. 13 due to a stronger secondary circulation near the bottom and inclined walls.

4.5 Overall Heat Transfer and Average Nusselt Numbers. Figures 15 and 16 illustrate the average Nusselt number variations along the bottom and inclined walls for various Rayleigh and Prandtl numbers. The average Nusselt numbers are obtained using

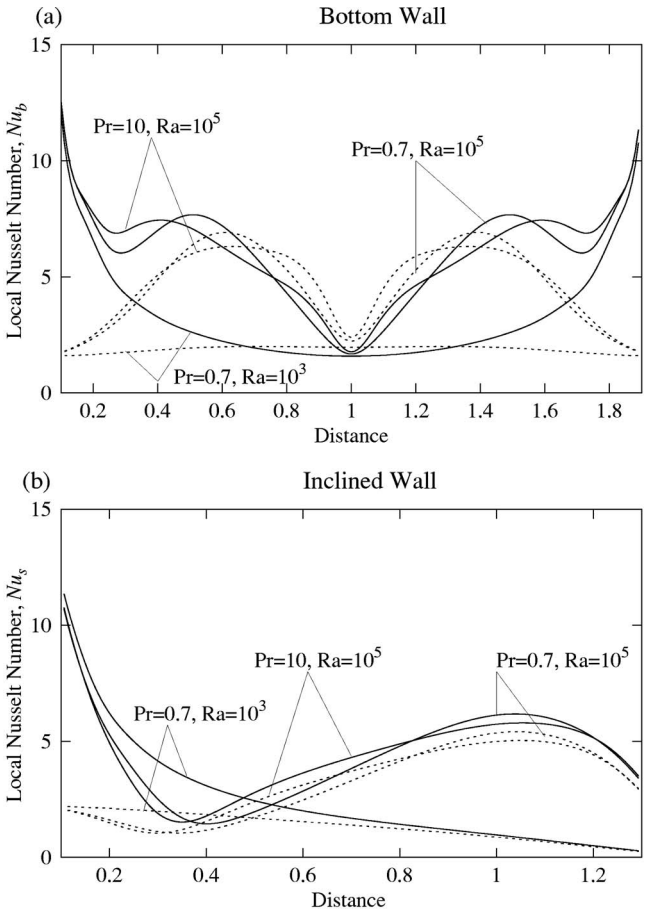

Fig. 14 Variation of the local Nusselt number with distance for high Pr at the (*a*) bottom wall and (*b*) inclined wall for uniformly (—) and nonuniformly (---) heated bottom walls and cold isothermal inclined walls.

Eqs. (18)–(20), where the integral is evaluated using Simpson's 1/3 rule. The inclined walls are kept at constant cold temperature, and due to the symmetry, the average Nusselt number of the left inclined wall is equal to that of the right inclined wall. The critical Rayleigh number is found from the semilog plot of the average Nusselt number versus the Rayleigh number, and at the critical Rayleigh number the transition from a conduction dominant mode to a convection dominant mode takes place. It is interesting to note that the average Nusselt number increases significantly with Prandtl number for a low Prandtl number regime (Pr =0.026–0.07); however, the increase in the average Nusselt number with Rayleigh number is nonmonotonic (see Fig. 15).

The nonmonotonic distribution of the average Nusselt number versus Ra has been explained via the distributions of local Nusselt numbers (Nu_b and Nu_s) versus the distance for Pr=0.026, as seen in inset plots of Fig. 15. Three representative values of Ra have been chosen within the regime $\mathrm{Ra}=2\times10^4-5\times10^4$, and the average Nusselt numbers show a smaller value at $\mathrm{Ra}=3\times10^4$ for both uniform and nonuniform heating cases. In the case of a uniform heating, it is observed that Nu_b is larger at the middle portion and at the right end of the bottom wall for $\mathrm{Ra}=2\times10^4$, whereas Nu_b is larger near the left corner point for $\mathrm{Ra}=5\times10^4$ (see the inset of Fig. 15(*a*)). The local heat transfer rate (Nu_b) at $\mathrm{Ra}=3\times10^4$ has intermediate values at the middle portion and two corners of the bottom wall. For the inclined wall, there are two local maxima of Nu_s at two interior points, and Nu_s is larger for $\mathrm{Ra}=5\times10^4$ whereas Nu_s has the intermediate value for $\mathrm{Ra}=3\times10^4$. For nonuniform heating, Nu_b has a larger magnitude at the

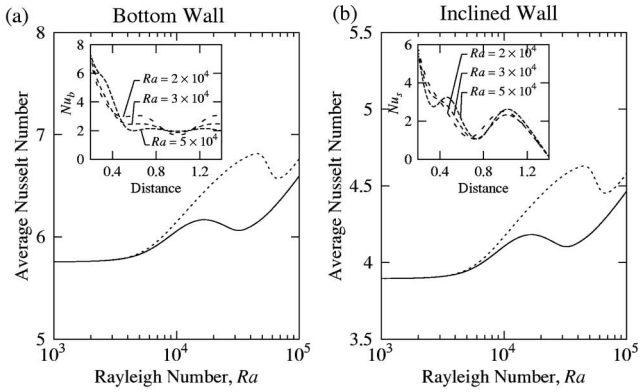

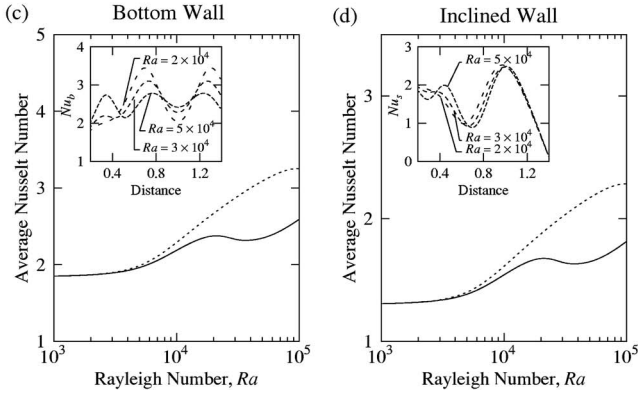

Fig. 15 Variation of the average Nusselt number with the Rayleigh number for uniformly heated ((*a*) and (*b*)) and nonuniformly heated bottom walls ((*c*) and (*d*)) with Pr=0.026 (—) and Pr=0.07 (---). The insets show the plot of local Nusselt numbers (Nu_b and Nu_s) versus the distance for three sets of Ra.

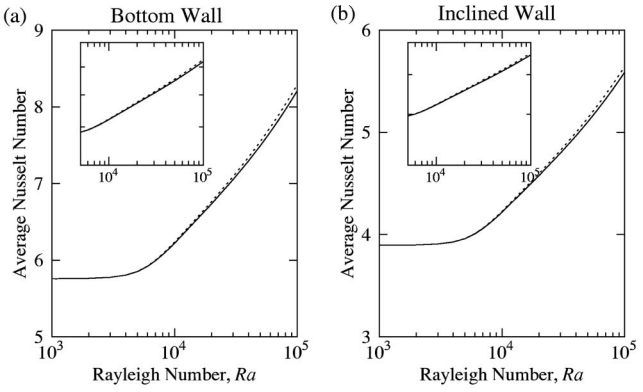

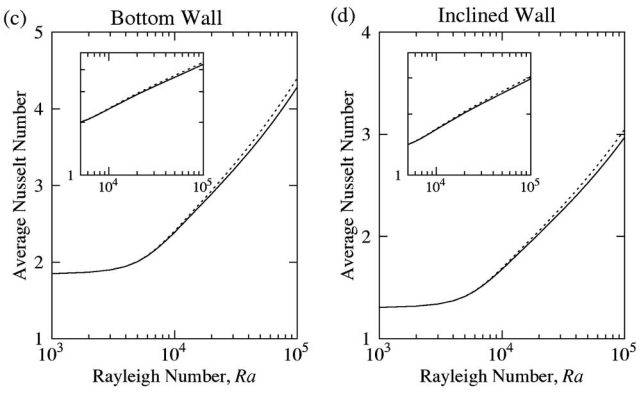

Fig. 16 Variation of the average Nusselt number with the Rayleigh number for uniformly heated ((*a*) and (*b*)) and nonuniformly heated bottom walls ((*c*) and (*d*)) with Pr=0.7 (—) and Pr=10.0 (---). The insets show the log-log plot of the average Nusselt number versus the Rayleigh number for convection dominant regimes.

center and near the right corner for $Ra=2\times10^4$ and has smallest values for $Ra=5\times10^4$, whereas Nu_s has a slightly lesser magnitude around the central regime of the sidewall for $Ra=5\times10^4$ (see insets of Figs. 15(*c*) and 15(*d*)). Similar to the uniform heating case, the intermediate values of Nu_b and Nu_s are attained at $Ra=3\times10^4$. Therefore, the wavy distribution of local Nusselt numbers due to secondary circulation at $2\times10^4\leqslant Ra\leqslant5\times10^4$ causes a nonmonotonic distribution of the average Nusselt number. It may be noted that nonmonotonicity occurs at a higher $Ra(5\times10^4\leqslant Ra\leqslant7\times10^4)$ for Pr=0.07 with uniform heating cases only. Therefore, the correlations of average Nusselt numbers and Rayleigh numbers could not be established for a low Prandtl number regime ($Pr\leqslant0.1$). It may be noted that the nonmonotonicity may occur at larger Pr for $Ra>10^5$; however, current study is based on the analysis within $Ra\leqslant10^5$.

At a high Prandtl number regime, the variation of the average Nusselt number is monotonic with the Rayleigh number, and therefore heat transfer correlations are found for those cases (Fig. 16). The insets show the log-log plot for the average Nusselt number versus the Rayleigh number for convection dominant regimes. It may be remarked that the overall heat transfer rate (average Nusselt number) is less in nonuniform heating than in uniform heating due to the less heat input to the system for all Prandtl number regimes. The log-log linear plot is obtained with more than 20 data sets. A least squares curve is fitted, and the overall error is limited within 1%. The following correlations with high Prandtl numbers (Pr=0.7 and 10) are obtained for Case I (uniform heating) and Case II (nonuniform heating) as follows:

Case I=uniform heating of bottom wall:

$$\begin{aligned}\overline{Nu_b} &= \sqrt{2}\overline{Nu_l}\\ &= 2.1646Ra^{0.1151} \quad Ra\geqslant5\times10^3 \quad Pr=0.7\\ &= 2.1065Ra^{0.1183} \quad Ra\geqslant5\times10^3 \quad Pr=10\end{aligned} \tag{21}$$

Case II=nonuniform heating of bottom wall:

$$\begin{aligned}\overline{Nu_b} &= \sqrt{2}\overline{Nu_l}\\ &= 0.2239Ra^{0.2569} \quad Ra\geqslant5\times10^3 \quad Pr=0.7\\ &= 0.2067Ra^{0.2663} \quad Ra\geqslant5\times10^3 \quad Pr=10\end{aligned} \tag{22}$$

5 Conclusions

The prime objective of the current investigation is to analyze the temperature and flow field with detailed analysis of heat transfer evaluation for natural convection in a triangular enclosure for a wide range of Pr (0.026–1000) with Ra varying within 10^3–10^5. The wide range of Prandtl numbers typically represents various fluid substances, e.g., molten metals, gases, water, oils, etc. Two cases with uniform and nonuniform (sinusoidal distribution) heating are studied, and the results may be useful to analyze various heating processes, such as material processing in a differentially heated cavity or heating applications for geophysical systems. The governing equations with appropriate boundary conditions are solved using the finite element method, which is particularly useful for analyzing the situation involving the singularity in temperature, and the biquadratic basis functions are used to obtain the

local and average Nusselt numbers. In addition, the mapping of a triangular domain into a square domain makes the method more generalized for complex geometries.

At the onset of the convection dominant mode, the temperature contour lines get compressed toward the bottom wall. As Ra increases, the secondary circulation start to develop along the regimes within the inclined walls and the bottom wall for Pr =0.026. At higher Ra, additional secondary circulations are also seen near the central regimes of the bottom wall and the inclined walls. For the nonuniform heating case, the intensity of the secondary circulation near the walls decreases and the stronger primary circulation at the center causes a high thermal gradient near the central regime of the bottom wall and near the top corners of the inclined wall at high Ra and Pr=0.026. It has also been observed that at higher Prandtl numbers, the primary circulation dominate and secondary circulation tend to disappear. The stronger circulation near the central regime causes a larger thermal gradient near the center of the bottom wall and the top corner of the inclined wall. Note that at low Pr, stream function contours are nearly circular in shape. At high Prandtl numbers, geometry has a considerable effect and stream function contours are nearly triangular in shape.

The overall heat transfer rates have been studied via local and average Nusselt numbers. The local Nusselt numbers at the bottom and inclined walls represent various interesting heating features. It is observed that the local Nusselt numbers are maximum at the bottom corner points, and due to secondary circulation, the local Nusselt number distribution shows a wavy nature for high Ra with Pr=0.026 for both uniform and nonuniform heating cases. For nonuniform heating cases, the sinusoidal distribution of the local Nusselt number at the bottom wall is observed for all Prandtl number regimes. The average Nusselt number illustrates overall lower heat transfer rates for nonuniform heating cases. It is interesting to observe that the average Nusselt number varies nonmonotonically with Rayleigh number for low Pr (Pr =0.026–0.07) due to effects of the secondary circulation, whereas the average Nusselt number is found to follow the power law variation with Rayleigh number for convection dominant regimes for high Pr (Pr=0.7–1000). It may be interesting to note that the power law correlation is almost invariant of Pr at a high Prandtl number regime.

We have investigated heat transfer studies for two cases involving uniform and nonuniform heating of bottom wall, in a triangular cavity with the angle of vertex being 90 deg and the aspect ratio being 0.5. It has been established that the local heat transfer rates at specific locations along the top and bottom walls may be enhanced either with uniform or nonuniform heating of the bottom wall for various Prandtl number regimes. The qualitative trend of heat transfer rates may be expected to be similar for various aspect ratios. The detailed analysis of heat transfer rates with various aspect ratios may be a subject of future research.

Acknowledgment

Authors would like to thank anonymous reviewers for constructive comments, which have improved the quality of the manuscript.

Nomenclature

g = acceleration due to gravity, m s^{-2}
k = thermal conductivity, W m^{-1} K^{-1}
L = height of the triangular cavity, m
Nu = local Nusselt number
p = pressure, Pa
P = dimensionless pressure
Pr = Prandtl number
Ra = Rayleigh number
T = temperature, K
T_h = temperature of hot bottom wall, K
T_c = temperature of cold vertical wall, K
u = x component of velocity
U = x component of dimensionless velocity
v = y component of velocity
V = y component of dimensionless velocity
X = dimensionless distance along the x coordinate
Y = dimensionless distance along the y coordinate

Greek Symbols

α = thermal diffusivity, m^2 s^{-1}
β = volume expansion coefficient, K^{-1}
γ = penalty parameter
θ = dimensionless temperature
ν = kinematic viscosity, m^2 s^{-1}
ρ = density, kg m^{-3}
Φ = basis functions
ψ = stream function
ξ = horizontal coordinate in a unit square
η = vertical coordinate in a unit square

Subscripts

b = bottom wall
l = left wall
r = right wall

Appendix

The name "isoparametric" derives from the fact that the same parametric function describing the geometry may be used for interpolating a spatial variable within an element. Figure 2 shows a triangular domain with trapezoidal elements with the mapping to a square domain. The transformation between (x,y) and (ξ,η) coordinates can be defined by

$$X = \sum_{k=1}^{9} \Phi_k(\xi,\eta) x_k$$

and

$$Y = \sum_{k=1}^{9} \Phi_k(\xi,\eta) y_k$$

Here, (x_k,y_k) are the X, Y coordinates of the k nodal points, as seen in Figs. 2(a) and 2(b), and $\Phi_k(\xi,\eta)$ is the basis function. The nine basis functions are

$$\Phi_1 = (1-3\xi+2\xi^2)(1-3\eta+2\eta^2)$$

$$\Phi_2 = (1-3\xi+2\xi^2)(4\eta-4\eta^2)$$

$$\Phi_3 = (1-3\xi+2\xi^2)(-\eta+2\eta^2)$$

$$\Phi_4 = (4\xi-4\xi^2)(1-3\eta+2\eta^2)$$

$$\Phi_5 = (4\xi-4\xi^2)(4\eta-4\eta^2)$$

$$\Phi_6 = (4\xi-4\xi^2)(-\eta+2\eta^2)$$

$$\Phi_7 = (-\xi+2\xi^2)(1-3\eta+2\eta^2)$$

$$\Phi_8 = (-\xi+2\xi^2)(4\eta-4\eta^2)$$

$$\Phi_9 = (-\xi+2\xi^2)(-\eta+2\eta^2)$$

The above basis functions are used for mapping the triangular domain or elements within the triangle into a square domain and the evaluation of integrals of residuals in finite element discretization.

References

[1] Ridouane, E., and Campo, A., 2006, "Relationship Between Thermal Convec-

tion Intensity and Aspect Ratio of Two Triangular Cavities Inscribed in Horizontal Rectangular Cavities," Int. J. Numer. Methods Heat Fluid Flow, **16**(2–3), pp. 338–355.
[2] Omri, A., Orfi, J., and Ben Nasrallah, S., 2005, "Natural Convection Effects in Solar Stills," Desalination, **183**(1–3), pp. 173–178.
[3] Farrow, D. E., and Patterson, J. C., 1994, "The Daytime Circulation and Temperature Structure in a Reservoir Sidearm," Int. J. Heat Mass Transfer, **37**(13), pp. 1957–1968.
[4] Sarris, I. E., Lekakis, I., and Vlachos, N. S., 2002, "Natural Convection in a 2D Enclosure With Sinusoidal Upper Wall Temperature," Numer. Heat Transfer, Part A, **42**(5), pp. 513–530.
[5] Perre, P., and May, B. K., 2001, "A Numerical Drying Model That Accounts for the Coupling Between Transfers and Solid Mechanics. Case of Highly Deformable Products," Drying Technol., **19**(8), pp. 1629–1643.
[6] Poulikakos, D., and Bejan, A., 1983, "The Fluid Dynamics of an Attic Space," J. Fluid Mech., **131**, pp. 251–269.
[7] Poulikakos, D., and Bejan, A., 1983, "Natural Convection Experiments in a Triangular Enclosure," ASME Trans. J. Heat Transfer, **105**, pp. 652–655.
[8] Karyakin, Y. E., Sokovishin, Y. A., and Martynenko, O. G., 1988, "Transient Natural Convection in Triangular Enclosures," Int. J. Heat Mass Transfer, **31**, pp. 1759–1766.
[9] Holtzman, G. A., Hill, R. W., and Ball, K. S., 2000, "Laminar Natural Convection in Isosceles Triangular Enclosures Heated From Below and Symmetrically Cooled From Above," ASME Trans. J. Heat Transfer, **122**, pp. 485–491.
[10] Salmun, H., 1995, "Convection Patterns in a Triangular Domain," Int. J. Heat Mass Transfer, **38**, pp. 351–362.
[11] Salmun, H., 1995, "The Stability of a Single Cell Steady State Solution in a Triangular Enclosure," Int. J. Heat Mass Transfer, **38**, pp. 363–369.
[12] Ridouane, E. H., and Campo, A., 2006, "Formation of a Pitchfork Bifurcation in Thermal Convection Flow Inside an Isosceles Triangular Cavity," Phys. Fluids, **18**(7), Art. No. 074102.
[13] Akinsete, V. A., and Coleman, T. A., 1982, "Heat Transfer by Steady Laminar Free Convection in Triangular Enclosures," Int. J. Heat Mass Transfer, **25**, pp. 991–998.
[14] Asan, H., and Namli, L., 2000, "Laminar Natural Convection in a Pitched Roof of Triangle Cross-Section: Summer Day Boundary Conditions," Energy Build., **33**, pp. 69–73.
[15] Asan, H., and Namli, L., 2001, "Numerical Simulation of Buoyant Flow in a Roof of Triangular Cross Section Under Winter Day Boundary Conditions," Energy Build., **33**, pp. 753–757.
[16] Ridouane, E. H., Campo, A., and Chang, J. Y., 2005, "Natural Convection Patterns in Right-Angled Triangular Cavities With Heated Vertical Sides and Cooled Hypotenuses," ASME Trans. J. Heat Transfer, **127**(10), pp. 1181–1186.
[17] Ridouane, E. H., Campo, A., and McGarry, M., 2005, "Numerical Computation of Buoyant Airflows Confined to Attic Spaces Under Opposing Hot and Cold Wall Conditions," Int. J. Therm. Sci., **44**(10), pp. 944–952.
[18] Roy, S., and Basak, T., 2005, "Finite Element Analysis of Natural Convection Flows in a Square Cavity With Non-Uniformly Heated Walls(s)," Int. J. Eng. Sci., **43**, pp. 668–680.
[19] Basak, T., Roy, S., and Balakrishnan, A. R., 2006, "Effects of Thermal Boundary Conditions on Natural Convection Flows Within a Square Cavity," Int. J. Heat Mass Transfer, **49**(23–24), pp. 4525–4535.
[20] Reddy, J. N., 1993, *An Introduction to the Finite Element Method*, McGraw-Hill, New York.
[21] Chung, T. J., 2002, *Computational Fluid Dynamics*, Cambridge University Press, London, UK.
[22] Batchelor, G. K., 1993, *An Introduction to Fluid Dynamics*, Cambridge University Press, London, UK.
[23] Jyotsna, R., and Vanka, S. P., 1995, "Multigrid Calculation of Steady, Viscous-Flow in a Triangular Cavity," J. Comput. Phys., **122**, pp. 107–117.
[24] Ganzarolli, M. M., and Milanez, L. F., 1995, "Natural Convection in Rectangular Enclosures Heated From Below and Symmetrically Cooled From the Sides," Int. J. Heat Mass Transfer, **38**, pp. 1063–1073.
[25] Corcione, M., 2003, "Effects of the Thermal Boundary Conditions at the Sidewalls Upon Natural Convection in Rectangular Enclosures Heated From Below and Cooled From Above," Int. J. Therm. Sci., **42**, pp. 199–208.

A Fast and Efficient Method for Predicting Fluid Flow and Heat Transfer Problems

Peng Ding

Xue-Hong Wu

Ya-Ling He

Wen-Quan Tao
e-mail: wqtao@mail.xjtu.edu.cn

State Key Laboratory of Multiphase Flow and Heat Transfer,
School of Energy and Power Engineering,
Xi'an Jiaotong University,
Shaanxi 710049, P.R. China

A fast and efficient method based on the proper orthogonal decomposition (POD) technique for predicting fluid flow and heat transfer problems is proposed in this paper. POD is first applied to an ensemble of numerical simulation results at design parameters to obtain the empirical coefficients and eigenfunctions, and then the fluid and temperature fields in the range of design parameters are resolved by a linear combination of empirical coefficients and eigenfunctions. The empirical coefficients at off-design parameters are obtained by a cubic spline interpolation method for steady problems and a Galerkin projection method for transient problems. Finally, the efficiency and accuracy of the algorithm are examined by three examples. The POD based algorithm can predict both the velocity and temperature fields in the range of design parameters accurately at a price of a large number of precomputed cases (snapshots). It also brings significant computational time savings for the new cases within the parameter range presimulated compared with the finite volume method with SIMPLE-like algorithm.
[DOI: 10.1115/1.2804935]

Keywords: proper orthogonal decomposition, fast and efficient method, numerical simulation of fluid flow and heat transfer

1 Introduction

Many important applications in science and engineering need robust online control and performance optimization design; examples are the control of distribution of velocity and temperature fields in the tin bath of float process to increase glass quality, the control of mixing patterns in chemical vapor deposition (CVD) reactors to enhance the reactor performance, the viscous drag reduction to minimize the drag force, and the control of microelectrical mechanical structure (MEMS) to manipulate microflows and adjust the temperature distribution in the microsystems. Fluid flow and heat transfer are the predominant processes in these problems, which are governed by a series of partial differential equations with infinite degrees of freedom, e.g., Navier–Stokes equation for the flow field, energy equation for the temperature field, and convection-diffusion equations for other scalar variable fields; if turbulence is present, appropriate turbulence models must be employed. The system states, such as temperature, concentration, pressure, and velocity in these systems, are generally functions of space and time. These computational fluid dynamics (CFD)-type models have a direct physical interpretation and can estimate rather accurately the flow fields and temperature fields in a broad parameter range using numerical techniques, such as the finite volume method (FVM), by dividing the spatial and time domain into an enormous number of control volumes to achieve good accuracy. Generally, we use iterative solvers to obtain the solutions of resulting algebraic equations, but this requires a large amount of computation cost, and these models are too slow for following the dynamics of the actual physical process. Applying these CFD-type models into the industrial online predictive control and optimization design is still a challenging work.

A method that has received growing attention recently is the proper orthogonal decomposition (POD), which has been used for data analysis, data compression, and development of reduced order models of distributed parameter systems. The greatest attraction of the POD technique comes from its energy-optimality characteristic: i.e., among all possible decompositions of a physical field, with the same number of modes, POD modes will, on average, contain the most energy. Bleris and Kothare [1] studied the problem of regulation of thermal transient in a microsystem using empirical eigenfunctions obtained from the POD technique. In Ref. [2], Azeez and Vakakis used the POD technique to analyze the dynamic characteristic of two vibroimpacting systems. Kirby and Sirovich [3] employed the POD technique for the characterization of human faces. Allery et al. [4] used the POD technique to predict the indoor air quality. Arjocu and Liburdy [5] used the POD technique to identify major spatially distributed features of the heat transfer coefficient of a 3×3 square array of submerged, elliptic impinging jets. In Ref. [6], Tyagi and Acharya performed the large eddy simulations in a periodic domain of a rotating square duct with normal rib turbulators; then, the POD technique was applied to the resulting flow fields to investigate the low dimensionality of the system.

In this paper, we introduce the basic idea of POD first, and then we examine the feasibility and efficiency of the POD based algorithm for the prediction of fluid flow and heat transfer problems by three examples: (1) steady natural convection in a cavity with an aspect ratio of 2 in the Rayleigh number range of $5000-2\times10^5$, (2) steady lid-driven cavity problem with a Reynolds number range of 500–6000, and (3) transient nonlinear heat conduction problem with a time-dependent heat source. Finally, some conclusions will be drawn.

2 Fundamentals of the Proper Orthogonal Decomposition

The mathematical formulations of the POD presented in this section closely follow the one in Ref. [1]. The most crucial notion

Contributed by the Heat Transfer Division of ASME for publication in the JOURNAL OF HEAT TRANSFER. Manuscript received August 31, 2006; final manuscript received March 30, 2007; published online March 6, 2008. Review conducted by Louis C. Burmeister.

of the POD is the snapshots $f(\mathbf{x},t_n)$, with $n=1,2,\ldots,N$ being a sample of solutions of the physical problem under consideration. The variable t represents some dependent variables; in transient problems it may denote the time variable, while in steady problems it may represent the Rayleigh number, Reynolds number, or such. It should be noted that the snapshots can be obtained either from the numerical simulation results or from experiments. Let us store a snapshot in a column vector with L entries. All snapshots of the system under consideration are stored in a rectangular $L \times N$ matrix $\{\mathbf{F}\}$.

The POD process aims at extracting a series of empirical eigenfunctions $\{\phi^k(\mathbf{x})_{k=1}^N\}$ and empirical coefficients $\alpha_k(t_k)$ from the snapshot matrix $\{\mathbf{F}\}$. According to the POD theory [7,8], the empirical eigenfunction $\phi(\mathbf{x})$ can be obtained by maximizing the normalized average projection of $\phi(\mathbf{x})$ onto $f(\mathbf{x},t_n)$. That is,

$$\text{Maximize}\left\{\lambda = \frac{\langle((\phi(\mathbf{x}),f(\mathbf{x},t_n))^2\rangle}{(\phi(\mathbf{x}),\phi(\mathbf{x}))}\right\} \tag{1}$$

where the brackets $\langle\cdot,\cdot\rangle$ mean the ensemble average of the snapshots and $(\cdot,\cdot)$ mean the standard Euclidean inner product. We define the linear operator H on $\phi(\mathbf{x})$ as

$$H\phi = \int_\Omega \frac{1}{N}\sum_{n=1}^{N} f(\mathbf{x},t_n)f(\mathbf{x}',t_n)\phi(\mathbf{x}')d\mathbf{x}' \tag{2}$$

then

$$(H\phi,\phi) = \int_\Omega \int_\Omega \frac{1}{N}\sum_{n=1}^{N} f(\mathbf{x},t_n)f(\mathbf{x}',t_n)\phi(\mathbf{x}')d\mathbf{x}'\phi(\mathbf{x})d\mathbf{x} \tag{3}$$

$$= \frac{1}{N}\sum_{n=1}^{N} \int_\Omega f(\mathbf{x},t_n)\phi(\mathbf{x})d\mathbf{x}\int_\Omega f(\mathbf{x}',t_n)\phi(\mathbf{x}')d\mathbf{x}' \tag{4}$$

$$= \frac{1}{N}\sum_{n=1}^{N} (f(\mathbf{x},t_n),\phi(\mathbf{x}))^2 \tag{5}$$

$$= \langle(\phi,f)^2\rangle \tag{6}$$

Thus, Eq. (1) can be written as

$$\text{Maximize}\left\{\lambda = \frac{\langle(H\phi,\phi)^2\rangle}{(\phi,\phi)}\right\} \tag{7}$$

Reference [7] shows that this leads to the eigenvalue problem of

$$\int_\Omega \frac{1}{N}\sum_{n=1}^{N} f(\mathbf{x},t_n)f(\mathbf{x}',t_n)\phi(\mathbf{x}')d\mathbf{x}' = \lambda\phi(\mathbf{x}') \tag{8}$$

Equation (8) can be solved by the direct method of Refs. [7,8]. While in practical numerical simulation, the resolution of the spatial domain is higher than the number of snapshots, directly evaluating the averaged autocorrelation function needs very large computation resources. A more accessible approach, which is referred to as the method of snapshots, was proposed by Sirovich [9]. This snapshot version of POD reduces the computation task to a much more tractable eigenvalue problem with a size of N equal to the number of the snapshots. The snapshot version of POD further makes the assumption that the spatial eigenfunctions are a linear combination of the snapshots

$$\phi^k(\mathbf{x}) = \sum_{n=1}^{N} \sigma_n^k f(\mathbf{x},t_n) \tag{9}$$

We introduce Eq. (9) into Eq. (8) which yields

$$\mathbf{A}\sigma^{(n)} = \lambda_n\sigma^{(n)} \quad n=1,\ldots,N \tag{10}$$

where $\mathbf{A}$ is an N-dimensional symmetric and positive semidefinite matrix. The elements of matrix $\mathbf{A}$ are defined as

$$A_{i,j} = \frac{1}{N}\int_\Omega f(\mathbf{x}',t_i)f(\mathbf{x}',t_j)d\mathbf{x}' \quad i=1,\ldots,N \quad j=1,\ldots,N \tag{11}$$

Now, the problem is reduced to finding the eigenvectors $\sigma^{(n)}$ of matrix $\mathbf{A}$, which can be easily solved by a standard numerical method. At last, Eq. (9) is used to resolve the empirical eigenfunction $\phi^k(\mathbf{x})$. According to the POD theory [7,8], the empirical eigenfunction $\phi^k(\mathbf{x})$ satisfies the following orthogonality condition:

$$(\phi^j(\mathbf{x}),\phi^j(\mathbf{x})) = \delta_{ij} = \begin{cases} 1 & i=j \\ 0 & i\neq j \end{cases} \tag{12}$$

and the magnitude of eigenvalue λ_k provides a measure of the amount of energy captured by the corresponding eigenfunction $\phi^k(\mathbf{x})$, while the energy measures the contribution of each eigenfunction to the overall system dynamics. So, in practice, we often order the eigenfunctions $\phi^k(\mathbf{x})$ by the magnitude of their corresponding eigenvalues λ_k, i.e., $\lambda_1>\lambda_2>\cdots>\lambda_N$.

Then, the snapshots of the system under consideration can be reconstructed by a combination of the eigenvectors as follows:

$$f(\mathbf{x},t_n) = \sum_{k=1}^{N} \alpha_k(t_n)\phi^k(\mathbf{x}) \tag{13}$$

where $\alpha_k(t_n)$ is the empirical coefficient, which can be analytically found by projecting flow fields (or any fields to be solved) onto each eigenfunctions,

$$\alpha_k(t_n) = (f(\mathbf{x},t_n),\phi^k(\mathbf{x})) \tag{14}$$

The reconstruction formula (Eq. (13)) may be truncated at a truncation degree of M as

$$f(\mathbf{x},t_n) = \sum_{k=1}^{M} \alpha_k(t_n)\phi^k(\mathbf{x}) \quad M\leqslant N \tag{15}$$

We define the participant energy coefficient ξ_n and the cumulative energy coefficient η_n as

$$\xi_n = \lambda_n \Big/ \sum_{n=1}^{N} \lambda_n \tag{16}$$

$$\eta_n = \sum_{n=1}^{M} \lambda_n \Big/ \sum_{n=1}^{N} \lambda_n \quad M\leqslant N \tag{17}$$

where ξ_n represents the energy in the total N modes that is contained in the nth eigenfunction, and η_n denotes the energy in the total N modes that is contained in the first n eigenfunctions. Generally, the truncation error will decrease with the increase of truncation degree M up to an optimal value; further increase in M will deteriorate the result since eigenfunctions with large index are contaminated by a roundoff error.

Now, we can summarize the POD based algorithm as follows.

1. Construct the snapshot matrix.
2. Solve the eigenvalue problem $\mathbf{A}\sigma^{(n)}=\lambda_n\sigma^{(n)}$, $n=1,\ldots,N$.
3. Resolve the eigenfunctions by $\phi^k(\mathbf{x})=\Sigma_{n=1}^N\sigma_n^k f(\mathbf{x},t_n)$.
4. Resolve the empirical coefficient $\alpha_k(t_n)$.
5. Reconstruct the physical fields by $f(\mathbf{x},t_n)=\Sigma_{k=1}^M\alpha_k(t_n)\phi^k(\mathbf{x})$.

3 Example 1: Natural Convection in a Cavity

In this section, we consider the problem of natural convection of fluid in a two-dimensional cavity. Natural convection is a challenging and complex problem due to the inherent coupling of the fluid flow and the energy transport. The geometry of the cavity and boundary conditions are schematically shown in Fig. 1. The height h of the cavity is two times of the width w of the short

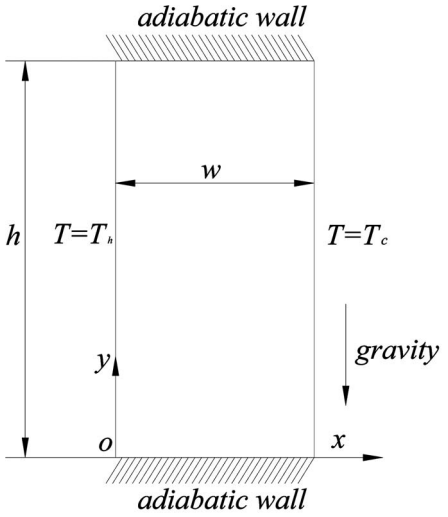

Fig. 1 Geometry of the cavity and boundary conditions, *h*/*w* =2

horizontal wall. The fluid in the cavity is air with a constant Pr number of 0.71. The left wall of the cavity is kept at a constant temperature T_h and the right wall at a constant lower temperature T_c. The other two surfaces are treated as adiabatic walls.

The equations governing the flow and temperature fields are those that express the conservation of mass, momentum, and energy. The flow, driven by buoyant forces, is assumed to be steady, laminar, and incompressible. The fluid properties are assumed constant, except for the density in the buoyancy term, where the Boussinesq approximation is valid. The mathematical formulation for this physical problem can be written in dimensionless form as

$$\frac{\partial U}{\partial X}+\frac{\partial V}{\partial Y}=0 \tag{18}$$

$$\frac{\partial (UU)}{\partial X}+\frac{\partial (UV)}{\partial Y}=-\frac{\partial P}{\partial X}+\frac{\partial^2 U}{\partial X^2}+\frac{\partial^2 U}{\partial Y^2} \tag{19}$$

$$\frac{\partial (UV)}{\partial X}+\frac{\partial (VV)}{\partial Y}=-\frac{\partial P}{\partial Y}+\frac{\partial^2 V}{\partial X^2}+\frac{\partial^2 V}{\partial Y^2}+\frac{\mathrm{Ra}}{\mathrm{Pr}}\theta \tag{20}$$

$$\frac{\partial (U\theta)}{\partial X}+\frac{\partial (V\theta)}{\partial Y}=\frac{1}{\mathrm{Pr}}\left(\frac{\partial^2 \theta}{\partial X^2}+\frac{\partial^2 \theta}{\partial Y^2}\right) \tag{21}$$

where the following dimensionless parameters are introduced:

$$X=\frac{x}{w} \quad Y=\frac{y}{w} \quad U=\frac{uw}{\nu} \quad V=\frac{vw}{\nu} \quad P=\frac{pw^2}{\rho\nu^2} \tag{22}$$

$$\theta=\frac{T-T_c}{T_h-T_c} \quad \mathrm{Pr}=\frac{\nu}{\alpha} \quad \mathrm{Ra}=\frac{g\beta(T_h-T_c)w^3}{\nu\alpha} \tag{23}$$

The parameters g, α, β, and ν are the acceleration due to gravity, the thermal diffusivity of the fluid, the coefficient of thermal expansion, and the fluid kinetic viscosity, respectively.

The boundary conditions are $U=V=0$ on all rigid walls, $\theta=1$ at $X=0$, $\theta=0$ at $X=1$, and $\partial\theta/\partial\mathbf{n}=0$ on the insulation walls, where $\mathbf{n}$ means the normal direction of walls.

The governing equations for mass, momentum, and energy are discretized by the widely used FVM [10,11]. The SIMPLE algorithm [10–12] is utilized for the treatment of the pressure-velocity coupling for the computation of the velocity and pressure fields on stagger grids. A high order QUICK [11,13] scheme is used to model the convective fluxes across the volume faces, and the conventional central difference scheme is used to approximate the diffusion terms. The set of linearized difference equations is solved with the tridiagonal matrix algorithm (TDMA). In this study, we use a 50×100 grid system, which is fine enough for the present problems, and the grid points are concentrated near the rigid walls where large physical variable gradients are expected. The computer code is validated by comparing the solutions with the benchmark solutions [14] for the case of natural convection in a square cavity, and the agreement is very good. For the simplicity of presentation, the results are not shown here since the main objective of this paper is the POD based algorithm.

3.1 Results and Discussion. The computations are first conducted at Rayleigh numbers from 5000 to 200,000 in increments of 5000, which gives a total of 40 solutions. In this example, the POD procedure is applied to the fluctuation part of the solutions. To do this, the average vector of the 40 solutions is first resolved as follows:

$$\bar{f}=\frac{1}{N}\sum_{n=1}^{N} f(\mathbf{x},t_n) \tag{24}$$

We form the snapshots by subtracting the average vector from the 40 solutions; then, the snapshots are assembled into the temperature snapshot matrix and the velocity snapshot matrix,

$$\Theta=\begin{bmatrix} \theta_{11} & \cdots & \theta_{1N} \\ \vdots & \ddots & \vdots \\ \theta_{L1} & \cdots & \theta_{LN} \end{bmatrix} \tag{25}$$

$$\mathbf{V}=\begin{bmatrix} U_{11} & \cdots & U_{1N} \\ V_{11} & \cdots & V_{1N} \\ \vdots & \ddots & \vdots \\ U_{L1} & \cdots & U_{LN} \\ V_{L1} & \cdots & V_{LN} \end{bmatrix} \quad N=1,\ldots,40 \tag{26}$$

As stated in Sec. 2, each column vector of the matrix represents the temperature or the velocity fields at a different design parameter, i.e., different Rayleigh number. Each row of the matrix represents the value of temperature at a specified grid point for different Ra numbers. There are a total of L rows for the temperature snapshot matrix and $2L$ rows in the velocity snapshot matrix since the velocity vector $\mathbf{V}$ has two components U and V, where U corresponds to the velocity in the x direction and V corresponds to the velocity in the y direction. The POD procedure is applied to these snapshot matrix to obtain the eigenfunctions $\phi_\theta(\mathbf{x})$ and $\phi_\mathbf{V}(\mathbf{x})$.

The velocity and the temperature fields can be expressed as a linear combination of the eigenfunctions $\phi_\theta(\mathbf{x})$, $\phi_\mathbf{V}(\mathbf{x})$ and the empirical coefficients as follows:

$$\theta^n_{\mathrm{POD}}(\mathbf{x})=\bar{\theta}+\sum_{k=1}^{M}\alpha_k(t_n)\phi^k_\theta(\mathbf{x}) \quad M\leqslant N \tag{27}$$

$$\mathbf{V}^n_{\mathrm{POD}}(\mathbf{x})=\bar{V}+\sum_{k=1}^{M}\beta_k(t_n)\phi^k_\mathbf{V}(\mathbf{x}) \quad M\leqslant N \tag{28}$$

To quantify the accuracy of the reconstruction formulas (Eqs. (27) and (28)), we define the relative error E as

$$E=\frac{\|f-f_{\mathrm{POD}}\|}{\|f\|} \tag{29}$$

where f means the finite volume solutions of the governing equations, and f_{POD} the solutions by means of the POD based algorithm; $\|\cdot\|$ means the L_2 norm.

In order to examine the accuracy of the POD at the off-design parameters, i.e., to test whether the POD procedure can be used to resolve the fluid and temperature fields at any Rayleigh numbers

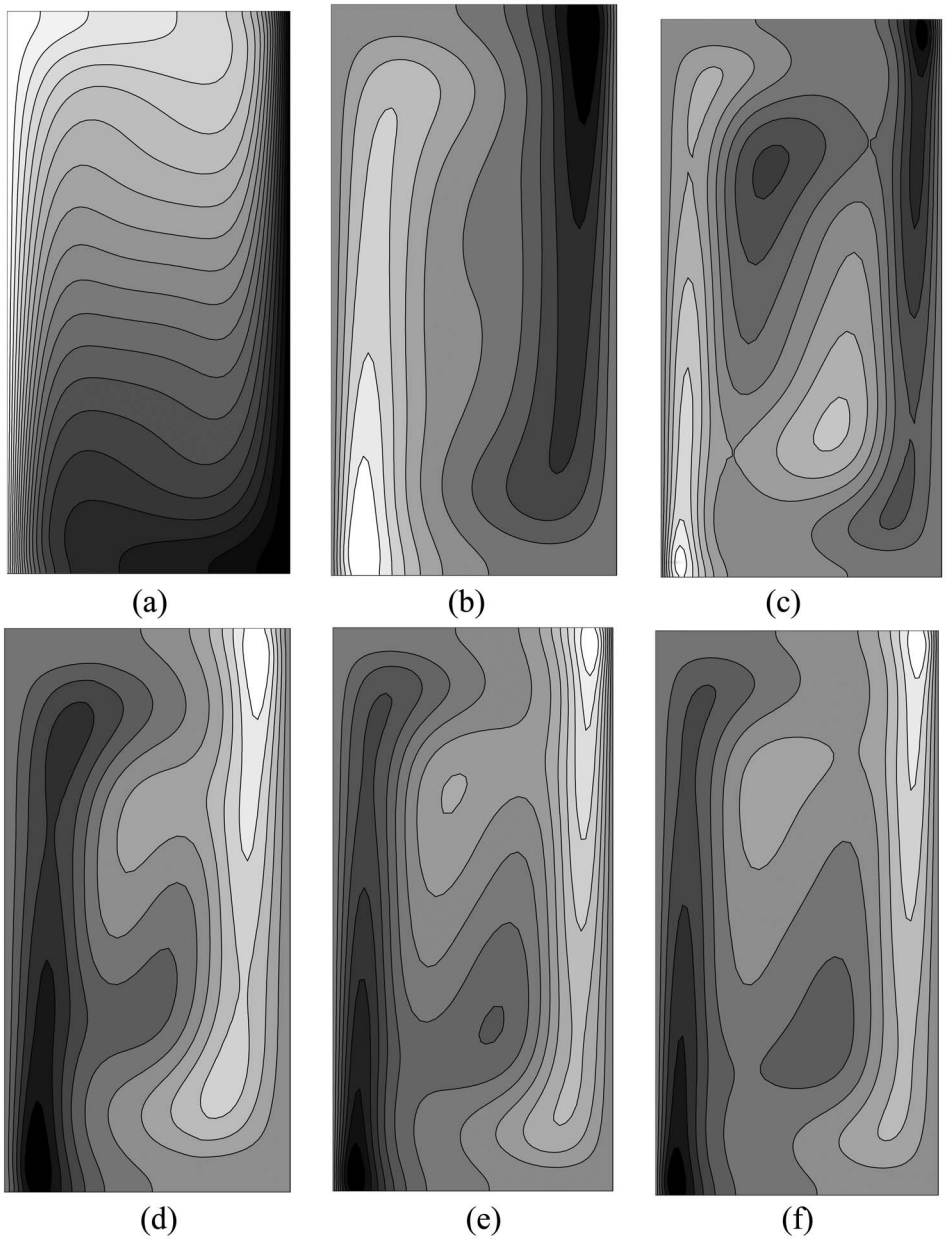

Fig. 2 Snapshots of temperature fields. (*a*) corresponds to the average temperature profile; (*b*)–(*f*) correspond to the fluctuation temperature fields at Ra=5000, Ra=50,000, Ra=100,000, 150,000, and Ra=200,000, respectively.

in the range of 5000 to 200,000, we also solve the governing equations at several representative Rayleigh numbers of 8150, 17,000, 85,700, and 168,800.

The average temperature field and the snapshots at Ra=5000, 50,000, 100,000, 150,000, and 200,000 are shown in Fig. 2. A total of 40 eigenvalues and 40 sets of eigenfunctions are obtained from the POD procedure. We arrange the eigenvalues according to their magnitude as $\lambda_1 \geqslant \lambda_2 \geqslant \cdots \geqslant \lambda_{40}$, and the first five largest eigenvalues of the temperature snapshots are listed in Table 1

Table 1 Eigenvalue and the energy distribution of velocity and temperature snapshots

n		1	2	3	4	5
ξ_n (%)	**U**	97.23	2.55	1.98×10^{-1}	1.29×10^{-2}	1.15×10^{-3}
	θ	95.44	4.28	2.09×10^{-1}	5.69×10^{-2}	3.06×10^{-3}
η_n (%)	**U**	97.233654	99.787496	99.985793	99.998766	99.999999
	θ	95.446871	99.730288	99.939785	99.996691	99.999756
λ_n	**U**	934,525.87	24545.32	1905.80	124.67	11.11
	θ	7.0941	0.3183	1.55×10^{-2}	4.22×10^{-3}	2.27×10^{-4}

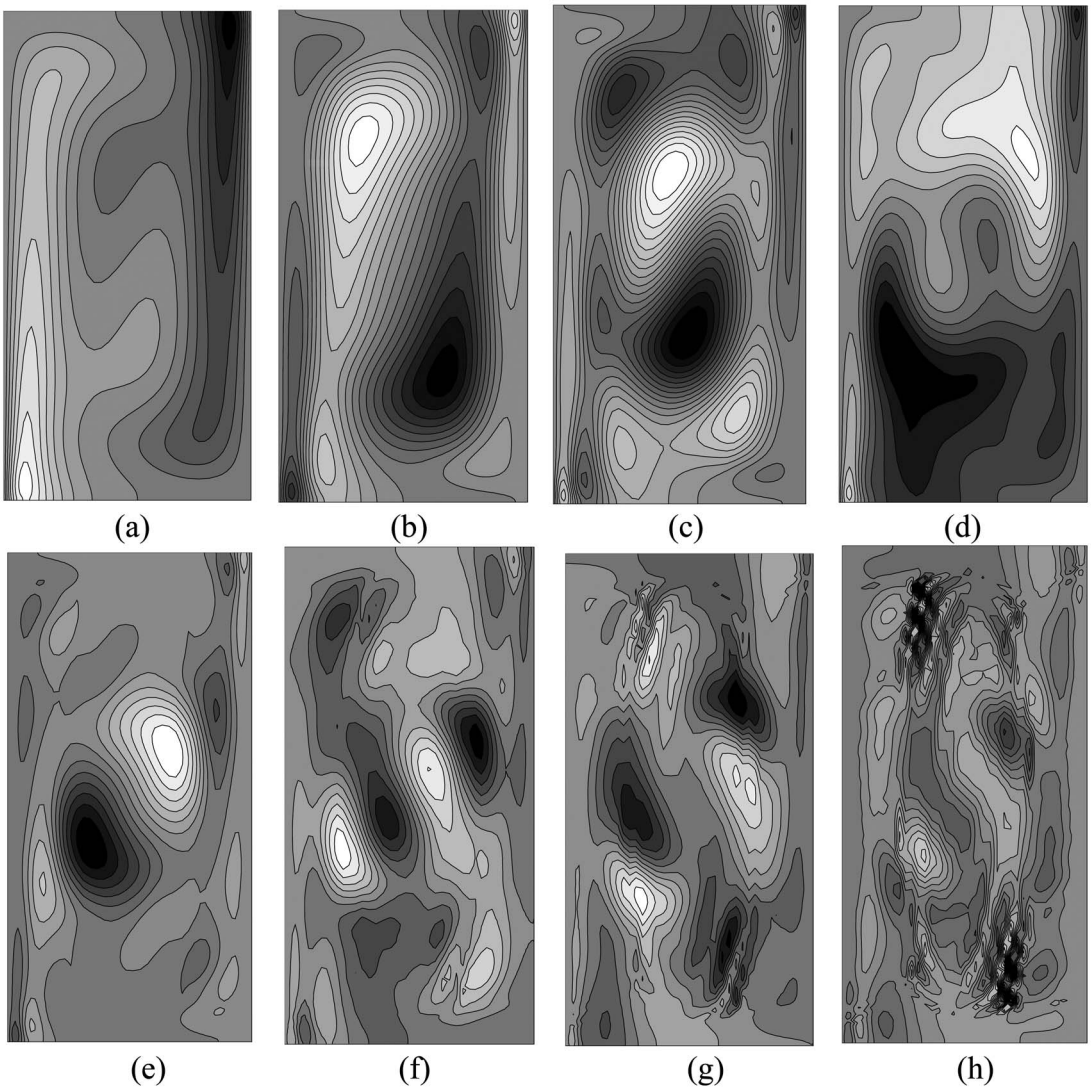

Fig. 3 The most dominant eight eigenfunctions obtained from the temperature snapshots by the POD technique

together with the participant energy coefficient ξ_n and the cumulative energy coefficient η_m. The energy optimality of the POD eigenfunctions is obvious in Table 1. For the temperature modes, it shows that the first eigenvalue have the largest magnitude and the most participant energy, and it alone captures 95.4468% of the total energy. The magnitude of the eigenvalue decreases drastically from the first value of 7.0941 to the second value of 0.3183 and the third value of 1.5571×10^{-2}. The second eigenfunction captures only 4.2834% of the total energy. The cumulative energy of the first two eigenvalues has reached 99.73028%. The later eigenvalues have much smaller eigenvalue and participant energy coefficients. For example, the 15th eigenvalue has a magnitude of 7.8198×10^{-10} and captures only 1.0521×10^{-8}% of the total energy. These smaller eigenvalues represent the contribution of the small scale structures to the total energy and cannot be truncated arbitrarily. Turning to the eigenvalues and the energy distribution of the velocity snapshots, a comparison with the eigenvalues; and the energy distribution of temperature snapshots shows that the magnitude of the velocity eigenvalues is much larger than temperature eigenvalues; the first velocity eigenfunction captures more energy than the first temperature eigenfunction. The variation trend is the same as that of the temperature snapshots.

The first eight temperature eigenfunctions and velocity eigenfunctions obtained by the POD procedure are shown in Figs. 3 and 4, respectively. Among all the eigenfunctions shown in Figs. 3 and 4, the eigenfunctions with large eigenvalues take the shape of large scale smooth structures, while the eigenfunctions with large index numbers have a tendency to include more small scale structures, and those small scale structures represent the structures not captured by the eigenfunctions of large eigenvalues, such as the velocity boundary layer or temperature boundary layer.

It should be noted that for the problems studied in this paper, there is no essential difference between applying the POD procedure to the fluctuation part and to the whole variable. Often, applying the POD procedure to the whole variable is more straightforward. We apply POD to the fluctuation part here just to show the versatility of the POD application.

3.2 Reconstruction and Extrapolation. The snapshots at the design parameters can be constructed by use of the reconstruction formula (Eqs. (27) and (28)). Since we have obtained the numerical solutions of velocity and the temperature fields at design conditions by FVM, we can resolve the empirical coefficients α_k and β_k analytically by projecting physical fields onto the POD eigenfunctions.

Figure 5 shows the logarithm of relative error E with 10 as the

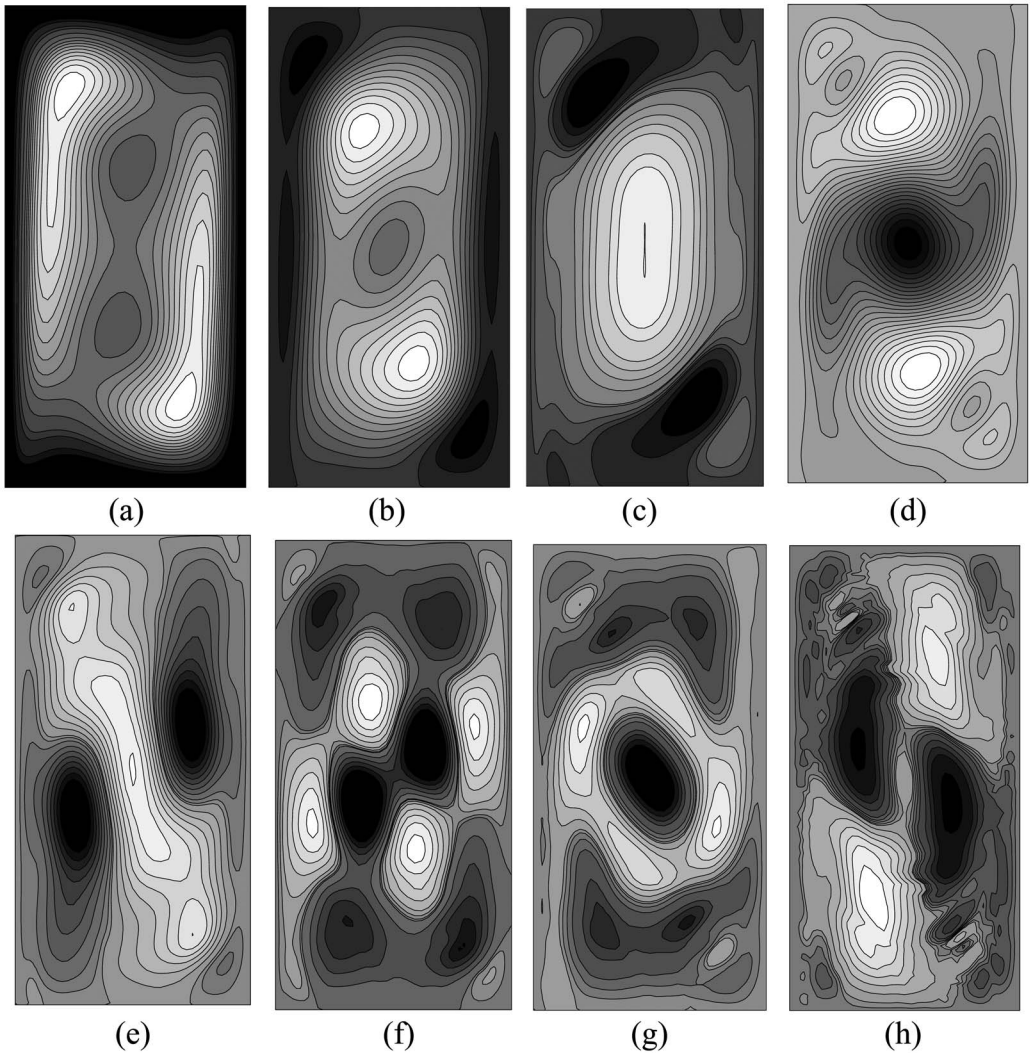

Fig. 4 The most dominant eight eigenfunctions obtained from the velocity snapshots by the POD technique (in streamline format)

base, between the numerical solutions obtained by FVM and the solutions obtained by POD procedure, where Fig. 5(*a*) corresponds to the relative error of temperature fields and Fig. 5(*b*) corresponds to the relative error of two components of the velocity fields. An overview of Fig. 5 shows that the physical fields can be reconstructed very well using the POD eigenfunctions as a basis. The relative error E decreases drastically as the increase of the truncation degree M, and the value of E takes the largest at the first few snapshots. For the temperature fields, with $M=4$, the relative error E is already less than 0.05%; the value of E may reach an order of 10^{-10} with $M=39$. There seems to be an increase in error when $M=40$ since the eigenfunctions with high index numbers may be contaminated by a roundoff error; the same phenomenon also exists for the velocity fields.

However, in practice, there are many cases in which the governing parameters are within the ranges prespecified. Not any parameter is exactly the same as any of the computed snapshots. We now demonstrate that by using the same POD eigenfunctions obtained at the design parameters, we are able to accurately reconstruct the physical fields at off-design parameters, too. It is this remarkable feature that makes POD very useful for the fast and accurate prediction of the fluid flow and heat transfer problems occurring in many industry processes. Assuming that no numerical solutions of the governing equations exist at the off-design parameters for the time being, we cannot resolve the empirical coefficients by projecting physical solutions onto the eigenfunctions. In this work, we use another method to evaluate the empirical coefficients needed for the reconstruction formula. We first fit a cubic spline through all the empirical coefficients at the design conditions, and then the empirical coefficients at the off-design parameters can be obtained by evaluating the cubic spline.

It is worth noting that even in the range of the design parameters, it is not a simple thing to directly interpolate the original snapshots for the solution desired. This is because the problems that we treat are strongly nonlinear, and it is difficult to know how to interpolate two neighboring snapshots even for a case positioned in space between the two snapshots.

The reconstruction physical fields at off-design parameters computed by the POD technique with a truncation degree of $M=6$ are compared with the FVM solutions in Fig. 6, and the plots show a remarkably good agreement.

It is interesting to compare the CPU time required for the POD based algorithm with that of the SIMPLE algorithm when simulating the natural convection heat transfer in a cavity. Table 2 says that the POD based algorithm is 100 times faster than the SIMPLE algorithm; it is also easy to find that the computation time for the POD technique is almost independent of the Rayleigh number and the truncation degree since the reconstruction of the physical field is a simple algebraic operation. It is expected that for more complicated situations, the saving in computational time may be much

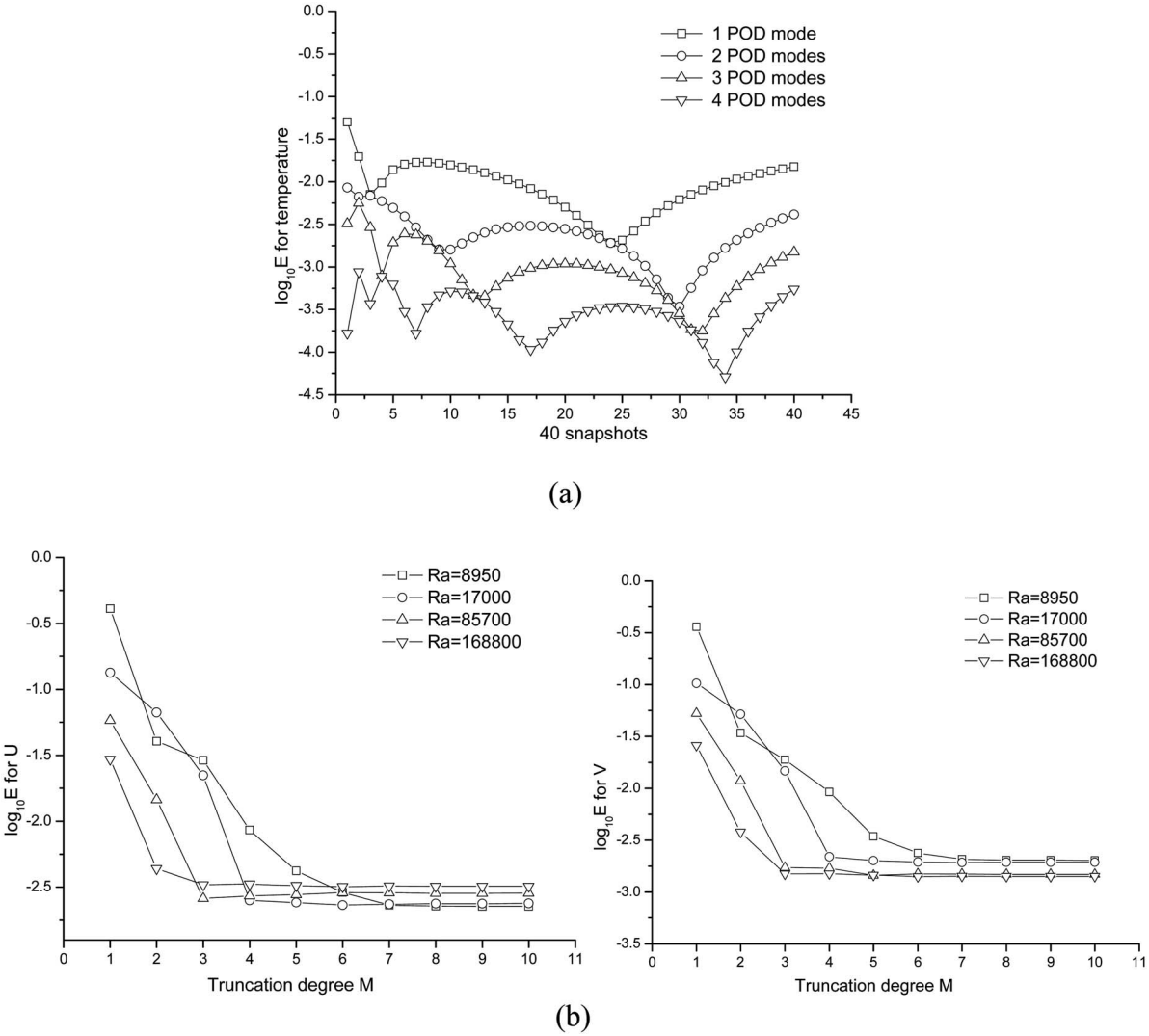

Fig. 5 The relative error between the numerical solutions and the POD reconstructions at design parameters. (*a*) corresponds to the relative error between the numerical temperature fields and the POD reconstruction fields of the 40 snapshots; (*b*) corresponds to relative error between the numerical velocity fields and the POD reconstruction fields of the 40 snapshots.

larger.

It should be noted that the computational time of each method was just picked up from the record in the computer. No conversion method was adopted between the FVM solution and the POD algorithm. This is because when both the POD and the FVM are used to provide information for the production control, it is this CPU computational time that makes sense. Of course, the process of creation of snapshots for POD based algorithm may consume a lot of computational resource and time. This is the expense that we pay for the later fast usage, and it is like the learning process or training process. However, once enough snapshots are collected, we may adopt the POD technique to obtain the required information in a very short time period. It is this quick response that is highly desired for control of a practical production process. By directly adopting the transient and multidimensional simulations in situ, we could not acquire the desired information in time although a lot of computational resource and time should also be paid. In addition, after the training process, a series of robust eigenfunctions and empirical coefficients can be used many times, and are valid over a useful range of governing parameters.

4 Example 2: Lid-Driven Cavity Flow

In this section, we consider a lid-driven cavity flow problem [15]. Figure 7 shows a schematic view of the cavity flow and its boundary conditions. The governing equations can be written in a dimensionless form as follows:

$$\frac{\partial U}{\partial X}+\frac{\partial V}{\partial Y}=0 \tag{30}$$

$$\frac{\partial (UU)}{\partial X}+\frac{\partial (UV)}{\partial Y}=-\frac{\partial P}{\partial X}+\frac{1}{\mathrm{Re}}\left(\frac{\partial^2 U}{\partial X^2}+\frac{\partial^2 U}{\partial Y^2}\right) \tag{31}$$

$$\frac{\partial (UV)}{\partial X}+\frac{\partial (VV)}{\partial Y}=-\frac{\partial P}{\partial Y}+\frac{1}{\mathrm{Re}}\left(\frac{\partial^2 V}{\partial X^2}+\frac{\partial^2 V}{\partial Y^2}\right) \tag{32}$$

where the characteristic length and characteristic velocity are the width of the cavity and the velocity of the lid, respectively.

The boundary conditions are

$$U=1, V=0 \quad \text{on the lid} \tag{33}$$

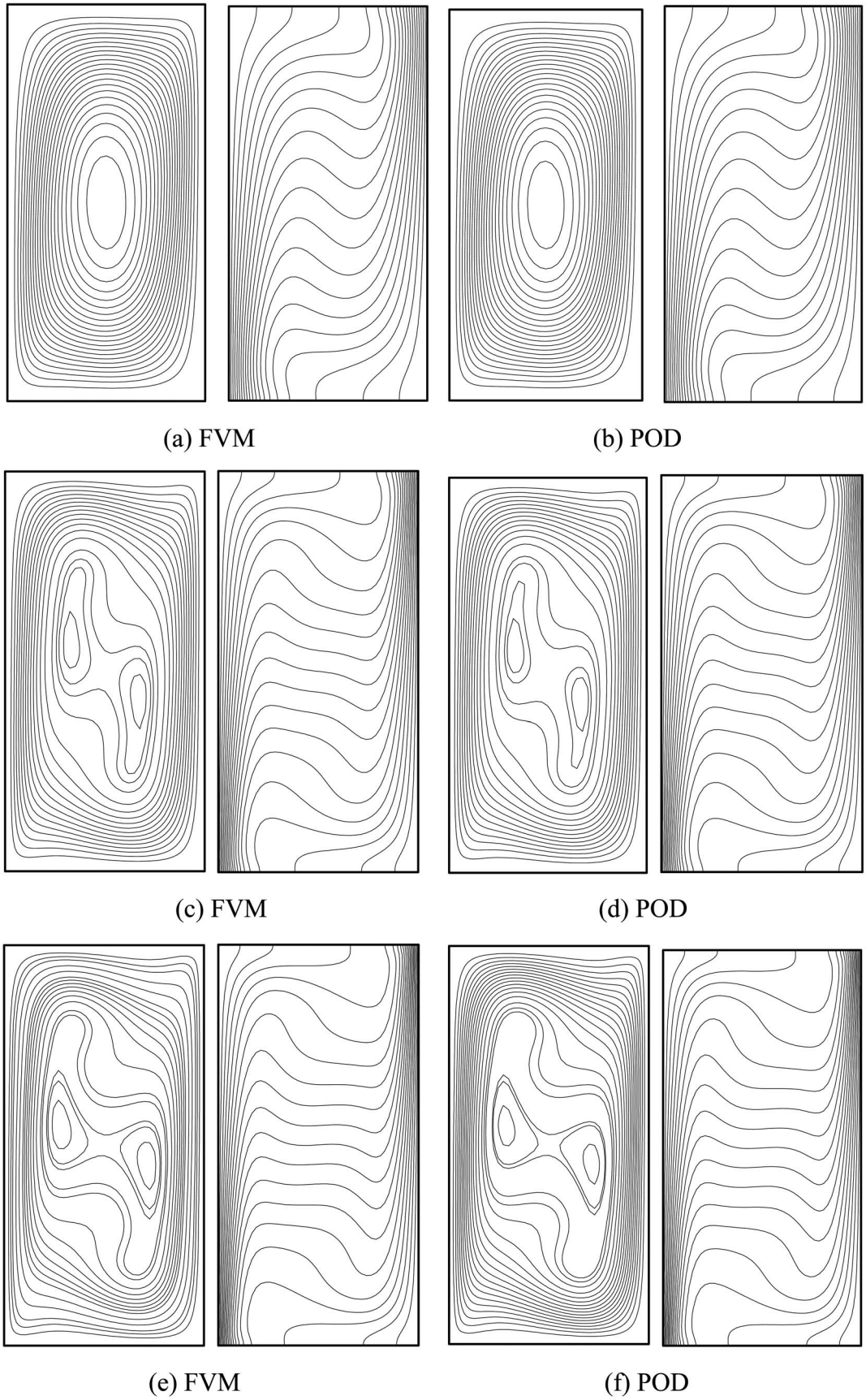

Fig. 6 Comparison between the POD and the FVM solutions for Ra numbers at off-design parameters, with *M*=6. (*a*) and (*b*) correspond to the streamline and isothermal at Ra=17,000; (*c*) and (*d*) correspond to the streamline and isothermal at Ra=85,700; (*e*) and (*f*) correspond to streamline and isothermal at Ra=168,800.

Table 2 Comparison of computation time between SIMPLE and POD (seconds)

Rayleigh number	8950	17,000	85,700	168,800
SIMPLE	137.36	131.08	117.96	116.09
POD with one mode	1.42	1.38	1.50	1.53
POD with five modes	1.45	1.49	1.53	1.49
POD with ten modes	1.53	1.56	1.56	1.56

$$U = 0, V = 0 \quad \text{on the wall} \tag{34}$$

It may be noted that although the lid-driven cavity flow is a pure fluid problem, it is still worth adopting this problem as an example. This is because the lid-driven cavity flow is a kind of classical problem in CFD and heat transfer area, and its benchmark solutions exist [15]. In addition, in many heat transfer problems, the working medium can be treated as one with constant thermophysical properties, and for such problems the solution of velocity fields is of crucial importance to obtain the temperature field. Therefore, we take this example to further verify the feasibility of POD for fluid flow and heat transfer problems.

4.1 Results and Discussion. The discretized equations are solved on an 80×80 grid system with the same numerical method and discretization scheme as that of Example 1. The solutions are obtained at Reynolds number from 500 to 6000 in increments of 500, which gives a total of 12 snapshots. Then, the POD technique is applied to these 12 snapshots to obtain the eigenvalues and eigenfunctions. In addition, numerical solutions at three off-design parameters corresponding to Re=800, 2700, and 5300 are also obtained.

Table 3 gives the first five largest eigenvalues, together with the participant energy coefficient ξ_n and the cumulative energy coefficient η_n. An overview of Table 3 shows that the same trend exists for the natural convection problem in Example 1. A comparison between Tables 1 and Table 3 shows that there is a big difference between the magnitudes of corresponding eigenvalues, the participant energy coefficient ξ_n and the cumulative energy coefficient η_n.

Figure 8 shows the first six dominant velocity eigenfunctions obtained from the POD technique. It is obvious that the eigenfunctions with large eigenvalues represent large scale flow structures, while the later eigenfunctions contain more and more small vortexes.

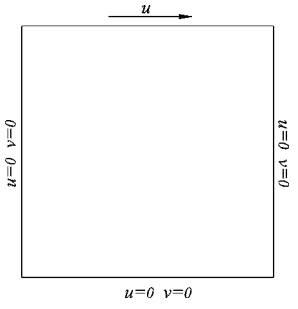

Fig. 7 Schematic view of driven cavity flow

4.2 Reconstruction and Extrapolation. Figure 9 shows the logarithm of relative error E with 10 as the base, between the numerical solutions obtained by FVM and the solutions obtained by the POD technique. Again, the physical fields at the design parameters are reconstructed very well. The relative error decreases drastically as the truncation degree M increases. With the truncation degree $M=4$, the relative error E has reached a value of no more than 1%. When the truncation degree is 12, the relative error E if of the order of 10^{-10}.

The extrapolation performance of the POD is shown in Fig. 10. The empirical coefficients needed in the reconstruction formulations are resolved by the same procedure as that in Example 1. From an overview of Fig. 10, it can be seen that the reconstruction is also good. The relative error E takes the minimum value of no more than 0.3% at the optimal truncation degree of $M=6$. Figure 11 shows the streamline obtained by the FVM and the POD based algorithm at Re=5300. The plots show a remarkably good agreement.

In terms of computational time, it requires almost 37 s to obtain a solution by the FVM method, but only 0.45 s to obtain a solution by the POD based algorithm.

5 Example 3: Heat Conduction Problem With a Time-Dependent Heat Source

In this section, we consider a transient nonlinear heat conduction problem where the heat source is a function of time and the thermal conductivity is a function of temperature, making the problem nonlinear both in space and in time. It will be shown that we can predict the temperature fields accurately at every time instant when the heat source varies arbitrarily by utilizing the POD based algorithm. The nondimensional governing equation and boundary conditions are as follows:

$$\frac{\partial \theta}{\partial t} = \frac{\partial}{\partial x}\left(\kappa(\theta)\frac{\partial \theta}{\partial x}\right) + S(t,x) \tag{35}$$

The term $S(t,x)$ in Eq. (35) represents a time-dependent heat source, which is defined as

$$S(t,x) = f(t)n/2\cosh^2(n(x-x_o)) \tag{36}$$

The term $S(t,x)$ will become a point source located at $x=x_0$ as n reaches infinity. In this work, we take $n=100$ and $x_0=0.25$. The relevant initial and boundary conditions are

$$\theta(x,0) = 0.01 \tag{37}$$

$$\theta(0,t) = 0.0 \tag{38}$$

$$\theta(1,t) = 0.0 \tag{39}$$

The temperature dependent thermal diffusivity is given by

$$\kappa(\theta) = 1 + \sigma\theta \tag{40}$$

where σ is a constant at a value of 0.01. The function $f(t)$ represents the time-dependent part of the heat source term. In this paper, the value of the $f(t)$ varies in the range of 0–20.

5.1 Construction of Snapshots and Galerkin Projection. The governing equation is discretized by the FVM with 100 control volumes, and the unsteady term is discretized by the first-

Table 3 Eigenvalue and the energy distribution of velocity snapshots

n	1	2	3	4	5
ξ_n (%)	97.28	2.41	2.82×10^{-1}	2.74×10^{-2}	2.34×10^{-3}
η_n (%)	97.282010	99.687427	99.969250	99.996646	99.998995
λ_n	461.11	11.40	1.34	1.29×10^{-1}	1.11×10^{-2}

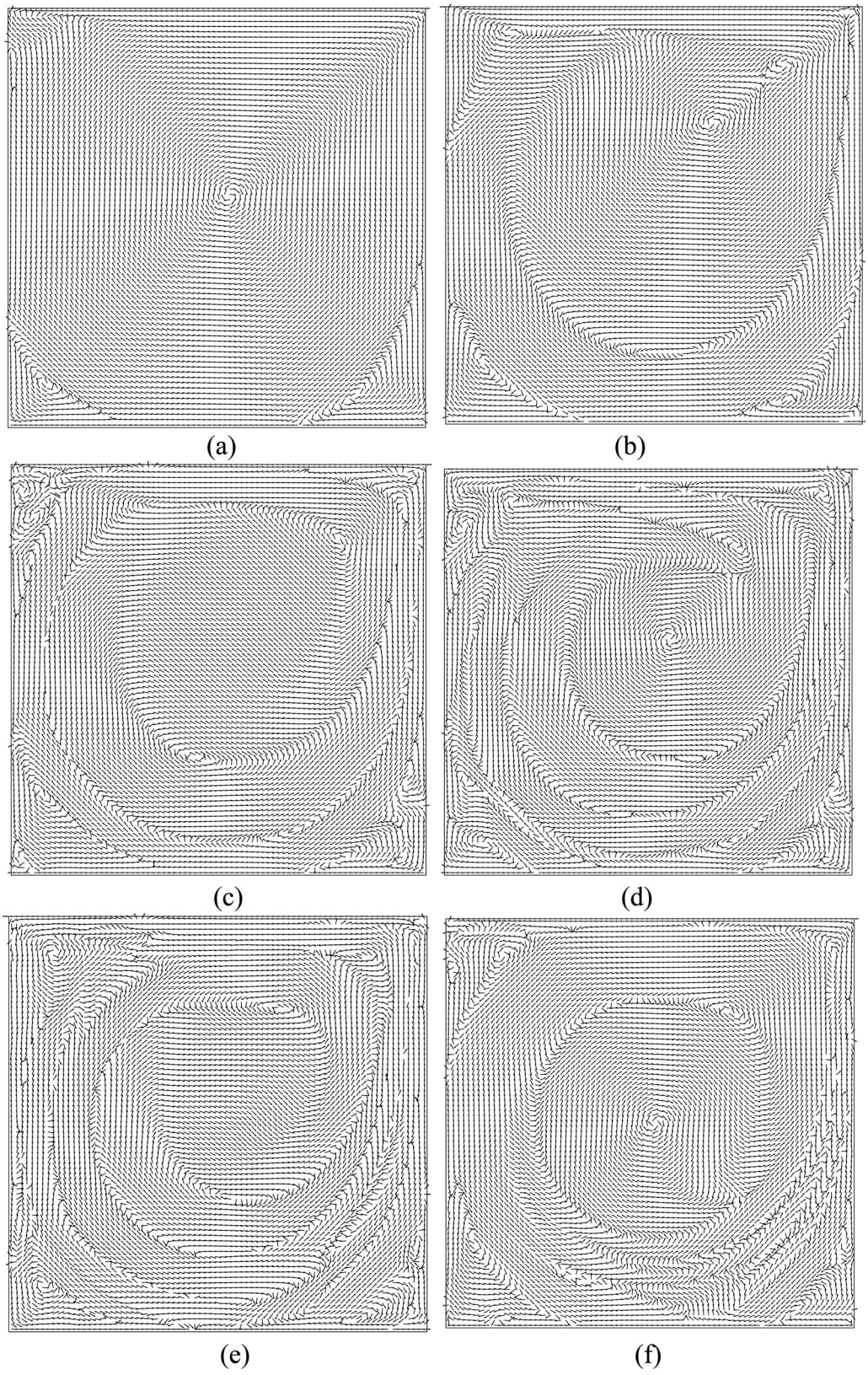

Fig. 8 The first six dominant velocity eigenfunctions obtained from the velocity snapshots by the POD technique

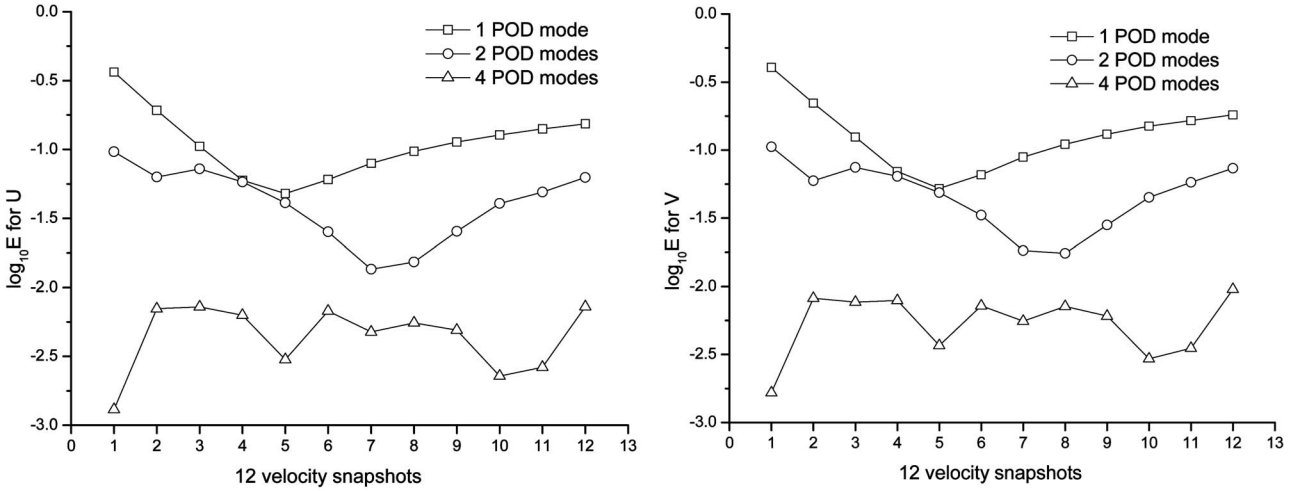

Fig. 9 The relative error between the numerical solution and the POD reconstruction at design parameters

order backward difference scheme. The set of discretized algebraic equations is solved by the Gaussian elimination method. Steady state is reached after 1520 time steps with a time step of $\Delta t = 0.0005$.

The construction of the snapshots is the most important step of the POD procedure for an unsteady problem since the eigenfunctions are obtained from the decomposition of the snapshot matrix. The snapshots must be representative of the dynamic characteristic of the system under consideration. We may take solutions at every time step as a snapshot, but it becomes impossible when we are solving very complex problems, e.g., the DNS of turbulence. In this problem, the temperature field varies greatly at the initial stage, and it varies less as time goes on. Thus, it is necessary to take more snapshots at the initial stage, and the number of the snapshots may be decreased as time elapses.

It will be demonstrated that the POD based algorithm can predict the temperature fields at off-design parameters very well with only 120 snapshots. We use the following method to take snapshots, 50 snapshots are obtained at the time interval of 0.0005 during the time period 0.000–0.025 s, other 50 snapshots are obtained at the time interval of 0.0055 during the time period 0.025–0.3 s, and the other 20 snapshots are obtained in the time period 0.3–0.76 s.

In Examples 1 and 2, we use a cubic spline polynomial to evaluate the empirical coefficients in the reconstruction formula. However, for the transient problem, the interpolation method cannot succeed. In order to get the empirical coefficients at the off-design parameters, a Galerkin procedure employing this empirical eigenfunction basis is applied to the governing equations. The Galerkin projection method can also be applied to the Navier–Stokes equations in Examples 1 and 2, but the method of cubic spline interpolation is very easy to implement and can give very accurate results.

First, we represent the temperature field θ as follows:

$$\theta(x,t) = \sum_{k=1}^{M} \alpha_k(t_n)\phi_\theta^k(x) \quad M \leqslant N \tag{41}$$

After substituting Eq. (41) into Eq. (35), applying the Galerkin procedure, and using the orthogonality property of eigenfunctions, we obtain

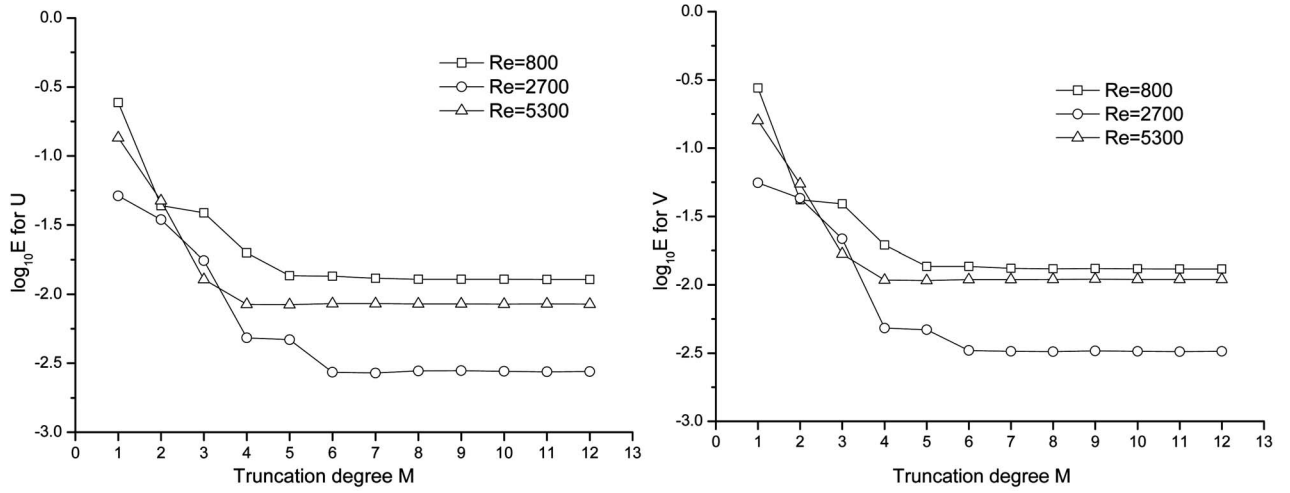

Fig. 10 Relative error versus the truncation degree *M* at off-design parameters

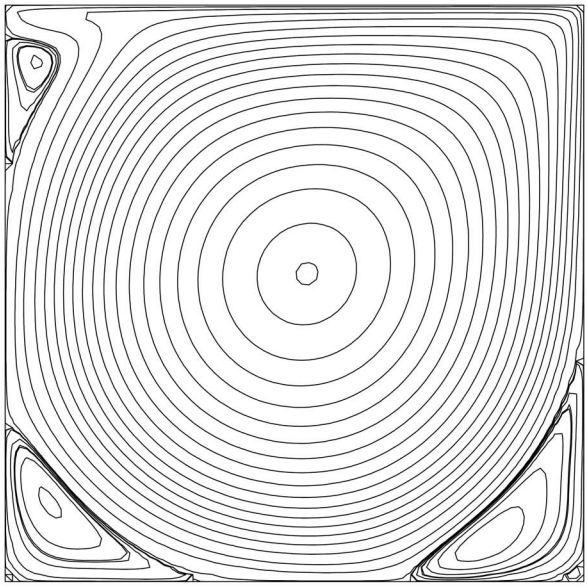

(a) FVM solution

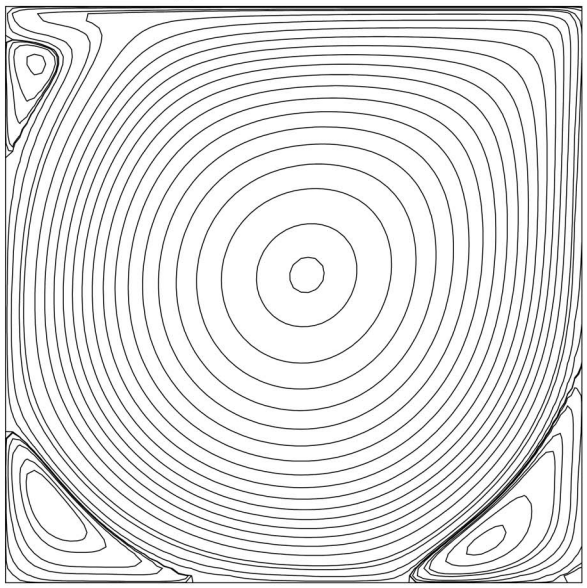

(b) POD solution

Fig. 11 Comparison between the POD and the FVM solutions for Re=5300 with *M*=6

$$\frac{d\alpha_i}{dt} = -\sum_{k=1}^{M} H_{ik}\alpha_k - \lambda\sum_{k=1}^{M}\sum_{l=1}^{M} Q_{ikl}\alpha_k\alpha_l + F_i \quad i = 1,2,\ldots,M \tag{42}$$

where

$$H_{ik} = \left(\frac{\partial\phi_i}{\partial x}, \frac{\partial\phi_k}{\partial x}\right) \tag{43}$$

$$Q_{ikl} = \left(\frac{\partial\phi_i}{\partial x}, \frac{\partial\phi_k}{\partial x}\right)\phi_l \tag{44}$$

$$F_i = (\phi_i, S(t,x)) \tag{45}$$

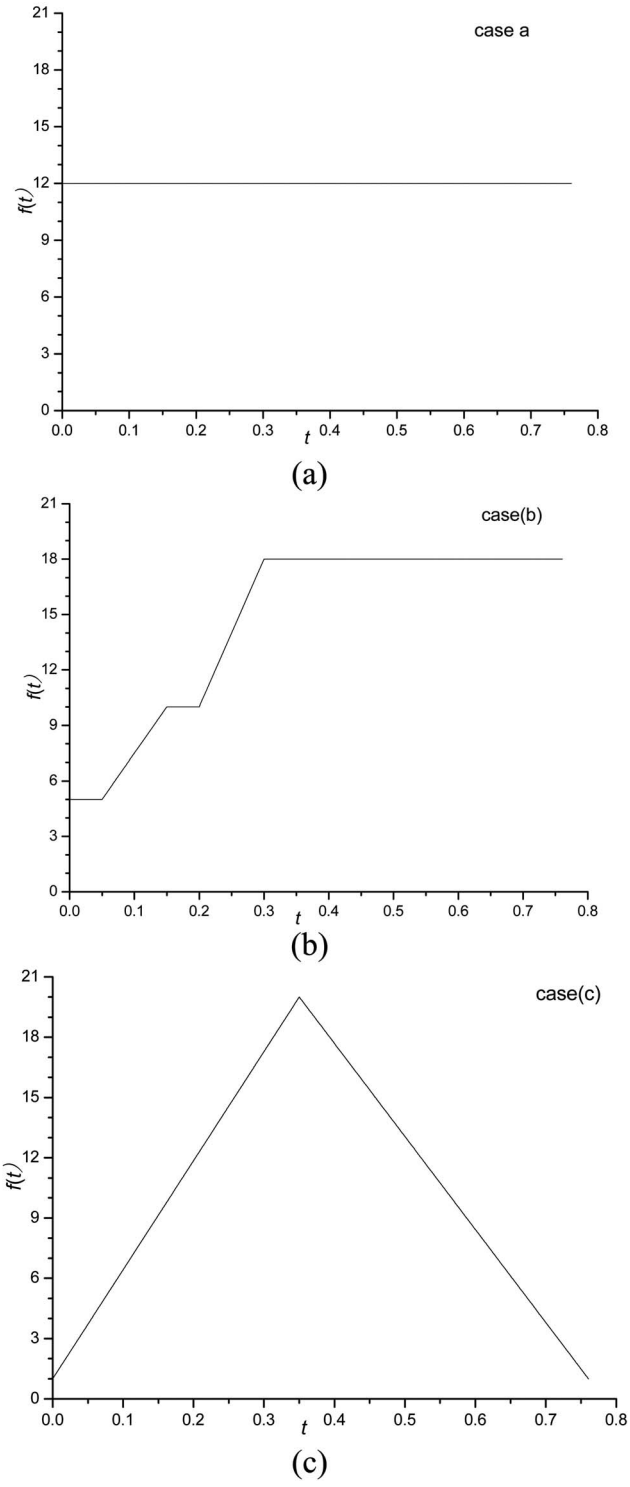

Fig. 12 Various shape of function *f*(*t*) used to examine the performance of the POD based algorithm. (*a*), (*b*), and (*c*) correspond to case (a), case (b), and case (c), respectively.

The ordinary differential (Eq. (42)) is solved by a sixth-order Runge–Kutta method with a time step of $\Delta t = 0.0005$. The initial value for the system is obtained by the projection of the initial value of θ onto the eigenfunctions,

$$\alpha_i(t_0) = (\theta(x,0), \phi_i) \tag{46}$$

Table 4 Eigenvalues and the energy distribution of temperature snapshots

n	1	2	3	4	5
ξ_n (%)	96.65	3.26	8.99×10^{-2}	4.42×10^{-3}	4.78×10^{-4}
η_n (%)	96.64582	99.90516	99.99507	99.99949	99.99997
λ_n	110.36	3.72	0.10	5.05×10^{-3}	5.46×10^{-4}

5.2 Results and Discussion. The POD procedure is applied to these 120 snapshots to yield eigenfunctions. Table 4 shows the first five dominant eigenvalues together with their participant energy coefficient ξ_n and the cumulative energy coefficient η_n at the design parameter $f(t)=20$. A comparison with the results of Examples 1 and 2 shows that the same trend exists for the transient problem; the first eigenvalue takes the largest value, and the corresponding eigenfunction captures the most energy. With the first five eigenfunctions, the cumulative energy coefficient η_n reaches a value of 99.99997%. Figure 13(a) gives the variation of the empirical coefficients $\alpha_i(t)$ with time for the case of $f(t)=20$. The empirical coefficients $\alpha_i(t)$ are obtained analytically by means of projection of the solutions onto the eigenfunctions. It is obvious that the first empirical coefficients $\alpha_1(t)$ vary in the smoothest way and the coefficients with large indices have large fluctuations during the initial stage, while both of them approach a constant value as the system reaches a steady state. The fourth empirical coefficient $\alpha_4(t)$ varies little with time and has a value very close to zero, which means that it contributes little to the reconstruction of the temperature fields. This can also be found in Table 4 since the fourth participant energy coefficient ξ_n has a value of 4.42×10^{-5}.

To examine the performance of the POD based algorithm, we consider three different cases of the time-dependent function $f(t)$, as shown in Fig. 12. In all these three cases, the empirical coefficients $\alpha_i(t)$ are obtained by solving Eq. (42) with an optimal truncation degree $M=6$; further increase in the value of the truncation degree M does not improve the accuracy of the reconstruction.

Figures 13(b)–13(d) give the shape of the empirical coefficients corresponding to case (a), case (b), and case (c), respectively. For case (a) and case (b), the variation of the empirical coefficients $\alpha_i(t)$ has the same pattern with that of the case at the design parameter. For case (d), the shape of the empirical coefficients takes a very different pattern since the time-dependent function $f(t)$ varies during the whole time interval of 0–0.76 s, and the system does not have a steady state.

Figures 14(a)–14(c) show the temporal variation of the relative error E for case (a), case (b), and case (c), respectively. From an overview of Fig. 14, it reveals that the relative error E takes the largest value at the initial stage, and there is also a large decrease of the error at the initial stage. As time elapses, the relative error E reduces to a constant value of no more than 0.8%. The variation of temperature at two points—$x=0.25$, which is close to the location of heat source, and $x=0.90$, which is close to the boundary for case (b) and case (c)—are indicated in Figs. 15(a) and 15(b). The agreement between the FVM solutions of the governing equation and the POD solutions is excellent.

In terms of computational time, about 8.63 s is required to obtain a solution by the FVM method and only 0.32 s is required to obtain a solution by the POD based algorithm. Further time saving can be expected when this method is applied to two-dimensional or three-dimensional nonlinear heat conduction problems.

6 Concluding Remarks

In this paper, an algorithm based on the POD, which can reduce the computation time tremendously for the prediction of the fluid flow and heat transfer problems without deteriorating accuracy, is developed. The performance of the algorithm is illustrated by three examples.

The empirical coefficients needed to reconstruct the physical fields can be obtained by an interpolation method for steady problems or the Galerkin projection method for transient problems.

It is observed that the relative error between the reconstruction physical fields and the exact physical fields can reach an order of 10^{-10} at the design parameters. For the physical fields at off-design parameters, the relative error can reach an order of 10^{-3} at least; for the scalar physical field the relative error may reach an order of 10^{-4}. It is this remarkable feature that makes the POD useful to control procedures where fluid flow and heat transfer dominate.

The optimal truncation degree is around $M=6$ in this investigation; further increase of the truncation degree does not affect the accuracy of the reconstruction.

The use of the POD based algorithm to predict the fluid and temperature fields yields a drastic time reduction compared with the FVM with SIMPLE algorithm. It is almost 100 times faster than the FVM, and it can be expected that the more complicated the process, the greater the saving in computational time.

Acknowledgment

This work was supported by the National Natural Science Foundation of China (Grant Nos. 50476046 and 50636050).

Nomenclature

h = height of the cavity
w = width of the cavity
H = linear operator defined in Eq. (4)
N = number of snapshots
M = truncation degree
Pr = Prandtl number
Ra = Rayleigh number
U = nondimensional velocity component in the x direction
V = nondimensional velocity component in the y direction
t = dependent variables
$\mathbf{n}$ = normal direction
$\mathbf{x}$ = vectors of coordinates
$\langle\cdot,\cdot\rangle$ = ensemble average
$(\cdot,\cdot)$ = inner product of two functions

Greek Symbols

ξ = participant energy coefficient
η = cumulative energy coefficient
λ = eigenvalues
θ = nondimensional temperature
ϕ = eigenfunction

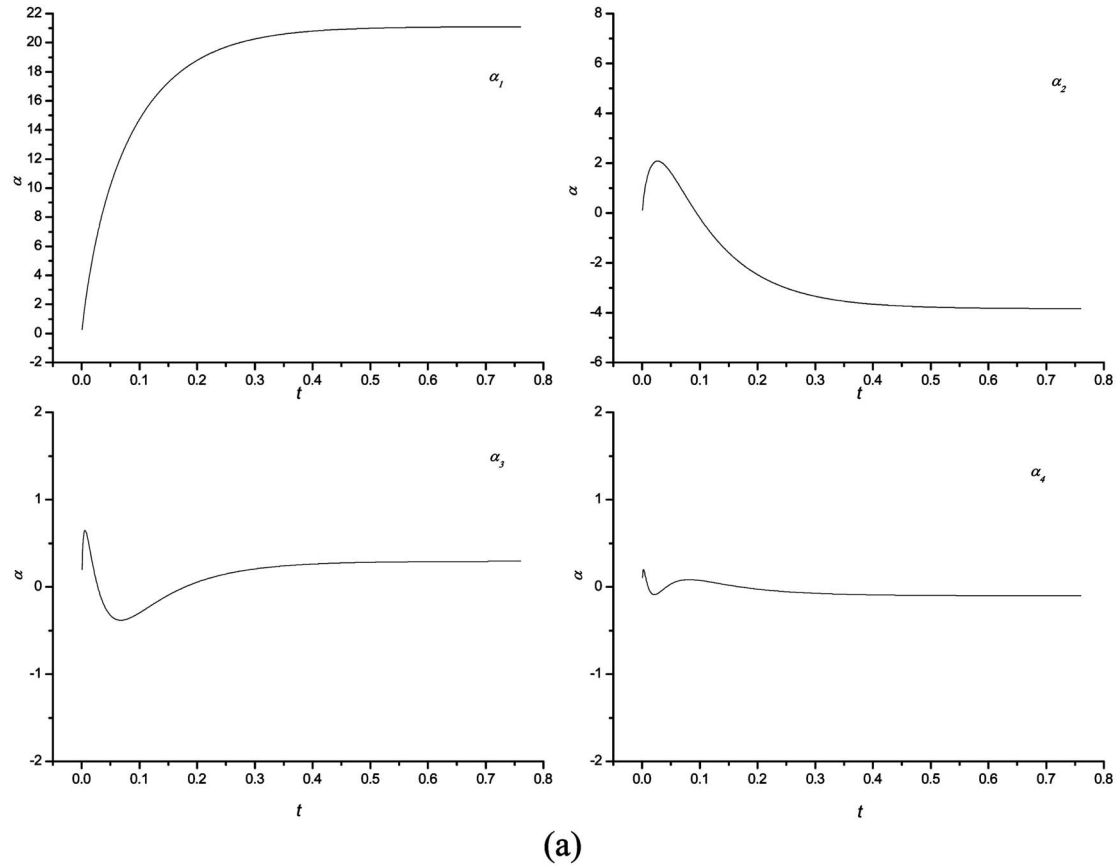

(a)

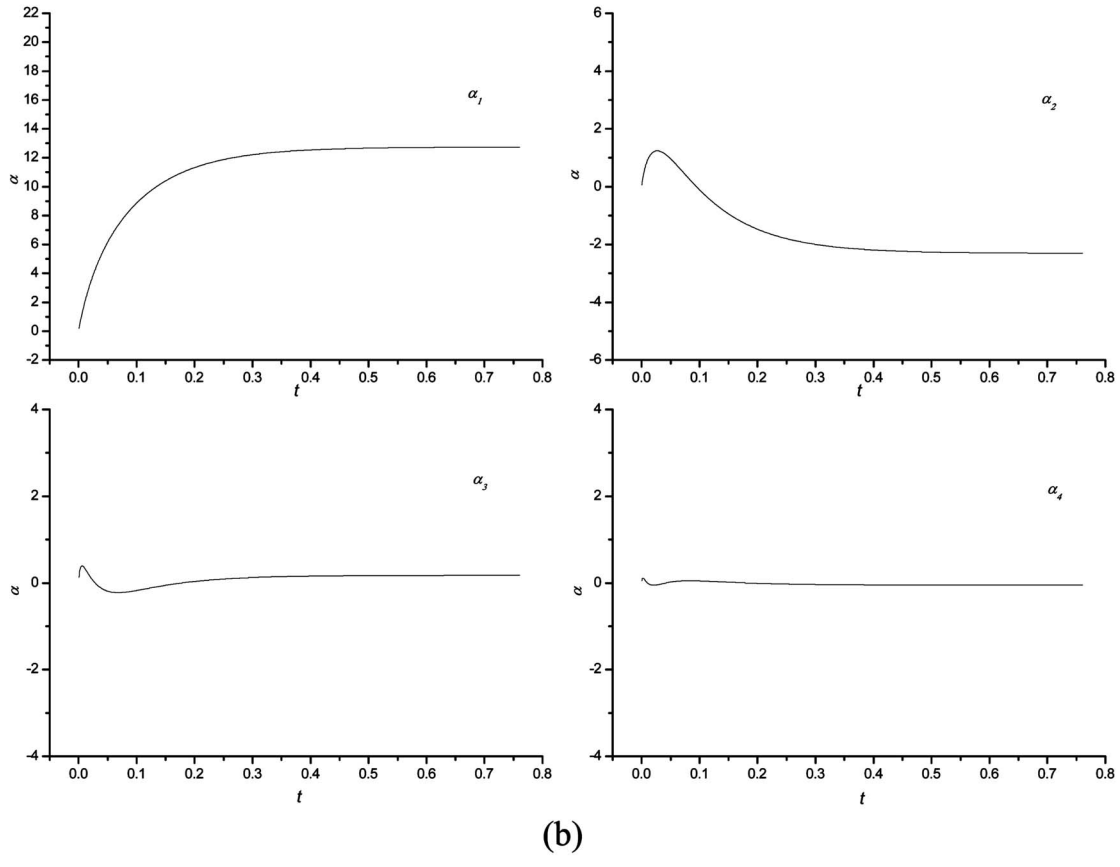

(b)

Fig. 13 The variation of empirical coefficients as a function of time. (*a*) corresponds to the function $f(t)=20$ at design parameters; (*b*), (*c*), and (*d*) correspond to function $f(t)$ at case (a), case (b), and case (c), respectively.

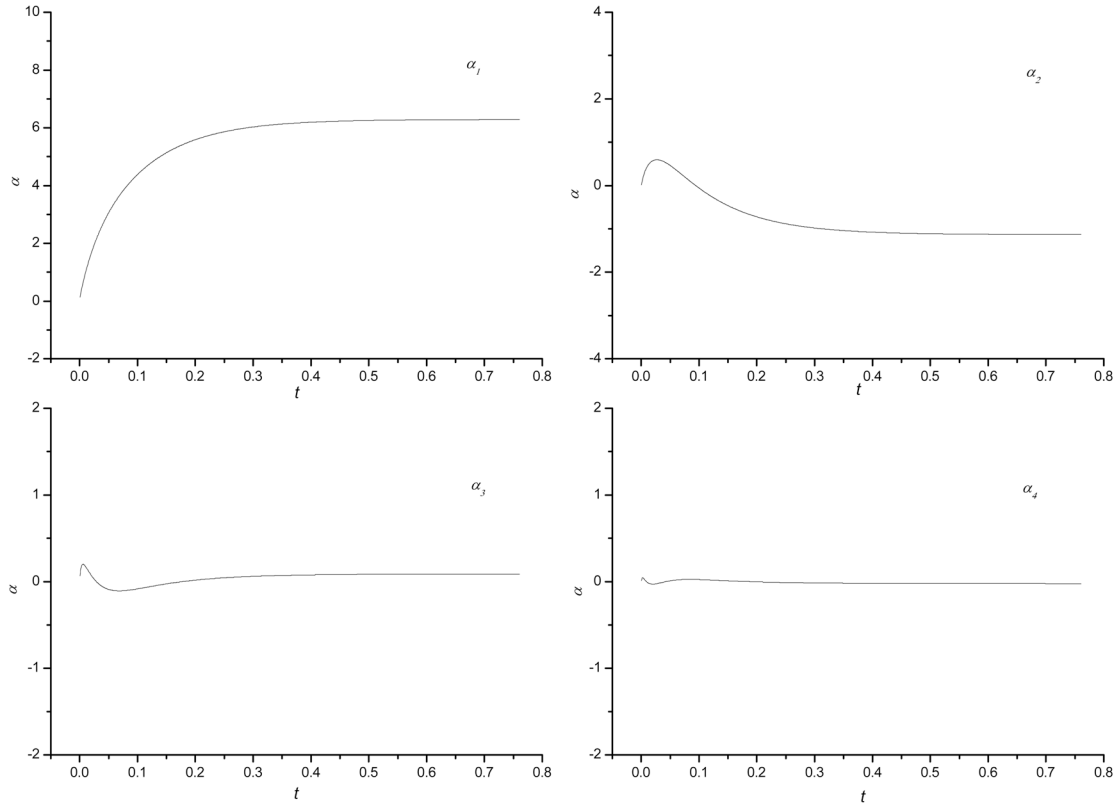

(c)

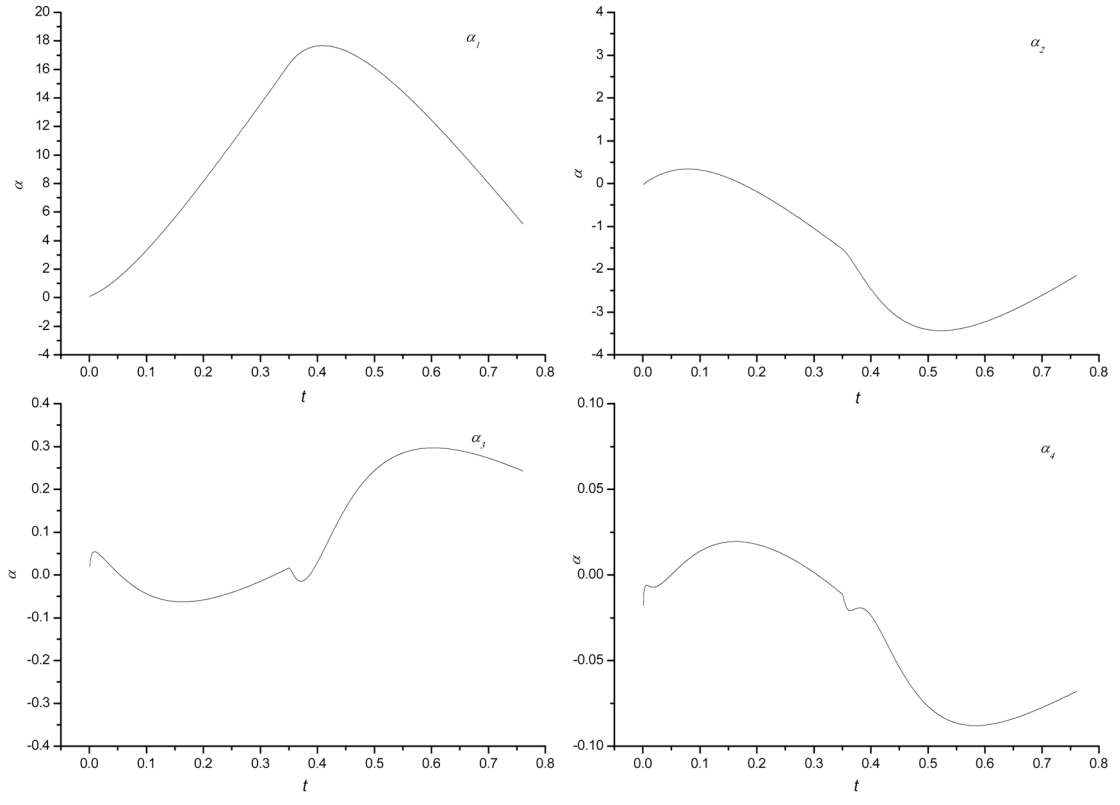

(d)

Fig. 13 (***Continued***).

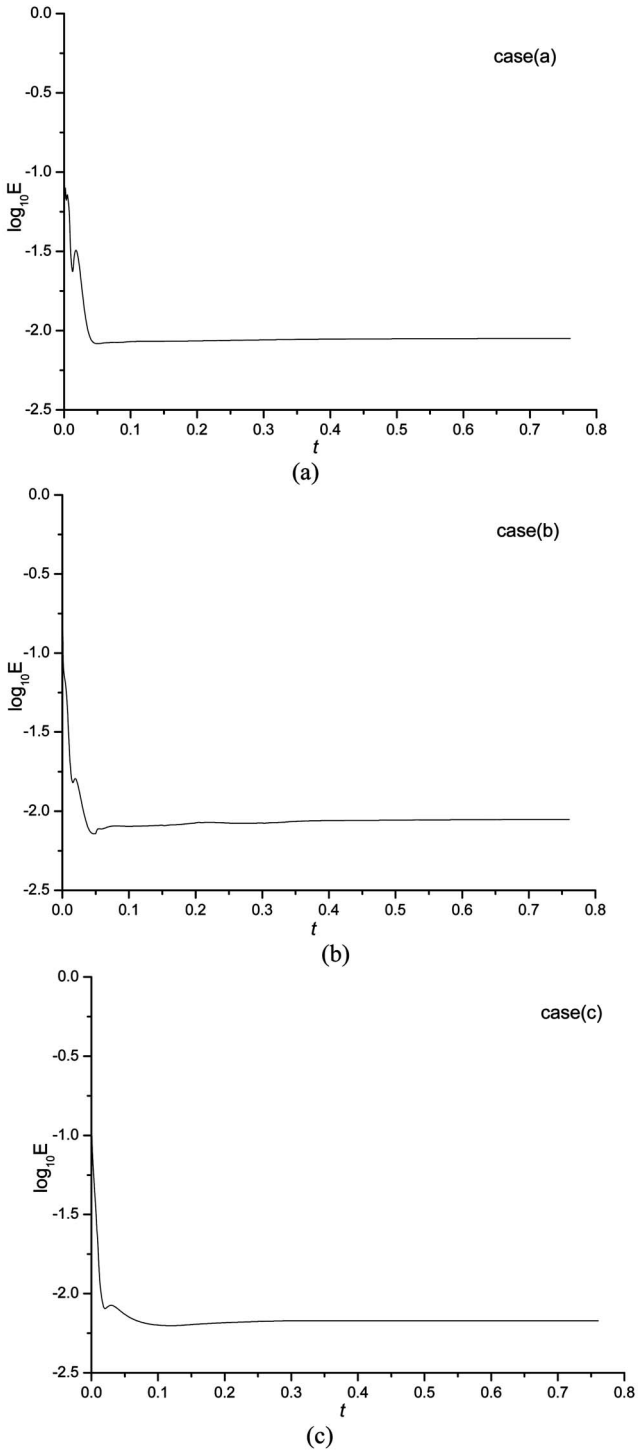

Fig. 14 The temporal variation of relative error between the numerical solutions and the POD solutions for different time-dependent function *f*(*t*). (*a*), (*b*), and (*c*) correspond to case (a), case (b), and case (c), respectively.

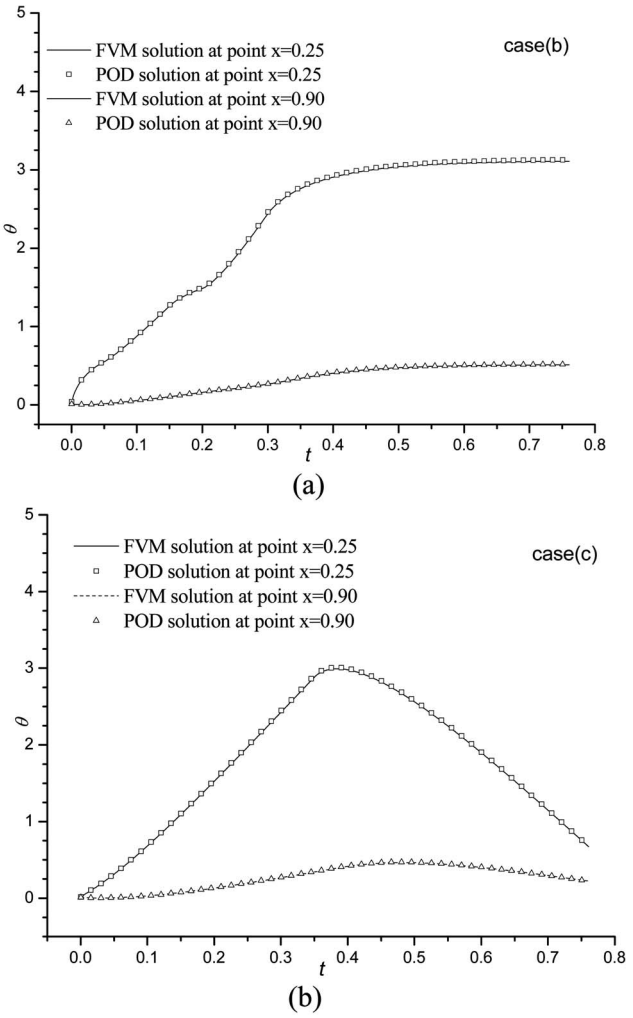

Fig. 15 The temporal variation of temperature at two points for different time-dependent functions *f*(*t*). (*a*) corresponds to the case (b); (*b*) corresponds to case (c).

Subscripts

h = hot side
c = cold side
n = the nth or the nth of a vector
POD = physical fields obtained by POD reconstruction

Superscripts

k = the kth column vector

References

[1] Bleris, L. G., and Kothare, M. V., 2005, "Reduced Order Distributed Boundary Control of Thermal Transients in Microsystems," IEEE Trans. Control Syst. Technol., **13**, pp. 853–867.

[2] Azeez, M. F. A., and Vakakis, A. F., 2001, "Proper Orthogonal Decomposition of a Class of Vibroimpact Oscillations," J. Sound Vib., **240**, pp. 859–889.

[3] Kirby, M., and Sirovich, L., 1990, "Application of the Karhunen-Loeve Procedure for the Characterization of Human Faces," IEEE Trans. Pattern Anal. Mach. Intell., **12**, pp. 103–108.

[4] Allery, C., Beghein, C., and Hamdouni, A., 2005, "Applying Proper Orthogonal Decomposition to the Computation of Particle Dispersion in a Two-Dimensional Ventilated Cavity," Commun. Nonlinear Sci. Numer. Simul., **10**, pp. 907–920.

[5] Arjocu, S. C., and Liburdy, J. A., 2000, "Identification of Dominant Heat Transfer Modes Associated With the Impingement of an Elliptical Jet Array," ASME J. Heat Transfer, **122**, pp. 240–247.

[6] Tyagi, M., and Acharya, S., 2005, "Large Eddy Simulations of Flow and Heat Transfer in Rotating Ribbed Duct Flows," ASME J. Heat Transfer, **127**, pp. 486–498.

[7] Berkooz, G., Holmes, P., and Lumley, J. L., 1993, "The Proper Orthogonal Decomposition in the Analysis of Turbulent Flows," Annu. Rev. Fluid Mech., **25**, pp. 539–575.

[8] Holmes, P., Lumley, J. L., and Berkooz, G., 1996, *Turbulence, Coherent Structures, Dynamical Systems and Symmetry*, Cambridge University Press, UK.

[9] Sirovich, L., 1987, "Turbulence and the Dynamics of Coherent Structure. Part I,II,III," Q. Appl. Math., **45**, pp. 561–571.

[10] Patankar, S. V., 1980, *Numerical Heat Transfer and Fluid Flow*, McGraw-Hill, New York.

[11] Tao, W. Q., 2001, *Numerical Heat Transfer*, 2nd ed., Xi'an Jiaotong University Press, Xi'an.
[12] Patankar, S. V., and Spalding, D. B., 1972, "A Calculation Procedure for Heat, Mass and Momentum Transfer in Three-Dimensional Parabolic Flow," Int. J. Heat Mass Transfer, **15**, pp. 1787–1806.
[13] Leonard, B. P., 1979, "A Stable and Accurate Convective Modeling Procedure Based on Quadratic Upstream Interpolation," Comput. Methods Appl. Mech. Eng., **19**, pp. 59–98.
[14] Hortmann, M., Peric, M., and Scheuerer, G., 1990, "Finite Volume Multigrid Prediction of Laminar Natural Convection: Bench-Mark Solutions," Int. J. Numer. Methods Fluids, **11**, pp. 189–207.
[15] Ghia, U., Ghia, K. N., and Shin, C. T., 1982, "High-Re Solutions for Incompressible Flow Using the Navier-Stokes Equations and a Multigrid Method," J. Comput. Phys., **48**, pp. 387–411.

Experimental Validation of Analytical Solutions for Vertical Flat Plate of Finite Thickness Under Natural-Convection Cooling

Vipin Yadav
Department of Mechanical Engineering,
The University of Auckland,
Auckland, New Zealand 1142
e-mail: v.yadav@auckland.ac.nz

Keshav Kant[1]
Department of Mechanical Engineering,
Indian Institute of Technology,
Kanpur 208 016, India
e-mail: keshav@iitk.ac.in

The analytical solution for a vertical heated plate subjected to conjugate heat transfer due to natural convection at the surface and conduction below is presented. The heated surface is split into two regions; the uniform heat flux region toward upstream and remaining fraction as the uniform wall temperature region. The fractional areas under the two regions are considered variable. Adopting thermally thin wall regime approximation, the possible solutions were investigated and found to satisfactorily deal with longitudinal conduction and temperature variation in the transverse direction. A test setup was developed and the experiments were conducted to obtain relevant data for comparison with the analytical solutions. The ranges for Rayleigh number and heat conduction parameter (α) *during various test conditions were* $2\times10^8-6\times10^8$*, and 0.001–1, respectively. The limiting solutions for stipulated conditions are analyzed and compared with experimental data. Reasonable agreement is observed between the experimental and analytical results.* [DOI: 10.1115/1.2804938]

Keywords: uniform wall temperature, uniform heat flux, natural convection, longitudinal conduction

1 Introduction

The conjugate heat transfer due to natural convection at the surface and conduction beneath is crucial for many heat transfer processes such as multilayered air cooled heat exchangers, plate heaters, hot film sensors, and printed circuit boards. The importance of the conjugate heat transfer problems is widely recognized in the literature and many analytical and numerical methods have been developed for convective flow conditions. The analysis is highly relevant for estimating the intensity of thermally induced mechanical stresses in the bodies subjected to conduction and convection simultaneously.

Trevino and Linan [1] studied the steady-state and transient processes of the external heating of a plate under a convective flow with the inclusion of the axial heat conduction through the plate using perturbation methods. Chen et al. [2] analyzed laminar free convection along horizontal, inclined, and vertical flat plates with, power-law variation of the wall temperature or of the surface heat flux. Sparrow et al. [3] described a combined experimental and analytical/numerical study of turbulent mass (or heat) transfer in a flat, rectangular duct with streamwise periodic, nonuniform mass (heat) transfer at one of the principal walls. Pozzi and Lupo [4] studied the integral thermo-fluid-dynamic field resulting from the coupling of natural convection along and conduction inside a heated flat plate by means of expansions based on Padé approximant technique and asymptotic solutions. Vallejo and Trevino [5] presented an analytical study for the cooling of a flat plate in a convective flow accounting the longitudinal heat conduction. It was found that for large but finite thermal conductivity of the plate, the temperature adjusts itself to pseudoequilibrium condition and further evolution of the plate temperature slows down. Naylor et al. [6] studied two-dimensional laminar free convection between isothermal vertical plates. It was shown that the full elliptic solution gave more accurate values of local heat transfer quantities when compared with boundary layer equations especially in the entrance region. Merkin and Pop [7] developed the technique for nondimensionalization of governing equations for conjugate free convection boundary layer flows over a vertical plate. An efficient finite difference scheme was used to solve the flow equations and it was shown that the asymptotic expansion gives reliable results even at moderate values of dimensionless distance along the plate. Shu and Pop [8] investigated the solution behavior for the forced convection thermal boundary layer on a flat plate with prescribed heating conditions. Keller box scheme in combination with the continuous transformation method was used for solving the governing equations. The agreement between numerical and asymptotic solutions was observed and later approach was found capable of capturing the essential features of the heat transfer characteristics. Mendez and Trevino [9] performed a theoretical investigation to study heat transfer characteristics of a thin vertical strip with internal heat generation. It was concluded that to avoid excessive thermal stresses inside the material, natural-convection process must be used with caution. Kazansky et al. [10] studied natural-convection heat transfer from a vertical electrically heated plate, which is symmetrically placed in a chimney of variable height. They analyzed the dependence of the temperature distribution on the flow field. Chen et al. [11] investigated the natural-convection heat transfer coupled with the effect of thermal conduction from a steel plate with discrete sources. The average heat transfer was correlated from the experimental data as the function of the relative heating space and Rayleigh number. Yadav and Kant [12,13] presented an experimental and numerical study for several different combinations of uniform heat flux and uniform wall temperature heating conditions on a single surface un-

[1]Corresponding author.

Contributed by the Heat Transfer Division of ASME for publication in the JOURNAL OF HEAT TRANSFER. Manuscript received September 8, 2006; final manuscript received August 19, 2007; published online March 6, 2008. Review conducted by Yogendra Joshi.

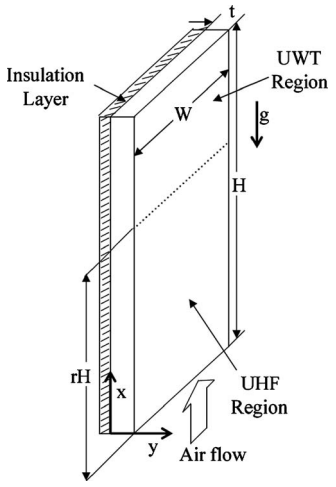

Fig. 1 Schematics of heated plate in vertical channel

der buoyancy assisted convection cooling. Empirical expressions for averaged Nusselt number for the considered values of thermal and flow parameters were developed. Often the information regarding the exact thermal conditions at the surfaces of the electronic packages for a given heat generation rate is obscure. However, the temperature profile information, including the maximum value and its location, is highly significant for estimating the performance reliability for various electronic components. Several investigators and authors have pointed out and discussed such issues in their work and important contributions are due to Anderson [14], Luikov [15], Ortega et al. [16], Incropera [17], Jaluria [18], Cole [19], and Sathe and Joshi [20].

The current work investigates conjugate heat transfer problem for a vertical heated plate subjected to natural convection at the surface and conduction below. A part of the total heated surface is kept at uniform heat flux (UHF) and remaining at uniform wall temperature (UWT) condition; areas under those two conditions are varied with matching temperature and heat flux values at the interface. The perspective of the solution approach is to take advantage of scaling laws and dimensionless parameters harmonious to simple geometry and steady flow conditions. Analytical solutions for dimensionless temperature and heat flux profiles are obtained based on thermally thin wall regime approximation. Subsequently, experiments are conducted to obtain relevant data for comparison purposes. Approximate ranges for Rayleigh number and heat conduction parameter are 2×10^8–6×10^8 and 0.001–1, respectively. Analytical results and experimental data are thoroughly analyzed and representative trends are presented.

2 Analytical Solution

Consider a flat plate, orientated vertically, with front surface subjected to natural-convection cooling and thermally insulated at the back. Lower right corner of the plate is at the origin of Cartesian coordinate system with the x axis pointing upward in the longitudinal direction and y axis is normal to the surface (see Fig. 1); height and thickness of the plate are H and t, respectively. Further to exclude edge effects, width W can be assumed to be sufficiently large compared to H.

Let us assume that plate is longitudinally divided into N number of strips or regions so that the length of each region is H/N. Let initial N_{UHF} numbers of regions are under UHF condition and remaining $(N-N_{\mathrm{UHF}})=N_{\mathrm{UWT}}$ (say) regions are with UWT condition. Thus, thermal condition at the plate surface is a combination of UHF and UWT conditions corresponding to the vertical lengths rH and $(1-r)H$, respectively, such that $r=N_{\mathrm{UHF}}/N$. Note that for the condition $N\to\infty$, r can be treated as a continuous variable. Such thermal condition is expected to result in the development of viscous nonisothermal boundary layer [19] at the vertical surface. To determine representative boundary layer thickness, assume a characteristic temperature T_c at the plate surface and the associated characteristic temperature difference $\Delta T_c=(T_c-T_\infty)$. The Rayleigh number and the orders of magnitude of boundary layer thickness, induced velocity, and heat flux across the fluid are given as [9]

$$\mathrm{Ra}_c=\frac{g\beta\Delta T_c H^3}{\nu^2}\,\mathrm{Pr}\quad \delta\sim\frac{H}{\mathrm{Ra}_c^{0.25}}\left(\frac{\Delta T_c}{\Delta T}\right)^{0.25}$$
$$u_c\sim\frac{\mathrm{Ra}_c^{0.5}\,\nu}{\mathrm{Pr}\,H}\left(\frac{\Delta T}{\Delta T_c}\right)^{0.5}\quad q=\frac{k(\Delta T)^{1.25}\,\mathrm{Ra}_c^{0.25}}{H(\Delta T_c)^{0.25}} \tag{1}$$

where q is the local surface heat generation. Let q_v be the average volumetric heat generation corresponding to q. Based on characteristic normal temperature drop, ΔT_a, thermal energy generated inside the plate is given as

$$e=\frac{k_a\Delta T_a}{t}\sim q_v t \tag{2}$$

Since conduction and convection are the only means of energy transfer, Eqs. (1) and (2) give

$$\frac{(\Delta T)^{1.25}}{(\Delta T_c)^{0.25}}\mathrm{Ra}_c^{0.25}\sim\frac{tH}{k}q_v \tag{3}$$

As only the order of magnitude is considered, the analysis will be unaffected if the order of magnitudes of ΔT_c and ΔT are taken the same. Thus,

$$\Delta T_c\,\mathrm{Ra}_c^{0.25}\sim\frac{tH}{k}q_v \tag{4}$$

The nondimensional longitudinal heat conductance of the strip is defined by $\alpha=k_a t/kH\mathrm{Ra}_c^{0.25}$, and aspect ratio by $\varepsilon=t/H$. The necessary condition for the thermally thin wall regime is $\alpha/\varepsilon^2\gg1$. Therefore, $\Delta T_c/\Delta T_a\sim\alpha/\varepsilon^2\Rightarrow\Delta T_c\gg\Delta T_a$. Consider steady-state laminar natural-convection flow with constant thermophysical properties. Introducing the Boussinesq approximation, the governing equations for the problem can be written as [7]

$$\frac{\partial u}{\partial x}+\frac{\partial v}{\partial y}=0$$
$$u\frac{\partial u}{\partial x}+v\frac{\partial v}{\partial y}=g\beta(T-T_\infty)+\nu\frac{\partial^2 u}{\partial y^2} \tag{5}$$
$$u\frac{\partial T}{\partial x}+v\frac{\partial T}{\partial y}=\frac{\nu}{\mathrm{Pr}}\frac{\partial^2 T}{\partial y^2}$$

where u and v are the velocity components in x and y directions, T is the temperature of fluid, and ν and Pr are the kinematic viscosity and the Prandtl number, respectively. Assuming dimensional and nondimensional stream functions as Ψ and f, respectively, we now introduce the following nondimensional independent variables:

$$\chi=\frac{x}{H}\quad \eta=\mathrm{Ra}_c^{0.25}\frac{y}{H\chi^{0.25}}\quad z=\frac{y}{t}$$
$$f=\frac{\mathrm{Pr}\,\Psi}{\nu\,\mathrm{Ra}_c^{0.25}\,\chi^{0.75}}\quad \theta=\frac{T-T_\infty}{\Delta T_c}\quad \theta_a=\frac{T_a-T_\infty}{\Delta T_c} \tag{6}$$

The nondimensional boundary layer flow equations for large values of Rayleigh number ($\sim10^{10}$) can be written as [7]

$$\frac{\partial^2\theta}{\partial\eta^2}+\frac{3}{4}f\frac{\partial\theta}{\partial\eta}=\chi\left(\frac{\partial f}{\partial\eta}\frac{\partial\theta}{\partial\chi}+\frac{\partial f}{\partial\chi}\frac{\partial\theta}{\partial\eta}\right) \tag{7}$$

$$\frac{\partial^3 f}{\partial \eta^3} + \theta = \frac{1}{\mathrm{Pr}}\left[\frac{1}{2}\left(\frac{\partial f}{\partial \eta}\right)^2 - \frac{3}{4} f \frac{\partial^2 \theta}{\partial \eta^2} + \chi\left(\frac{\partial f}{\partial \eta}\frac{\partial^2 f}{\partial \chi \partial \eta} - \frac{\partial f}{\partial \chi}\frac{\partial^2 f}{\partial \eta^2}\right)\right] \tag{8}$$

$$\alpha \frac{\partial^2 \theta_a}{\partial \chi^2} + \frac{\alpha}{\varepsilon^2}\frac{\partial^2 \theta_a}{\partial z^2} + \frac{q}{q_v} = 0 \tag{9}$$

For each region under the UHF condition, heat generation below the surface must be identical.

Let $q=q_i$ for ith strip ($i=1,\ldots,N_{\mathrm{UHF}}$). Then, q_v can be estimated as

$$q_v = \frac{1}{rH}\int_0^{rH} q\,dx = \left.\frac{1}{N_{\mathrm{UHF}}}\sum_{i=1}^{N_{\mathrm{UHF}}} q_i\right|_{N_{\mathrm{UNF}}\to\infty} \tag{10}$$

Therefore, Eq. (9) takes the form

$$\alpha \frac{\partial^2 \theta_a}{\partial \chi^2} + \frac{\alpha}{\varepsilon^2}\frac{\partial^2 \theta_a}{\partial z^2} + 1 = 0 \tag{11}$$

For UWT surface, let for jth $T_a=T_j$, we can estimate surface temperature γ as

$$\gamma = \frac{1}{(1-r)H\Delta T_c}\int_0^{(1-r)H} (T_j - T_\infty)\,dx = \left.\frac{1}{N_{\mathrm{UWT}}\Delta T_c}\sum_{j=1}^{N_{\mathrm{UWT}}} (T_j - T_\infty)\right|_{N_{\mathrm{UWT}}\to\infty} \tag{12}$$

Note that Eqs. (10) and (12) are to be used for experimental verification of results as it is inconceivable to practically maintain exactly the same heat flux value for all N_{UHF} strips corresponding to the UHF region over a portion of heated plate and precisely the same temperature for all N_{UWT} strips under the UWT region over the remaining portion.

As γ is independent of χ, therefore Eq. (11) takes the form

$$\frac{\alpha}{\varepsilon^2}\frac{\partial^2 \theta_a}{\partial z^2} + \frac{q}{q_v} = 0 \tag{13}$$

We need to solve Eqs. (7), (8), and (11) for the range $0<\chi\leqslant r$ subjected to the following boundary conditions. At $\eta=0$,

$$z=0 \quad f = \frac{\partial f}{\partial \eta} = 0 \quad \theta = \theta_a \quad \frac{\partial \theta}{\partial \eta} = \frac{\alpha \chi^{0.25}}{\varepsilon^2}\frac{\partial \theta_a}{\partial z} \tag{14}$$

For $z=-1$,

$$\frac{\partial \theta_a}{\partial z} = 0 \tag{15}$$

For $\eta\to\infty$,

$$\frac{\partial f}{\partial \eta} = \theta_a = 0 \tag{16}$$

For $\chi=0$,

$$\frac{\partial \theta_a}{\partial \chi} = 0 \tag{17}$$

For the range $r<\chi<1$, we need to solve Eqs. (7), (8), and (13) subjected to the boundary conditions (14)–(17) and

$$\theta_a = \gamma \quad \frac{\partial \theta_a}{\partial \chi} = 0 \quad \text{for } \chi = r \tag{18}$$

In order to determine the solution for the case $\alpha\to\infty$, consider a general function Θ corresponding to properties of fluid like f and θ, and assume the following two series:

$$\theta_a = \sum_{j=0}^{\infty}\frac{1}{\alpha^j}\theta_{a,j}(\chi) \quad \text{and} \quad \Theta = \sum_{j=0}^{\infty}\frac{1}{\alpha^j}\Theta_{a,j}(\chi) \tag{19}$$

For the range $0<\chi\leqslant r$, integrating Eq. (11) along the normal coordinate, we get

$$\alpha \frac{\partial^2 \theta_a}{\partial \chi^2} z + \frac{\alpha}{\varepsilon^2}\frac{\partial \theta_a}{\partial z} + z = F_1(\chi,\theta) \tag{20}$$

F_1 is a function governed by boundary conditions.

Substituting Eqs. (15), (16), and (18) as boundary conditions in Eq. (20), we get

$$\alpha \frac{\partial^2 \theta_a}{\partial \chi^2} = -\left(\chi^{-0.25}\left.\frac{\partial \theta}{\partial \eta}\right|_0 + 1\right) \tag{21}$$

Substituting Eq. (19) into Eq. (21), we get

$$\frac{\partial^2 \theta_{a0}}{\partial \chi^2} = 0$$

$$\frac{\partial^2 \theta_{a1}}{\partial \chi^2} = -\left(\chi^{-0.25}\left.\frac{\partial \theta_0}{\partial \eta}\right|_0 + 1\right) \tag{22}$$

$$\frac{\partial^2 \theta_{aj}}{\partial \chi^2} = -\chi^{-0.25}\left.\frac{\partial \theta_{j-1}}{\partial \eta}\right|_0$$

This set of equations is to be solved using adiabatic boundary condition

$$\frac{\partial \theta_{aj}}{\partial \chi} = 0 \quad \text{at } \chi = 0 \quad \text{for the entire range of } j \tag{23}$$

For the range $r<\chi\leqslant 1$, Eq. (20) is to be replaced by

$$\frac{\alpha}{\varepsilon^2}\frac{\partial \theta_a}{\partial z} + \frac{q}{q_v} z = F_2(\chi,\theta) \tag{24}$$

F_2 is a function governed by boundary conditions. Using Eq. (15) in Eq. (24), we get

$$\frac{\alpha}{\varepsilon^2}\frac{\partial \theta_a}{\partial z} + \frac{q}{q_v}(z+1) = 0 \tag{25}$$

Now, using Eq. (13) in Eq. (24), we get

$$\frac{q}{q_v} = -\chi^{-0.25}\left.\frac{\partial \theta}{\partial \eta}\right|_0 \tag{26}$$

Here, the leading variable θ_{a0} is a constant [21].

$$\left.\frac{\partial \theta}{\partial \eta}\right|_0 = -\Gamma_0 \theta_{a0}^{1.25} = -0.75 \tag{27}$$

where Γ_0 is a function of fluid Prandtl number [9] and given as

$$\Gamma_0(\mathrm{Pr}) \approx 0.75\left(\frac{0.4\,\mathrm{Pr}}{1+2\,\mathrm{Pr}^{0.5}(1+\mathrm{Pr}^{0.5})}\right)^{0.25} \tag{28}$$

$$\Rightarrow \theta_{a0} = \left(\frac{3}{4\Gamma_0(\mathrm{Pr})}\right)^{0.8} \tag{29}$$

For the UWT surface, using Eq. (27) in Eq. (26), we get

$$\frac{q}{q_v} = \chi^{-0.25}\Gamma_0\theta_{a0}^{1.25} = 0.3852\,\gamma^{1.25}\chi^{-0.25} \tag{30}$$

$$q_v = 2.596\,\gamma^{-1.25}\chi^{0.25} q \tag{31}$$

Thus, if we can know local heat generation at some point on the plate surface in the region $r<\chi\leqslant 1$, it is possible to estimate mean heat generation for the entire region.

By the definition of q_v, we have

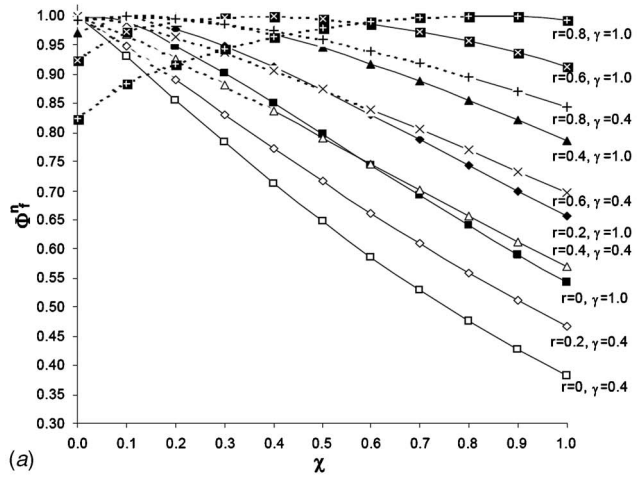

(a)

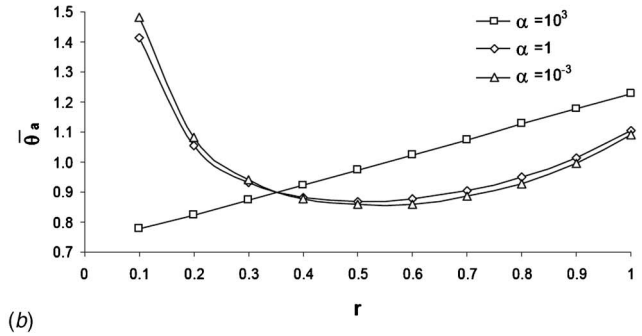

(b)

Fig. 2 (*a*) Comparison of Φ_f^n along the plate height for different values of UWT/UHF fraction r and dimensionless mean temperature γ. (*b*) Comparison of leading order solution for average nondimensional temperature at the plate surface as a function of r and α with $\gamma=1.0$.

$$q_v d\chi + (1-r)dq_v = q d\chi \tag{32}$$

Using Eq. (31), we have

$$\frac{dq}{q} = [0.385\gamma^{1.25}\chi^{-0.25} - (1-r) - 0.25\chi]d\chi$$

The integral solution for the above is

$$q = q_0 \exp(0.513\gamma^{1.25}\chi^{0.75} - (1-r)\chi - 0.125\chi^2) \tag{33}$$

q_0 is an integration constant and can be calculated by assuming

$$q = 1 \quad \text{for } \chi = r \text{ and } \gamma = 0 \tag{34}$$

Applying the above condition on Eq. (33), we get

$$q_0 = \exp\{r(1-0.875r)\} \tag{35}$$

From Eq. (33), we can write the heat flux ratio Φ_f as

$$\Phi_f = \exp\{0.513\gamma^{1.25}\chi^{0.75} - (1-r)\chi - 0.125\chi^2\}$$

Let $q_{\max}$ be the maximum value for q for some χ value. Using $q_{\max}$ as normalization parameter, we write the normalized heat flux ratio as $\Phi_f^n = q/q_{\max}$.

Figure 2(*a*) compares normalized heat flux for different values of UWT/UHF fraction, r and γ. The values of Φ_f^n corresponding to χ beyond the range $r<\chi\leq 1$ also appear. The trends in the variation pattern shown by various curves can be put into three categories as mentioned below.

(a) Those originating at unity, the value of Φ_f^n reduces monotonically as χ increases, e.g., those corresponding to $r=0$, $\gamma=0.4$ and $r=0.2$, $\gamma=0.4$.

(b) Those beginning with intermediate values of Φ_f^n, however, attain unity for some $r<\chi<1$ before ending up again at some intermediate ordinate value, e.g., those corresponding to $r=0.4$, $\gamma=1$ and $r=0.6$, $\gamma=0.4$.

(c) Those monotonically terminating at unity, e.g., those corresponding to $r=0.8$, $\gamma=1$ and $r=1$, $\gamma=1$.

For the UHF surface, using Eq. (29) in Eq. (22), we get

$$\frac{\partial^2 \theta_{a1}}{\partial \chi^2} = \chi^{-0.25}\Gamma_0 \theta_{a0}^{1.25} - 1 \tag{36}$$

Equation (36) when subjected to boundary conditions in Eq. (23) yields the following first order solution:

$$\theta_{a1} = \zeta_0 + \zeta_1\chi + \zeta_2\chi^2 + \zeta_3\chi^{7/4} \tag{37}$$

Here, $\zeta_1=0$ is due to Eq. (23); $\zeta_2=-0.5$ and $\zeta_3=(16/21)\Gamma_0\theta_{a0}^{1.25}=0.57$. ζ_0 can be chosen based on flux distribution over the plate in the region $0<\chi\leq r$. Now, Eqs. (18) and (37) give

$$\theta_{a1} = \gamma r^{-2}(0.57r^{-0.25} - 0.50)^{-1} - 0.50\chi^2 + 0.57\chi^{7/4} \tag{38}$$

The average nondimensional temperature over the entire plate surface (up to the term of order $1/\alpha$) can be given by

$$\begin{aligned}\bar{\theta}_a &= \int_0^r \theta_a d\chi + \int_r^1 \theta_a d\chi = \left(\theta_{a0} + \frac{1}{\alpha}\bar{\theta}_{a1}\right)r + \gamma(1-r) \\ &= \gamma\{1 + (0.57r^{-0.25} - 0.50)^{-1}r^{-1}\alpha - r - 1\} \\ &\quad + 1.704r + \alpha^{-1}(0.207r^{11/4} - 0.166r^3)\end{aligned} \tag{39}$$

Figure 2(*b*) presents the comparison of trends in leading order solution for average nondimensional temperature at the plate surface for different values of UWT/UHF fraction r and thermal parameter α. For α with order 1 or less, $\bar{\theta}_a$ has tendency to start with value above unity and as r increases, it drops rapidly until $r=0.37$ and then gradually rise with further increase in r. The slope of the curve in the first (decreasing) phase has limiting value that corresponds to $\alpha=1$; all the curves show concavity upward in the second (rising) phase. For the curves corresponding to α with order higher than unity, the slope in the first phase is lesser when compared with previously discussed cases; during the next phase ($r>0.37$), the slope vanishes and $\bar{\theta}_a$ attains a near linear relation with r.

Let us consider $\bar{\theta}_{\max}$ as a maximum value for $\bar{\theta}_a$ corresponding to a particular set of values for γ and α. Taking $\bar{\theta}_{\max}$ as a normalization parameter, θ_a^n is the normalized value of $\bar{\theta}_a$. The effect of variation in γ and α on the trends in r versus θ_a^n is shown in Fig. 3. For $\alpha=10^3$, r versus θ_a^n curves exhibit a linear pattern with the higher slope for the line corresponding to the lower γ value. It can also be observed from Fig. 3(*a*) that all lines corresponding to different γ values tend to converge to near equal values at $r=1$; at the point of convergence, $\theta_a^n=1.355$, 1.358, and 1.362 for $\gamma=0.4$, 0.7, and 1.0 respectively. For $\alpha<10^3$, θ_a^n shows a typical drop and rising phases in succession as r increase. With the increase in γ, the first phase extends up to larger r. It can be observed from Fig. 3(*b*), for $\alpha=10$, that the minima for r versus θ_a^n curves lie in the first quarter of the range for r.

Observation of trends indicates up to 2.5 times larger θ_a^n at the end of second phase as compared to the onset of first phase. The described features are prominently observed for $10>\alpha>1$. Observation of trends in r versus θ_a^n curves for $\alpha=1$ and $\alpha=10^{-3}$, as shown in Figs. 3(*c*) and 3(*d*), indicates 27% reduced θ_a^n at the end of second phase as compared to that at the onset of first phase; also, lowest θ_a^n values lie beyond the first quarter of the range for r values. Curves associated with a small γ are found to have successively reducing slope in rising (second) phase for $\alpha<1$. No

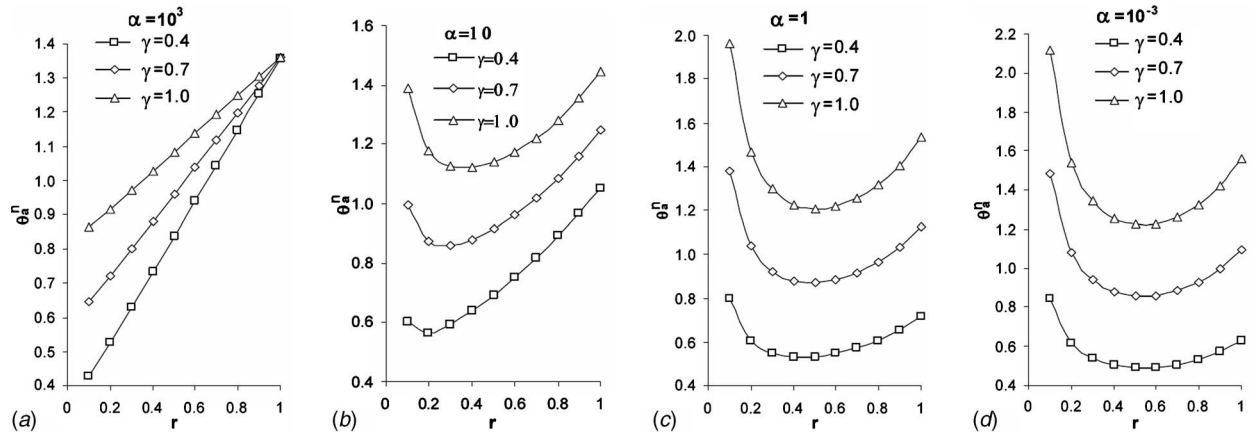

Fig. 3 Comparison of normalized first order solution for nondimensional temperature, θ_a^n, as a function of r for different α and γ

significant difference is observed among the trends in variation pattern for θ_a^n versus r curves when $O(\alpha) < 10^{-4}$.

In order to determine the solution for the case $\alpha \to 0$, for the range $0 < \chi \leqslant r$, Eq. (11) is replaced by

$$\frac{\alpha}{\varepsilon^2}\frac{\partial^2 \theta_a}{\partial z^2} + 1 = 0 \tag{40}$$

Substituting Eqs. (15) and (16) as boundary condition, Eq. (40) reduces to

$$\chi^{-0.25}\frac{\partial \theta_a}{\partial \eta}\bigg|_0 = -1 \tag{41}$$

For this particular case, the possible solution is in the form

$$\theta_a = \theta_0' \chi^{0.2} \tag{42}$$

To obtain $\bar{\theta}_0$, we need to make the following substitution in Eqs. (7) and (8):

$$\eta = \chi^{-0.05}\eta' \quad f = \chi^{0.05} f' \quad \theta = \chi^{0.2}\theta' \quad \text{and} \quad \theta_a = \chi^{0.2}\theta_0' \tag{43}$$

As a result, we get

$$\frac{\partial^2 \theta'}{\partial \eta'^2} + \frac{4}{5} f' \frac{\partial \theta'}{\partial \eta'} - \frac{1}{5}\theta' \frac{\partial f'}{\partial \eta'} = 0 \tag{44}$$

$$\frac{\partial^3 f'}{\partial \eta'^3} + \theta' = \frac{1}{\mathrm{Pr}}\left[\frac{3}{5}\left(\frac{\partial f'}{\partial \eta'}\right)^2 - \frac{4}{5} f' \frac{\partial^2 \theta'}{\partial \eta'^2}\right] \tag{45}$$

These are to be solved subject to the following boundary conditions: at $\eta' = 0$,

$$f' = \frac{\partial f'}{\partial \eta'} = 0 \quad \frac{\partial \theta'}{\partial \eta'} = -1 \tag{46}$$

for $\eta' \to \infty$

$$\frac{\partial f'}{\partial \eta'} = \theta_a' = 0 \tag{47}$$

An attempt to find analytical solution results into complexity. Solving the problem numerically using finite difference (FD) method provided easy solution. The following FD expressions are used:

$$f_{k+1} = f_{k-1} + A_k \frac{\theta_{k+1}}{\theta_k} + B_k \frac{\theta_{k+1}}{\theta_k} - C_k \tag{48}$$

where

$$A_k = 4f_k + \frac{10}{\Delta \eta_{k+1}} \quad B_k = \frac{10}{\Delta \eta_{k+1}} - 4f_k \quad \text{and}$$

$$C_k = 10\left(\frac{1}{\Delta \eta_{k+1}} + \frac{1}{\Delta \eta_k}\right)$$

$$\theta_{k+1} = -D_k \theta_{k-1} + (D_k + 1)\theta_k + E_k \frac{(f_{k+1} - f_{k-1})^2}{f_k} + F_k \frac{f_{k+1}}{f_k} + G_k \frac{f_{k-1}}{f_k} + H_k \tag{49}$$

where

$$D_k = \frac{\Delta \eta_{k+1}}{\Delta \eta_k} \quad E_k = \frac{15 D_k}{32(1 + D_k)} \quad F_k = \frac{5\mathrm{Pr}}{4\Delta \eta_k} \quad \text{and}$$

$$G_k = \frac{5\mathrm{Pr} D}{4\Delta \eta_k}\left(\frac{\Delta \eta_k + \Delta \eta_{k+1}}{\Delta \eta_{k-1}}\right)$$

In addition to the above, forward difference and backward difference expressions were substituted in place of central difference to ensure implementation of boundary conditions.

Successive iteration was carried out for $k = 0, 1, 2, \ldots, M$, where M represented the value such that

$$|f_M - f_{M-1}| < \varepsilon_1 \quad \text{and} \quad |\theta_M - \theta_{M-1}| < \varepsilon_2$$

Values of ε_1 and ε_2 were kept sufficiently close to zero. For the case of air (Pr=0.72), $\theta_0' \approx 1.95$ has been obtained.

Analytical solution is not possible for the range $r < \chi \leqslant 1$ when $\alpha \to 0$ as Eq. (9) results in $q \approx 0$ (i.e., there is negligible heat generation in the region).

3 Experimental Setup

The setup consisted of test section and intake unit is shown in Fig. 4(*a*). The test section was a rectangular duct oriented vertically and having a provision for holding two vertical plates in parallel; a lead screw mechanism was provided to move these nearer or apart in such a way that the region formed in between remained symmetrically placed. The test section was 700 mm high with 300×200 mm^2 lateral dimensions. In order to facilitate panoramic viewing inside the unit, a shatter resistant (plate safety) glass material with a specified thermal conductivity of 3.7 W/m K (approximately) was used for construction. The test configuration comprised heated regions of total vertical length 500 mm and a downstream unheated region of length 100 mm. The heated regions were divided into five heated zones appearing one after another in channel formed in-between plate specimen and insulated wall. A maximum horizontal dimension of the region of interest was 80 mm. A separate heating unit was embedded in each section. The schematic for the heated plate design is shown in Fig. 4(*b*).

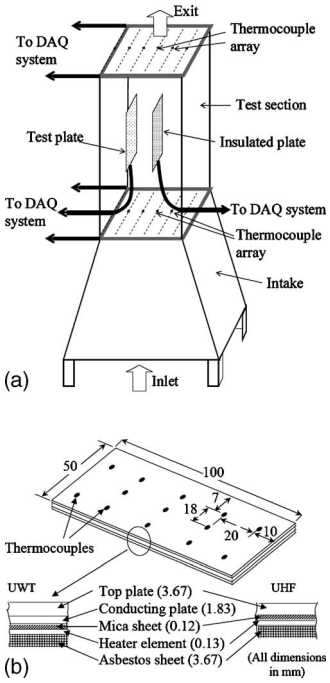

Fig. 4 Schematics for (*a*) experimental setup and (*b*) heated plate

The thermopiles were placed at both sides of top plate. The difference in the temperature at the two surfaces was measured and used for calculating temperature gradient and determining the heat flux at the surface using the relation

$$Q = -k\frac{\Delta T}{\Delta x} \tag{50}$$

The UWT condition was simulated by selecting a material of high thermal conductivity (aluminum) for placing underneath of top plate. Under steady state, this denigrated the temperature gradients along the longitudinal direction of the top plate; a maximum of 0.21% temperature difference was observed at the two ends of the top plate (along the flow direction) while the mean temperature at the surface was maintained near or below 100°C. For simulating UHF condition, it was ensured that the foil used in making heating element is uniform in thickness (130 ± 1 μm) so that there was homogeneous resistance all over the heater surface area. A stainless steel foil was opted as heater material. During the experimentation, a maximum variation of heat flux for UHF surface was found lower than 4%. The heated plate assembly was designed incorporating the flexibility of comfortable replacement of top plate. For experimentation purpose, aluminum, Teflon, and FR4 were used as top plate materials. The power supplied to each heater was monitored and precisely controlled separately, keeping basic dc accuracy near 0.025% for both the voltage and current.

4 Measurement Methods Adopted

J-type thermocouples prepared from 30 gauge Omega brand thermocouple wires were used for temperature measurement. Thermocouples were connected in differential mode to the AMUX 64-T DAQ card from National Instruments; PCI-6024E DAQ card was used for data acquisition purpose. LABVIEW software was used for monitoring, storage, and analysis of the data. Velocity measurement was also carried out but manually using a vane anemometer at the exit of test section. The zone surface temperature was monitored by an array of thermocouples, as shown in Fig. 4(*b*).

Five thermocouples were placed at the upstream locations of the heated zone, while another five thermocouples were located at the downstream side. Three thermocouples were placed at the middle of each of the zones. The ambient air temperature was measured at the leading edge of the channel. In order to evaluate the conductive heat losses, five thermocouples were affixed to the rear surface of both the heated wall and the insulated surface in their centerline, 10 mm, 30 mm, 50 mm, 70 mm, and 90 mm downstream of the inlet section. Thermocouple voltages were recorded to an accuracy of 1 μV. Each thermocouple was calibrated in a 0.01 K thermostatic bath by means of a reference standard thermometer. The calibration of the temperature measuring system showed an estimated precision of the thermocouple-readout system of ± 0.2 K [12]. While maintaining two different kinds of thermal conditions at the test plate surface, the temperature selected for the UWT surface was such that the temperature at the beginning of the following UHF surface remains as close as possible to the temperature at the preceding surface.

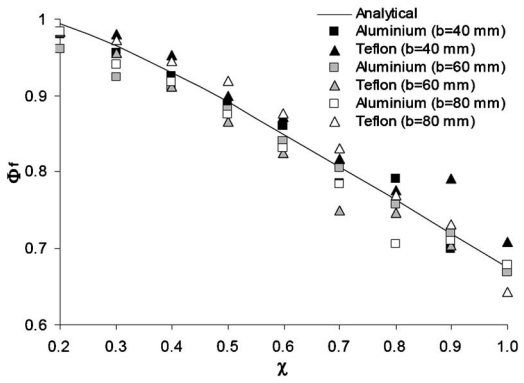

Fig. 5 Variation of normalized heat flux at the plate surface with increase in nondimension distance over the surface from leading edge

5 Results and Discussion

The variation in the heat conduction parameter was achieved by varying the top plate material. The experimental data were obtained for three materials, viz., Aluminum, Teflon, and FR4 for which the values of heat conduction parameter were $\alpha = 1.17$, 1.09×10^{-3}, and 1.63×10^{-3}, respectively. Dimensions for the heated surface were invariant. The distance between the test plate and the insulated plate was kept sufficiently larger than the theoretically calculated order of magnitude for boundary layer thicknesses in the flow and thermal fields over the test plate. For the assumed thermal condition over the surface, the leading order analytical solution for the UHF case and average nondimensional temperature $\bar{\theta}_a$ up to the order $1/\alpha$ was obtained and used for comparison with the experimental data. As extreme temperature gradients were expected to occur for the UHF condition [3,12] over the total surface (i.e., $r = 0$), therefore this condition was opted to quantify the variation in measured values due to the presence of insulated wall. Three distances between the test plate and the insulated plate, i.e., $b = 40$ mm, 60 mm, and 80 mm, were chosen. The normalized heat flux Φ_f^n as a function of nondimensional longitudinal coordinate χ for three plate separations is shown in Fig. 5. The analytical results due to Eq. (33) are also presented. The value of Rayleigh number was maintained close to 5.4×10^8. For greater plate separation, Φ_f^n values are found to be larger toward the lower edge of the plate as compared to those for smaller plate separation; however, the opposite trend is observed toward the upper edge. For various plate separations, all the data were found to lie within 7% of the mean value. A discrepancy between the analytical and experimental data was found to be less than 6%.

Figure 6 presents the experimental data for normalized heat generation Φ_f^n when the initial 1/5th portion of the plate surface

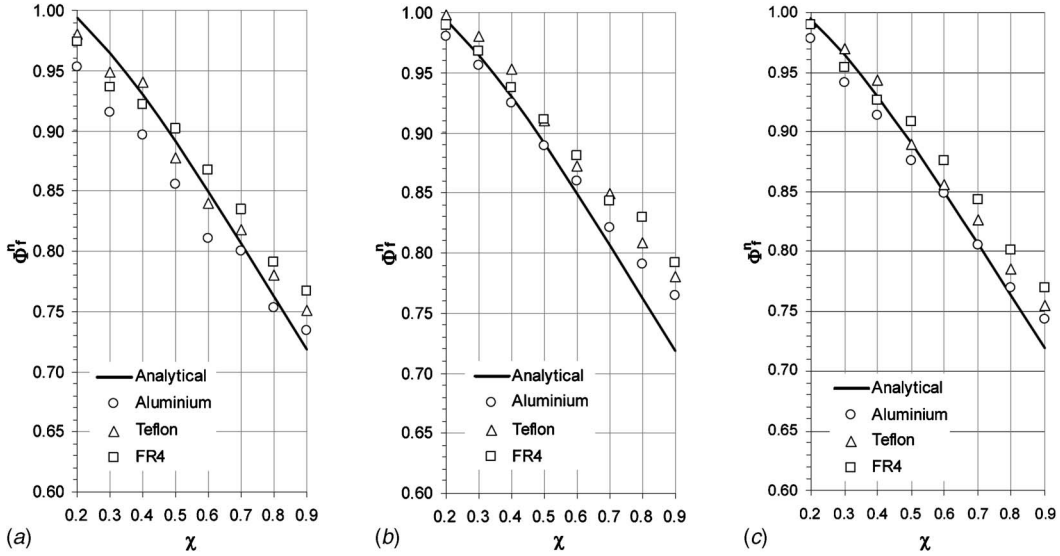

Fig. 6 Dependence of normalized heat generation under the plate surface upon the nondimensional plate height for r=0.2 and (*a*) γ=0.2 and (*b*) γ=1.0

was heated to UHF and the remaining portion was maintained at UWT condition (r=0.2). The experimental data are also compared with the analytical solution given by Eq. (33). For both the cases, Φ_f^n decrease with the increase in χ. For γ=0.2, the experimental values corresponding to Teflon as plate material are found nearest to analytical solution; at γ=0.5, the excellent agreement occurs for aluminum for $\chi<0.7$. For γ=1.0 and up to a medium value of χ, better agreement is observed between the analytical and the experimental values for Teflon and FR4; at higher χ, agreement within 3% is observed for the aluminum. A discrepancy between the analytical and experimental values is maximum (up to 10%) at γ=0.5 and occurs near the upper end of plate. The probable cause may be the inclusion of large disturbances in natural-convection flow pattern as the fluid progresses toward the upper edge of the test surface.

The experimental data for the case when the initial 2/5th portion of the plate surface was heated to UHF and the remaining portion was maintained at UWT condition (r=0.4) are presented by Fig. 7. It can be observed that Φ_f^n decrease with increase in χ. For γ=0.2, the experimental values corresponding to aluminum as plate material are found nearest to analytical solution. For γ =0.5, the best agreement occurs for Teflon; up to 3% agreement occurs for aluminum but for $\chi\leqslant 0.7$. Φ_f^n values for three materials tend to spread out at the upper end of the heated surface; however, the spreading remains within 3% of the mean value. For γ=1.0, better agreement is observed for Teflon particularly toward the lower and upper edges. For all γ, experimental data for aluminum exhibit the highest values while those corresponding to FR4 are the lowest.

The experimental and analytical data trends for χ versus θ_a^n are shown in Fig. 8. At lower γ, experimental data trends show more inclination toward the results due to Eq. (42). The spread in experimental data for three materials tends to reduce with the increase in χ as well as with the increase in γ; a maximum spread of near 4% about the mean value occurs for γ=0.2. Also, the mini-

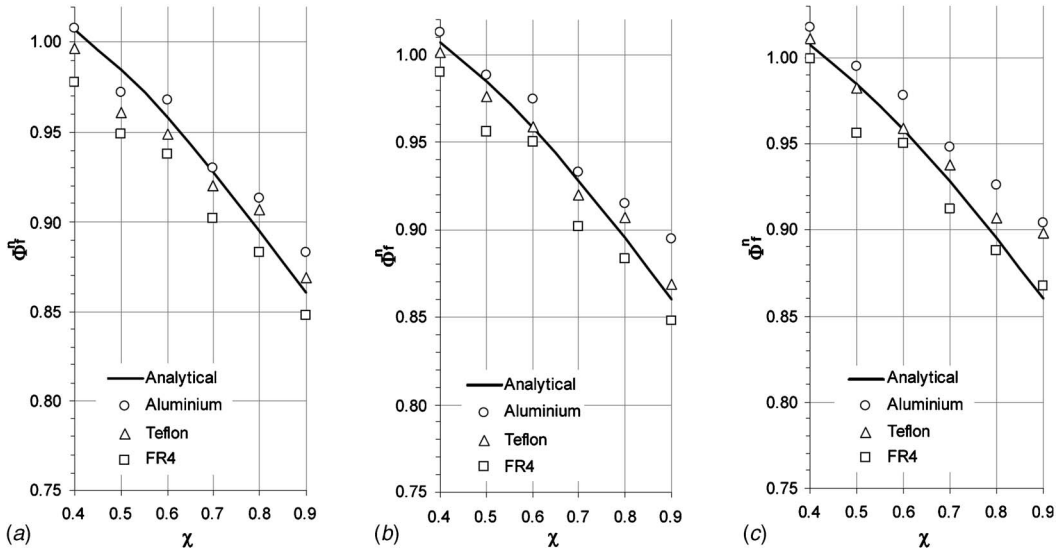

Fig. 7 Dependence of normalized heat generation under the plate surface upon the nondimensional plate height for r=0.4 and γ=0.5

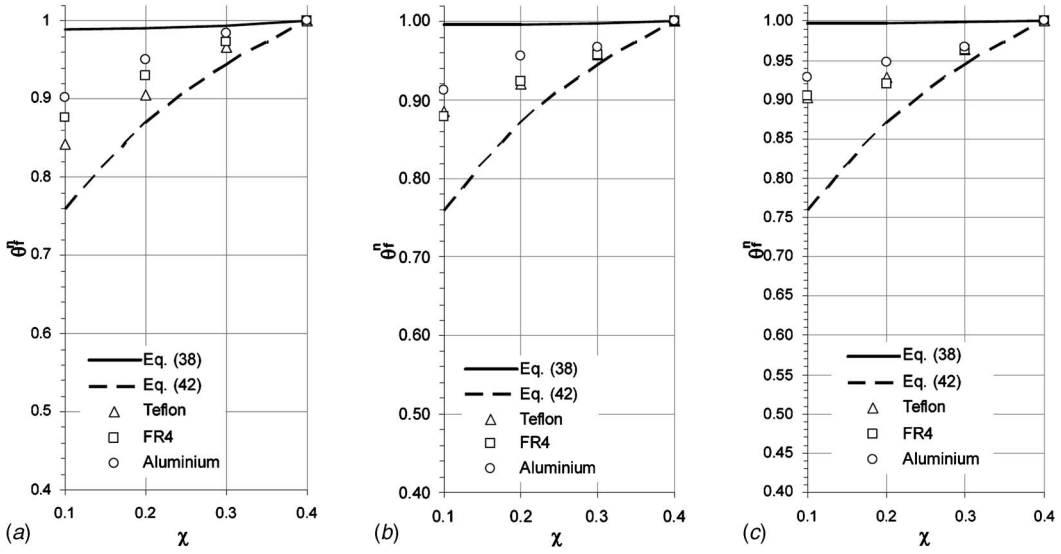

Fig. 8 Dependence of dimensionless surface temperature at the plate surface upon the nondimensional plate height for $r=0.4$ and (*a*) $\gamma=0.2$, (*b*) $\gamma=0.5$, and (*c*) $\gamma=1.0$

mum discrepancy (of less than 9%) occurs between experimental data for FR4 and solution due to Eq. (42). In general, the data points for Teflon are nearer to value due to Eq. (42), while the data points for aluminum show more proximity toward the data values due to Eq. (38). The slope in the analytical trends due to Eq. (38) is found to reduce with the increase in γ, while the trend due to Eq. (42) remains unaffected. For $\gamma=0.5$, majority of experimental data for Teflon and FR4 overlap and are closer to Eq. (42). At $\gamma=1.0$, the region for spread of experimental data lies midway between the analytical values corresponding to Eqs. (38) and (42). The minimum discrepancy occurs between the experimental values for aluminum and values corresponding to Eq. (38), which is near 10%. Apparently, the exact overlapping of experimental and analytical data values at $\chi=0.4$ is due to normalization rather than absolute lack of any discrepancy within the set of results.

Figures 9 and 10 show the experimental data and the analytical trends for the case when the initial 3/5th portion of the plate surface was heated to UHF condition and the remaining portion was under UWT condition ($r=0.6$). As observed for the previously discussed results, Fig. 9 shows normalized heat flux at the plate surface to reduce with the increment in nondimensional distance from the leading edge; however, the slope is nearly one-third to that observed for $r=0.4$ case. Also, the trends in experimental data seem much affected by change in γ values as the difference in Φ_f^n at a particular value of χ seems to widen with the increase in γ. A careful observation shows proximity of analytical results toward experimental data for aluminum for lower γ and also favorable for FR4 data for higher γ. Φ_f^n values for three materials tend to spread out uniformly with the rise in χ values.

Variation in θ_a^n at the plate surface under UHF condition due to increase in χ is indicated in Fig. 10 along with analytical solutions. The highest spread in experimental data decreases from near 7% to near 3% about the mean value as γ increase from 0.2 to 1.0. The relative tendencies in experimental data for three materials exhibit nearly the same trends as discussed for case at $r=0.4$. At

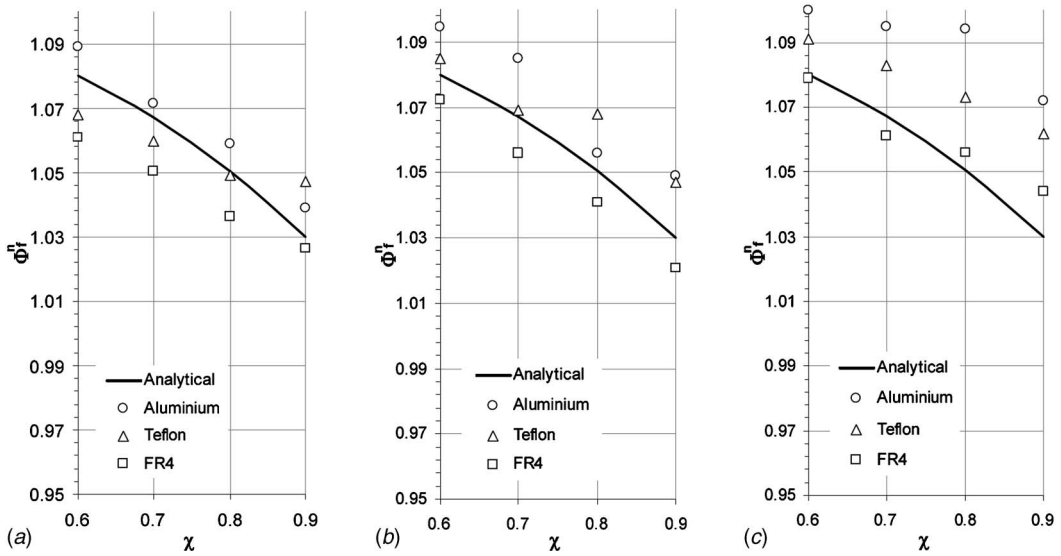

Fig. 9 Dependence of normalized heat generation under the plate surface upon the nondimensional plate height for $r=0.6$ and (*a*) $\gamma=0.2$, (*b*) $\gamma=0.5$, and (*c*) $\gamma=1.0$

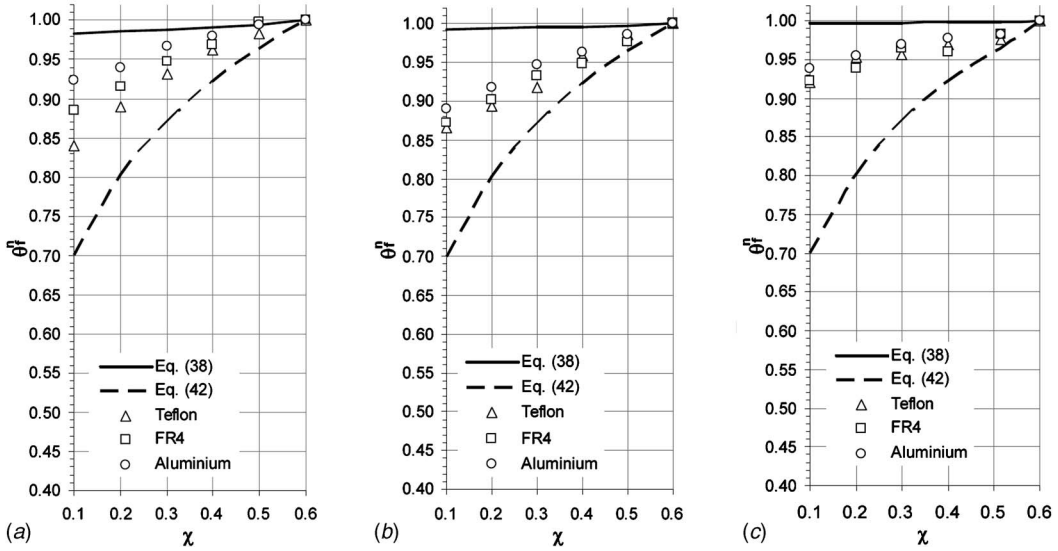

Fig. 10 Dependence of dimensionless surface temperature at the plate surface upon the nondimensional plate height for r=0.6 and (*a*) γ=0.2, (*b*) γ=0.5, and (*c*) γ=1.0

the highest occurring value for γ, the experimental data are closer to the analytical values due to Eq. (38) with a maximum discrepancy of around 9%.

Figure 11 presents the variations in θ_a^n with χ for the plate surface under UHF condition for the case when the initial 4/5th portion of the plate surface was heated to UHF condition and the remaining portion was under UWT condition (r=0.8). The slope in χ versus θ_a^n curve for Eq. (38) is found to reduce with the rise in γ; apparently, 50% reduction in slope occurs as γ increased from 0.2 to 0.5, followed by about 40% reduction as γ increased from 0.5 to 1.0. The relative trends among the experimental data points for three different materials are not much affected by the increase in r from 0.4 to 0.8. The spread in the experimental data reduces from about 12% to nearly 5% as the value of γ increases from 0.2 to 1.0. When Teflon is the plate material, the discrepancy between the experimental data and analytical results due to Eq. (42) at a particular value of χ is minimum (less than 10%) for the lowest value of γ. However, toward highest value of γ, for experimental data and analytical results due to Eq. (38), the discrepancy is found to be minimum for the case of aluminum as plate material (less than 11%).

Figure 12 presents the analytical solutions due to Eqs. (38) and (42), the experimental results (r=0.8), and the data from the literature. Both the analytical solutions are at the upper side of the data values due to Pozzi and Lupo [4] and Merkin and Pop [7]; note that the data from the former reference are based on the singular asymptotic expansion by means of Pade approximant techniques, while the latter one resulted from the FD scheme employing Robin boundary condition. The data due to Vallejo and Trevino [5], which is based on the asymptotic analysis with multiple scale techniques for laminar flow pattern, are in best agreement with the current work for maximum of the χ range. Maximum deviations of approximately 10% and 15% occur for solutions due to Eqs. (38) and (42), respectively. The values due to Shu and Pop [8] start with the good agreement with current analytical solution; however, deviation up to 50% occurs at higher

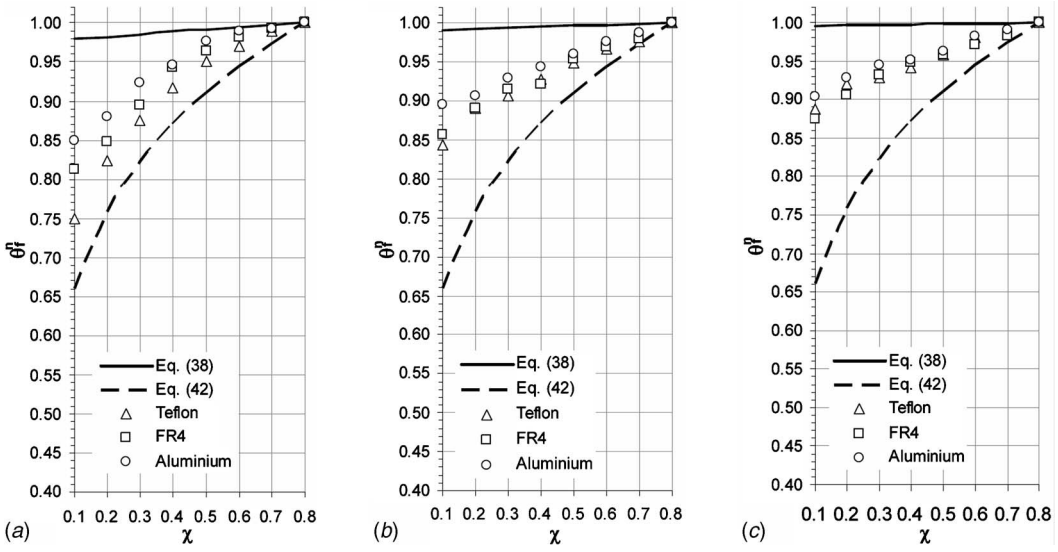

Fig. 11 Dependence of dimensionless surface temperature at the plate surface upon the nondimensional plate height for r=0.8 and (*a*) γ=0.2, (*b*) γ=0.5, and (*c*) γ=1.0

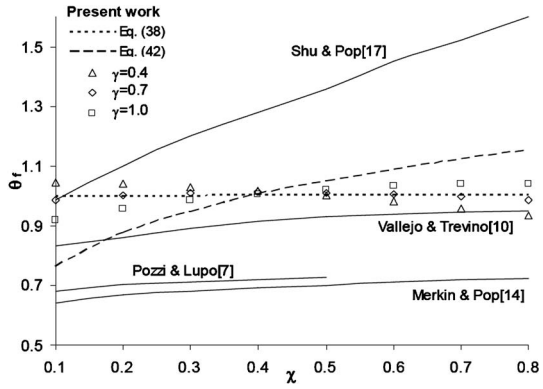

Fig. 12 Comparison of current work with data from the literature

values of χ. Note that their results are for forced convection situation with a prescribed surface heat flux profile. The objective of introducing forced convection data for comparison purpose is to emphasize considerable resemblance of overall profile in results out of analytical solution due to Eq. (42) with it.

6 Experimental Uncertainty Analysis

The uncertainty in the calculated quantities was determined according to the standard single sample analysis recommended by Moffat [22]. The uncertainty of a dependent variable R as a function of the uncertainties in the independent variable X_i is given by the relation

$$\delta R = \left[\left(\frac{\partial R}{\partial X_1} \delta X_1 \right)^2 + \left(\frac{\partial R}{\partial X_2} \delta X_2 \right)^2 + \cdots + \left(\frac{\partial R}{\partial X_n} \delta X_n \right)^2 \right]^{1/2} \tag{51}$$

The uncertainty in the values of thermophysical properties of the air was assumed to be negligible [23]. Due to the level of complexity involved in monitoring and regulation of the heater powers to maintain desired thermal conditions simultaneously at various test plate sections and minor variations in the ambient condition, perfect replication of the mix heating condition for different test specimens was practically impossible [12]. However, the test was repeated and it was found that maximum differences between any temperature level and its average value were 3.8%, 4.1%, and 3.1% for Teflon, FR4, and aluminum, respectively. The corresponding differences between any heat flux level and the average value were below 3.4%, 4.4%, and 2.1% for three plate materials in the same order. The heat lost by radiation from the heated surface was assumed less than 5% [14]. Results indicated less than 6% uncertainty in the surface heat flux measurements. Estimated uncertainty in dimensionless temperature was less than 2%, while the corresponding value for dimensionless heat flux was less than 9%. Experimental uncertainty is based on a 95% confidence level.

7 Conclusions

The conjugate heat transfer problem was investigated both analytically and experimentally for a vertical plate with natural convection at the surface and conduction below considering thermally thin wall regime approximation. Thermal specifications at the plate surface were a combination of UHF and UWT conditions with matching temperature conditions at the interface. The plate surface was divided into five heated zones (i.e., $N=5$). Comparative analysis is presented for first order analytical solution for dimensionless temperature and dimensionless heat flux for limiting case of $\alpha \to \infty$ with the experimental data for three values of α, i.e., 1.17, 1.09×10^{-3}, and 1.63×10^{-3}. Analytical solution for dimensionless temperature for the limiting case of $\alpha \to 0$ was also presented and compared with the experimental data. Reasonably, good agreement was observed for normalized heat flux values with the corresponding experimental data and therefore the analytical results for limiting case of $\alpha \to \infty$ can be practically used for $\alpha \geqslant 10^{-3}$ with an error less than 9%. Fair agreement was also observed for analytical solutions for dimensionless temperature for the two limiting cases. However, the solution for limiting case of $\alpha \to 0$ resulted in values within 10% of the experimental data for α with an order of magnitude 10^{-3}, and for limiting case of $\alpha \to \infty$ gave better predictions (within 11%) for $\alpha \approx 1$.

Experimental investigation using materials with properties resulting in wider range of heat conduction parameter, larger heated zone subdivisions for smooth variation in temperature and heat flux profiles, and exploration for both the numerical and analytical solutions under such parametric values constitutes the potential objectives.

Acknowledgment

The authors gratefully acknowledge the efforts of Dr. V. Raghuram, Senior Research Engineer of Department of Mechanical Engineering, IIT-Kanpur; Mr. P. S. Chauhan, Instrumentation Engineer of Department Chemical Engineering, IIT-Kanpur; and Mr. Sushil K. Mishra, Senior Technical Assistant of Heat Transfer Laboratory of Department of Mechanical Engineering.

Nomenclature

b = distance between heated plate and insulated wall
c = specific heat, kJ/kg K
f = nondimensional stream function
g = acceleration due to gravity, m/s^2
H = height of plate, m
k = thermal conductivity of fluid, kJ/mK
p = pressure, Pa
Pr = Prandtl number
q = surface heat generation
q_v = average heat generation over the surface
Ra = Rayleigh number
t = plate thickness, m
T = temperature, °C
u,v = x,y velocity component, m/s
x,y = Cartesian coordinate
z = nondimensional normal coordinate to the strip

Greek Symbols

α = heat conduction parameter
β = volumetric expansion coefficient
δ = boundary layer thickness, m
ϵ = aspect ratio of the plate (h/L)
η = nondimensional normal coordinate for the flow
μ = dynamic viscosity, m^2/s
ν = kinematic viscosity, kg/m s
ρ = density of fluid, kg/m^3
θ = nondimensional temperature
$\bar{\theta}$ = average nondimensional temperature
χ = nondimensional longitudinal coordinate
Φ_f = heat flux ratio
Γ_0 = fluid nondimensional temperature at the strip
Θ = function defined by Eq. (19)
Ψ = stream function

Superscript

$( )^n$ = normalized quantity

Subscripts

$( )_c$ = characteristic
$( )_a$ = wall
$( )_{\max}$ = maximum value
$( )_\infty$ = ambient

References

[1] Trevino, C., and Linan, A., 1984, "External Heating of a Flat Plate in a Convective Flow," Int. J. Heat Mass Transfer, **27**, pp. 1067–1073.

[2] Chen, T. S., Tien, H. C., and Armaly, B. E., 1986, "Natural Convection on Horizontal, Inclined and Vertical Plates With Variable Surface Temperature or Heat Flux," Int. J. Heat Mass Transfer, **29**, pp. 1465–1478.

[3] Sparrow, E. M., Garcia, A., and Chuck, W., 1987, "Turbulent Duct Flow With Streamwise Non-Uniform Heating at the Duct Wall," Int. J. Heat Mass Transfer, **30**, pp. 175–185.

[4] Pozzi, A., and Lupo, M., 1988, "The Coupling of Conduction With Laminar Natural Convection Along a Flat Plate," Int. J. Heat Mass Transfer, **9**, pp. 1807–1814.

[5] Vallejo, A., and Trevino, C., 1990, "Convective Cooling of a Thin Plate in Laminar and Turbulent Flows," Int. J. Heat Mass Transfer, **33**, pp. 543–554.

[6] Naylor, D., Floryan, J. M., and Tarasuk, J. D., 1991, "A Numerical Study of Developing Free Convection Between Isothermal Vertical Plates," ASME J. Heat Transfer, **113**, pp. 620–626.

[7] Merkin, J. H., and Pop, I., 1996, "Conjugate Free Convection on a Vertical Surface," Int. J. Heat Mass Transfer, **39**, pp. 1527–1534.

[8] Shu, J. J., and Pop, I., 1998, "On Thermal Boundary Layers on a Flat Plate Subjected to a Variable Heat Flux," Int. J. Heat Fluid Flow, **19**, pp. 79–84.

[9] Mendez, F., and Trevino, C., 2000, "The Conjugate Conduction-Natural Convection Heat Transfer Along a Thin Vertical Plate With Non-Uniform Internal Heat Generation," Int. J. Heat Mass Transfer, **43**, pp. 2739–2748.

[10] Kazansky, S., Dubovsky, V., Ziskind, G., and Letan, R., 2003 "Chimney-Enhanced Natural Convection From a Vertical Plate: Experiments and Numerical Simulators," Int. J. Heat Mass Transfer, **46**, pp. 497–512.

[11] Chen, L., Tian, H., Li, Y., and Zhang, D., 2006, "Experimental Study on Natural Convective Heat Transfer From a Vertical Plate With Discrete Heat Sources Mounted on the Block," Energy Convers. Manage., **47**, pp. 3447–3455.

[12] Yadav, V., 2005, "Thermal Modeling of Electronic Packages Subjected to Buoyancy Assisted Convective Cooling in Air," Ph.D. thesis, Indian Institute of Technology, Kanpur, India.

[13] Yadav, V., and Kant, K., 2007, "Convective Cooling of a PCB Like Surface With Mixed Heating Conditions in a Vertical Channel," ASME J. Electron. Packag., **129**, pp. 129–143.

[14] Anderson, A. M., 1994, "Decoupling Conductive and Convective Heat Transfer Using the Adiabatic Heat Transfer Coefficient," ASME J. Electron. Packag., **116**, pp. 310–316.

[15] Luikov, A. V., 1974, "Conjugate Heat Transfer Problems," Int. J. Heat Mass Transfer, **17**, pp. 257–265.

[16] Ortega, A., Wirth, U. S., and Kim, S. J., 1996, "Conjugate Forced Convection From a Discrete Heat Source on a Plane Conducting Surface," *Air Cooling Technology for Electronic Equipment*, S. J. Kim and S. W. Lee, eds., CRC, Cleveland, OH, Chap. 4.

[17] Incropera, F. P., 1988, "Convection Heat Transfer in Electronic Equipment Cooling," ASME J. Heat Transfer, **110**, pp. 1097–1111.

[18] Jaluria, Y., 1985, "Interaction of Natural Convection Wakes Arising From Thermal Sources on a Vertical Surface," ASME J. Heat Transfer, **107**, pp. 883–892.

[19] Cole, K. D., 1997, "Conjugate Heat Transfer From a Small Heated Strip," Int. J. Heat Mass Transfer, **40**, pp. 2709–2719.

[20] Sathe, S. B., and Joshi, Y., 1991, "Natural Convection Arising From a Heat Generating Substrate-Mounted Protrusion in a Liquid Filled Two Dimensional Enclosure," Int. J. Heat Mass Transfer, **34**, pp. 2149–2163.

[21] Kays, W. M., and Crawford, M., 1980, *Convective Heat and Mass Transfer*, McGraw-Hill, New York.

[22] Moffat, R. J., 1988, "Describing the Uncertainties in Experimental Results," Exp. Therm. Fluid Sci., **1**, pp. 3–17.

[23] Moffat, R. J., 2004, "$h_{adiabatic}$ and u'_{max}," ASME J. Electron. Packag., **126**, pp. 501–509.

Numerical Investigation on the Effects of Pressure Drop on Thermal Behavior of Porous Burners

M. Khosravy El-Hossaini

M. Maerefat
e-mail: maerefat@modares.ac.ir

K. Mazaheri

Mechanical Engineering Department,
Tarbiat Modares University,
P.O. Box 14115-143,
Tehran, Iran

This article aims to study the effect of pressure drop on the thermal behavior of porous burners. Since the reticulated ceramics are used in the burners' construction, in the previous researches pressure drop arising from flow velocity was ignored. This research has showed that due to the increase of speed resulting from combustion, the consequence pressure drop creates considerable effects on the thermal performance of porous burners. To study this subject, the temperature of a point on the burner axis has been taken to be constant. The burned gas and exit surface temperature were obtained almost the same for two conditions, one with the pressure held constant and the other with a pressure drop. Results show that the firing rate was decreased up to 18%, compared to the constant pressure case. The thermal radiative efficiency of radiant porous burners, in which the pressure drop has been considered, was increased about 3–5% for the studied equivalence ratio of methane-air combustion. [DOI: 10.1115/1.2804947]

Keywords: pressure drop, porous burners, numerical modeling

Introduction

Advanced combustion systems have been highly motivated by the increasing needs for efficient heat transfer with low emission of NO_x and other pollutants. In premixed combustion within porous inert media (PIM), the heat released during reaction is transferred to the solid matrix through an effective convection.

Several mathematical models with varying degrees of sophistication have been proposed for combustion/heat transfer in porous media. Most of the numerical studies published so far focus on the one-dimensional analysis as well as the effect of the main parameters [1].

Similar to laminar premixed flame, the velocity varies only with density to satisfy continuity equation in one-dimensional porous inert media. There are some parameters that affect velocity distributions, which do not fit in this modeling. Pressure field is one of the most important parameters so far as porous buried combustion is concerned. In this case, since flow velocity is low enough, incompressible flow assumption is valid with neglecting the thermodynamic pressure. However, variation in the hydrodynamic pressure introduces a significant effect on the combustion characteristics especially in porous burners, which so far have not been addressed by previous researchers [1,2].

Premixed combustion of hydrocarbon fuel in porous inert media is commissioned to release the fuel chemical energy in the form of a product stream enthalpy or directed radiation energy. Premixed fuel and air enter the porous matrix where they are convectively heated as they pass through interstitial voids. The matrix ceramic is also heated by radiation emitted toward the upstream side from the reaction zone and by conduction through the solid matrix. Combustion of porous media has been the subject of numerous experimental and theoretical studies [3–5]. Most of the previous studies had simulations only in one dimension and employed simple chemical kinetic models. However, the current research applies two distinct energy equations for solid and gas phases with multistep chemical mechanisms [6,7]. Excellent reviews of the theoretical background of the combustion in porous media are found in Howell et al. [1], Viskanta and Gore [2], and Kamal and Mohamad [8]. Mohamad et al. [9] also developed a model to simulate combustion and heat transfer in a 2D packed bed combustor heater. They assumed one step reaction for gas phase energy equation and nonthermal equilibrium between the gas and the solid matrix. Brenner et al. [10] used a 2D pseudohomogeneous heat transfer and flow model for a porous burner with the aim to optimize the combustion process as well as to test the burner design. During the course of study, they considered conservation equations—two momentum equations and one energy equation for 20 species. They also assumed a local thermal equilibrium between the gas and the solid phases. However, they neglected the radiative heat transfer. Among other researchers, Malico and Pereira [11] studied the influence of solid radiative properties on a 2D cylindrical porous burner performance. Furthermore, Mishra et al. [12] analyzed heat transfer in a 2D rectangular porous radiant burner where the simulation showed the effects of the pore characteristic length on the rate of heat transfer, especially the thermal radiation of porous burners.

In order to study the effect of pressure drop, numerical modeling of 2D porous radiant burners has been utilized in the present work. Porous radiant burners are usually made up of reticulated ceramic fibers, possessing high percentage of porosities. Due to the burner's short length and the kind of internal flow, the pressure drop arising from flow was neglected in the past researches. The present research showed that pressure drop obtained from equation solution has considerable effects on the performance of heat porous burner, even in the lowest flow velocity in lean combustion region and therefore cannot be neglected. The rest of the paper discusses the governing equations and the solution methods. The results are then compared to an experimental research sample. Study about the flow pattern and as such, the effect of pressure drop on temperature distribution and firing rate of porous burners, forms other sections of this paper.

Contributed by the Heat Transfer Division of ASME for publication in the JOURNAL OF HEAT TRANSFER. Manuscript received November 6, 2006; final manuscript received June 26, 2007; published online March 5, 2008 Review conducted by Jose L. Lage.

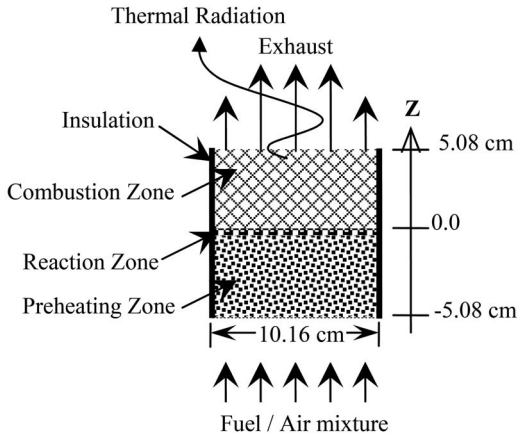

Fig. 1 Schematic diagram of the studied burner

Problem Description and Governing Equations

The proposed problem is schematically shown in Fig. 1. The burner is two dimensional and has an axisymmetric circular cross section with 10.6 cm diameter and 10.6 cm height. These dimensions have been used to successfully validate the present numerical results compared with available experimental data by Smucker and Ellzey [13]. The porous burners consist of two zones, a preheating zone made of partially stabilized zirconia (PSZ) and a flame barrier with larger pore diameter made of yttria-stabilized zirconia (YZA).

Table 1 shows the material properties used for the computations, where C and m are constants used in correlation of the volumetric Nusselt number.

This Nusselt number shows convective heat transfer rate between gas flow and the solid matrix in the pore scale.

$$\mathrm{Nu} = C\,\mathrm{Re}^m \tag{1}$$

The GRI 3.0 chemical reaction mechanism is used for the present computations. It consists of 325 elementary chemical reactions in which associated rate coefficient expressions and thermochemical parameters are involved for 53 species.

The governing equations at these two zones for a laminar, nonisothermal, steady flow of a chemically reacting mixture of Newtonian, perfect gases are as follows.

In momentum equation,

$$\frac{\rho_f}{\varepsilon}\langle(\nu\cdot\nabla)\nu\rangle = -\frac{\mu}{K}\langle\nu\rangle - \frac{\rho_f F\varepsilon}{\sqrt{K}}[\langle\nu\rangle\,.\,\langle\nu\rangle]J + \frac{\mu}{\varepsilon}\nabla^2\langle\nu\rangle - \nabla\langle P\rangle \tag{2}$$

where ρ_f and μ are density and viscosity of gas, respectively, and J is Darcy velocity unit vector. While the porosity of porous is shown by ε, K and F are permeability and geometric function, respectively, which are defined as follows:

$$K = \frac{\varepsilon^3 d_p^2}{150(1-\varepsilon)^2} \qquad F = \frac{1.75}{\sqrt{150\varepsilon^3}}$$

where d_p is mean pore diameter.

In gas flow energy equation,

$$\varepsilon\rho_f C_{P,f}\frac{\partial\langle T_f\rangle}{\partial t} + \left(\rho_f C_{P,f}\langle\nu\rangle - \varepsilon\sum_{k=1}^{K}\rho_f C_{P,k} D_{kN}\nabla\langle Y_k\rangle\right).\nabla\langle T_f\rangle$$

$$= \nabla\,.\,(k_{f,\mathrm{eff}}\nabla\langle T_f\rangle) + h_v(\langle T_s\rangle - \langle T_f\rangle) - \varepsilon\sum_{k=1}^{K} h_k\langle\dot{\omega}_k\rangle \tag{3}$$

where $C_{P,f}$, D_{kN}, $k_{f,\mathrm{eff}}$, h_v, h_k, and $\dot{\omega}_k$ are constant pressure heat capacity of the kth species, binary diffusion coefficient, mixture effective thermal conductivity, volumetric heat transfer coefficient, specific enthalpy of the kth species, and molar rate of production by chemical reaction of the kth species per unit volume, respectively.

The effective thermal conductivity is $k_{f,\mathrm{eff}}=\varepsilon k_f$ for mixture and $k_{s,\mathrm{eff}}=(1-\varepsilon)k_s$ in solid.

In solid matrix energy equation,

$$\nabla\,.\,(k_{s,\mathrm{eff}}\nabla\langle T_s\rangle) - h_v(\langle T_s\rangle - \langle T_f\rangle) - \nabla q_{\mathrm{rad}} = 0 \tag{4}$$

Here ∇q_{rad} is the gradient of thermal radiation from solid.

In species conservation,

$$\varepsilon\rho_f\frac{\partial\langle Y_k\rangle}{\partial t} + \nabla(\rho_f\langle\nu\rangle\langle Y_k\rangle) = \varepsilon\,\nabla\,(\rho_f D_{kN}\nabla\langle Y_k\rangle) + \varepsilon W_k\langle\omega_k\rangle \tag{5}$$

where W_k is the molecular weight of kth species.

In equation of state for gas mixture,

$$\rho_f = \frac{P\bar{W}}{RT_f} \tag{6}$$

where $\bar{W}$ and R are mean molecular weight of the mixture and universal gas constant respectively.

Boundary Conditions

The conditions specified at the inlet are temperature, species, and velocity of the unburned mixture. The boundary conditions for the gas flow energy are no diffusive flux of energy through the upstream and downstream boundaries. The boundary conditions for the solid temperature have written assuming that the solid loses heat convectively to the gas. As solid temperature boundary condition, it is assumed that the solid loses heat convectively to the gas. It is also assumed that solid matrix radiates to a blackbody at 298 K and also convective heat transfer exists between

Table 1 Materials' properties data of studied porous media [7]

	Preheating zone (upstream)	Combustion zone (downstream)
Porous media	PSZ with 26.5 pore/cm	PSZ with 3.9 pore/cm
Porosity, ε	0.835	0.87
Extinction coefficient, σ_e	17.07 cm^{-1}	3.76 cm^{-1}
Conductivity, k_s	0.2 W/m k	0.1 W/m k
Scattering albedo, ω	0.8	0.8
Coeff. of Eq. (1) C	0.638	0.146
Coeff. of Eq. (1) m	0.42	0.96
Radiation emissivity, ε_r	1.0	
Density, ρ	510 $\mathrm{kg/m}^3$	
Heat capacity, C_p	824 J/kg K	

the solid and the hot gases at burner outlet. At the downstream end of computational domain, gradients of velocity and mass fraction are zero.

Numerical Model

A SIMPLE algorithm is used in the numerical studies to simulate the steady state of incompressible flow. To solve chemical species systems of conservation equations together with the gas flow energy equation, the explicit Runge–Kutta–Chebyshev scheme of Verwer [14] was used. While the solid energy equation was solved through finite volume discretization, the thermal radiation was modeled using discrete ordinate method. The solution procedure is thus as follows:

1. At first step, one-dimensional conservation equations are solved in order to obtain approximate values of gas temperature and species concentrations. These values will be used as initial values in two-dimensional solutions, significantly reducing the computational costs.
2. Through the above-mentioned initial values, thermophysical properties are obtained and the flow field is calculated from the momentum equation.
3. To ascertain gas temperature profiles and species concentrations, transient solutions of energy and momentum equations are carried out.
4. Radiative heat transfer and energy conservation equations of the solid matrix are solved; new temperature profiles and species concentrations are obtained, and the thermophysical properties are updated.
5. The calculation procedure is repeated from step 2, until the required accuracy is obtained.

The calculations started on coarse grid of about 12–20 points in the flow direction and an adaptive procedure is used to refine grid points. Further, a regrid approach is adapted to complete the refinement procedure [15] due to the moving flame location in transient approach. The thermophysical properties are calculated using CHEMKIN subroutines [16].

In order to find the effects of pressure drop on characteristics of porous radiant burners, the temperature of one point computational domain is determined at porous radiant burner (PRB) centerline along burner axis. Consequently, the inlet velocity will be an eigenvalue and must be determined as part of the solution [17].

Results and Discussion

Comparison to Experimental Results. In order to study the pressure drop in porous radiant burners, the calculated pressure drop along porous burner has been compared with the reported experimental data, which is in reference to the findings of experimental investigation of Smucker and Ellzey [13]. A little modification (changing downstream partially stabilized zirconia (PSZ) with yttria-stabilized zirconia (YZA)) must be made in order to compare with the above-mentioned experimental data.

Wharton et al. [18] studied the exit flows for both reacting and nonreacting conditions, which were measured at different downstream distances and for various inlet conditions. They found that various factors contribute to the pressure drop such as pore diameter, pore structure, and porosity. The wide variation of the pressure drop indicates that there were significant variations from sample to sample. To overcome this inconsistency, mean pore diameter has been calculated numerically. With fixing porosity, effective mean pore diameter may minimize discrepancy between experimental and numerical pressure drops in nonreacting flow through porous media.

Figure 2 shows this comparison for cold flow and reacting flow of various mixture fractions. The present calculations have considered only flames that are stabilized at or just downstream of the interface. The good agreements of calculated results with experimental data have generally been obtained except in equivalence

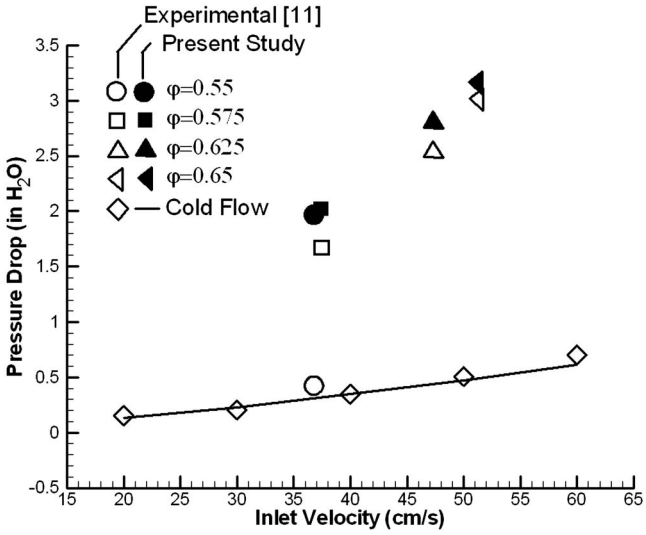

Fig. 2 Pressure drop across the burner for various equivalence ratios

ratio of 0.55. Pressure drop increases with the increasing flow speed and it is significantly higher for a reacting flow than for cold flow conditions. As the gas flows through the reaction zone, its density decreases and hence its velocity increases, resulting in greater frictional losses and larger pressure drop. Thus, it can be said that deviation of numerical and experimental results of pressure drop in equivalence ratio of 0.55 is due to the follows:

1. Decrease of peak temperature because of the radial heat loss, which has more effect at lower equivalence ratios.
2. Flame front movement in downstream zone toward the burner exit plane leading to the flow velocity increase at a small zone, which causes a decrement in the pressure drop.

Porous Radiant Burner Exit Temperature. As expected, with fixing temperature of one point at the burner axis ($T_f(x=0) = 1075$ K) for all mixture fractions, the exit temperature is nearly unchanged in both cases (i.e., neglecting or considering pressure drop along with the burner axis). Figure 3 shows gas and solid temperatures at the exit plane of the burner with the assumption of

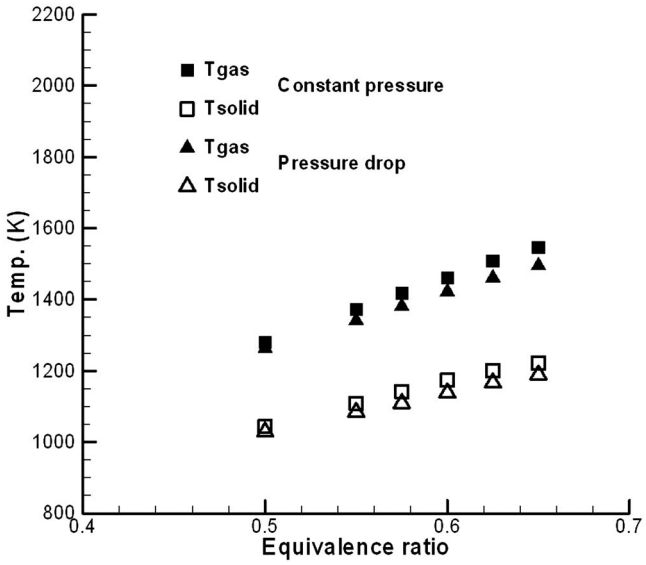

Fig. 3 Gas and solid temperature at exit of the burner

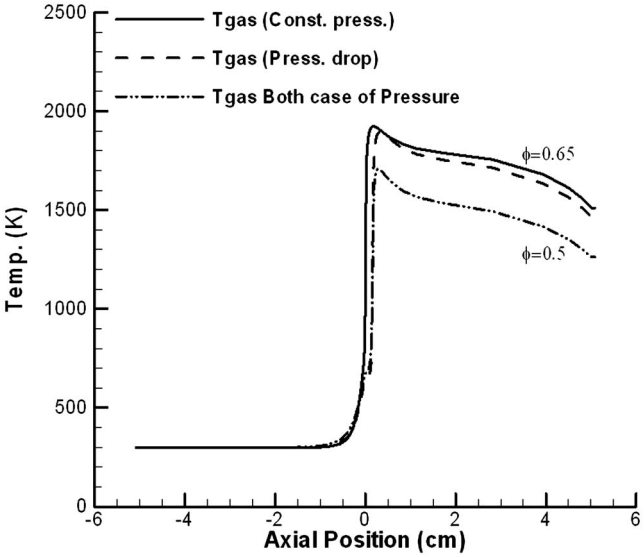

Fig. 4 Gas temperature profile along burner axis for two mixture fractions

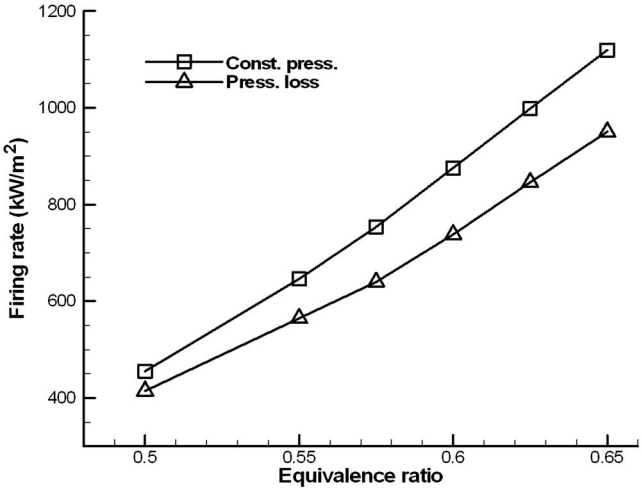

Fig. 5 Effect of pressure drop in burner firing rate

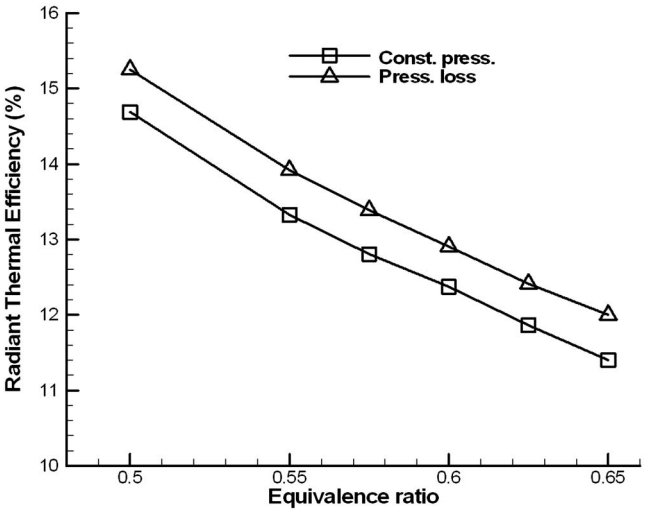

Fig. 6 Effect of pressure drop in burner's radiant thermal efficiency

combustion taking place at atmospheric pressure and real case of pressure drop. Further investigation reveals that in the case of pressure drop, flame front moves a little forward comparing fixing pressure at one atmospheric point (Fig. 4).

It is worthy to note that the difference between the solid and the gas temperatures depends only on the Nusselt number, which is related to the flow velocity (Eq. (1)). As shown in Fig. 4, there is not any difference between solid and gas temperatures in two cases studied here (i.e., the constant pressure and the pressure drop cases) for equivalence ratio about 0.5. As the equivalence ratio increases, a small temperature difference between the gas and the solid appeared. This is due to the change of the inlet gas flow velocity, which caused by considering the pressure drop.

Radiant Efficiency of the Burner. For each equivalent ratio, there is a specific flow rate for which a stable flame could be obtained at a fixed location. The total flow rate is a function of burner size and therefore, the results are presented as a function of flame speed that was defined as the result of dividing the volumetric flow rate by the burner's cross section area. The flow rate of the fuel characterizes the firing rate (power density) of the burner, which is defined as the thermal power input per unit surface area of the burner.

Another important operational characteristic of porous burners is the thermal radiation, which defines the maximum possible theoretical radiation output. Thus, it seems that porous burner radiates to a blackbody at 298 K.

The ratio of thermal radiation to firing rate has been defined as the radiant thermal efficiency. Figures 5 and 6 show variation in burner firing rate and radiant thermal efficiency with the equivalence ratio. As shown in Fig. 5, considering pressure drop due to fluid flow along porous material, the firing rate has been lowered. Also the gaps between two predictions increased in higher mixture fraction. The stated change of firing rates is from 9% at equivalence ratio of 0.5 to 18% at equivalence ratio of 0.65. The deviations of radiant thermal efficiency in the case of negligible pressure drop are 3–5% for lean combustion (Fig. 6).

Conclusion

In the present study, a two-section porous burner has been numerically analyzed, using complete chemical mechanism of methane/air combustion. The pressure drop was calculated for porous burner in the flow condition with and without reaction of stable burning in the central axis zone at the two porous material intersections for different equivalence ratios. Since the presence of combustion causes an increase in temperature and a decrease in gas density with the subsequent increase in flow velocity, the pressure drops for reacting flows are always higher than the corresponding cold flow values. Several equivalence ratios in lean combustion zone have been taken into consideration. With due attention to the constant temperature at a fixed point of flame axis, solution of momentum equation or the pressure drop have caused decrease in flow inlet and as a result decrease in burning strength. It was also found that the temperature at the burner exit surface with a fixed point temperature did not influence the pressure drop. With the increase of equivalence ratio, the firing rate increases too, but the radiant thermal efficiency decreases. If the pressure drop is ignored across the burner, the calculated radiant efficiency of burner will be less than the actual value. The deviations of radiant efficiency in the studied porous burner were 3%–5% for lean methane/air laminar premixed buried flames.

References

[1] Howell, J., Hall, M., and Ellzey, J. L., 1996, "Combustion of Hydrocarbon Fuel Within Porous Inert Media," Prog. Energy Combust. Sci., **22**, pp. 121–145.

[2] Viskanta, R., and Gore, J. P., 2000, "Overview of Cellular Ceramic Based

Porous Radiant Burners for Supporting Combustion," Int. J. Environ. Technol., **1**, pp. 167–203.
[3] Yoshizawa, Y., Echigo, R., and Sasaki, K., 1988, "Analytical Study on the Structure of Radiation Controlled Flame," Int. J. Heat Mass Transfer, **31**, pp. 311–319.
[4] Min, D. K., and Shin, H. D., 1991, "Laminar Premixed Flame Stabilized Inside a Honeycomb Ceramic," Int. J. Heat Mass Transfer, **34**, pp. 341–355.
[5] Zhou, X. Y., and Pereira, J. C., 1997, "Numerical Study of Combustion and Pollutants Formation in Inert Non-Homogeneous Porous Media," Combust. Sci. Technol., **130**, pp. 335–364.
[6] Hsu, P. F., Howell, J. R., and Matthews, R. D., 1993, "A Numerical Investigation of Premixed Combustion Within Porous Inert Media," ASME J. Heat Transfer, **115**, pp. 744–750.
[7] Barra, A. J., Diepvens, G., Ellzey, J. L., and Henneke, M. R., 2003, "Numerical Study of the Effect of Material Properties on Flame Stabilization in a Porous Burner," Combust. Flame, **134**, pp. 369–379.
[8] Kamal, M. M., and Mohamad, A. A., 2006, "Combustion in Porous Media," Proc. Inst. Mech. Eng., Part A, **220**(A5), 487–508.
[9] Mohamad, A. A., Viskanta, R., and Ramadhyani, S., 1994, "Numerical Predictions of Combustion and Heat Transfer in a Packed Bed with Embedded Coolant Tubes," Combust. Sci. Technol., **96**, pp. 387–407.
[10] Brenner, G., Pickenacker, K., Pickenacker, O., Trimis, D., Wawrzinek, K., and Weber, T., 2000, "Numerical and Experimental Investigation of Matrix-Stabilized Methane/Air Combustion in Porous Inert Media," Combust. Flame, **123**, pp. 201–213.
[11] Malico, I., and Pereira, J. C. F., 2001, "Numerical Study on the Influence of Radiative Properties in Porous Media Combustion," ASME J. Heat Transfer, **123**, pp. 951–957.
[12] Mishra, S. C., Steven, M., Nemoda, S., Talukdar, P., Trimis, D., and Durst, F., 2006, "Heat Transfer Analysis of a Two-Dimensional Rectangular Porous Radiant Burner," Int. Commun. Heat Mass Transfer, **33**, pp. 467–474.
[13] Smucker, M. T., and Ellzey, J. L., 2004, "Computational and Experimental Study of a Two Section Porous Burner," Combust. Sci. Technol., **176**, pp. 1171–1189.
[14] Verwer, J. G., 1996, "Explicit Runge–Kutta Methods for Parabolic Partial Differential Equations," Appl. Numer. Math., **22**, pp. 359–379.
[15] Kee, R. K., Grcar, J. F., Smooke, M. D., and Miller, J. A., 1985, "A. Fortran Program for Modeling Steady Laminar One-Dimensional Premixed Flames," Sandia National Laboratories Report No. SAND85-8240.
[16] Kee, R. K., Rupley, F. M., and Miller, J. A., 1993, "CHEMKIN II., A. Fortran Chemical Kinetics Package for the Analysis of Gas-Phase Chemical Kinetics," Sandia Laboratories Report No. SAND 89-8009B.
[17] Smooke, M. D., Miller, J. A., and Kee, R. K., 1983, "Determination of Adiabatic Flame Speeds by Boundary Value Methods," Combust. Sci. Technol., **34**, pp. 79–90.
[18] Wharton, J. A., Ellzey, J. L., and Bogard, D. G., 2005, "An Experimental Study of Turbulence Intensities and Non-Uniformities in the Exit Flow from a Porous Combustor," Exp. Fluids, **38**, pp. 701–707.

Tomography-Based Determination of the Effective Thermal Conductivity of Fluid-Saturated Reticulate Porous Ceramics

Jörg Petrasch

Birte Schrader

Department of Mechanical and Process Engineering, ETH Zurich, 8092 Zurich, Switzerland

Peter Wyss

Laboratory for Electronics/Metrology, EMPA Material Science and Technology, 8600 Dübendorf, Switzerland

Aldo Steinfeld

Department of Mechanical and Process Engineering, ETH Zurich, 8092 Zurich, Switzerland and Solar Technology Laboratory, Paul Scherrer Institute, 5232 Villigen, Switzerland
e-mail: aldo.steinfeld@eth.ch

The effective thermal conductivity of reticulate porous ceramics (RPCs) is determined based on the 3D digital representation of their pore-level geometry obtained by high-resolution multiscale computer tomography. Separation of scales is identified by tomographic scans at 30 μm digital resolution for the macroscopic reticulate structure and at 1 μm digital resolution for the microscopic strut structure. Finite volume discretization and successive over-relaxation on increasingly refined grids are applied to solve numerically the pore-scale conduction heat transfer for several subsets of the tomographic data with a ratio of fluid-to-solid thermal conductivity ranging from 10^{-4} to 1. The effective thermal conductivities of the macroscopic reticulate structure and of the microscopic strut structure are then numerically calculated and compared with effective conductivity model predictions with optimized parameters. For the macroscale reticulate structure, the models by Dul'nev, Miller, Bhattachary and Boomsma and Poulikakos, yield satisfactory agreement. For the microscale strut structure, the classical porosity-based correlations such as Maxwell's upper bound and Loeb's models are suitable. Macroscopic and microscopic effective thermal conductivities are superimposed to yield the overall effective thermal conductivity of the composite RPC material. Results are limited to pure conduction and stagnant fluids or to situations where the solid phase dominates conduction heat transfer. [DOI: 10.1115/1.2804932]

Keywords: reticulate porous ceramics, effective thermal conductivity, computer tomography, pore-scale, multiscale, conduction heat transfer

1 Introduction

RPCs [1] are employed as exhaust gas filters [2], as catalyst carriers for autothermal reformers [3], as porous radiant burners [4–6], and more recently as radiant absorbers in high-temperature solar thermal [7] and solar thermochemical [8] processes. RPCs made of SiC foams and coated with Rh catalyst are currently being employed for the solar steam reforming of hydrocarbons at above 1100 K in the framework of the EU project SOLREF [9]. A sample of this RPC, developed at the DLR German Space Agency, is used in the present study.

The analysis of heat and mass transport phenomena in RPCs requires the application of volume-averaging models, where the solid and fluid phases are treated as interpenetrating continua [10,11]. The accuracy of these models relies heavily on the determination of effective transport parameters, such as the effective thermal conductivity k_e. In particular, the accurate determination of k_e is of importance for RPCs since many of their applications are based on temperature distributions resulting from heat conduction in the solid matrix. In general, k_e depends on the ratio of the thermal conductivities of the solid and fluid phases, the spatial distribution of the phases, the contact resistance between nonconsolidated particles, and the mean free molecular path in the fluid phase [10].

Determination of the effective transport parameters is accomplished either experimentally [12–17] or analytically by assuming simplified geometries [18–24] and/or calculating statistical properties [25]. The former approach is expensive and time consuming, and the validity of the results is usually limited to the experimental conditions. The latter approach is limited by the validity of the underlying assumptions for the complex geometry. Some of these limitations can be overcome by the combined experimental-numerical technique presented herein.

In the present paper, computer tomography (CT) is used to obtain the 3D digital representation of the RPC geometry, which is then combined with pore-scale numerical analysis of conductive heat transfer to determine its effective thermal conductivity. CT-based Monte Carlo analysis of radiative heat transfer has been previously applied in the determination of the RPC's effective radiative properties, namely, the extinction coefficient and the scattering phase function [26–28]. Direct pore-level numerical simulation of conduction heat transfer in sedimentary rock based on tomographic data has been used for model validation purposes [29,30]. Direct pore-level simulation has also been used for analyzing open-cell metal foams based on idealized unit cells [31].

In this study, CT is performed for two relevant length scales: (1) macroscopic pores with typical diameters of 2.5 mm are resolved in scans using a MicroCT 80 scanner of Scanco Medical at 30 μm digital resolution [32] and (2) microscopic pores and cracks inside the strut material are resolved using a Phoenix X-ray CT at 1 μm digital resolution [33]. Pore-scale numerical simulation of conduction heat transfer is then carried out for representative samples to determine the macroscale effective thermal conductivity of the macroscopic reticulate structure $k_{e,\mathrm{macro}}$ as a

Contributed by the Heat Transfer Division of ASME for publication in the JOURNAL OF HEAT TRANSFER. Manuscript received August 30, 2006; final manuscript received May 31, 2007; published online March 6, 2008. Review conducted by Jamal Seyed-Yagoobi.

Table 1 RPC samples used in this work

Specimen	Description	Digital resolution (μm)	Number of slices	Image size (pixel)
A	Low ε, 10 pores/in.	30	1198	1800×1800
B	High ε 10 pores/in.	30	1168	1600×1600
C	Single strut	1	500	920×756

function of the fluid thermal conductivity $k_{f,\text{macro}}$, and the microscale effective thermal conductivity of the microscopic strut material $k_{e,\text{macro}}$ as a function of the fluid phase thermal conductivity $k_{e,\text{macro}}$ and the solid phase conductivity k_s. Results are limited to pure conduction and stagnant fluids. Various geometrical and statistical models on the effective thermal conductivity, generally applicable to porous media or especially developed for reticulate structures, are applied to the macroscopic reticulate structure and their model parameters are optimized by comparison to the results from the macroscale direct numerical simulation. Classical models for lower porosity materials are applied to the microscopic strut structure in an analogous manner.

2 Experiment

Macroscale Computer Tomography. A low-porosity (average porosity of 81%) 10 pores/in. Rh-catalyst coated SiC-made RPC sample (Specimen A) and a high-porosity (average porosity of 90%) 10 pores/in. Rh-catalyst coated SiC-made RPC sample (Specimen B) are scanned using a MicroCT 80 scanner of Scanco Medical at 30 μm digital resolution [32]. Details of the scans are compiled in Table 1.

Figure 1 shows a photograph of Specimen A of 50 mm diameter and 35 mm height. Figure 2 shows a cross-sectional CT reconstruction of Specimen A, with a pixel size of 30×30 μm^2. In this figure, the macroscopic structure and the central channels of the struts are well resolved, but the microscopic pore structure of the struts is not visible. Thus, length-scale separation is identified. Figure 3 shows a rendered digital reconstruction of Specimen A based on the CT data set. The solid-fluid segmentation gray value is determined by the mode method [34].

Microscale Computer Tomography. A 1 μm digital resolution tomographic scan of a single strut sample (Specimen C) was performed by Phoenix X-ray [33]. Figure 4 shows a photograph of the strut sample, which has been cut from a larger RPC sample. Figure 5 shows a cross-sectional CT reconstruction of Specimen C, with a pixel size of 1×1 μm^2. The central triangular channel, the catalyst coating, and the microscale pores that result from incomplete sintering are resolved in great detail. The central triangular channels originate from the polyurethane (PU) foam skeleton that serves as a core structure for the RPC during manufacturing. The PU skeleton decomposes during the sintering process. The geometry of the channels depends on the PU foam geometry; it is, however, independent of the RPC porosity. Figure 6 shows a rendered 3D digital reconstruction of Specimen C, based on the microscale CT data set.

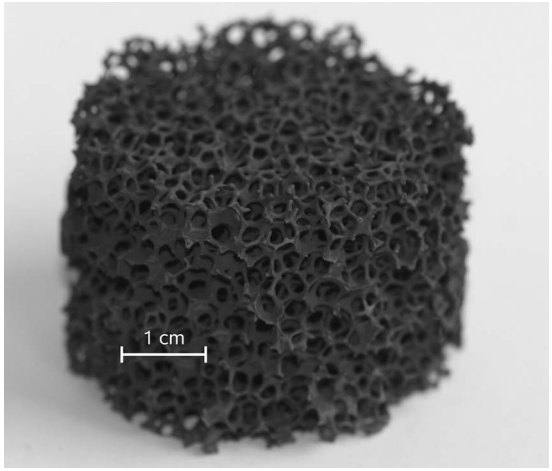

Fig. 1 Photograph of Specimen A: a low-porosity (average porosity of 81%) cylindrical 10 pores/in. Rh-catalyst coated SiC-made RPC sample

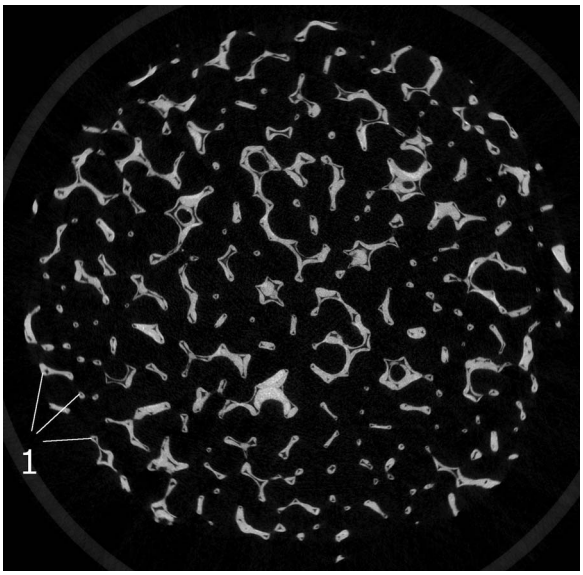

Fig. 2 CT reconstruction of a cross section of the RPC's Specimen A. Some central channels are indicated by 1.

3 Modeling

Governing Equations. The steady-state heat conduction equations within the solid and the stagnant fluid phase of a porous medium are

$$\nabla\cdot[k_s\nabla T_s]=0$$

$$\nabla\cdot[k_f\nabla T_f]=0 \tag{1}$$

The boundary conditions at the solid-fluid interface are given by

$$T_s=T_f$$

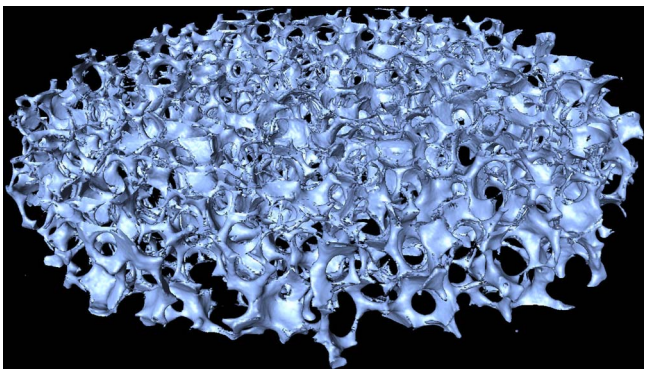

Fig. 3 3D digital reconstruction of a slice of the RPC's Specimen A, based on the macroscale CT data set and the isosurface at the segmentation gray value

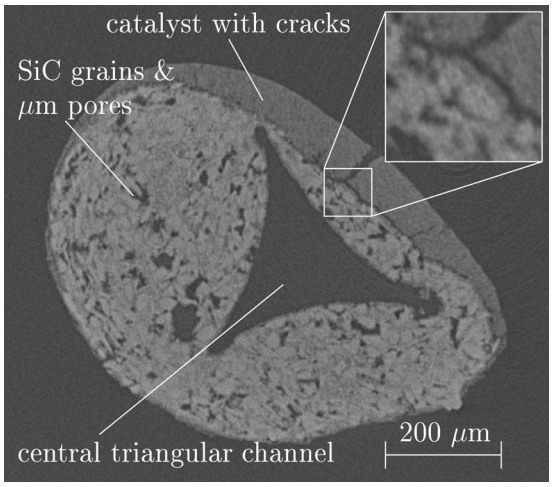

Fig. 5 CT cross-sectional reconstruction of the strut Specimen C

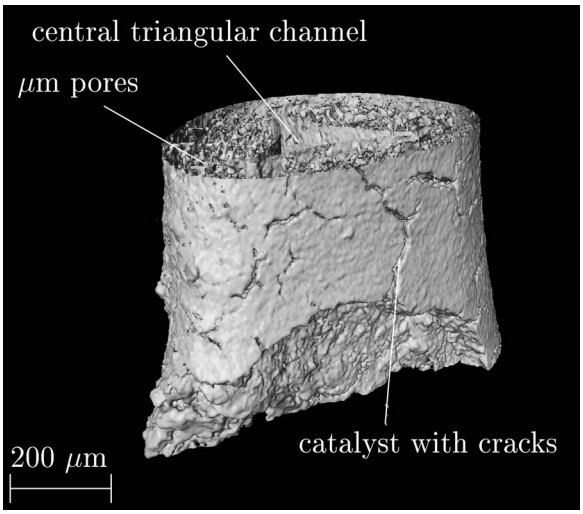

Fig. 6 3D digital reconstruction of the strut Specimen C, based on the microscale CT data set and the isosurface at the segmentation gray value

$$\mathbf{n} \cdot k_s \nabla T_s = \mathbf{n} \cdot k_f \nabla T_f \tag{2}$$

Equations (1) and (2) can be solved numerically at the pore level on the 3D digital representation obtained from the macroscale and microscale CT scans.

For relatively large pieces of porous media consisting of millions of individual pores, i.e., for a system-scale analysis, volume-averaging models have been developed. The volume-averaged one-equation model is applicable when the physical properties of the two phases are close enough [35] or when the thermal conductivities of the two phases differ by order of magnitude such that one phase dominates the heat transfer in the two-phase system [36]. The latter case is usually valid for fluid-saturated RPCs. The one-equation model for steady-state isotropic conduction reduces to [10,37]

$$\nabla \cdot [k_e \nabla \langle T \rangle] = 0 \tag{3}$$

Identification Methodology. For a 1D case with temperature boundary conditions, the solution of Eq. (3) yields a linear temperature profile. The heat flow per unit area is then given as

$$\langle q'' \rangle = k_e \nabla \langle T \rangle = k_e \frac{T_1 - T_2}{L} \tag{4}$$

However, at the pore level, asymmetric 3D temperature profiles result from solving locally Eqs. (1) and (2) as a result of the complex structure of the porous matrix. A quasi-1D situation is simulated by selecting representative cubic samples of the RPC with temperature boundary conditions T_1 and T_2 on two of the opposing faces of the cube and adiabatic conditions on the remaining four faces of the cube, as depicted in Fig. 7. Thus, the heat flux across the cube at any given cross-sectional plane perpendicular to the main heat flow direction is given by

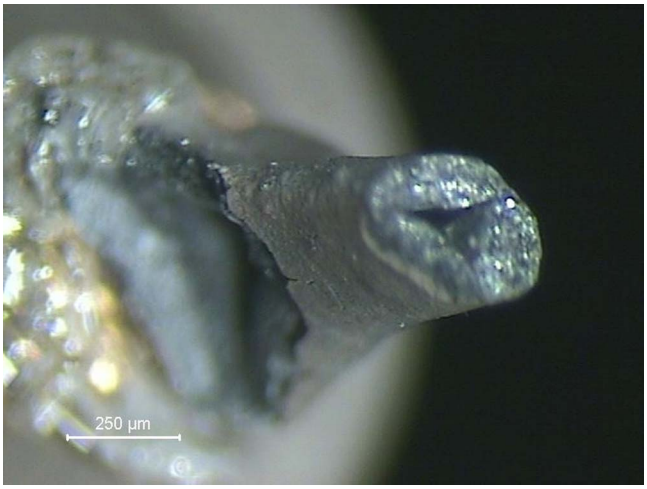

Fig. 4 Photograph of Specimen C: a single strut sample of the Rh-catalyst coated SiC-made RPC sample, showing the triangular cross-sectional geometry of the central channel

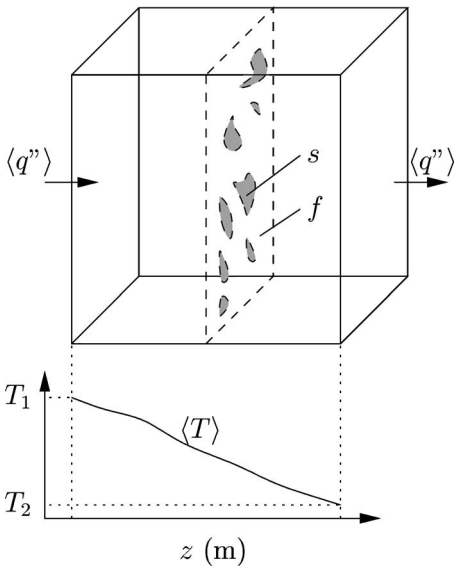

Fig. 7 Schematic of steady-state conduction heat transfer through a two-phase cubic sample of RPC, with temperature boundary conditions T_1 and T_2 on two of the opposing faces of the cube and adiabatic conditions on the remaining four faces of the cube

$$\langle q'' \rangle = \frac{-\int_{A_s} k_s \nabla T_s \cdot \mathbf{n} dA_s - \int_{A_f} k_f \nabla T_f \cdot \mathbf{n} dA_f}{A_s + A_f} \quad (5)$$

If the local temperature profiles T_f and T_s are known, as it is the case for the pore-level numerical simulation, one obtains the effective thermal conductivity as

$$k_e = L \frac{-\int_{A_s} k_s \nabla T_s \cdot \mathbf{n} dA_s - \int_{A_f} k_f \nabla T_f \cdot \mathbf{n} dA_f}{(T_1 - T_2)(A_s + A_f)} \quad (6)$$

In the current approach, Eq. (6) is applied without further simplifications. The method used relies on the full local temperature fields as computed from direct pore-level numerical simulation. The temperature profiles are 3D locally, while the averaged temperature profile is 1D due to the boundary conditions (see Fig. 7).

Numerical Method. The CT data obtained from the measurements consist of a set of 1 byte (0–255) optical density values of $\Psi_{i,j,k}$ at each voxel, arranged on a 3D uniform Cartesian grid. In order to eliminate boundary effects, a $9 \times 18 \times 27$ mm^3 central subvolume equivalent to $300 \times 600 \times 900$ voxels is extracted from the normal resolution scan. The methodology to create a continuous gray-value function $\Psi(x,y,z)$ from these data has been described previously in detail [26]. For two-phase materials, the histogram of $\Psi_{i,j,k}$ exhibits two maxima. The gray value Ψ_0 for the solid-fluid interface is the minimum between these two maxima [34]. The computational domain is defined as a cubic sample and is subdivided into uniformly spaced cubic finite volumes. The cubic finite volume P is classified as solid phase if $\Psi(x_P, y_P, z_P) > \Psi_0$, where (x_P, y_P, z_P) is the location of the center of the finite volume. Otherwise, it is classified as fluid phase. The finite volume (FV) technique is employed for the discretization of the heat conduction equation on the individual FVs:

$$a_P T_P = a_B T_B + a_T T_T + a_S T_S + a_N T_N + a_E T_E + a_W T_W \quad (7)$$

$$a_B = k_b h \quad a_T = k_t h, \quad \ldots \quad (8)$$

$$a_P = a_B + a_T + a_S + a_N + a_E + a_W \quad (9)$$

Heat flux between volume elements is formulated based on the harmonic mean between the associated conductivities [38],

$$k_b = \frac{2k_P k_B}{k_P + k_B} \quad k_t = \frac{2k_P k_T}{k_P + k_T} \quad \ldots \quad (10)$$

If an element is surrounded by elements of the same phase, e.g., $k_P = k_B$, the truncation error of the method is of order h^2 (h being the grid size spacing). If a neighbor element is in a different phase, the truncation error is of order h.

The microscale pore-level simulation assumes constant material properties of each phase because their local variation can be neglected. The resulting system of linear equations is solved using successive over-relaxation (SOR) on increasingly refined grids [39]. Firstly, a solution is found on a coarse grid that only roughly resolves the geometrical structure of the porous medium. Then, the converged solution is used as the initial guess for solving on a finer grid by interpolation. Finally, this procedure is done repeatedly until a sufficiently fine grid is reached. The accuracy of the numerical code is determined by solving three idealized geometries with known exact analytical solutions: serial slabs ($\varepsilon = 0.68$), parallel slabs ($\varepsilon = 0.68$), and a small immersed sphere ($\varepsilon = 0.90$). For the ratio of fluid-to-solid conductivity $\nu = 0.001$, the maximum deviation from the analytical result is 0.54% (immersed sphere, $126 \times 126 \times 126$ grid points).

Effective Thermal Conductivity Models. Effective conductivity models have been developed to predict k_e as a function of porosity ε, solid and fluid thermal conductivities k_f and k_s, and geometrical parameters. These k_e models and their corresponding references are listed in Tables 2–4 and grouped according to the following: (1) applied to the macroscopic reticulate structure of Figs. 1–3 with satisfactory fitting, (2) applied to the macroscopic reticulate structure of Figs. 1–3 with unsatisfactory fitting, and (3) applied to the microscopic strut structure of Figs. 4–6. The criterion for satisfactory fitting is arbitrarily chosen such that the root mean square of the difference between the results obtained by direct numerical simulation and those obtained by applying a k_e model is less than 12%.

4 Results

Effective Thermal Conductivity of the Macroscopic Reticulate Structure. A grid convergence study is firstly performed by solving Eqs. (1) and (2) in a small subset of the 3D geometry: volume = 1.5 mm^3 (or $50 \times 50 \times 50$ voxels), $k_{f,\text{macro}}/k_{e,s} = 10^{-2}$, and $h = 75$ to 4.688 μm. The grid convergence index (GCI) is then defined as [40]

$$\text{GCI} = F \left| \frac{k_{e,h} - k_{e,2h}}{k_{e,h}} \right| \Big/ (2^p - 1) \quad (11)$$

where $k_{e,h}$ and $k_{e,2h}$ are the effective thermal conductivities calculated with grid spacings h and $2h$, respectively, p is the convergence order of the numerical method, and F is a safety factor of 1.25. A first order accuracy is found in this numerical test as a result of the strong influence of the solid-fluid boundary. Based on these calculations, $h = 18$ μm (GCI = 3%) is chosen as the grid spacing for further parametric computations. The maximum grid size that can be processed on the available computer hardware is $501 \times 501 \times 501$, which leads to a sample size of $9 \times 9 \times 9$ mm^3. This is close to the size of the representative elementary volume (REV) for continuum in the RPC sample, as calculated previously [26]. Six nonoverlapping $9 \times 9 \times 9$ mm^3 samples are extracted from the macroscale CT data set obtained for each of Specimens A and B. The porosity varies between 0.86 and 0.94 for Specimen A and between 0.8 and 0.82 for Specimen B.

An example of the temperature distribution obtained from pore-level direct numerical simulation of conduction heat transfer on a subset of Specimen A is shown in Fig. 8. Isothermal contour lines of the normalized temperature distribution $(T - T_2)/(T_1 - T_2)$ in a cross-sectional plane were calculated for $T = T_1$ at the bottom ($z = 0$ mm) and $T = T_2$ at the top ($z = 9$ mm). The solid areas are depicted in black.

Figure 9 shows the ratio of the macroscale effective thermal conductivity for the macroscopic reticulate structure ($k_{e,\text{macro}}$) to the microscale effective thermal conductivity for the microscopic strut structure ($k_{e,\text{micro}}$) as a function of the ratio of the fluid-to-strut thermal conductivities ($k_{f,\text{macro}}/k_{e,\text{micro}}$), obtained by the macroscale numerical simulation of 12 nonoverlapping subsamples of Specimens A and B with varying porosity. The fluid-to-strut thermal conductivity ratio ($k_{f,\text{macro}}/k_{e,\text{micro}}$) considered is in the range 10^{-4}–1. Our method is also applicable for $k_{f,\text{macro}}/k_{e,\text{micro}} > 1$, but this range is omitted from consideration because gas conductivities are significantly smaller than solid conductivities in the current application. The 12 data sets are grouped into four groups of similar porosity. Obviously, $k_{e,\text{macro}}/k_{e,\text{micro}}$ equals 1 when $k_{f,\text{macro}} = k_{e,\text{micro}}$. As expected, $k_{e,\text{macro}}$ decreases and converges to constant values as $k_{f,\text{macro}}/k_{e,\text{micro}}$ decreases since the fluid phase does not significantly contribute to the heat transfer for low fluid thermal conductivities. For $k_{f,\text{macro}}/k_{e,\text{micro}} < 1$, $k_{e,\text{macro}}$ decreases as the porosity ε increases because of the reduced contribution to the heat transfer by the solid phase; this effect is more pronounced for small $k_{f,\text{macro}}/k_{e,\text{micro}}$. The mean GCI for the samples with minimum and maximum porosities are 7.65% and 2.89%, respectively. The mean GCI of all data points is 4.95%; the maximum GCI is 18.6% for the sample with porosity of

Table 2 Effective thermal conductivity models applied to the macroscopic reticulate structure of Figs. 1–3 with satisfactory fitting. $\mu = k_{e,\mathrm{macro}}/k_{e,\mathrm{micro}}$, $\nu = k_{f,\mathrm{macro}}/k_{e,\mathrm{micro}}$

Model	Analytical expression	Optimum parameters	rms error (%)
Parallel slabs	$\mu = \varepsilon\nu + (1-\varepsilon)$	N/A	119
Serial slabs	$\mu = \left(\frac{\varepsilon}{\nu} + 1 - \varepsilon\right)^{-1}$	N/A	73.9
Dul'nev, 1969, Refs. [20,21]	$a=-1$, $\varphi = \arccos(1-2\varepsilon)$ for $0 \leqslant \varepsilon \leqslant 0.5$ $a=1$, $\varphi = \arccos(2\varepsilon-1)$ for $0.5 \leqslant \varepsilon \leqslant 1$ 270 deg $\leqslant \varphi \leqslant$ 360 deg $c = 0.5 + a\cos\left(\frac{\varphi}{3}\right)$ $\mu = c^2 + \nu(1-c)^2 + \frac{2\nu(1-c)}{\nu c + 1 - c}$	N/A	8.46
Three-resistor model	$\mu = f(\varepsilon\nu + (1-\varepsilon)) + (1-f)\left(\frac{\varepsilon}{\nu} + 1 - \varepsilon\right)^{-1}$	$f=0.3823$	11.2
Calmidi and Mahajan, 1999, analytical, Ref. [22]	$\chi = \frac{b}{L} = \frac{-r + \sqrt{r^2 + \frac{2}{\sqrt{3}}(1-\varepsilon)(2 - r(1+\frac{4}{\sqrt{3}}))}}{\frac{2}{3}(2 - r(1+\frac{4}{\sqrt{3}}))}$ $\mu = \frac{\sqrt{3}}{2}\left(\frac{r\chi}{\nu + (1+\chi)\frac{1-\nu}{3}} + \frac{(1-r)\chi}{\nu + \frac{2}{3}\chi(1-\nu)} + \frac{\frac{2}{\sqrt{3}} - \chi}{\nu + \frac{4}{3\sqrt{3}}r\chi(1-\nu)}\right)^{-1}$	$r=0.1022$	11.9
Bhattacharya et al., 1999, Ref. [23]	$\xi = \frac{l}{L} = \frac{-\sqrt{3} - 2r + \sqrt{(\sqrt{3}+2r)^2 + 6\sqrt{3}(2\sqrt{3}r^2 - 4r + \sqrt{3})(1-\varepsilon)}}{2(2\sqrt{3}r^2 - 4r + \sqrt{3})}$ $\chi = \frac{t}{L} = 2r\xi$ $\mu_{\mathrm{I}} = \nu + (1-\nu)(\frac{1}{3} + \frac{2}{3}\xi - \frac{1}{6\sqrt{3}}\chi)$ $\mu_{\mathrm{II}} = \nu + \frac{1}{3}(1-\nu)(1-\xi)$ $\mu_{\mathrm{III}} = \nu + (1-\nu)(\frac{2}{3}\xi - \frac{2}{3\sqrt{3}}\chi)$ $\mu_{\mathrm{IV}} = \nu + \frac{4}{3\sqrt{3}}(1-\nu)\chi$ $\mu = \left(\frac{2\chi}{\sqrt{3}\mu_{\mathrm{I}}} + \frac{2(\sqrt{3}\xi - 2\chi)}{\sqrt{3}\mu_{\mathrm{II}}} + \frac{2\chi}{\sqrt{3}\mu_{\mathrm{III}}} + \frac{1-2\xi}{\mu_{\mathrm{IV}}}\right)^{-1}$	$r=0.1541$	4.11
Boomsma and Poulikakos,2001, Ref. [24]	$d = \sqrt{\frac{\sqrt{2}(2 - \frac{5\sqrt{2}}{8}e^3 - 2\varepsilon)}{\pi(3 - 4\sqrt{2}e - e)}}$ $R_A = \frac{4d}{(2e^2 + \pi d(1-e))(1-\nu) + 4\nu}$ $R_B = \frac{(e-2d)^2}{e^2(e-2d)(1-\nu) + (2e-4d)\nu}$ $R_C = \frac{(\sqrt{2}-2e)^2}{2\pi d^2(1-2e\sqrt{2})(1-\nu) + (2\sqrt{2}-4e)\nu}$ $R_D = \frac{2e}{e^2(1-\nu) + 4\nu}$ $\mu = \frac{\sqrt{2}}{2(R_A + R_B + R_C + R_D)}$	$e=0.3311$	7.37
Calmidi and Mahajan, 1999, empirical, Ref. [22]	$\mu = \varepsilon\nu + A(1-\varepsilon)^n$	$A=0.7662$ $n=1.3168$	9.5
Miller, 1969 upper bound, Ref. [25]	$\mu = \nu\left(1 + (1-\varepsilon)\left(\frac{1}{\nu} - 1\right) - \left(\frac{\frac{1}{3}\varepsilon(\varepsilon-1)(\frac{1}{\nu}-1)^2}{1 + (\frac{1}{\nu}-1)((1-\varepsilon) + 3(\varepsilon^2 G_1 - (1-\varepsilon)^2 G_2))}\right)\right)$	$G_1=0.1508$ $G_2=0.1111$	3.6

Table 3 Effective thermal conductivity models applied to the macroscopic reticulate structure of Figs. 1–3 with unsatisfactory fitting

Model	Optimum parameters	rms (%)
Schuhmeister, 1877 Ref. [51]	N/A	14.6
Hsu et al., 1994, Ref. [41]	N/A	28.4
Bruggemann, 1935, Ref. [42]	N/A	48.3 (slices), 70.2 (spherical)
Loeb, 1954, Ref. [43]	N/A	58.1
Ribaud, 1937, Ref. [44]	N/A	58.7
Eucken, 1932, Ref. [45]	N/A	60.7
Odelevskii, 1951, Ref. [46]	N/A	60.7
Russell, 1935, Ref. [19]	N/A	63.9
Fraction weighted geometric mean, Ref. [47]	N/A	69.1
Pawel et al., 1988, Ref. [48]	$A=0.38232$	11.2
Bhattacharya et al., empirical, 1999, Ref. [23]	$A=0.16215$	14.6

93.64% at $k_{f,\text{macro}}/k_{e,\text{micro}}=10^{-4}$.

The k_e models listed in Tables 2–4 are applied to Specimens A and B and their optimal parameters are determined by least-squares fitting. Figure 10 shows $k_{e,\text{macro}}/k_{e,s}$ versus $k_{f,\text{macro}}/k_{e,s}$, obtained by the macroscale direct numerical simulation and by selected k_e models. The root mean square of the difference between the results is reported as "rms" for each model considered.

Figure 10(*a*) contains the prediction of four classical k_e models. The serial-slab and parallel-slab models provide the lower and upper bounds, respectively, for any two-phase material. The three-resistor model combines the serial-slab and parallel-slab models with a single parameter f, fraction of the serial contribution, whose optimum value is 0.3823 with rms=11.2%. The three-resistor model is identical with the empirical model proposed by Bhattacharya et al. [49]. Dul'nev's model, which is based on a simple unit cell with interpenetrating phases, is dependent on ε only, with rms=8.46%.

Figure 10(*b*) contains the optimum prediction of three k_e models developed for reticulate foam structures. It includes Calmidi and Mahajan's model for 2D unit cells representing a hexagonal strut geometry with square intersection nodes, the model of Bhattacharya et al. model for 2D unit cells representing a hexagonal strut geometry with hexagonal intersection nodes, and Boomsma and Poulikakos's model for 3D unit cells representing a tetrakaidecahedron geometry with cubic intersection nodes. For Calmidi and Mahajan's model, the optimum parameter r, node thickness to strut thickness, equals 0.1022, with rms=11.9%. For the model of Bhattacharya et al., the optimum parameter r, node thickness to strut thickness, equals 0.1541, with rms=4.11%. For Boomsma and Poulikakos's model, the optimum parameter e, node thickness to strut length, equals 0.3311, with rms=7.37%. The model of Bhattacharya et al. best reproduces the strong porosity dependence at low $k_{f,\text{macro}}/k_{e,\text{micro}}$.

Figure 10(*c*) contains the results of two two-parameter k_e models. For Miller's upper bound model, the best fit is obtained for $G_1=0.1508$ and $G_2=1/9$, which indicates needle shaped solids and spherical voids, respectively, with rms=3.6%. For Calmidi and Mahajan's empirical model, the optimum parameters are $A=0.7662$ and $n=1.3168$, with rms=9.5%. Miller's upper bound is a general statistical bound for two-phase media. Calmidi and Mahajan's empirical model has been successfully applied to experimental data for reticulated structures [22]

Additional k_e models have been screened (see Tables 2–4) but failed to reproduce $k_{e,\text{macro}}$ satisfactorily, giving rms$>$12%. Models for packed beds [10] usually do not agree well when applied to RPCs because of their high porosity and the high degree of solid connectivity of reticulate and foam structures.

All results presented in this section were calculated based on 10 pores/in. foams. They are equally valid for geometrically similar, scaled materials of the same porosity, provided the continuum assumption is satisfied. It has been shown that k_e is independent of pore size for high porosities [50].

Effective Thermal Conductivity of the Microscopic Strut Structure. Assuming an operation temperature of 1100 K, a gas pressure inside the pores of 1 bar, a pore diameter of $d_{\text{micro}}=5$

Table 4 Effective conductivity models applied to the microscopic strut structure of Figs. 4–6. $\mu=k_{e,\text{micro}}/k_s$, $\nu=k_{f,\text{micro}}/k_s$.

Model	Analytical expression	Optimum parameters	rms error (%)
Parallel slabs	See Table 3	N/A	9.71
Serial slabs	See Table 3	N/A	78.0
Maxwell upper bound	$\mu=\dfrac{2+\nu-2\varepsilon(1-\nu)}{2+\nu+\varepsilon(1-\nu)}$	N/A	4.34
Loeb, 1954, Ref. [43]	$\mu=\dfrac{\varepsilon^{1/3}-\varepsilon+\nu(1-\varepsilon^{1/3}+\varepsilon)}{\varepsilon^{1/3}+\nu(1-\varepsilon^{1/3})}$	N/A	3.48
Russell, 1935, Ref. [19]	$\mu=\dfrac{\nu\varepsilon^{2/3}+1-\varepsilon^{2/3}}{\nu(\varepsilon^{2/3}-\varepsilon)+1-\varepsilon^{2/3}+\varepsilon}$	N/A	7.87
Miller, 1969, Ref. [25]	See Table 3	$G_1=0.1287$ $G_2=0.2157$	0.184

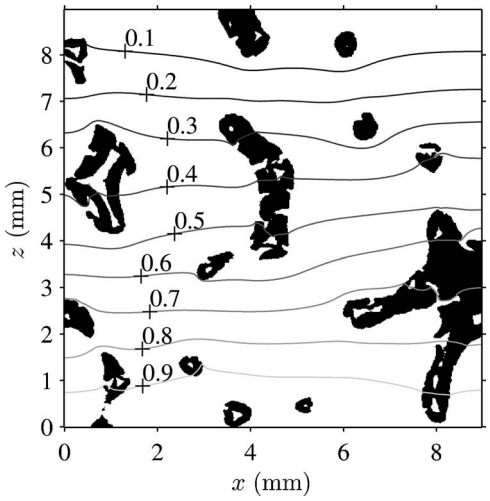

Fig. 8 Isothermal contour lines of the normalized temperature distribution $(T-T_2)/(T_1-T_2)$ in a cross-sectional plane obtained from pore-level direct numerical simulation of conduction heat transfer on a subset of Specimen A. Boundary conditions: $T=T_1$ at the bottom (z=0 mm) and $T=T_2$ at the top (z=9 mm). The solid areas are depicted in black.

$\times 10^{-6}$ m, and a molecular radius of gases inside the microscopic pores on the order of magnitude of the molecular radius of water $2R_m=4.6\times10^{-10}$ m,

$$\mathrm{Kn}=\frac{k_BT}{2^{5/2}\pi R_m^2 p d_{\mathrm{micro}}}=0.032 \tag{12}$$

Thus, the continuum assumption and Eqs. (1) and (2) are valid. These are typical operation conditions for high-temperature RPCs in chemical engineering (e.g., steam reforming of methane).

The amount of data obtained from microscale CT was significantly smaller than that obtained from macroscale CT. Thus, it was not possible to extract nonoverlapping sets of tomography data. The largest possible cube of the internal strut structure, without central triangular channel and without coating, has 263 voxel edge length. Using a $501\times501\times501$ computational grid, $h=0.514$ μm for $k_{f,\mathrm{micro}}/k_s=10^{-2}$ and GCI=1.27% with first order convergence.

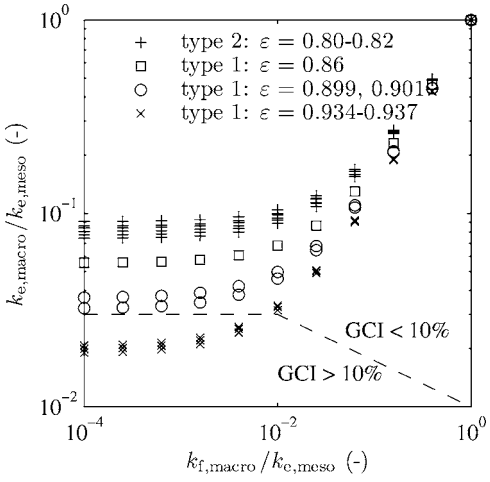

Fig. 9 Ratio of the macroscale and microscale effective thermal conductivities ($k_{e,\mathrm{macro}}/k_{e,\mathrm{micro}}$) as a function of the ratio of the fluid and strut thermal conductivities ($k_{f,\mathrm{macro}}/k_{e,\mathrm{micro}}$), obtained by the macroscale direct numerical simulation of 12 nonoverlapping subsamples of Specimens A and B with varying porosity. Indicated by a dashed line are the regions where the GCI is below and above 10%.

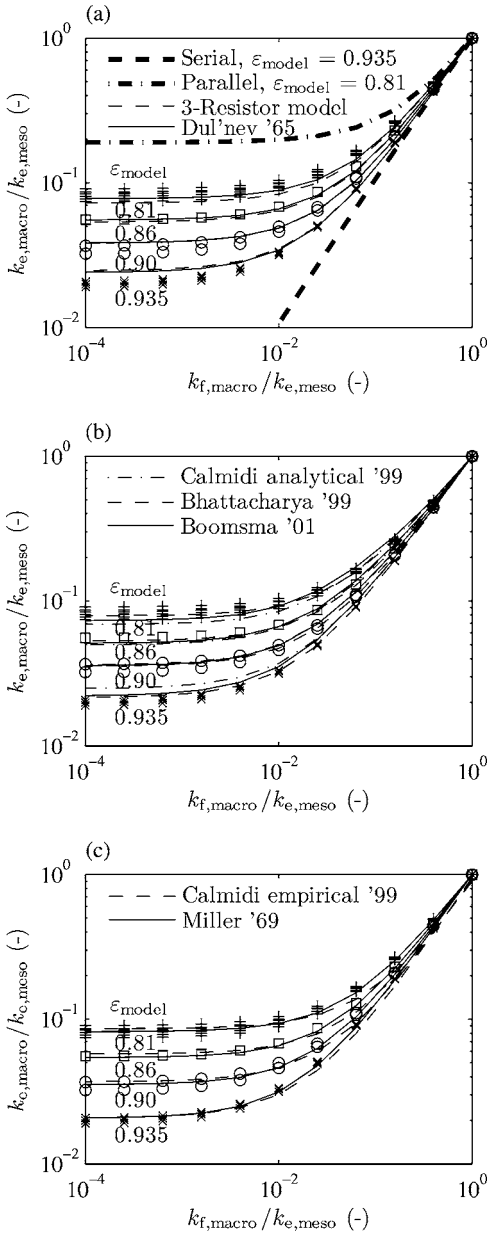

Fig. 10 Ratio of the macroscale and microscale effective thermal conductivities ($k_{e,\mathrm{macro}}/k_{e,\mathrm{micro}}$) as a function of the ratio of the fluid and strut thermal conductivities ($k_{f,\mathrm{macro}}/k_{e,\mathrm{micro}}$), obtained by the macroscale direct numerical simulation and by the k_e models: (*a*) parallel and serial bounds, Dul'nev's model, and three-resistor model; (*b*) Calmidi's and Mahajan's model (analytical), model of Bhattacharya et al., and Boomsma and Poulikakos's model for reticulate structures; (*c*) Calmidi and Mahajan's (empirical) and Miller's models

Figure 11 shows the ratio of the microscale effective thermal conductivity for the microscopic strut structure to the pure solid thermal conductivity ($k_{e,\mathrm{micro}}/k_s$) as a function of the ratio of the fluid-to-solid thermal conductivities ($k_{f,\mathrm{micro}}/k_s$), obtained by the microscale direct numerical simulation and by the k_e models. Maxwell's upper bound and Loeb's models predict k_e with a rms of 4.3% and 3.5%, respectively. These models depend on the po-

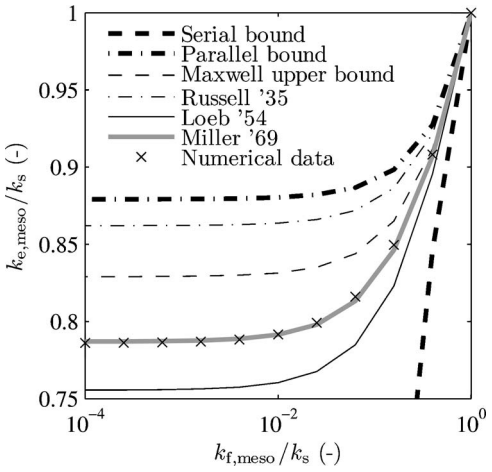

Fig. 11 Ratio of the microscale effective thermal conductivity to the pure solid thermal conductivity ($k_{e,micro}/k_s$) as a function of the ratio of the fluid-to-solid thermal conductivities ($k_{f,micro}/k_s$), obtained by the microscale direct numerical simulation and by the k_e models

rosity only; no free parameter is available. For Miller's model, the optimal parameters are $G_1=0.1287$ and $G_2=0.2157$, with rms $=0.18\%$.

Combined Effects of Macro- and Microscales. The k_e of the overall RPC composite material is given by the superposition of the effects of the microscale and macroscale effective thermal conductivities $k_{e,\text{macro}}$ and $k_{e,\text{micro}}$ as

$$\frac{k_{e,\text{macro}}}{k_s} = \left(\frac{k_{e,\text{macro}}}{k_{e,\text{micro}}}\right)\left(\frac{k_{e,\text{micro}}}{k_s}\right) \tag{13}$$

Figure 12 shows the contour lines of the ratio of the overall effective thermal conductivity to the pure solid thermal conductivity ($k_{e,\text{macro}}/k_s$) as a function of microscale fluid-to-solid thermal conductivity ratio ($k_{f,\text{micro}}/k_s$) and macroscale fluid-to-solid thermal conductivity ratio ($k_{f,\text{macro}}/k_s$), calculated by direct numerical simulation for a macroscopic porosity of 0.9 and a microscopic porosity of 0.12. As expected, $k_{e,\text{macro}}/k_s$ increases with increasing $k_{f,\text{macro}}/k_s$. For most of the parameter range considered, the influence of $k_{f,\text{macro}}/k_s$ is dominant because of the higher porosity of the macroscopic structure. A shift toward higher $k_{e,\text{macro}}$ is observed as $k_{f,\text{micro}}/k_s$ increases.

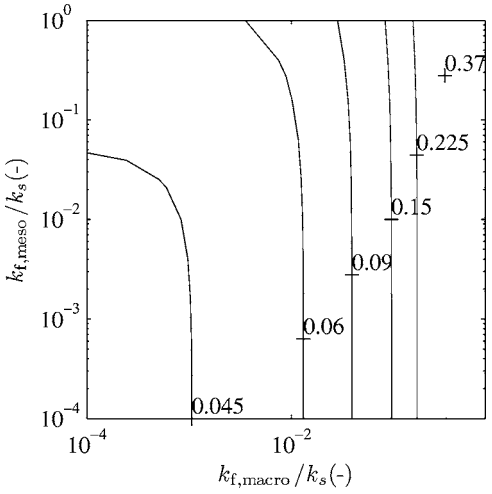

Fig. 12 Contour map of the ratio of the overall effective thermal conductivity to the pure solid thermal conductivity ($k_{e,\text{macro}}/k_s$) as a function of microscale fluid-to-solid thermal conductivity ratio ($k_{f,\text{micro}}/k_s$) and macroscale fluid-to-solid thermal conductivity ratio ($k_{f,\text{macro}}/k_s$). $\varepsilon_{\text{macro}}=0.90$, $\varepsilon_{\text{micro}}=0.12$.

5 Summary and Conclusion

We have applied high-resolution CT to determine the effective thermal conductivities of RPCs saturated with a fluid. The 3D geometrical representation of the RPC structure to the level of the sintered ceramic strut material is obtained by tomographic scans at 30 μm digital resolution for the macroscopic reticulate structure and at 1 μm digital resolution for the microscopic strut structure. The pore-level direct numerical simulation of conduction heat transfer in cubic samples is carried out using FV discretization and SOR on increasingly refined grids. The effective thermal conductivities $k_{e,\text{macro}}$ and $k_{e,\text{micro}}$ are thus calculated based on the macroscale and microscale CT data, respectively. The numerical error is estimated by the GCI at an average of 4.5% for the macroscopic reticulate structure and 1.3% for the microscopic strut structure. Generally, small fluid-to-solid thermal conductivity ratios and large porosities lead to relatively larger errors.

Results obtained by the direct numerical simulation are compared to those predicted by k_e models with optimal free parameters identified via least-squares fitting. Miller's model predicted $k_{e,\text{macro}}$ and $k_{e,\text{micro}}$ with rms errors of 3.6% and 0.18%, respectively. The reasonably good agreement is due to the two free parameters and the underlying three-point correlation model. Dul'nev's model predicted $k_{e,\text{macro}}$ with a rms error of 8.5%. Since Dul'nev's model does not rely on a free parameter, it is particularly suited for quick rough predictions of RPC's effective thermal conductivities. The models especially developed for reticulate structures usually have one free parameter. After optimization, Calmidi and Mahajan's model predicted $k_{e,\text{macro}}$ with a rms error of 11.9%, Boomsma and Poulikakos's model with 7.37%, and the model of Bhattacharya et al. gave the best results with a rms error of 4.11%. The model of Bhattacharaya et al. and Boomsma and Poulikakos's model agree better than Calmidi and Mahajan's model because they are able to represent the RPC structure more realistically. However the 3D geometry of Boomsma and Poulikakos's model does not provide improved accuracy vis-à-vis the model of Bhatacharya et al. Maxwell's upper bound overpredicted $k_{e,\text{micro}}$ (rms error of 4.34%), whereas Loeb's model underpredicted $k_{e,\text{micro}}$ (rms error of 3.4%).

Results from micro- and macroscale analyses were superimposed to obtain the overall effective thermal conductivity of the RPC composite material. The influence of the macroscale fluid-to-solid thermal conductivity ratio is dominant because of the higher porosity of the macroscopic reticulate structure. In general, tomography-based direct numerical simulation of conduction heat transfer can be applied to determine with high accuracy the effective thermal conductivity of complex two-phase structures. The method does not suffer from the limiting assumptions associated with analytical treatments and eliminates contact-resistance problems associated with experimental techniques. Further, radiation heat transfer can be treated as a completely separate phenomenon.

Acknowledgment

This work has been carried out within the framework of the project SOLREF funded by the European Commission under Contract No. SES6-CT-2004-502829 SOLREF. The numerical calculations have been performed on the ETH's high-performance cluster "Gonzales." We thank S. Moeller from the DLR German Space Agency for providing the RPC samples and P. Stämpfli from EMPA for experimental support.

Nomenclature

A = area, parameter for Calmidi and Mahajan's empirical correlation

CT = computed tomography
d = diameter (m)
e = correlation parameter for Boomsma and Poulikakos' model
F = safety factor for GCI calculation
f = correlation parameter for three-resistor model
FV = finite volume
G = correlation parameter for Miller's model
GCI = grid convergence index
h = grid size spacing (m)
k = thermal conductivity
k_B = Boltzmann constant ($=1.30865\times10^{-23}$ J/K)
Kn = Knudsen number
L = sample length (m)
n = exponent in Calmidi and Mahajan's empirical correlation
$\mathbf{n}$ = normal vector
p = convergence order of numerical method
r = correlation parameter for Calmidi and Mahajan's analytical model and the model of Bhattacharya et al.
R_m = molecular radius
rms = root mean square
RPC = reticulate porous ceramic
SOR = successive over-relaxation

Greek Symbols

ε = porosity $(-)$
μ = ratio of effective and solid thermal conductivities $(-)$
ν = ratio of fluid and solid thermal conductivities $(-)$
$\Psi_{i,j,k}$ = tomographic gray levels (discrete levels, discrete in spatial location)
$\Psi(x,y,z)$ = gray level as a function of spatial location (continuous function).

Subscripts

B = bottom element (FV discretization)
E = east element (FV discretization)
e = effective
e,macro = effective, macroscale
e,micro = effective, microscale
f = fluid
f,macro = fluid, macropores
f,micro = fluid, micropores
i = counter in tomography data matrix, x direction
j = counter in tomography data matrix, y direction
k = counter in tomography data matrix, z direction
N = north element (FV discretization)
P = central element (FV discretization)
s = solid
S = south element (FV discretization)
T = top element (FV discretization)
W = west element (FV discretization)

References

[1] Lange, F., and Miller, K., 1987, "Open-Cell, Low-Density Ceramics Fabricated From Reticulated Polymer Substrates," Adv. Ceram. Mater., **2**(4), pp. 827–831.
[2] van Setten, B. A., Bremmer, J., Jelles, S. J., Makkee, M., and Moulijn, J. A., 1999, "Ceramic Foam as a Potential Molten Salt Oxidation Catalyst Support in the Removal of Soot From Diesel Exhaust Gas," Catal. Today, **53**(4), pp. 613–621.
[3] Dhamrat, R., and Ellzey, J., 2005, "Numerical and Experimental Study of the Conversion of Methane to Hydrogen in a Porous Media Reactor," Combust. Flame, **144**(4), pp. 698–709.
[4] Howell, J., Hall, M., and Ellzey, J., 1999, "Combustion of Hydrocarbon Fuels Within Porous Inert Media," Prog. Energy Combust. Sci., **22**(2), pp. 121–145.
[5] Barra, A., Diepvens, G., Ellzey, J., and Henneke, M., 2003, "Numerical Study of the Effects of Material Properties on Flame Stabilization in a Porous Burner," Combust. Flame, **134**, pp. 369–379.
[6] Barra, A., and Ellzey, J., 2004, "Heat Recirculation and Heat Transfer in Porous Burners," Combust. Flame, **137**(1–2), pp. 230–241.
[7] Fend, T., Hoffschmidt, B., Pitz-Paal, R., Reutter, O., and Rietbrock, P., 2004, "Porous Materials as Open Volumetric Solar Receivers: Experimental Determination of Thermophysical and Heat Transfer Properties," Energy, **29**(5–6), pp. 823–833.
[8] Steinfeld, A., and Palumbo, R., 2001, "Solar Thermochemical Process Technology," *Encyclopedia of Physical Science and Technology*, R. A. Meyers, ed. Academic, New York, pp. 237–256.
[9] Petrasch, J., and Steinfeld, A., 2006, "Dynamics of a Solar Thermochemical Reactor for Steam Reforming of Methane," Chem. Eng. Sci., **62**(16), pp. 4214–4228.
[10] Kaviany, M., 1995, *Principles of Heat Transfer in Porous Media*, Springer-Verlag, New York.
[11] Whitaker, S., 1999, *The Method of Volume Averaging*, Kluwer, Dordrecht.
[12] Touloukian, Y. S., Powell, R. W., Ho, C. Y., and Klemens, P. G., 1970, *Thermal Conductivity Nonmetallic Solids*, IFI/Plenum, New York.
[13] Wyllie, M. R. J., and Southwick, P. F., 1954, "An Experimental Investigation of the S. P., and Resistivity Phenomena in Dirty Sands," J. Alloys Compd., **6**, pp. 44–57.
[14] Woodside, W., and Messmer, J. H., 1961, "Thermal Conductivity of Porous Media. I. Unconsolidated Sands," J. Appl. Phys., **32**(9), pp. 1688–1699.
[15] Woodside, W., and Messmer, J. H., 1961, "Thermal Conductivity of Porous Media. II. Consolidated Rocks," J. Appl. Phys., **32**(9), pp. 1699–1706.
[16] Sullins, A. D., and Daryabeigi, K., 2001, "Effective Thermal Conductivity of High Porosity Open Cell Nickel Foam," 35th AIAA Thermophysics Conference, Anaheim, CA, Jun. 11–14, 2001.
[17] Tseng, C., Yamaguchi, M., and Ohmori, T., 1997, "Thermal Conductivity of Polyurethane Foams From Room Temperature to 20 K," Cryogenics, **37**(6), pp. 305–312.
[18] Maxwell, J. C., 1891, *A Treatise on Electricity and Magnetism*, Clarendon, Oxford.
[19] Russell, H. W., 1935, "Principles of Heat Flow in Porous Insulators," J. Am. Ceram. Soc., **18**, pp. 1–5.
[20] Dul'nev, G. N., 1965, "Heat Transfer Through Solid Disperse Systems," J. Eng. Phys., **9**(3), pp. 399–404.
[21] Dul'nev, G. N., and Komkova, L. A., 1965, "Analysis of Experimental Data on the Heat Conductivity of Solid Porous Systems," J. Eng. Phys., **9**(4), pp. 517–519.
[22] Calmidi, V. V., and Mahajan, R. L., 1999, "The Effective Thermal Conductivity of High Porosity Fibrous Metal Foams," ASME J. Heat Transfer, **121**(2), pp. 466–471.
[23] Bhattacharya, A., Calmidi, V., and Mahajan, R., 1999, "An Analytical-Experimental Study for the Determination of the Effective Thermal Conductivity of High Porosity Fibrous Foams," *Application of Porous Media Methods for Engineered Materials*, R. M. Sullivan, ed., AMD Vol. 233, ASME, New York, pp. 13–20.
[24] Boomsma, K., and Poulikakos, D., 2001, "On the Effective Thermal Conductivity of a Three-Dimensionally Structured Fluid-Saturated Metal Foam," Int. J. Heat Fluid Flow, **44**, pp. 827–836.
[25] Miller, M. N., 1969, "Bounds for Effective Electrical, Thermal, and Magnetic Properties of Heterogeneous Materials," J. Math. Phys., **10**(11), pp. 1988–2004.
[26] Petrasch, J., Wyss, P., and Steinfeld, A., 2007, "Tomography-Based Monte Carlo Determination of Radiative Properties of Reticulate Porous Ceramics," J. Quant. Spectrosc. Radiat. Transf., **105**, pp. 180–197.
[27] Zeghondy, B., Iacona, E., and Taine, J., 2006, "Determination of the Anisotropic Radiative Properties of a Porous Material by Radiative Distribution Function Identification (RDFI)," Int. J. Heat Mass Transfer, **49**, pp. 2810–2819.
[28] Zeghondy, B., Iacona, E., and Taine, J., 2006, "Experimental and RDFI Calculated Radiative Properties of Mullite Foam," Int. J. Heat Mass Transfer, **49**, pp. 3702–3703.
[29] Widjajakusuma, J., Manwart, C., Biswal, B., and Hilfer, R., 1999, "Exact and Approximate Calculations for the Conductivity of Sandstone," Physica A, **270**, pp. 325–331.
[30] Widjajakusuma, J., Biswal, B., and Hilfer, R., 2003, "Quantitative Comparison of Mean Field Mixing Laws for Conductivity and Dielectric Constants of Porous Media," Physica A, **318**, pp. 319–333.
[31] Krishnan, S., Murthy, J. Y., and Garimella, S. V., 2006, "Direct Simulation of Transport in Open-Cell Metal Foam," ASME J. Heat Transfer, **128**, pp. 793–799.
[32] Scanco Medical, http://www.scanco.ch/cgi-bin/scanco.pl?menu=home&site=prod_uct80
[33] Phoenix X-ray, http://www.microfocus-x-ray.com/frameset.php?Language=en
[34] Weszka, J., 1978, "A Survey of Threshold Selection Techniques," Comput. Graph. Image Process., **7**, pp. 259–265.
[35] Truong, H. V., and Zinsmeister, G. E., 1978, "Experimental Study of Heat Transfer in Layered Composites," Int. J. Heat Mass Transfer, **21**, pp. 905–909.
[36] Batchelor, G. K., and O'Brien, R. W., 1977, "Thermal or Electrical Conduction Through a Granular Material," Proc. R. Soc. London, Ser. A, **355**, pp. 313–333.
[37] Quintard, M., and Whitaker, S., 2000, "One- and Two Equation Models in Two-Phase Systems," Adv. Heat Transfer, **23**, pp. 369–464.
[38] Patankar, S., 1980, *Numerical Heat Transfer and Fluid Flow*, Taylor & Francis, London.

[39] Press, W. H., Teukolsky, S. A., Vetterling, W. T., and Flannery, B. P., 1992, *Numerical Recipes in C: The Art of Scientific Computing*, Cambridge University Press, Cambridge.
[40] Roach, P. J., 1998, *Verification and Validation in Computational Science and Engineering*, Hermosa, Albuquerque.
[41] Hsu, C. T., Cheng, P., and Wong, K. W., 1994, "Modified Zehner-Schlünder Models for Stagnant Thermal Conductivity of Porous Media," Int. J. Heat Mass Transfer, **37**(17), pp. 2751–2759.
[42] Bruggeman, D. A. G., 1935, "Berechnung Verschiedener Physikalischer Konstanten von Heterogenen Substanzen, I. Dielektrizitätskonstanten und Leitfähigkeiten der Mischkörper aus Isotropen Substanzen," Ann. Phys., **5**(24), pp. 636–679.
[43] Loeb, A. L., 1954, "Thermal Conductivity: VIII. A Theory of Thermal Conductivity of Porous Materials," J. Am. Ceram. Soc., **37**(2), pp. 96–99.
[44] Ribaud, 1937, "Conductibilité Thermique des Materiaux Poreux et Pulverulents. Etude Théorique," Chaleur et Industrie, **18**, pp. 36–43.
[45] Eucken, A., 1932, "Die Wärmeleitfähigkeit Keramischer, Fester Stoffe—Ihre Berechnung aus der Wärmeleitfähigkeit der Bestandteile," VDI Forschungsheft 353, Beilage zu, Forschung auf dem gebiet des Ingenieurwesens, Ausgabe B, Band 3.
[46] Odelevskii, V. I., 1951, "Calculation of a Generalized Conductivity of Heterogeneous Systems," J. Tech. Phys., **21**(6), pp. 667–677.
[47] Lichtenecker, K., 1924, "Der Elektrische Leitungswiderstand Künstlicher und Natürlicher Aggregate," Phys. Z., **25**(10), pp. 225–233.
[48] Pawel, R. E., McElroy, D. L., Weaver, F. J., and Graves, R. S., 1988, "High Temperature Thermal Conductivity of a Fibrous Alumina Ceramic," *19th International Thermal Conductivity Conference*.
[49] Bhattacharaya, A. Calmidi, V. V., and Mahajan, R. L., 2002, "Thermophysical properties of high porosity metal foams," Int. J. Heat Mass Transfer, **45**, pp. 1017–1031.
[50] Mantle, W. J., and Chang, W. S., 1991, "Effective Thermal Conductivity of Sintered Metal Fibers," J. Thermophys. Heat Transfer, **5**(4), pp. 545–549.
[51] Dul'nev, G. N., and Zarichnyak, Y. P., 1970, "A Study of the Generalized Conductivity Coefficients in Heterogeneous Systems (Review)," Heat Transfer-Sov. Res., **2**(4), pp. 89–107.

Heat Transfer During Compression and Expansion of Gas

Masutaka Ota

Yoshihiko Haramura
e-mail: haramura@mech.kanagawa-u.ac.jp

Department of Mechanical Engineering,
Kanagawa University,
3-27-1 Rokkakubashi,
Kanagawa-ku, Yokohama,
Kanagawa 221-8686, Japan

Heat transfer during compression and expansion of gas is investigated to obtain a correlation that is easy to use in the design of the reciprocating energy conversion machines. We carried out experiments to measure the heat transfer characteristics to/from gas during compression and expansion to obtain the correlation. These measurements were performed using a piston-cylinder assembly over a range of volume ratios, frequencies, mean pressures, gases, and internal extended surface areas. The heat transfer was estimated thermodynamically from experimental pressure-volume data. Dimensionless groups for heat transfer are discussed in order to correlate the data. The product of the dimensionless heat transfer and specific heat ratio was found to be optimal and was correlated with only the Peclet number for a wide range of conditions, even for gases having different specific heat ratios. The temperature amplitude of the center of the test space was obtained, and it is found that the penetration depth reached the center when the Peclet number is in the range from 20 to 30. [DOI: 10.1115/1.2804949]

Keywords: heat transfer, compression and expansion, cyclic change, thermodynamic prediction of heat transfer

1 Introduction

Compression or expansion of gas occurs in many energy conversion machines, and heat transfer in the process affects the efficiency of the system. In particular, heat transfer is important in cycles in which the isothermal process is ideal, such as the Stirling cycle, which is notable because such cycles are important in the utilization of waste heat or realization of refrigerators that do not require freon. A number of studies have been conducted to correlate the heat transfer in reciprocal flow related to the design of Stirling cycle machines. The heat transfer has been shown to correlate with the Reynolds number based on the average flow velocity, as shown by Organ [1]. This implies that the temperature distribution in the gas is assumed to approach that of the steady state in a sufficiently short time.

Studies on heat transfer during compression and expansion of gas under approximately stationary conditions were carried out concerning the hysteresis loss in internal combustion engines, hydraulic accumulators, and gas springs. Lee [2] studied heat transfer and hysteresis loss analytically by solving the one-dimensional energy equation for an incompressible medium with a heat source corresponding to compression work. He presented explicit analytical expressions for the heat flux in a complex form and the hysteresis loss as, respectively,

$$q = -\frac{\lambda T_a}{l} z \tanh z \quad \text{with } z = (1+i)\frac{l}{\delta} \quad \text{and } \delta = \sqrt{\frac{2\alpha}{\omega}} \tag{1}$$

$$\frac{W_{\text{loss}}}{P_0 V_0} = \frac{\pi}{2}\left(\frac{P_a}{P_0}\right)^2 \frac{\gamma-1}{\gamma}\left(\frac{1}{y}\right)\frac{\cosh y \sinh y - \sin y \cos y}{\cosh^2 y - \sin^2 y} \tag{2}$$

with

$$y = l\sqrt{\omega/2\alpha} = (\text{Pe}_\omega/8)^{1/2} \tag{3}$$

where l is the distance between the wall and the midplane of the gas space and is equal to $D_h/4$. Several studies have considered only hysteresis loss. Among these, those of Pourmovahed and Otis [3] and Kornhauser and Smith [4] are noteworthy. In their analytical study, Pourmovahed and Otis [3] assumed a lumped heat capacity of gas and characterized the behavior with a thermal time constant, which is the ratio of heat capacity to heat conductance between the gas and the walls. Although the expressions developed using the thermal time constant model agree well with experimentally obtained results, the experiments were limited to a very low range of frequencies. Kornhauser and Smith [4] used the Peclet number

$$\text{Pe}_\omega = \omega D_h^2/4\alpha \tag{4}$$

as an independent dimensionless parameter when they correlated hysteresis loss, unlike Faulkner and Smith [5] or Lawton [6] who used the Reynolds number. Kornhauser and Smith [4] presented the correlation of hysteresis loss in the same form as Eq. (2), but y was replaced with an empirical correlation

$$y = 0.49(\text{Pe}_\omega/8)^{0.43} \tag{5}$$

Lawton [6] measured the wall heat flux using a fast response thermocouple mounted flushed to the wall surface in a cylinder of a four-cylinder diesel engine with only the fuel injector removed. He first correlated the heat flux at the top dead center and then correlated the deviation of the heat flux from the top dead center. The heat flux was described as

$$q = \frac{\lambda}{d}[0.28\text{Re}^{0.7}(T_{\text{bulk}} - T_w) - 2.75LT_w] \quad \text{with } L = \frac{\gamma-1}{V}\frac{dV}{dt}t_0 \tag{6}$$

The experiments were limited to high frequencies, and so it is necessary to extend the range.

Kornhauser and Smith [7] determined the heat flux thermodynamically from measured pressures and kinematically estimated volumes. The heat flux was obtained from the change in the internal energy and the work. The change in internal energy was

Contributed by the Heat Transfer Division of ASME for publication in the JOURNAL OF HEAT TRANSFER. Manuscript received November 21, 2006; final manuscript received June 9, 2007; published online March 5, 2008. Review conducted by Ramendra P. Roy.

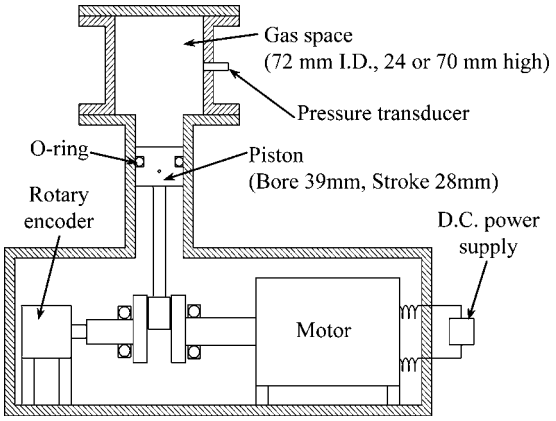

Fig. 1 Apparatus

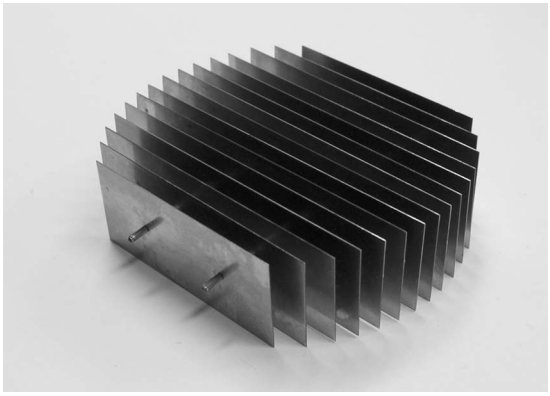

Fig. 2 Extended surface with 4 mm interval

obtained from the derivative of the temperature. To simulate the phase lead of heat flux with respect to the temperature difference, they extended the Nusselt number based on hydraulic diameter D_h to the complex expression $\mathrm{Nu}_r + i\mathrm{Nu}_i$. The components were obtained as the mean square of deviation from the correlated heat flux ($\Sigma(q_i - q)^2 \rightarrow minimum$, where q is given by Eq. (7))

$$q = \frac{\lambda}{D_h}\left[\mathrm{Nu}_r(T - T_w) + \frac{\mathrm{Nu}_i}{\omega}\frac{dT}{dt}\right] \tag{7}$$

is minimized for each run and they were correlated as

$$\mathrm{Nu}_r = \mathrm{Nu}_i = 0.56\mathrm{Pe}_\omega^{0.69} \quad \text{for } \mathrm{Pe}_\omega > 100 \tag{8}$$

Although Kornhauser and Smith [7] successfully developed their complex Nusselt number correlation, which predicts the instantaneous heat flux including phase lead, the correlation is difficult to use, especially for low Peclet number. Their Nusselt number expression contains the mean temperature of gas, which is unknown and must be determined from the heat transfer. For design use, a correlation with only the explicit variables is favorable.

Kornhauser and Smith [4] reported that the hysteresis loss was maximal near $\mathrm{Pe}_\omega = 10$, which indicates that the heat transfer is considerable when $\mathrm{Pe}_\omega < 100$. Therefore, the heat transfer for lower frequencies, corresponding to $\mathrm{Pe}_\omega < 100$, is important in the design of Stirling cycle machines that utilize heat transfer positively. Only the uncorrelated data of Kornhauser and Smith [7] have been reported in this range. Therefore, we carried out experiments to measure the heat transfer to/from the gas during compression and expansion in order to obtain the correlation over a wider range of conditions. The construction of dimensionless parameter based on the heat transferred in an isothermal process is discussed in Sec. 3.

2 Description of the Experiments

2.1 Apparatus. The apparatus is shown schematically in Fig. 1. The gas in the gas space is compressed and expanded with a piston having a diameter of 39 mm and a stroke of 28 mm. The diameter of the volume above the cylinder is 72 mm, and the height of the volume is 70 mm or 24 mm for volume ratio (maximum volume divided by minimum volume) of 1.1 or 1.25, respectively. The crankshaft is connected to a dc motor with speed control. The crankshaft, the motor, and a rotary encoder are placed in a pressure vessel. The pressure in the vessel is adjusted along with that of the gas space. To change the gas space volume, the head of the gas space is replaced.

In most of the experiments, the gas space was provided with an extended heat transfer surface. This surface is a bundle of stainless steel plates, as shown in Fig. 2. The plates are 20 mm in height and 0.2 mm in thickness and are tied up at an interval of 4 mm or 8 mm with stainless steel tubes (1.4 mm o.d.) as spacers. One stage of this is installed in the gas space for a volume ratio of 1.25. The bundle is suspended as the ends of the plates push the cylinder wall with its elasticity. There are about 2 mm high clearance zones above and below the bundle. For a volume ratio of 1.1, three stages of bundles were installed in the gas space with the plate surfaces of the upper and lower bundles alternately perpendicular to each other. There are also clearance zones above, below, and between the bundles. This configuration provides uniform spacing of extended surface during the change of gas volume.

The pressure in the gas space is measured with a semiconductor pressure transducer (Toyoda PD64S-500K) mounted on the wall of the gas space. The transducer has a range of 0–600 kPa. The volume is calculated from the kinetics of the crank and the connecting rod (112 mm long) corresponding to the phase angle of the crank measured with a rotary encoder having a sensitivity of 1 deg. The frequency or crank speed is controlled by a digital signal processor, which deals with the rotary encoder signal. These signals are recorded with a digital data acquisition system (Yokogawa WE7000).

The test conditions are shown in Table 1. Measurements were carried out for all combinations of gases, frequencies, mean pressures, and surface areas, except for the combination of volume ratio of 1.25 and mean pressure of 500 kPa. The data were composed of 1212 total points. The thermal diffusivity of helium is comparatively large. Therefore, Pe_ω is smaller. The values of Pe_ω for helium, argon, and nitrogen ranged from 1 to 4.4×10^3, 9 to 3.8×10^4, and 9 to 3.5×10^4, respectively.

The measurements were conducted as follows. After the extended surface was installed in the gas space, the gas space and the pressure vessel were evacuated and then charged with a designated gas to 500 kPa or 400 kPa. The motor speed was set to the desired value in the ascending order from 3 Hz to 52 Hz. After waiting for 30–60 s for steady state, data were sampled and stored for 20 revolutions. After storing the data for 52 Hz, the motor was stopped and the pressure was adjusted to the next desired value. After several minutes, the measurement was started again with the same procedure at the higher pressure. The measurements were repeated until 50 kPa pressure.

Table 1 Test conditions

Gas	Helium, argon, nitrogen	
Frequency (Hz)	3, 5, 7, 10, 15, 20, 30, 40, 52	
Gas space volume at midstroke (cm^3)	336	148
Volume ratio	1.1	1.25
Mean pressure (kPa)	50, 100, 150, 200, 250, 300, 400,500	
Gas space surface area at midstroke (cm^2)	315, 902, 1440	201, 397, 576
D_h (mm)	42.8, 14.7, 9.0	29.6, 14.8, 10.1

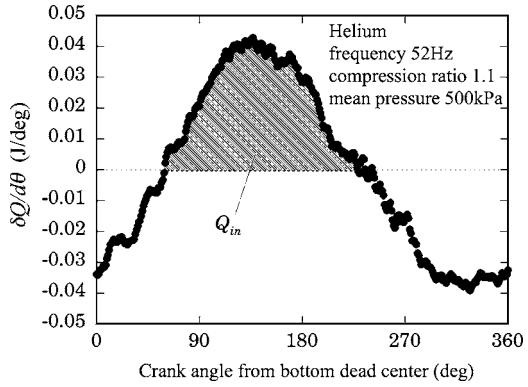

Fig. 3 Example of $\delta Q/d\theta$

2.2 Method Used to Estimate the Amount of Heat Transfer. The amount of heat incoming to the working gas during the change of state can be obtained from the first law of thermodynamics:

$$\delta Q = dU + PdV \tag{9}$$

If ideal gas behavior and constant specific heat are assumed, the instantaneous internal energy of the gas is obtained by integration:

$$U = \int_{\text{total volume of gas}} c_v T dm = \frac{c_v}{R}\int_0^V PdV \tag{10}$$

Assuming that instantaneous pressure is uniform at every instance, we have

$$U = \frac{c_v}{R}PV \tag{11}$$

independent of any temperature profile. Consequently,

$$\frac{\delta Q}{d\theta} = \frac{c_v}{R}\frac{d}{d\theta}(PV) + P\frac{dV}{d\theta} \tag{12}$$

The amount of heat incoming to the working gas, Q_{in}, is obtained by integrating Eq. (12) while $dQ > 0$. To suppress the influence of noise, pressures at every phase of 20 successive compressions and expansions were averaged, and then Savitzky-Golay smoothing filters [8] were applied to the measured pressures. The filter replaces each measured pressure with a midpoint value approximated with a fourth-order polynomial using 33 (16 are earlier and 16 are later) points. An example of $\delta Q/d\theta$ is shown in Fig. 3. Q_{in} corresponds to the shaded area. Q_{in} is approximately equal (the difference is less than about 5%) to the amount of heat transfer outgoing from the working gas in the rest of the cycle period. This suggests that the measurement was performed in a sufficiently steady (steady periodic) state and the amount of heat outgoing from the working gas can be also evaluated from Q_{in}.

2.3 Error Estimation. The error in evaluating the amount of heat transfer is caused mainly by the origin of the crank angle, gas space volume, and inaccuracy of pressure measurements.

The uncertainty of the crank angle is estimated to be ± 0.25 deg from the accuracy limitation of the setting of the origin and the sensitivity of the rotary encoder. This causes more significant error than the other factors on the heat transfer for high Peclet numbers. The uncertainty of volume at midstroke is ± 0.5 cm^3. Its effect on Q_{in} is proportional to the ratio of the uncertainty of volume at midstroke to the average volume and is very small.

The pressure measurement errors are due to the stability and natural frequency of the pressure transducer and the zero stability level of the amplifier. The accuracy of the transducer is $\pm 0.1\%$ of full range, which is equal to 0.5 kPa. The natural frequency is 6 kHz and its effect is small. The sensitivity of the transducer is 0.22 μV/Pa, and the zero stability level of the amplifier is ± 1 μV/°C. Assuming that the change in the room temperature during the experiment is less than 5 °C, the uncertainty is estimated to be 0.02 kPa and thus very small. The error due to the accuracy of the transducer is more significant than the other factors for intermediate Peclet numbers. In Eq. (12), the first term is zero for isothermal process, and the first and second terms cancel each other for adiabatic process. Therefore, we estimate the error of Q_{in} as that of the second term: the product of the error of pressure (0.5 kPa) and the swept volume of the piston (33.4 cm^3). Some data of Q_{in} are not large enough compared with this error. We present data only when the estimated error is less than 20% of Q_{in}, as calculated from measurements.

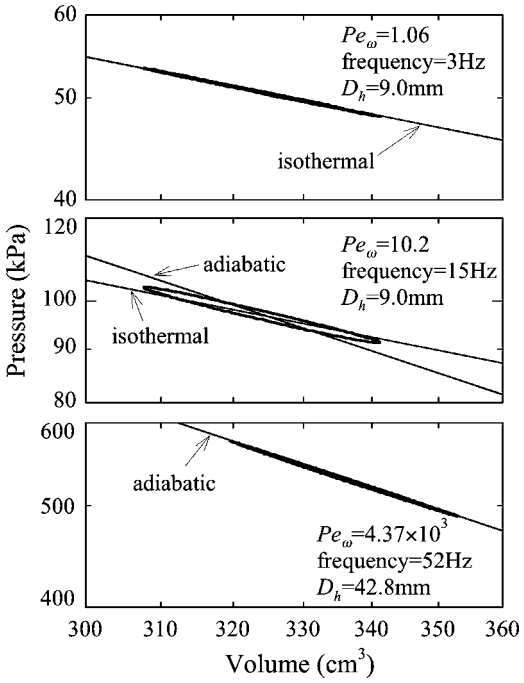

Fig. 4 Pressure-volume diagram for helium and compression ratio of 1.1 (log-log plot)

To verify the universality of the present experiment, we also compared the power loss per cycle calculated from the present data with that reported by Kornhauser and Smith [4] and Lee [2]. Examples of pressure-volume diagram are shown in log-log plot (the abscissa is expanded by a factor of 5) in Fig. 4. The slopes are -1.02 for $\text{Pe}_\omega = 1.06$ and -1.66 for $\text{Pe}_\omega = 4.37 \times 10^3$, which correspond to isothermal and adiabatic processes, respectively. The losses are very small in these two cases. For $\text{Pe}_\omega = 10.2$, the path traverses counterclockwise and non-negligible work is dissipated in every cycle.

To correlate the power loss per cycle, the dimensionless loss

$$W_{\text{loss,nd}} = \frac{\oint PdV}{P_0 V_0 \left(\frac{P_a}{P_0}\right)^2 \frac{\gamma - 1}{\gamma}} \tag{13}$$

as proposed by Kornhauser and Smith [4], was used. Since the measured pressure variation was not sinusoidal, the approximation

$$\frac{P_a}{P_0} = \frac{P_{\max} - P_{\min}}{P_{\max} + P_{\min}} \tag{14}$$

was employed, where $P_{\max}$ and $P_{\min}$ were the maximum and minimum of the data after the application of the Savitzky-Golay filter.

The dimensionless loss has a maximum of approximately 1.2 at

a Pe_ω of about 15. When Pe_ω is large, the dimensionless loss is small because both compression and expansion occur nearly adiabatically. When Pe_ω is small, it is also small because the gas compresses and expands nearly isothermally. The loss is maximal at intermediate Pe_ω when the gas is cooled after compression and heated after expansion. These results coincide well with each other for the three gases, nine frequencies, eight mean pressures, three surface areas, and two volume ratios, and had a tendency that was similar to the results reported by Kornhauser and Smith [4] and Lee [2].

3 Prediction of Heat Transfer

3.1 Amount of Heat Transferred in Periodic Heat Conduction. To derive the reference amount of heat transfer, heat conduction in an incompressible medium in a semi-infinite region is considered.

The condition in the present experiment is that the temperature of the bulk gas changes periodically with amplitude T_a, and the wall temperature is kept constant. This situation is analogous to that in which the wall temperature changes periodically as $T_w = T_0 + T_a \cos \omega t$, while the bulk temperature T_0 is kept constant. When a semi-infinite region gas is in contact with the wall at $x = 0$, the temperature profile in the gas is

$$T = T_0 + T_a \exp\left(-\sqrt{\frac{\omega}{2\alpha}}x\right)\cos\left(\omega t - \sqrt{\frac{\omega}{2\alpha}}x\right) \tag{15}$$

The wall heat flux is

$$q = \lambda\sqrt{\frac{\omega}{\alpha}}T_a \cos\left(\omega t + \frac{\pi}{4}\right) \tag{16}$$

Integrating Eq. (16) for $q > 0$, the amount of heat incoming to the working gas is

$$Q_{\text{in}} = 2\sqrt{\frac{\rho c_p \lambda}{\omega}}AT_a \tag{17}$$

3.2 Amount of Heat Transferred During Isothermal Process. To obtain the effect of specific heat ratio γ, we consider the amount of heat transferred during an isothermal process.

When the volume changes slightly from $V_0 - V_a$ to $V_0 + V_a$ isothermally, the amount of heat transfer is given by

$$Q_{\text{in}}^{\text{isoth}} = P_0 V_0 \log_e \frac{V_0 + V_a}{V_0 - V_a} \approx 2P_0 V_0 \frac{V_a}{V_0} \tag{18}$$

Dividing Eq. (18) by Eq. (17), heat transfer in a dimensionless form is

$$Q_{\text{nd}}^{\text{isoth}} = \frac{\sqrt{\text{Pe}_\omega}}{2}\frac{\gamma - 1}{\gamma}\frac{T_0}{T_a}\frac{V_a}{V_0} \tag{19}$$

with Pe_ω given by Eq. (4). T_a does not exist in an isothermal process, but the driving temperature of heat transfer is the temperature change due to adiabatic expansion $T_{a,\text{adia}}$, for which

$$\frac{T_{a,\text{adia}}}{T_0} \approx (\gamma - 1)\frac{V_a}{V_0} \tag{20}$$

Substituting $T_{a,\text{adia}}/T_0$ in Eq. (20) into T_a/T_0 in Eq. (19), we obtain

$$Q_{\text{nd,adia}}^{\text{isoth}} = \frac{1}{2\gamma}\sqrt{\text{Pe}_\omega} \tag{21}$$

The product $\gamma Q_{\text{nd,adia}}$ is a function of Pe_ω when the frequency approaches zero.

4 Experimental Results

All experimental data were correlated with the Peclet number as defined in Eq. (4).

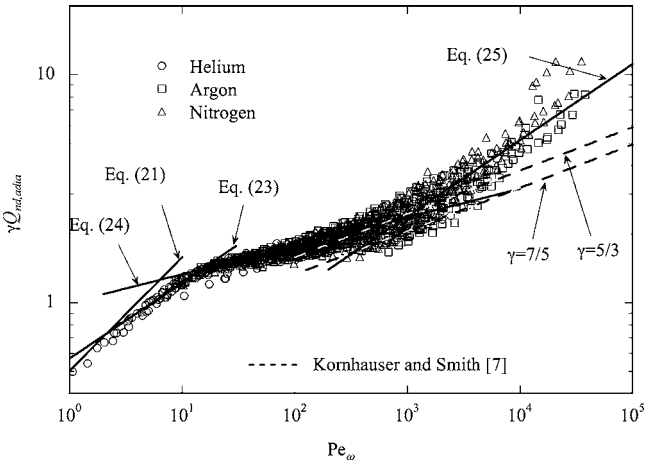

Fig. 5 Dimensionless heat transfer as a function of the Peclet number

4.1 Heat Transfer. By dividing Q_{in} by Eq. (17), the dimensionless heat transfer is defined as

$$Q_{\text{nd,adia}} = \frac{Q_{\text{in}}}{2\sqrt{\rho c_p \lambda/\omega}AT_{a,\text{adia}}} \tag{22}$$

Here, temperature amplitude $T_{a,\text{adia}}$ calculated from the volume change assuming an adiabatic change is taken for T_a.

Figure 5 shows the relationship between the product $\gamma Q_{\text{nd,adia}}$ and Pe_ω. This figure shows that the data obtained for three gases, nine frequencies, eight mean pressures, three gas space surface areas, and two volume ratios are correlated with a single curve. Thus, $\gamma Q_{\text{nd,adia}}$ can be correlated as

$$\gamma Q_{\text{nd,adia}} = \begin{cases} 0.5\text{Pe}_\omega^{1/2} & (\text{Pe}_\omega < 2.2) \quad (21') \\ 0.57\text{Pe}_\omega^{1/3} & (2.2 < \text{Pe}_\omega < 15) \quad (23) \\ \text{Pe}_\omega^{1/8} & (15 < \text{Pe}_\omega < 1000) \quad (24) \\ 0.24\text{Pe}_\omega^{1/3} & (1000 < \text{Pe}_\omega) \quad (25) \end{cases}$$

At low values of Pe_ω, which correspond to low frequencies, the process occurs nearly isothermally. The same amount of heat is added (or removed) per cycle at these values of Pe_ω. Since heat transfer rate is proportional to $Q_{\text{in}}\omega$ ($\propto Q_{\text{nd,adia}}\omega^{1/2}$) and $\text{Pe}_\omega \propto \omega$, it increases in proportion to cycle frequency in the range of Eq. (21). The exponent on Pe_ω becomes smaller in the ranges of higher Pe_ω, which means that less amount of heat is transferred per cycle as Pe_ω becomes larger. However, heat transfer rate increases with increasing cycle frequency. There may be an effect of turbulence due to stepwise expansion of cross-sectional area, but this effect would be restricted to the gas space volume near the exit of the cylinder for a low Peclet number as the Reynolds number $(D_h\omega \times (\text{a half of the piston stroke})/\alpha \times (\text{Prandtl number})$, Prandtl number$=0.7$) is much less than 2300 where flow tends to remain laminar. The fact that heat transfer was correlated well for different configurations with one and three stages of extended surface indicates a small effect of turbulence for low Pe_ω.

Figure 5 also shows Eq. (8) of Kornhauser and Smith [7] for $\gamma = 5/3$ and $7/5$. All of the present data are correlated with $\gamma Q_{\text{nd,adia}}$ regardless of the value of γ, while Eq. (8) takes different values according to γ. The effect of γ appears to be correlated better with Eqs. (24) and (25) than with Eq. (8). Further investigations will be required to clarify the heat transfer characteristics in high Pe_ω region, especially the exponent on Pe_ω, because the present data may be affected by the turbulence at the cylinder exit.

4.2 Temperature Amplitude. Compression or expansion work is done on/by the gas and its temperature tends to change. The wall has a much larger thermal time constant than the gas, as

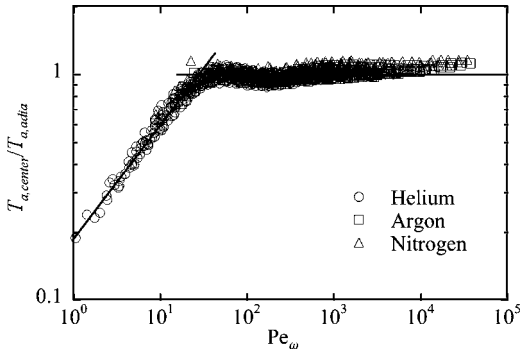

Fig. 6 $T_{a,\text{center}}/T_{a,\text{adia}}$ as a function of the Peclet number

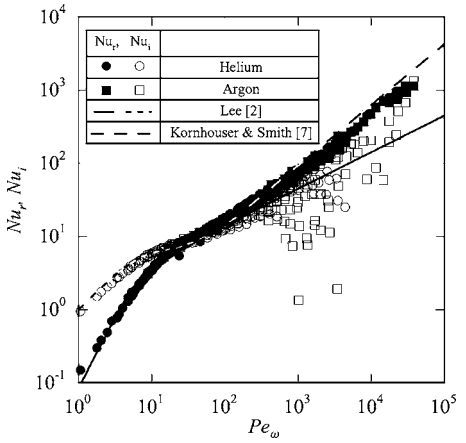

Fig. 7 Complex Nusselt number for helium and argon for volume ratio of 1.1

demonstrated by Faulkner and Smith [5]. Therefore, the wall temperature is essentially constant. Hence, the temperature of the gas on the wall is kept constant, and this suppresses the temperature change of the gas near the wall. Therefore, in order to understand the mechanism of heat transfer, it is important to clarify the conditions in which the effect of the wall reaches the centerline (the midplane between two opposing walls) of the gas space. Since the temperature obtained from measured pressure and kinematically estimated volume is the mixed-mean temperature of the gas, we must obtain the temperature at the centerline.

Lee [2] derived the temperature distribution in the gas between two opposing walls located at $x=0$ and $x=2l=2\delta z/(1+i)$ (δ and z are defined in Eq. (1)) as

$$T(x,t) = T_0 + T_{a,\text{adia}}\left\{1 - \frac{e^{-z}}{e^z+e^{-z}}e^{(1+i)x/\delta} - \frac{e^z}{e^z+e^{-z}}e^{-(1+i)x/\delta}\right\}e^{i\omega t} \tag{26}$$

where T_0 is the wall temperature and $T_{a,\text{adia}}$ the amplitude of temperature due to adiabatic compression and expansion. This agrees well with the present data for $\text{Pe}_\omega < 100$ as shown in the next section. The centerline temperature is

$$T_{\text{center}}(t) = T_0 + T_{a,\text{adia}}\left\{1 - \frac{2}{e^z+e^{-z}}\right\}e^{i\omega t} \tag{27}$$

and the mixed mean temperature is

$$T_{\text{mm}}(t) = \frac{1}{l}\int_0^l T(x,t)dx = T_0 + T_{a,\text{adia}}\left\{1 - \frac{\tanh(z)}{z}\right\}e^{i\omega t} \tag{28}$$

The temperature amplitude is obtained in the experiment using $T_{\text{mm}}(t)$, and $T_{a,\text{center}}(t)$ can be estimated by multiplying $T_{\text{mm}}(t)$ by the factor

$$\eta = \left|\left\{1 - \frac{2}{e^z+e^{-z}}\right\} \Big/ \left\{1 - \frac{\tanh(z)}{z}\right\}\right| \tag{29}$$

Figure 6 shows $T_{a,\text{center}}/T_{a,\text{adia}}$ as a function of the Peclet number. $T_{a,\text{center}}/T_{a,\text{adia}}$ is unity when $\text{Pe}_\omega > 30$. In this region, the effect of the wall temperature does not extend to the center, and the gas near the center changes adiabatically. $T_{a,\text{center}}/T_{a,\text{adia}}$ decreases from unity when $\text{Pe}_\omega < 20$. In this range, the effect of the wall temperature extends to the center. $T_{a,\text{center}}/T_{a,\text{adia}}$ is proportional to the square root of the Peclet number. Consequently, we can conclude that the penetration depth reaches the center when Pe_ω is in the range from 20 to 30.

4.3 Expression as a Complex Nusselt Number. Our dimensionless heat transfer $Q_{\text{nd,adia}}$ is related to that proposed by Kornhauser and Smith [7]. Therefore, it is meaningful to convert our data to their Nusselt number, Eq. (7). Kornhauser and Smith used the mixed-mean temperature of the gas to define the number. However, the explicit expression is more favorable for design use and, as such, the adiabatic temperature amplitude is selected.

The results for helium and argon with a volume ratio of 1.1 are shown in Fig. 7. Equation (1) by Lee [2] and Eq. (8) by Kornhauser and Smith [7] are also plotted. Nu_r and Nu_i of Lee merge toward large Pe_ω. Those of Kornhouser and Smith are plotted for their application range of $\text{Pe}_\omega \geqslant 100$. Kornhauser and Smith [7] presented similar plots. The plots of Eqs. (1) and (8) presented in their paper are different from those shown in Fig. 7 due to the definition of gas temperature.

There is a rather wide scatter of Nu_i at high Pe_ω, especially in the case of argon. This appears to be due to the fact that the heat transfer is so small that the measurement error is amplified. Neglecting this scatter, both of the components of the complex Nusselt number can be concluded to be nearly equal for $\text{Pe}_\omega > 100$, which indicates that the heat flux leads the temperature by approximately 45 °C. Assuming a constant phase lead, Eq. (25) yields $\text{Nu}_r, \text{Nu}_i \propto \text{Pe}_\omega^{0.83}$.

The data lie near Kornhauser and Smith's correlation, Eq. (8), in their application range of $\text{Pe}_\omega \geqslant 100$. The exponent of 0.69 of Pe_ω in the correlation of Kornhauser and Smith is somewhat smaller than that of the present study, possibly because their Pe_ω range is extended to regions where the exponent is smaller ($\text{Pe}_\omega < 1000$). The extended heat transfer surface in their case comprise concentric fins made from brass tubes. Some were on the piston and the others were on the cylinder head, and they overlapped when the gas space was compressed. As such, the gap between opposing walls in Ref. [7] was different in the spaces depending on whether the tubes overlapped or not, while the gap is kept constant in the gas space in the present experiment. Their configuration is inevitable in experiments for high compression ratio, but the heat transfer would be a sum of heat transfer in the two spaces. Actually, we obtained results related to nonuniform gap spacing in our preliminary tests. We measured power loss for a configuration in which one-third volume of the gas space was filled with the extended surface with an interval of 4 mm. Surface area was 690 cm^2 and the extended surface occupied 54% of this area. When the frequencies were set to where Pe_ω was around 15 where the power loss has a maximum, measured losses were about 70% of the maximum, while power losses for other Pe_ω had the same characteristics as those obtained for the gas space in which the extended surface was uniformly installed. This can be interpreted as follows. Each space with different gap spacing causes power loss according to different Pe_ω reflecting different D_h. D_h in a part of the gas space with the extended surface is 41–48% of overall D_h and that in the rest space is 1.9–2.2 times of overall D_h. There is no space where Pe_ω is in the range to make power loss large as the maximum. This results in the lower power loss. Since heat

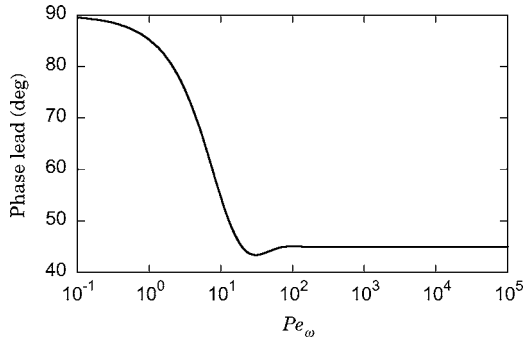

Fig. 8 Phase lead of heat flux against volume change

transfer varies monotonically against Pe_ω, the effect of nonuniform gap spacing cannot be observed clearly. However, it is still important for the reliability of data.

The present data fall above the values given by Lee's equation. Since the exponent in our case is larger than that of Lee, phenomena different from pure conduction, for example, convection, probably affect heat transfer here.

On the other hand, both Nu_r and Nu_i show excellent agreement with Lee's equation for $\mathrm{Pe}_\omega < 100$. As Pe_ω approaches zero, Nu_i becomes dominant. The heat flux is maximum at midstroke, where volume change rate is maximum. The heat transfer can be explained by the periodic heat conduction when $\mathrm{Pe}_\omega < 100$, although Lee's analysis assumes incompressible medium. The phase lead of the heat flux with respect to Pe_ω is summarized in Fig. 8. Based on the above considerations, it is possible to approximate the instantaneous heat flux from Eqs. (21) and (23)–(25), with the phase lead shown in Fig. 8.

5 Conclusions

Heat transfer during compression and expansion of gas was measured and correlated in a form that is more useful in design work. The mechanism of heat transfer was discussed. The results are summarized as follows.

(1) $\gamma Q_{\mathrm{in}}/(2\sqrt{\rho_0 c_p \lambda/\omega} A T_{a,\mathrm{adia}})$ is the best choice of dimensionless group for the heat transfer and can be correlated with only the Peclet number $\omega D_h^2/4\alpha$, even for gases with different specific heat ratios. The correlation is described in Eqs. (21) and (23)–(25).
(2) The instantaneous heat flux during the change of state can be obtained approximately from Eqs. (21) and (23)–(25) with the phase lead given in Fig. 8.
(3) At frequencies of $\mathrm{Pe}_\omega < 100$, the heat transfer results from periodic heat conduction in the gas.
(4) At frequencies of $\mathrm{Pe}_\omega > 100$, the dependence of Pe_ω on heat transfer is stronger than that of heat conduction. Heat transfer is probably affected by convection in this region.
(5) The value of $T_{a,\mathrm{center}}/T_{a,\mathrm{adia}}$ is unity for $\mathrm{Pe}_\omega > 30$. $T_{a,\mathrm{center}}/T_{a,\mathrm{adia}}$ is proportional to the square root of the Peclet number when $\mathrm{Pe}_\omega < 20$. The penetration depth of wall temperature reaches the centerline when Pe_ω is in the range from 20 to 30.

Nomenclature

A = surface area (m^2)
c_v = specific heat at constant volume (J/kg K)
c_p = specific heat at constant pressure (J/kg K)
d = cylinder bore (m)
D_h = hydraulic diameter, $4V/A$
i = $\sqrt{-1}$
L = compressibility number defined by Lawton [6]
Nu_i = imaginary part of the Nusselt number defined by Eq. (7)
Nu_r = real part of the Nusselt number defined by Eq. (7)
P, P_0 = pressure, mean pressure (Pa)
Pe_ω = Peclet number, $\omega D_h^2/4\alpha$
q = heat flux ($\mathrm{W/m}^2$)
Q = amount of heat transfer during a half-cycle (J/cycle)
R = gas constant (J/kg K)
Re = Reynolds number, $u_p d/\nu$
t = time (s)
t_0 = time constant used by Lawton [6] (s)
T = temperature (K)
T_w = wall temperature (K)
U = internal energy (J)
V, V_0 = volume, mean volume (m^3)
W_{loss} = hysteresis work loss (J/cycle)
x = distance from wall (m)
z = $(1+i)l/\delta$

Greek Symbols

α = thermal diffusivity (m^2/s)
δ = length corresponding penetration depth (m)
γ = specific heat ratio
η = temperature amplitude ratio defined with Eq. (29)
θ = crank angle (deg)
λ = thermal conductivity (W/m K)
ρ = density ($\mathrm{kg/m}^3$)
ω = angular frequency (rad/s)

Subscripts

a = amplitude
adia = adiabatic change
center = centerline
in = direction from wall to gas
max = maximum
min = minimum
mm = mixed mean
nd = dimensionless number

Superscript

isoth = isothermal change

References

[1] Organ, A. J., 1997, *The Regenerator and the Stirling Engine* Mechanical Engineering, London, pp. 51–65.
[2] Lee, K. P., 1983, "A Simplistic Model of Cyclic Heat Transfer Phenomena in Closed Spaces," *Proceedings of the 18th IECEC*, pp. 720–723.
[3] Pourmovahed, A., and Otis, D. R., 1984, "Effects of Thermal Damping on the Dynamic Response of a Hydraulic Motor-Accumulator System," ASME J. Dyn. Syst., Meas., Control, **106**, pp. 21–26.
[4] Kornhauser, A. A., and Smith, J. L., Jr., 1993, "The Effects of Heat Transfer on Gas Spring Performance," ASME J. Energy Resour. Technol., **115**, pp. 70–75.
[5] Faulkner, H. B., and Smith, J. L., Jr., 1983, "Instantaneous Heat Transfer during Compression and Expansion in Reciprocating Gas Handling Machinery," *Proceedings 18th IECEC*, pp. 724–730.
[6] Lawton, B., 1987, "Effect of Compression and Expansion on Instantaneous Heat Transfer in Reciprocating Internal Combustion Engines," Proc. Inst. Mech. Eng., **201**, pp. 175–186.
[7] Kornhauser, A. A., and Smith, J. L., Jr., 1994, "Application of a Complex Nusselt Number to Heat Transfer During Compression and Expansion," ASME J. Heat Transfer, **116**, pp. 536–542.
[8] Press, W. H., Teukolsky, S. A., Vetterling, W. T., and Flannery, B. P., 1992, *Numerical Recipes in Fortran 77 Second Edition*, Cambridge University Press, Cambridge, UK, pp. 644–649.

Numerical Study of Dielectric Fluid Bubble Behavior Within Diverging External Electric Fields

Matthew R. Pearson
e-mail: pearmat@iit.edu

Jamal Seyed-Yagoobi
e-mail: yagoobi@iit.edu

Two-Phase Flow and Heat Transfer Enhancement Laboratory,
Mechanical, Materials, and Aerospace Engineering Department,
Illinois Institute of Technology,
10 W. 32nd Street,
Chicago, IL 60616

A three-dimensional mathematical model is presented that models bubble deformation of a dielectric fluid due to the presence of a nonuniform electric field and calculates the net dielectrophoretic force that is exerted by the electric field on the bubble. The study includes the development of a method of predicting the shape of a bubble based on the arbitrary distribution of stresses over its surface without requiring an axisymmetric configuration. The reciprocal effect of the bubble's presence on the electric field is also incorporated into the model, and dimensional analysis is used to obtain a single key parameter that governs the bubble deformation phenomenon. Numerical implementation of the mathematical model shows that the bubble deformation can be significant. Furthermore, bubble deformation and electric field distortion can have significant effects on the dielectrophoretic behavior of bubbles in nonuniform fields, especially within small-scale devices where the bubble size and electrode spacing are similar in magnitude.
[DOI: 10.1115/1.2804937]

Introduction

As electronic chip components become faster and more compact, the magnitude of the generated heat flux is rapidly rising and it is becoming increasingly difficult to effectively remove this heat from the core of the chip to maintain performance and reliability. As microchips continue to grow in power and capability, it is crucial to find new ways of transporting heat away from the chip. Early central processing units (CPUs) in personal computers required little or no thermodynamic consideration during their design. In the latest computers, it is not uncommon to find a heat sink that dwarfs the microchip, along with a multitude of cooling fans, in order to prevent the overheat of the processor.

Microheat pipes (MHPs) have shown great potential as a highly effective way of removing very high heat fluxes from sources of heat such as CPUs. Conventional heat pipes utilize the capillary force existing in wicking structures to pump the liquid to an evaporator section, where the liquid evaporates and returns to the condenser section. Due to the two-phase nature of the flow, very high heat fluxes can be achieved. A MHP concept, which combined phase-change heat transfer with microelectromechanical systems (MEMS) was first proposed by Cotter [1]. Babin et al. [2] further described an MHP as "a wickless, noncircular channel." Instead of using a wicking structure, the capillary forces in MHPs exist in the corners of a noncircular flow channel with microscale cross-sectional dimensions. Many researchers, including Mallik et al. [3], Peterson and Ma [4], Peterson [5], Le Berre et al. [6], and Lee et al. [7], have used MHP designs with a triangular cross section.

The performance of a MHP depends on many factors, including the properties of the working fluid, the magnitude of the capillary forces, the dimensions of the heat pipe, and the operating conditions. Its maximum heat transport rate is subsequently limited by various physical phenomena, which include the capillary limitation, entrainment limitation, viscous limitation, sonic limitation, and boiling limitation [8]. The capillary limitation is reached when the capillary pressure difference generated in the corners of the noncircular MHP can no longer overcome the viscous and hydrostatic pressure losses. When this limitation is reached, the liquid in the condenser section cannot be pumped quickly enough to the evaporator section, causing the heat pipe evaporator to dry out. As a consequence, the transport of heat from the evaporator to the condenser shuts down. The entrainment limitation also results in the dry-out of the heat pipe evaporator due to the liquid droplet entrainment by the liquid/vapor interfacial shear stress. The other limitations, such as the viscous, sonic, and boiling limitations, limit the heat transport capacity of the heat pipe due to the dominant viscous forces, the choked flow, and the blocked liquid flow by bubbles, respectively.

All of these limitations serve to narrow the selectable operating conditions for satisfactory MHP performance. However, Babin et al. [2] suggested that the most restrictive limitation governing maximum heat transport capacity of a MHP is almost always the capillary limitation. When this limit is reached, the only way to improve the performance of the MHP is to provide an additional body force to help pump the liquid from the condenser to the evaporator.

One such body force that can be introduced is an electric body force, but there has been little research to investigate how electrohydrodynamic (EHD) phenomena may be able to help overcome this capillary limitation of MHPs. However, these EHD phenomena are well researched in other areas of heat transfer, especially pool boiling. EHD phenomena involve the interaction of electric fields and flow fields in a dielectric fluid medium, and this interaction can induce a fluid motion by an electric body force. The electric body force density acting on the molecules can be expressed as [9]

$$\mathbf{f}_e = \rho_f \mathbf{E} - \frac{1}{2} E^2 \nabla \varepsilon + \frac{1}{2} \nabla \left[E^2 \rho \frac{\partial \varepsilon}{\partial \rho} \right] \tag{1}$$

The first term represents the Coulomb force, which is the force acting on the free charges in an electric field. The second and third terms, titled dielectrophoretic and electrostriction forces, respectively, represent the polarization force acting on polarized charges. The third term is relevant only for compressible fluids. Thus, in the case of incompressible fluids, the electric body force requires either a free space charge or a gradient in permittivity within the fluid. In many fluids used for cooling, especially cryogenics, the Coulomb force is weak but the difference in permittivity between

Contributed by the Heat Transfer Division of ASME for publication in the JOURNAL OF HEAT TRANSFER. Manuscript received September 5, 2006; final manuscript received May 25, 2007; published online March 6, 2008. Review conducted by Raj M. Manglik. Paper presented at the Ninth AIAA/ASME Joint Thermophysics and Heat Transfer Conference, 2006.

the liquid and vapor phases allows the dielectrophoretic force to exist and enhance separation of the two phases. In theory, this separation enhancement can be used to augment or even replace the capillary force generated in a MHP, thereby helping to overcome the capillary limitation and improve the maximum attainable heat flux.

Therefore, unlike most previous dielectrophoretic force studies that have investigated the use of the force as a method of improving the heat flux of an evaporator by assisting in the removal of vapor bubbles from the heated surface (e.g., Refs. [10,11]), the motivation for this study is significantly different—to investigate the application of dielectrophoretic force as the underlying pumping mechanism for a two-phase heat transport device. Although there have been several studies of macroscale heat pipes with EHD enhancement (e.g., Ref. [12]) and limited studies of EHD-assisted MHPs (e.g., Ref. [13]), none of these studies has investigated the deformation that bubbles exhibit when subject to a nonuniform electric field or the corresponding changes to net dielectrophoretic force that result from this deformation.

This study investigates the full 3D deformation of a bubble when subject to a nonuniform electric field, in order to better understand the effect that dielectrophoretic force may have on a MHP as a system. Past studies of bubble deformation have typically utilized uniform fields, but to achieve the objective of enhanced separation of liquid and vapor phases within a MHP, there should be a gradient of electric field intensity. Consequently, uniform fields are unsuitable for use in this context. The fundamental equations that govern the shape of a three-dimensional bubble in an arbitrary, nonuniform electric field are derived and studied from first principles. These equations are vastly more complicated than in previous axisymmetric studies because the curvature of a surface is a much more complex subject than the curvature of a line. A comprehensive nondimensionalization procedure, presented here, reduces the number of parameters governing the bubble deformation to one. Finally, a numerical simulation predicts the bubble shape and the net dielectrophoretic force that acts on the bubble.

Previous Studies

Early research by Garton and Krasuchi [14] studied the effect of a uniform dc electric field on a bubble when suspended in a bulk, liquid medium. The presence of the field was shown to cause the bubbles to deform into prolate spheroids, with the elongation occurring along the electric field lines. Other studies by Melcher and Taylor [15] and Miksis [16] also focused on suspended bubbles or droplets with similar findings. Later, Ogata and Yabe [17] presented a numerical and experimental study of the deformation of vapor bubbles attached to a wall when exposed to a uniform electric field that was generated between two parallel plate electrodes.

The experimental portion of the study by Ogata and Yabe [17] used a high-speed video camera to record the deformation of a vapor bubble that was injected into the liquid medium through a hole in the lower electrode. The experimental findings showed that, in the presence of a uniform electric field, the bubbles generated by the injection hole became elongated, and their departure from the lower electrode appeared to be inhibited. The numerical study sought to quantitatively verify the experimental findings by modeling the electric forces that affect the bubble behavior. Due to the homogeneity of the imposed electric field, an axis of symmetry existed along the vertical centerline of the bubble, reducing the dimensionality of the problem to two and greatly simplifying many of the governing equations. First, the potential field was solved, recognizing that the presence of the bubble has an effect on the field. From the potential field, the electric field intensity and the Maxwell stresses were found on the surface of the bubble interface. The bubble geometry was then found from a stress balance at the liquid-vapor interface. The potential field and bubble shape were iterated until both reached convergence. The numerical results verified that a vertical component of the electrostatic forces (i.e., Maxwell stresses and electrostriction effects) existed that pushed the bubble against the grounded plate electrode. Due to axisymmetry, the net horizontal force was zero. The numerical study was designed to replicate the specific conditions and dimensions of the experimental setup, so a full dimensional analysis was not completed to reduce the number of parameters involved in the equations.

Any previous studies of bubble behavior within nonuniform fields have assumed that bubbles do not undergo deformation. The effect of nonuniform electric fields on bubble motion was studied by Jones and Bliss [18] by considering the induced dipole of a small, electrically insulating sphere of radius R_0 and the resulting dielectrophoretic force caused by a nonuniform electric field. The resulting force was given by

$$\mathbf{F}_e = 2\pi R_0^3 \frac{\varepsilon_l(\varepsilon_v - \varepsilon_l)}{\varepsilon_v + 2\varepsilon_l} \nabla E^2 \tag{2}$$

An equivalent expression for the force on a prolate spheroid was also presented but required known lengths of the major and minor axes. Jones and Bliss [18] and Hara and Wang [19] used the dielectrophoretic force on a sphere, predicted by Eq. (2), along with approximations of buoyancy and drag forces, to numerically simulate bubble trajectories with a range of different imposed, nonuniform electric fields. Jones and Bliss [18] used the field generated between the two diverging plate electrodes, while Hara and Wang [19] generated a field between a plate and a cylinder. Experimental studies replicated the same electrode geometries as the numerical simulation, and in both studies, the numerically predicted bubble trajectories agreed well with experimental observations. However, the amount of bubble deformation observed during experiments was noted to be small, thereby improving the validity of Eq. (2) and contributing to the accuracy of the numerical solution. Jones and Bliss [18] attributed the small amount of bubble deformation in experiments to the bubbles being very small in size when compared to the electrode spacing.

In order to enhance the separation of the liquid and vapor phases, nonuniform fields are required to impart a net dielectrophoretic force on the bubble. However, for a small-scale heat transport device such as a MHP, the size of the bubbles can be the same order of magnitude as the device dimensions. Even under uniform electric fields, Ogata and Yabe [17] showed significant bubble deformation and distortion of the surrounding electric field when the bubble radius and electrode spacing are the same order of magnitude, so the same deformation effects are expected to be present in equal or greater amounts when the imposed electric field is not uniform. Therefore, it is not appropriate to use Eq. (2) to predict the bubble motion under such circumstances. However, no studies of bubble deformation have attempted to predict the bubble shape when the imposed conditions are not axisymmetric with respect to the bubble centerline.

Numerical Model

The fundamental challenge associated with extending bubble deformation modeling from 2D axisymmetric to full 3D arises from the equations that govern the shape of a bubble that is subject to an arbitrary distribution of stresses over its surface. The axisymmetric assumption greatly simplifies the analysis because the curvature of a line is much more easily calculated than the curvature of a surface. Due to the presence of surface tension at the interface, the curvature and shape of a bubble are directly related to the distribution of stresses over the interface. The equation giving the curvature of an axisymmetric bubble can be found in many engineering textbooks that discuss two-phase flow, but curvature equations of arbitrary surfaces are generally found only in advanced geometry textbooks, and the process of finding a three-dimensional surface based solely on its curvature distribution is largely unexplored. Furthermore, the potential and electric fields must be computed in three dimensions, whereas the previ-

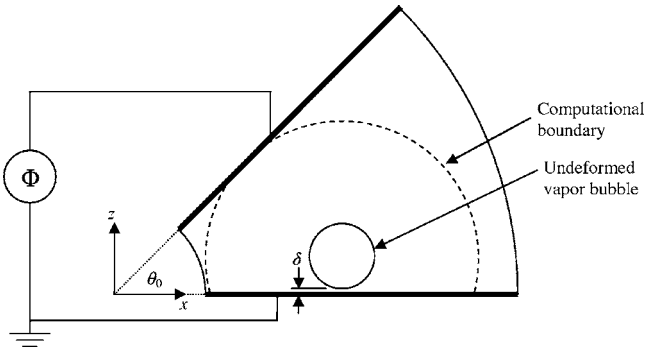

Fig. 1 Schematic of electrode configuration

ously cited works have used two-dimensional fields. An overview of the numerical model is provided here. A more detailed description and derivation of the governing equations involved in the numerical model can be found in Ref. [20].

Potential and Electric Fields. The electrode configuration used to impose the nonuniform electric field is illustrated in Fig. 1. Two plate electrodes are positioned a small distance apart with a fixed angle of $\theta_0=45$ deg between them. Note that the domain is three dimensional and therefore there is a y-coordinate axis pointing out of the page in Fig. 1. Because of the nonuniform nature of the field, the bubble cannot be expected to remain axisymmetric. However, a plane of symmetry does exist in the xz plane, passing through the center of the bubble. Taking advantage of this plane of symmetry allows the computational workload to be halved. This study models the deformation of a bubble that already exists (either due to evaporative heat transfer or by injection of vapor) and that has an internal pressure such that, in the absence of any electric field, its shape would be a sphere of radius R_0. The modeling is based on the following assumptions:

1. The bubble is static and the effects of gravity on the bubble shape are negligible.
2. The pressure inside the deformed bubble is uniform and has a known value.

In addition, the bubble is assumed to have just departed from the lower plate so that the effects of contact angle, microlayer, and disjoining pressure can be neglected. Therefore, the lowermost point on the bubble is tangent to the lower plate electrode, separated from it by an arbitrary, small distance, δ. For this study, a value of $\delta=0.01R_0$ is used. A nonzero value of δ is also necessary to avoid singularities in the numerical code.

The following nondimensional variables are defined:

$$\phi^* \equiv \frac{\phi}{\Phi} \quad E^* \equiv \frac{E}{E_0} \quad \sigma_M^* \equiv \frac{\sigma_M}{(\varepsilon_l - \varepsilon_v)E_0^2} \quad \Delta P^* \equiv \frac{\Delta P}{\sigma/R_0}$$

$$H^* \equiv R_0 H \quad R^* \equiv \frac{R}{R_0} \tag{3}$$

where the characteristic electric field intensity E_0 is expressed in terms of the applied potential Φ and the length scale R_0 as

$$E_0 \equiv \frac{\Phi}{R_0} \tag{4}$$

Note that R_0 is essentially a length scale that is formed by the prescribed hydrostatic pressure difference across the liquid-vapor interface and the interfacial surface tension. Due to the assumption that pressure inside the bubble is uniform, $\Delta P^*=2$ because the pressure difference across the interface of an undeformed (spherical) bubble with the same internal pressure as the prescribed pressure of the deformed bubble is given by the Young–Laplace equation as

$$\Delta P = \frac{2\sigma}{R_0} \tag{5}$$

In the absence of free charges in the liquid volume, the potential field in the liquid is governed by the Laplace equation,

$$\nabla^{*2}\phi^* = 0 \tag{6}$$

with $\phi^*=1$ at the upper electrode plate boundary, $\phi^*=0$ at the lower electrode plate boundary, and $\partial\phi^*/\partial n=0$ at all other domain boundaries, which corresponds to an electrically insulating boundary condition. The vapor bubble is also treated as an insulator (the conductivity of the vapor phase of a fluid is typically several orders of magnitude less than the conductivity of the liquid phase), so $\partial\phi^*/\partial n=0$ is also applied as a boundary condition to the liquid-vapor interface of the bubble. The definition of electric field allows direct solution from the potential field,

$$\mathbf{E}^* = -\nabla^*\phi^* \tag{7}$$

Interfacial Stress Balance. Maxwell stresses at the liquid-vapor interface are caused by the sharp permittivity gradient that exists. In the absence of any stress components caused by electrostriction effects, the dimensionless Maxwell stresses are related to the electric field at the surface by

$$\sigma_M^* = -\frac{1}{2}(E^*)^2 = -\frac{1}{2}\mathbf{E}^* \cdot \mathbf{E}^* \tag{8}$$

By assuming that the vapor has a permittivity approximately equal to vacuum permittivity and obeys the Clausius–Mossotti relation, then from the relation it follows that electrostriction is negligible in the vapor phase. Electrostriction also has no effect in the liquid phase if the liquid is incompressible [21]. Note that although Ogata and Yabe [17] neglected electrostriction in the vapor phase, the contribution of electrostriction in the liquid phase was incorrectly included.

A stress balance at the interface governs the equilibrium shape of the bubble. In the absence of additional stresses such as Maxwell stresses, the hydrostatic pressure difference between the vapor and the liquid phases is balanced by the surface tension and curvature of the interface, which gives rise to the Young–Laplace equation. With additional stress components present, these components are introduced as additional terms in the stress balance. Accounting for hydrostatic pressure differences, surface tension effects, and Maxwell stresses, the mean curvature of the interface H must everywhere satisfy Eq. (9) for equilibrium of normal stresses to exist.

$$H^* = -\frac{1}{2}(\Delta P^* + \mathrm{Bo}_E \sigma_M^*) \tag{9}$$

The parameter introduced into Eq. (9) is the dielectric Bond number, representing the ratio of Maxwell stresses to surface tension stresses, and defined as

$$\mathrm{Bo}_E = \frac{(\varepsilon_l - \varepsilon_v)E_0^2 R_0}{\sigma} \tag{10}$$

Note that the only value that must be prespecified for the numerical simulation to operate is the value of the parameter Bo_E and that bubble deformation behavior depends entirely on the value of this single parameter. The value of Bo_E depends both on fluid properties and on the potential that is applied to the high-voltage electrode, Φ. Therefore, for a given fluid, increasing the value of Bo_E corresponds to increasing the magnitude of this applied voltage. Inspection of this parameter reveals that bubble deformation may be minimal for very small bubbles when they are within a comparatively large electrode configuration (corresponding to low values of σ_M^*). Under such conditions, bubble deformation can be

negligible, as noted visually by Jones and Bliss [18], and Eq. (2) may be sufficiently accurate. However, within a microscale heat transfer device, bubble size may take the same order of magnitude as the characteristic electrode spacing, resulting in significant bubble deformation and dielectrophoretic force alteration even for relatively low values of Bo_E.

Prescribed Mean Curvature Surface. The equations governing potential field, electric field, Maxwell stresses, and stress balance are well known. However, the concept of solving a quasisteady surface from an arbitrary, asymmetric, prescribed mean curvature (PMC) field is not well studied mathematically or numerically, especially in a spherical coordinate system. The mean curvature distribution given by Eq. (9) must be translated into a geometric surface that represents the interface between the liquid bulk and the vapor bubble. This work presents a finite-difference method of solving a PMC surface. The surfaces studied here are spherical in nature, but the same approach could be used for any type of surface.

The mean curvature of an arbitrary surface, defined by a vector function $\mathbf{x}(\theta,\varphi)$ of two parameters θ and φ, is given by [22]

$$H = \frac{(\mathbf{x}_{\theta\theta}\mathbf{x}_\theta\mathbf{x}_\varphi)\|\mathbf{x}_\varphi\|^2 - 2(\mathbf{x}_{\theta\varphi}\mathbf{x}_\theta\mathbf{x}_\varphi)(\mathbf{x}_\theta\cdot\mathbf{x}_\varphi) + (\mathbf{x}_{\varphi\varphi}\mathbf{x}_\theta\mathbf{x}_\varphi)\|\mathbf{x}_\theta\|^2}{2(\|\mathbf{x}_\theta\|^2\|\mathbf{x}_\varphi\|^2 - (\mathbf{x}_\theta\cdot\mathbf{x}_\varphi)^2)^{3/2}} \tag{11}$$

where subscripts denote partial derivatives and the scalar triple product is defined as

$$(\mathbf{abc}) \equiv \mathbf{a}\cdot(\mathbf{b}\times\mathbf{c}) \tag{12}$$

For a spherical bubble that is centered at the origin, spherical coordinates can be used to most simply represent the interface as

$$\mathbf{x} = R_0\begin{Bmatrix}\cos\theta\cos\varphi\\ \sin\theta\cos\varphi\\ \sin\varphi\end{Bmatrix} \tag{13}$$

where R_0 is a constant equal to the bubble radius. The parameters θ and φ now represent the azimuth and inclination angles of a spherical coordinate system. The origin of this coordinate system can be placed anywhere in relation to the two plate electrodes, therefore allowing the position of the bubble to be prescribed.

By relaxing the requirement that the radius be constant everywhere, a more generalized interface surface can be parametrized as

$$\mathbf{x} = R(\theta,\varphi)\begin{Bmatrix}\cos\theta\cos\varphi\\ \sin\theta\cos\varphi\\ \sin\varphi\end{Bmatrix} \tag{14}$$

where R is an unknown function of the two parameters. With this choice of parametrization vector $\mathbf{x}$, Eq. (11) becomes

$$H(\theta,\varphi) = \frac{(R^2+\tilde{R}_\theta^2)R_{\varphi\varphi} - 2\tilde{R}_\theta R_\varphi \tilde{R}_{\theta\varphi} + (R^2+R_\varphi^2)\tilde{R}_{\theta\theta}}{2R(R^2+\tilde{R}_\theta^2+R_\varphi^2)^{3/2}} - \frac{R(2R^2+3\tilde{R}_\theta^2+3R_\varphi^2) + R_\varphi(R^2+2\tilde{R}_\theta^2+R_\varphi^2)\tan\varphi}{2R(R^2+\tilde{R}_\theta^2+R_\varphi^2)^{3/2}} \tag{15}$$

where

$$\tilde{R}_\theta = R_\theta\sec\varphi \quad \tilde{R}_{\theta\theta} = R_{\theta\theta}\sec^2\varphi \quad \tilde{R}_{\theta\varphi} = R_{\theta\varphi}\sec\varphi \tag{16}$$

Equation (15) also applies to the dimensionless variables by replacing H with H^* and R with R^*. The left hand side of the dimensionless form of Eq. (15) is known from Eq. (9), making it a second-order, nonlinear partial differential equation that must be solved to give $R^*(\theta,\varphi)$, using the boundary conditions illustrated in Fig. 2.

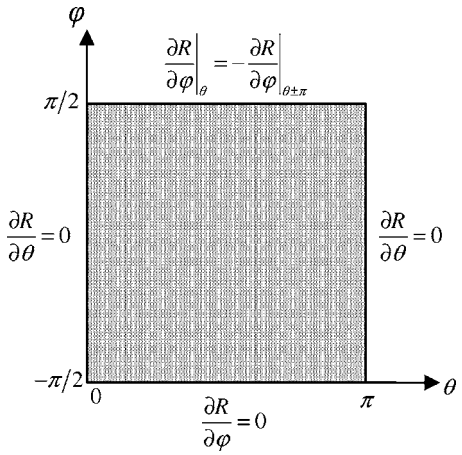

Fig. 2 Boundary conditions for Eq. (15)

The left and right boundary conditions are reflective due to the xz plane of symmetry through the center of the bubble. The lower and upper boundaries represent the south and north pole singularities of the spherical coordinate system. (Just as 2D polar coordinates have an intrinsic singularity at $r=0$, 3D spherical coordinates have singularities at $r=0$ and $\varphi=\pm\pi/2$.) At these two locations, the governing equation is modified to remove the coordinate singularities. This is accomplished by parametrizing the bubble surface in a second spherical coordinate system in which the poles are located elsewhere, and using the governing equation in this second coordinate system to obtain values of R at the poles. The lower boundary condition is then imposed to ensure that the south pole of the bubble is tangent to the lower electrode plate. The upper boundary condition ensures that the bubble surface remains smooth across the north pole. The resulting numerical solution of $R(\theta,\varphi)$ can be used in Eq. (14) to describe a surface of an arbitrary shape (not necessarily a sphere) that represents the interface between the vapor phase of the bubble and the liquid phase of the surrounding fluid. The only limitation on the extent of bubble deformation that can be modeled with this scheme is the requirement that $R(\theta,\varphi)$ be single valued.

Dielectrophoretic Force. With a converged bubble shape and potential field distribution, the net dielectrophoretic force acting on the bubble is computed by integrating the Maxwell stresses over the surface of the interface,

$$\mathbf{F}_e^* = \oiint_S \sigma_M^*\hat{\mathbf{n}}dA^* \tag{17}$$

where the dimensionless force and dimensionless area are defined as

$$\mathbf{F}_e^* = \frac{\mathbf{F}_e}{\mathrm{Bo}_E\sigma R_0} \quad A^* = \frac{A}{R_0^2} \tag{18}$$

Both the unit normal vector field to the surface and the differential areas of the surface, required in Eq. (17), can be evaluated directly from the surface parametrization [22]:

$$\hat{\mathbf{n}}(\theta,\varphi) = \frac{\mathbf{x}_\theta\times\mathbf{x}_\varphi}{\|\mathbf{x}_\theta\times\mathbf{x}_\varphi\|} = \frac{1}{\sqrt{R^2+\tilde{R}_\theta^2+R_\varphi^2}} \cdot\begin{Bmatrix}(R\cos\varphi+R_\varphi\sin\varphi)\cos\theta+\tilde{R}_\theta\sin\theta\\ (R\cos\varphi+R_\varphi\sin\varphi)\sin\theta-\tilde{R}_\theta\cos\theta\\ R\sin\varphi-R_\varphi\cos\varphi\end{Bmatrix} \tag{19}$$

$$dA = \|\mathbf{x}_\theta \times \mathbf{x}_\varphi\| d\theta \wedge d\varphi = R \cos\varphi \sqrt{R^2 + \tilde{R}_\theta^2 + R_\varphi^2}\, d\theta \wedge d\varphi \quad (20)$$

where "$\wedge$" is the wedge product.

Discussion of Solution Multiplicity. There may be multiple solutions that satisfy Eq. (15) subject to the boundary conditions in Fig. 2, for example, when the mean curvature over the entire surface is a constant equal to $-1/R_0$. The most obvious solution to this mean curvature field is a sphere that is centered at the origin, having $R(\theta,\varphi)=R_0$. However, a sphere centered at an arbitrary location will also satisfy the mean curvature field, provided that the radius is still equal to R_0. For example, a sphere centered at the Cartesian location (a,b,c) with radius R_0 and satisfying $a^2+b^2+c^2 \leq R_0^2$ will have a radius function of

$$R(\theta,\varphi) = (a\cos\theta\cos\varphi + b\sin\theta\cos\varphi + c\sin\varphi) + \sqrt{(a\cos\theta\cos\varphi + b\sin\theta\cos\varphi + c\sin\varphi)^2 - (a^2+b^2+c^2) + R_0^2} \quad (21)$$

Substitution of Eq. (21) into Eq. (15) gives $H=-1/R_0$ for any value of a, b, and c. The left and right boundary conditions in Fig. 2 require that $b=0$, and the lower boundary condition further requires that $a=0$. However, none of the boundary conditions constrains the value of c, the vertical (z) location of the sphere center. Thus, an infinite number of solutions exist. For this reason, the numerical procedure is constrained to require that the south pole of the bubble be a fixed distance δ from the lower plate electrode.

Numerical Method

Early results were obtained by numerically computing the potential field within the entire volume between the two electrode plates. However, it was noted from these results that the potential field is only affected by the presence of the bubble in a thin layer near the bubble surface, and that the potential field outside this layer is approximated very accurately by the analytical expression for the potential field in the domain with no bubble present, Eq. (22). To reduce the computational load and to improve grid independence, the potential field is solved numerically only within the volume between the bubble surface and a predefined outer computational boundary surface, which is drawn as a dashed line in Fig. 1. This volume represents a boundary layer within which the potential field is altered significantly due to the bubble's presence, while the changes to the potential field outside the boundary are negligible. In this study, the computational boundary surface was defined as a sphere of radius 4, centered at the origin of the spherical coordinate system on which the bubble radius function is based. For all of the numerical cases in this study, this outer computational boundary surface was sufficiently large that further enlargement affected the numerical results by less than 1%.

The potential field outside this computational boundary is approximately governed by [23]

$$\phi^* = \frac{\theta}{\theta_0} \quad (22)$$

Equation (22) is the exact solution to the potential field between the two electrode plates in the absence of a bubble. This nominal field is used as a Dirichlet condition on the outer computational boundary surface.

To solve the potential field within the numerical domain, the volume between the arbitrarily shaped bubble and the outer boundary surface is mapped, using a coordinate transformation, into a computational domain representing the volume between two concentric spheres. The surface of the inner sphere then represents the bubble interface, and the surface of the outer sphere represents the outer boundary surface. A proprietary multigrid iterative solver is used within MATLAB® to relax the potential field distribution within the computational domain. During each iteration, the Maxwell stresses are recalculated based on the latest potential field distribution, giving a PMC field over the bubble surface. The nonlinear solvers within the MATLAB Optimization Toolbox are then used to relax the bubble shape, based on this PMC field. Every time the bubble shape is relaxed, the mapping between the physical and computational domains must be modified.

All terms of the differential operators are approximated using second-order-accurate, central differences. A $33\times33\times65$ grid is used in this study to generate the solution data, which provides sufficiently grid-independent results. During grid dependence trials, the truncation error on this grid was found to be no greater than 1.3×10^{-3} when compared to a grid that was twice as fine ($65\times65\times129$). The solution is considered to be converged once the maximum relative error of both the potential field and the bubble radius function are less than 10^{-5}. Under typical situations, the bubble radius converges more quickly and often reaches a relative error of almost 10^{-6} by the time the potential field has satisfied the convergence criterion.

Numerical Model Validation. To support the validity of the developed numerical model, numerical results were obtained and compared to an experimental study by Herman et al. [24], which visualized the shape of bubbles in microgravity under a nominal electric field that was approximately uniform. The experimental setup generated bubbles by injection of air into a liquid. The liquid was 3M™ Performance Fluid PF-5052, which has an electric permittivity (ε_v) of 1.5×10^{-11} F/m and interfacial surface tension (σ) of 1.3×10^{-2} N/m [24]. The electric field was imposed by two parallel disks, spaced 20 mm apart and each having a diameter of 15 mm. The bubble was injected through a 1.5 mm diameter hole drilled through the center of lower electrode. A dc voltage was applied to the upper electrode and the lower electrode was grounded.

For numerical comparisons, the two electrodes were taken to have infinite diameter, and the 10 kV applied voltage case was used. For convenience, the characteristic length scale R_0 was taken as the distance between the two electrodes, rather than as an undeformed bubble radius. Consequently, the dimensionless pressure ΔP^* no longer had a value of 2 and was instead treated as the sole parameter, adjusted to provide optimal results. Substituting the fluid properties, applied voltage, and characteristic length scale into Eq. (10), the experimental case was characterized by a dielectric Bond number of $\mathrm{Bo}_E=2.3$.

The numerical bubble shape data are shown in Fig. 3 as the white wire mesh, superimposed onto the photograph of the bubble under the aforementioned experimental conditions. Note that the second, departed bubble was assumed to have no effect on the shape of the main, departing bubble. The numerical electrode locations can be seen on the figure as white bars, aligned with the actual location of the electrodes in the photograph. Figure 3 clearly shows a very close match between numerical and experimental data, except at the lower side, where the "pinching" effect relating to the bubble's contact angle with the solid plate is still evident—the bubble has not quite finished departing from the plate. The numerical simulation currently does not model contact angles, so this effect must be ignored.

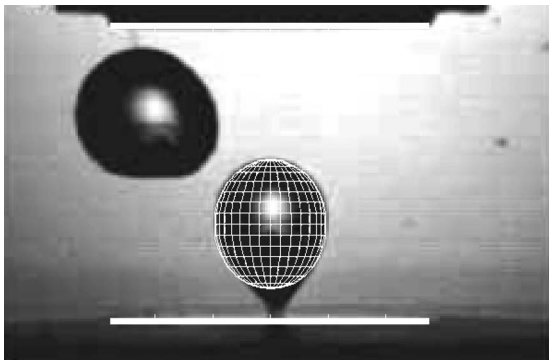

Fig. 3 Comparison of numerically computed and experimentally observed bubble shapes [24]

Recalling that the dimensionless pressure ΔP^* was treated as a parameter, the value that produced the numerical data in Fig. 3 corresponds to an actual pressure difference of 7.51 Pa. In the absence of an electric field, a bubble with this interfacial pressure difference would be a sphere of radius 3.46 mm (from the Young–Laplace equation) with a departure volume of 174 mm^3. This value agrees extremely well with the experimentally observed departure volume of 177 mm^3 under the absence of any electric field. The close agreement of the bubble shapes in Fig. 3 coupled with the similar values of bubble departure volume serves to confirm the validity of the numerical scheme that has been developed.

Numerical Results and Discussion

Bubble Geometry and Maxwell Stress Intensity. For the nonuniform electric field geometry given in Fig. 1, numerical data were obtained for three values of the dielectric Bond number, Bo_E. The bubble is positioned at $x^*=5$, immediately adjacent to the lower electrode. Figures 4–6 show the numerically predicted bubble shape for dielectric Bond numbers of 2.5, 5.0, and 7.5, respectively, when viewed in the xz plane.

Coloring of the bubble surface is based on the local magnitude of the dimensionless Maxwell stress intensity. The actual dimensionless Maxwell stress intensity values are everywhere negative, and therefore act from the outside of the bubble (liquid phase) toward the inside of the bubble (vapor phase). Note that the coloration is also related to the local electric field intensity by Eq. (8). The axes of the figure are equally scaled to ensure that the true geometric shape of the bubble is correctly portrayed.

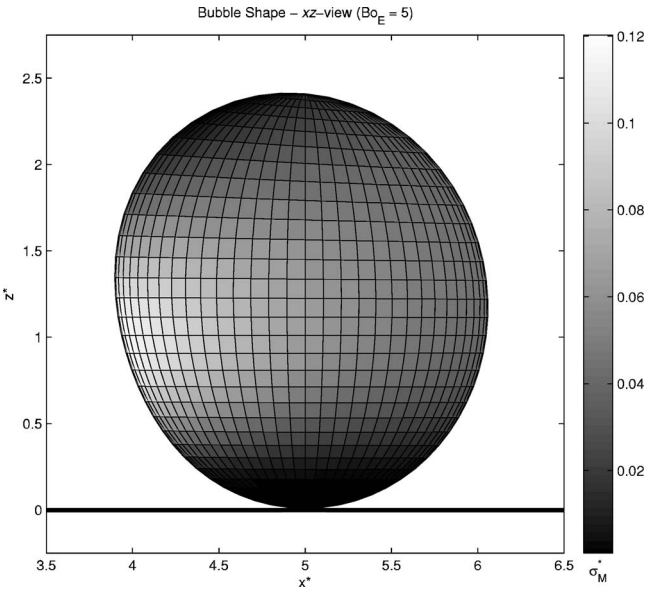

Fig. 5 Bubble shape—*xz* view, Bo_E=5.0

It is clear that as the dielectric Bond number increases, the deformation of the bubble becomes more pronounced. The bubbles become more elongated, and this elongation appears to occur approximately along the lines of constant nominal electric field intensity—the field in the absence of any bubbles, as given by substituting Eq. (22) into Eq. (7). These lines run in an arc from the high-voltage electrode to the ground electrode, as illustrated schematically in Fig. 7. The elongation can be quantified by the elongation angle Θ, which is also illustrated in Fig. 7 and represents the angle between the two extremities of the bubble interface, measured from the meeting point of the two electrode plates. The elongation angles for each value of Bo_E, normalized by the elongation angle Θ_0 of the undeformed bubble (a sphere of radius R_0), are shown in Table 1. For a value of Bo_E=0, the

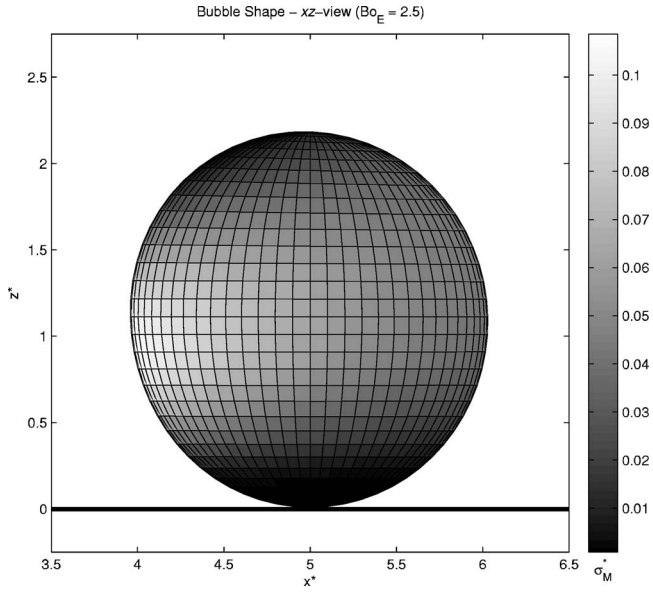

Fig. 4 Bubble shape—*xz* view, Bo_E=2.5

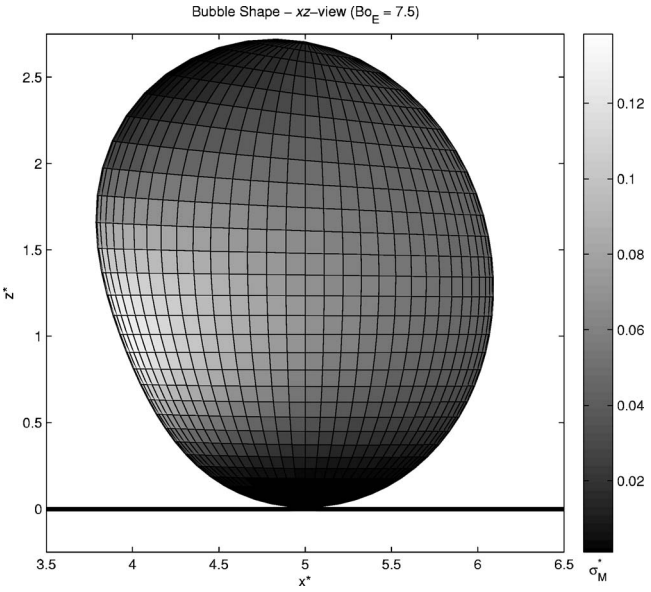

Fig. 6 Bubble shape—*xz* view, Bo_E=7.5

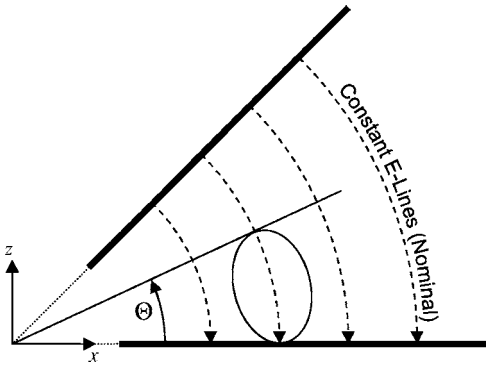

Fig. 7 Schematic of constant electric field lines and elongation angle

bubble does not deform, so Θ/Θ_0 is unity for this case.

Comparison of Figs. 4–6 show that the peak, dimensionless Maxwell stress intensity felt by each bubble also appears to increase slightly with the dielectric Bond number. In addition to this higher peak intensity, the geometric reaction of the bubble is also enhanced by the increased value of Bo_E, meaning that the Maxwell stresses make a larger contribution to the total stress at the surface relative to the hydrostatic pressure difference. For values of Bo_E much above 7.5, the bubble elongates beyond the location of the upper electrode and out of the domain, which is an unacceptable condition. The dimensions of the electrode geometry studied here are the same order of magnitude as the bubble radius. Therefore, the intensity of the nondimensional Maxwell stresses is relatively high and thus low values of dielectric Bond number are studied. For plates that are positioned further apart, the dimensionless Maxwell stresses would be weaker and larger values of Bo_E could be studied without the bubble elongating beyond the boundaries of the domain.

Figures 8–10 show a yz view of the bubbles for each of the three Bo_E values, where the x axis points into the page. The bubbles are symmetric in these figures due to the plane of symmetry at $y^*=0$. The vertical elongation is clearly visible as the value of Bo_E increases. As a direct consequence of this bubble elongation, larger Maxwell stresses act over a larger surface area.

External Potential Field Distribution. Figures 11–13 illustrate the lines of isopotential inside the domain along the plane of symmetry at $y^*=0$, for the three cases of $\mathrm{Bo}_E=2.5$, $\mathrm{Bo}_E=5.0$, and $\mathrm{Bo}_E=7.5$, respectively. The bold lines represent portions of the two plate electrodes. The isopotential contours represent a linearly spaced range of potential field values from $\phi^*=0$ on the lower electrode to $\phi^*=1$ on the upper electrode. Note that in the near vicinity of the bubble, the distribution of the potential field is significantly altered due to the insulating boundary condition that is imposed at the bubble interface. However, the bubble's effect on the potential distribution is much localized—even a short distance away from the bubble the potential field is effectively unaltered. Thus, there is a potential field boundary layer near the interface of the bubble. These isopotential contour plots also illustrate the computational boundaries within which the potential field is numerically computed. Outside the region in which contours are drawn, the analytical potential field solution, Eq. (22), is used to approximate the distribution of electric potential.

Table 1 Bubble elongation angle

Bo_E	Θ/Θ_0
0	1.000
2.5	1.088
5.0	1.207
7.5	1.366

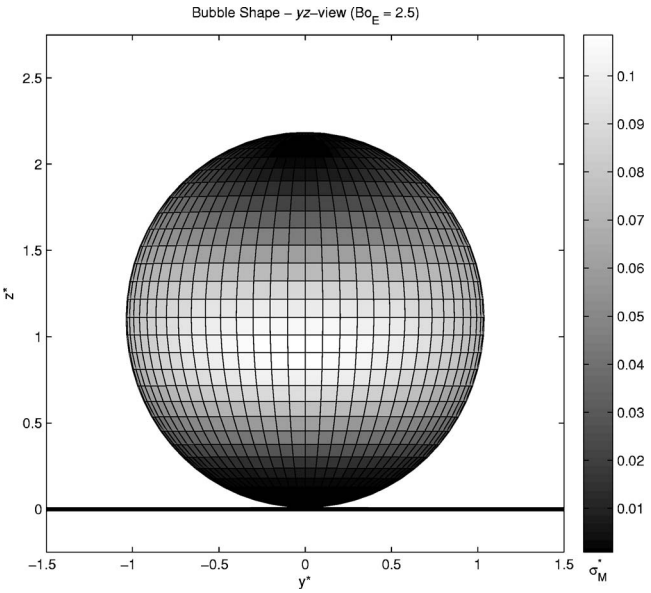

Fig. 8 Bubble shape—yz view, $\mathrm{Bo}_E=2.5$

Dielectrophoretic Force Components. The most interesting and important aspect of the numerical results is the resulting prediction of the dielectrophoretic force vector acting on the bubble, obtained from Eq. (17) by integrating the Maxwell stresses over the surface of the bubble. When the bubble is immediately adjacent to the lower electrode plate, the numerical data in Table 2 show that at low Bo_E values the dielectrophoretic force can have a downward component that serves to press the bubble against the plate. Note that $F_y=0$ for all cases due to the plane of symmetry through the center of the bubble at $y^*=0$.

This is a deviation from the expected behavior that the bubbles move along lines of isopotential. For example, the dielectrophoretic force exerted on a small, spherical, insulating bubble in the presence of an external electric field is predicted by Eq. (2). In general, $\varepsilon_v<\varepsilon_l$ and the net dielectrophoretic force will act oppo-

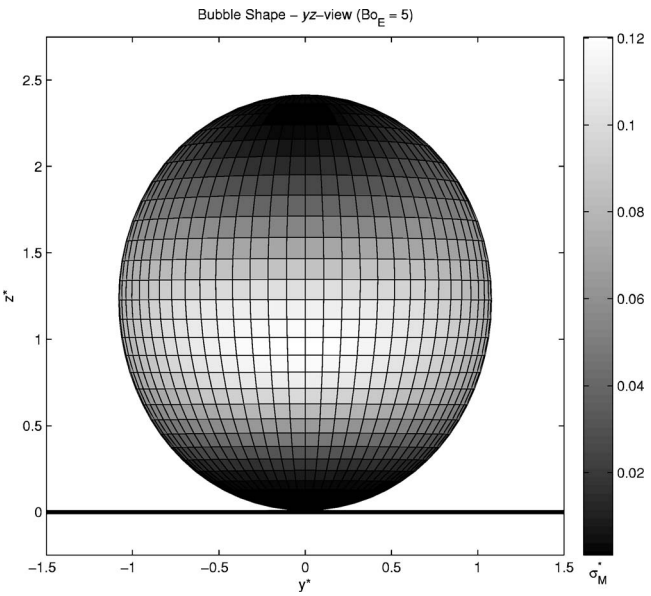

Fig. 9 Bubble shape—yz view, $\mathrm{Bo}_E=5.0$

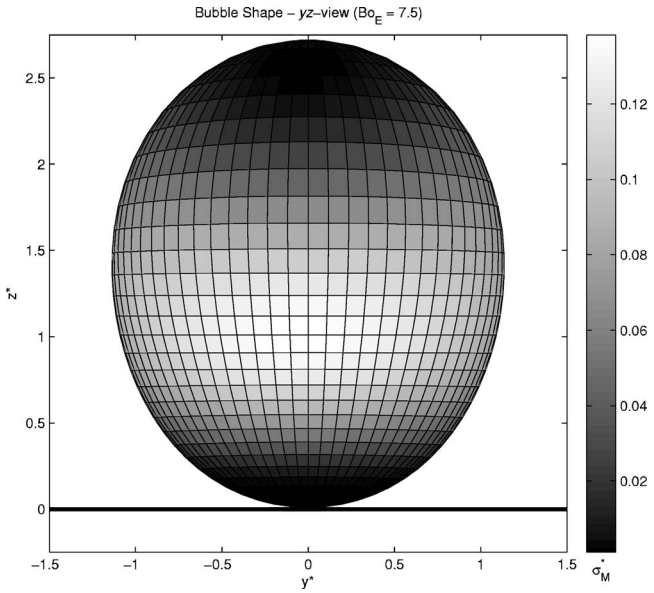

Fig. 10 Bubble shape—*yz* view, Bo_E=7.5

site to the gradient of electric field intensity (from stronger electric field to weaker electric field). For the electrode geometry studied here, lines from stronger electric field to weaker electric field, in the absence of any bubbles, run from the origin where the two plates would meet, spanning radially outwards, in the same way as the nominal isopotential lines. Therefore, in terms of Cartesian components, the net dielectrophoretic force on the bubble should have positive x and z components when the influence of the bubble on the local electric field intensity is ignored.

In contrast, the numerical results show that a downward component can exist due to attraction of the bubble to the electrode. This component is due to the distortion of the electric field close to the bubble surface and the ground electrode, not because of the nonuniformity of the nominal electric field, as studies in uniform electric fields [17] have discovered this downward component also. However, this electrode-attraction force is overcome at a Bo_E value between 2.5 and 5.0. This reversal of vertical force direction appears to occur because large elongation of the bubble causes the center of the bubble to be moved upwards within the domain, to a point where the negative gradient of nominal electric field intensity has a larger upward component. The largest values of Maxwell stress now act on surfaces that are more inclined and so these stresses induce a greater upward component of force, allowing the downward electrode-attraction force to be overcome.

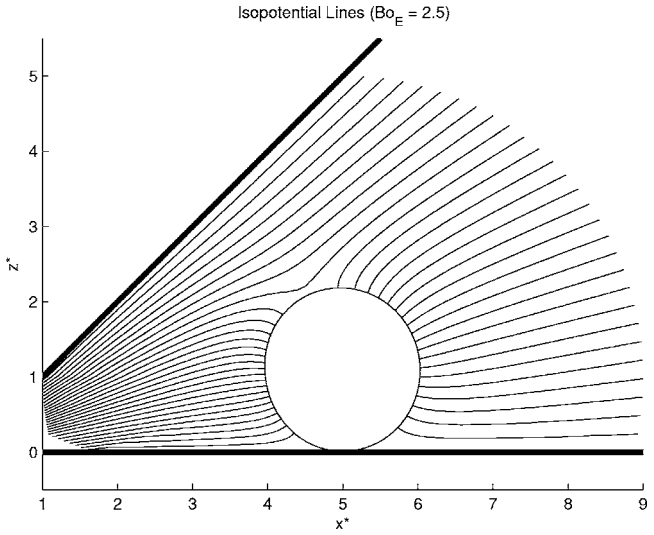

Fig. 11 Isopotential lines—y^*=0, Bo_E=2.5

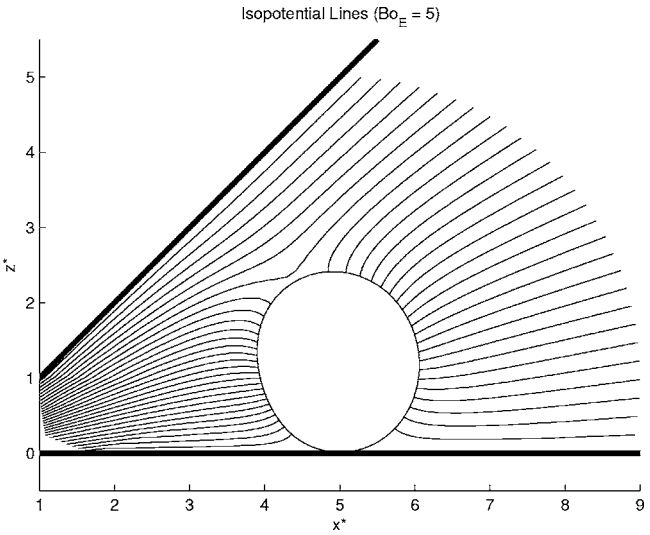

Fig. 12 Isopotential lines—y^*=0, Bo_E=5.0

The Maxwell stresses depend on the squared intensity of the electric field E^2 and not on the direction of the electric field or the value of the potential field. Therefore, reversing the roles of the two electrodes (applying a high voltage to the lower electrode plate and grounding the upper electrode plate) has no effect on the deformation of the bubble or the resulting dielectrophoretic force. Therefore, a bubble that comes into the vicinity of the upper, high-voltage electrode would feel a similar attraction toward it.

The positive x component of dielectrophoretic force is caused by large Maxwell stresses at the left hand side of Figs. 4–6 being

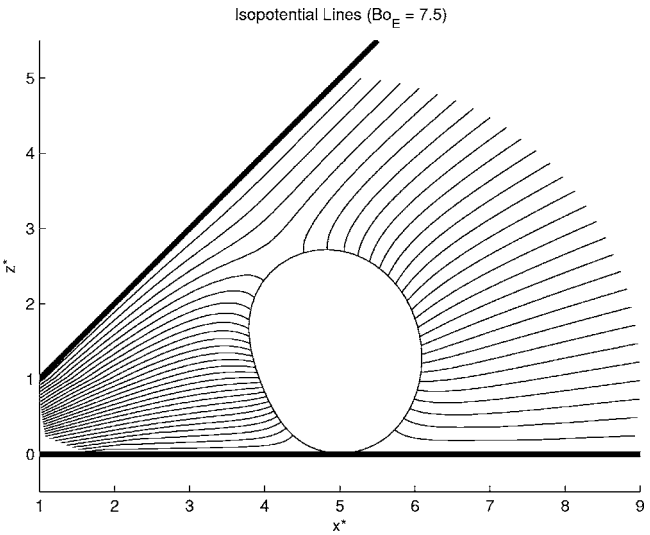

Fig. 13 Isopotential lines—y^*=0, Bo_E=7.5

Table 2 Dielectrophoretic force components

Bo_E	F_x^*	F_z^*
2.5	0.0825	−0.0109
5.0	0.1035	0.0163
7.5	0.1386	0.0649

insufficiently balanced by the Maxwell stresses at the right hand side. Since the Maxwell stresses act inwards across the bubble surface, from the liquid phase to the vapor phase, the horizontal net force acts to the right, in the positive x direction. As the dielectric Bond number increases, the x component of the dimensionless force increases. This increase appears to be caused by the increase in surface area of the bubble due to the elongation process. Elongation of the bubble occurs along the arcs of constant nominal electric field. Larger values of Maxwell stress intensity exist along these elongated sides, as seen in Figs. 4–6, so these large stresses then act over the enlarged surface area, resulting in a greater total net force. From Eq. (18), the actual force increases with Bo_E relative to the dimensionless force, so the overall effect is that increasing Bo_E causes an even larger increase in the dielectrophoretic force on the bubble.

Conclusions

The results of bubble deformation in nonuniform fields imposed by diverging plate electrodes appear to conform qualitatively to previous, axisymmetric studies of bubbles in uniform electric fields [17], but the behavior is now generalized to diverging plate electrodes and the formulation of the governing equations enables the study of bubble behavior within arbitrary, three-dimensional electrode geometries.

A full nondimensionalization procedure reveals that the static deformation of a bubble depends on a single dimensionless parameter, the dielectric Bond number (Bo_E), which is a ratio of Maxwell stresses to surface tension. The amount of deformation that the bubble exhibits in response to the electric field imposed by a given electrode configuration depends on the value of the parameter Bo_E. Larger values of Bo_E cause bubbles to exhibit more significant elongation in the presence of the electric field, and due to the asymmetry of the imposed electric field, there is asymmetry in the bubble deformation. The direction of the net dielectrophoretic force predicted by the numerical simulation differs greatly from the analytical expression given by Eq. (2). A downward force component, caused by the close proximity of the bubble to the electrode, attracts the bubble to the lower electrode. For larger dielectric Bond numbers, the bubble elongation is more pronounced and the effect of the bubble shape and the distribution of Maxwell stresses allow the downward component to be overcome. It follows that a bubble that is exactly equidistant between the two electrodes is not subject to an attractive force because a case of symmetry exists, but a bubble that is a small distance from this centerline experiences a small attractive force toward the nearest electrode. This attractive force is negligible until the bubble reaches the near vicinity of the electrode, since the distortion of potential field around the bubble is mostly confined to a boundary layer.

The influence of this downward dielectrophoretic force component on a heat transfer device may be significant or insignificant, depending on the magnitudes of other forces acting on the bubble. For example, in normal earth gravity, buoyancy forces may easily overcome this attractive dielectrophoretic force component. However, in the absence of buoyancy, such as in microgravity applications, the dielectrophoretic force can dominate and greatly influence the behavior of the bubble and the corresponding heat transfer characteristics of the device, requiring careful consideration of electrode design and the value of Bo_E under which a system will operate. This fundamental study of bubble deformation in nonuniform electric fields and the numerical data generated provide great insight into some unobvious considerations that must be made in the design of a thermal heat transfer device powered by dielectrophoretic force.

Acknowledgment

The authors thank NASA Headquarters—Microgravity Fluid Physics Program—and NASA Goddard Space Flight Center for their financial support of this research project.

Nomenclature

Bo_E = dielectric Bond number
$\mathbf{E}$ = electric field vector
E = electric field magnitude
E_0 = characteristic electric field intensity
$\mathbf{f}_e$ = electric body force
$\mathbf{F}_e$ = total dielectrophoretic force exerted on bubble
H = mean curvature of interface
$\hat{\mathbf{n}}$ = outer-normal unit vector to interface surface
ΔP = interfacial pressure difference (vapor pressure minus liquid pressure)
R = local radius function of deformed bubble
R_0 = radius of spherical bubble with same interfacial pressure difference, ΔP
$\mathbf{x}$ = parameterized vector of the interface surface
δ = small spacing between bubble and lower electrode
ε = absolute electric permittivity
ρ = mass density
ρ_f = charge density
Φ = potential of high-voltage electrode
ϕ = potential field
φ = spherical inclination angle
θ = spherical azimuth angle
θ_0 = interior angle between two plate electrodes
Θ = bubble elongation angle
Θ_0 = undeformed bubble elongation angle
σ = interfacial surface tension
σ_M = Maxwell stress intensity

Subscripts

l = liquid
v = vapor

References

[1] Cotter, T. P., 1984, "Principles and Prospects of Micro Heat Pipes," *Proceedings of the Fifth International Heat Pipe Conference*, K. Oshima, Y. Kobayashi, M. Murakami, and K. Negishi, eds., Japan Technology & Economics Center, Tokyo, pp. 328–335.
[2] Babin, B. R., Peterson, G. P., and Wu, D., 1990, "Steady-State Modeling and Testing of a Micro Heat Pipe," ASME J. Heat Transfer, **112**(3), pp. 595–601.
[3] Mallik, A. K., Peterson, G. P., and Weichold, M. H., 1995, "Fabrication of Vapor-Deposited Micro Heat Pipe Arrays as an Integral Part of Semiconductor Devices," J. Microelectromech. Syst., **4**(3), pp. 119–131.
[4] Peterson, G. P., and Ma, H. B., 1996, "Theoretical Analysis of the Maximum Heat Transport in Triangular Grooves: A Study of Idealized Micro Heat Pipes," ASME J. Heat Transfer, **118**(4), pp. 734–739.
[5] Peterson, G. P., 2000, "Applications of Microscale Phase Change Heat Transfer: Micro Heat Pipes and Micro Heat Spreaders," *Handbook of Microelectromechanical Systems*, M. Gad-el-Hak, ed., CRC, New York, pp. 301–326.
[6] Le Berre, M., Launay, S., and Lallemand, M., 2003, "Fabrication and Experimental Investigation of Silicon Micro Heat Pipes for Cooling Electronics," J. Micromech. Microeng., **13**(3), pp. 436–441.
[7] Lee, M., Wong, M., and Zohar, Y., 2003, "Integrated Micro-Heat-Pipe Fabrication Technology," J. Microelectromech. Syst., **12**(2), pp. 138–146.
[8] Peterson, G. P., 1994, *An Introduction to Heat Pipes: Modeling, Testing, and Applications*, Wiley, New York, Chaps. 3 and 4.
[9] Melcher, J., 1981, *Continuum Electromechanics*, MIT, Cambridge, MA.
[10] Bryan, J. E., and Seyed-Yagoobi, J., 2001, "Influence of Flow Regime, Heat Flux, and Mass Flux on Electrohydrodynamically Enhanced Convective Boiling," ASME J. Heat Transfer, **123**(2), pp. 355–367.
[11] Darabi, J., Ohadi, M. M., and Dessiatoun, S. V., 2000, "Augmentation of Thin Falling-Film Evaporation on Horizontal Tubes Using an Applied Electric Field," ASME J. Heat Transfer, **122**(2), pp. 391–398.
[12] Bryan, J. E., and Seyed-Yagoobi, J., 1997, "Heat Transport Enhancement of Monogroove Heat Pipe With Electrohydrodynamic Pumping," J. Thermophys. Heat Transfer, **11**(3), pp. 454–460.
[13] Yu, Z., Hallinan, K. P., Bhagat, W., and Kashani, R. A., 2002, "Electrohydrodynamically Augmented Micro Heat Pipes," J. Thermophys. Heat Transfer,

16(2), pp. 180–186.
[14] Garton, C. G., and Krasuchi, Z., 1964, "Bubbles in Insulating Liquids: Stability in an Electric Field," Proc. R. Soc. London, Ser. A, **208**, pp. 211–226.
[15] Melcher, J. R., and Taylor, G. I., 1969, "Electrohydrodynamics: A Review of the Role of Interfacial Shear Stress," Annu. Rev. Fluid Mech., **1**, pp. 111–146.
[16] Miksis, M. J., 1981, "Shape of a Drop in an Electric Field," Phys. Fluids, **24**(11), pp. 1967–1972.
[17] Ogata, J., and Yabe, A., 1993, "Basic Study on the Enhancement of Nucleate Boiling Heat Transfer by Applying Electric Fields," Int. J. Heat Mass Transfer, **36**(3), pp. 775–782.
[18] Jones, T. B., and Bliss, G. W., 1977, "Bubble Dielectrophoresis," J. Appl. Phys., **48**(4), pp. 1412–1417.
[19] Hara, M., and Wang, Z., 1994, "An Analytical Study of Bubble Motion in Liquid Nitrogen Under D. C. Non-uniform Electric Fields," *Proceedings of the Fourth International Conference on Properties and Applications of Dielectric Materials*, IEEE, New York, pp. 459–462.
[20] Pearson, M. R., 2006, "Deformation and Motion Behavior of a Bubble Due to Non-Uniform Electric Fields," M.S. thesis, Illinois Institute of Technology, Chicago, IL.
[21] Stratton, J. A., 1941, *Electromagnetic Theory*, McGraw-Hill, New York.
[22] Gray, A., 1998, *Modern Differential Geometry of Curves and Surfaces With Mathematica*, 2nd ed., CRC, New York.
[23] Crowley, J. M., 1999, *Fundamentals of Applied Electrostatics*, Laplacian, Morgan Hill, CA.
[24] Herman, C., Iacona, E., Földes, I. B., Suner, G., and Milburn, C., 2002, "Experimental Visualization of Bubble Formation from an Orifice in Microgravity in the Presence of Electric Fields." Exp. Fluids, **32**(3), pp. 396–412.

Heat-Transfer Analysis of High Porosity Open-Cell Metal Foam

Indranil Ghosh
Cryogenic Engineering Centre,
Indian Institute of Technology,
Kharagpur 721 302, India
e-mail: indranil@hijli.iitkgp.ernet.in

Forced convection heat transfer in high porosity metal foam, either attached to an isothermal surface or confined between two isothermal plates, has been analyzed, assuming a repetitive simple cubic structure for the foam matrix. The model, in the microscopic level takes account of the forced convective heat transfer coupled with heat conduction through the foam fibers. Analytical expressions have been derived for the gas-solid temperature difference, total heat transfer through the foam, and efficiency of foam as an extended surface. The resulting expressions have strong resemblance with those of the conventional finned surface. The effect of porosity and foam density on the heat transfer in metallic foam has been established through parametric studies. Significant heat-transfer augmentation due to cross connections in metal struts has been noticed. [DOI: 10.1115/1.2804941]

Keywords: metal foam, heat transfer, analytical, porosity, pore density

Introduction

In metal foam, continuously connected slender filaments form an open-celled structure. High porosity metallic foams are characterized by the cell shape, cell size, relative density, properties of the cell wall, and degree of anisotropy. However, manufacturers commonly specify two parameters to characterize the open-cell foam structure, pore size (in pores per inch or ppi) and relative density [1]. These characteristics are independent foam variables, which provide great flexibility in product design. Porous media with porosity of 0.3 and 0.6 have been researched for many decades, and an excellent review of that study has been summarized by Kaviany [2]. However, high porosity metal foam with porosity more than 0.9 is relatively a new development. Metal foam owing to its high heat-transfer surface area density, open porosity, and ability to mix the fluid by promoting eddies is considered to have the potentiality of being used in compact heat exchangers for air borne equipments [3,4], heat sinks for power electronics [5–7]. Their use and applications are widening [8]. In order to use metal foam in heat transferring devices, its physical property data must be supplemented with the thermohydraulic characterization and a realistic heat-transfer model.

Literature review reveals that the research on transport properties, such as effective thermal conductivity, permeability, friction factor, and thermal characterization by analytical as well as experimental means, has been carried out by many researchers [9–14]. Several research groups have performed the numerical analysis and modeling of flowthrough porous medium [15–17], while some of the researchers have used the methods of computational fluid dynamics [18]. Experimental techniques have been adopted to generate accurate and reliable data of heat transfer (Coburn j factor or Nusselt number) and pressure drop. These data are essential for the design and simulation of heat exchangers/heat sinks using metal foam [12,19,20].

Modeling of forced convective heat transfer through a porous block attached to a plate (in case of heat sinks) or confined within two layers (for plate fin heat exchanges) is equally important for using them in practical devices. Heat-transfer model often assumes a fluid saturated porous medium as a continuum with local thermal equilibrium between solid matrix and fluid flow. However, the validity of this assumption is restricted to the low Reynolds number domain, and this equilibrium does not exist when the Reynolds number becomes high. Lu et al. [3] tried to obtain a functional relationship between the cellular structure and the heat-transfer characteristics for forced convective flows through open-celled metal foams without local gas-solid thermal equilibrium. The analytical model assumes simple cubic cell structures for metal foam with unidirectional heat flow which resembles flow across a bank of cylinders.

More recently, Dukhan et al. [4] presented a macroscopic lumped-parameter engineering treatment to determine the temperature distribution as a function of porosity and area density in open-cell metal foams when they are used in a forced convective heat-transfer mode. However, this macroscopic lumped-parameter model does not take account of heat transfer in a microscopic level.

Assuming a simple cubic structure of metal foam, the present article attempts an in-depth analysis of heat transfer in the microscopic level and the effect of porosity and pore density on it. A closed-form solution for the gas-solid temperature difference involving the characteristic dimensions of metallic foam has been established. The resulting expression, depending on the foam boundary conditions can predict heat transfer in heat sinks for electronic cooling or in plate fin heat exchangers with foam as an extended surface.

Heat-Transfer Model

The metal foam microstructure described by a complex geometry renders modeling of the heat transfer and fluid flow very complicated. In mathematical models, this can be dealt with by assuming a simplified and repeated microstructure and by describing the microstructure using macroscopic properties such as the pore size and relative density. The commonly used geometry for unit foam cell is to consider a cube of slender tubes of diameter d_f and length d_p, as shown in Fig. 1 [3,11,21].

The strut diameter (d_f) can be related to the pore size (d_p) of cubic cell by the following relation [11]:

$$\frac{d_f}{d_p} = 2\sqrt{\frac{1-\varepsilon}{3\pi}}\frac{1}{G} \tag{1}$$

where $G = 1 - e^{-(1-\varepsilon)/0.04}$.

A simple relation between the pore size (d_p) and pore density (ppi) can be established from the cubic schematic representation of foam in two dimensions as shown in Fig. 2,

$$d_p = \frac{(25.4 - d_f)}{\mathrm{PPI}} - d_f \tag{2}$$

However, estimation of d_f requires the value of d_p as well as foam porosity (ε). Consequently, Eqs. (1) and (2) have been used to calculate d_p in an iterative process starting with an initial guess value of $d_p = (25.4)/\mathrm{ppi}$. Finally, strut diameter d_f is obtained from the relation given in Eq. (1) when the pore size d_p is known.

A comparison between the approximate value of the pore size (d_p) reported by the manufacturer and the estimated one shows a good agreement (Fig. 3).

Contributed by the Heat Transfer Division of ASME for publication in the JOURNAL OF HEAT TRANSFER. Manuscript received September 13, 2006; final manuscript received June 25, 2007; published online March 5, 2008. Review conducted by Jose L. Lage.

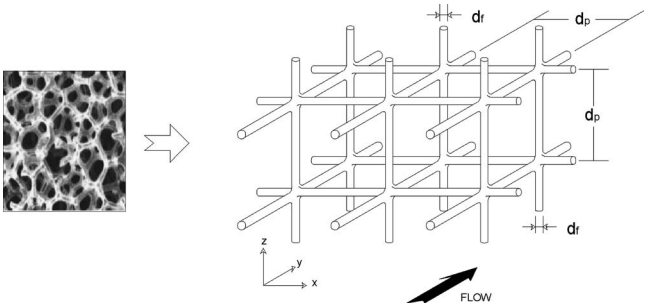

Fig. 1 Simple cubic representation of the metal foam from its original structure

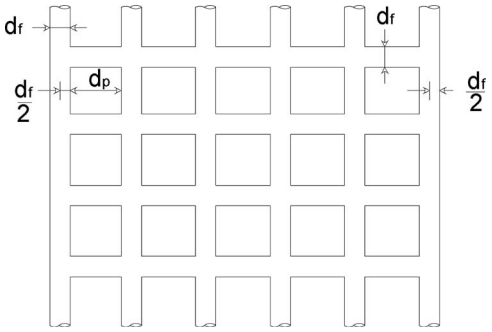

Fig. 2 Simple cubic representation of foam in two dimensions to relate d_p and pore density

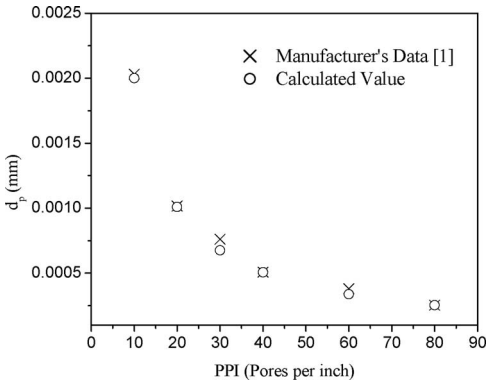

Fig. 3 A comparison between the estimate value of d_p and the data reported by manufacturer

Governing Equations

Figure 4 illustrates the geometry and nomenclature of the differential foam element for heat-transfer analysis with one end of the foam being attached to a surface at constant temperature T_1. An element dx is considered between x and $(x+dx)$, with T_x being the temperature of strut intersection within the element. The direction of fluid flow is along the y axis. At $x=0$, convective heat transfer occurs between the fluid and the primary surface at temperature T_1. This convective heat transfer can easily be quantified through Newton's laws of cooling,

$$q_{\text{plate}} = hA_{\text{plate}}\{T_1 - T_\infty\} \tag{3}$$

In addition to this, heat transfer also occurs by conduction through the struts or secondary surfaces with convective fluid flowing over them. Due to finite thermal conductivity of the foam material, there exists a temperature gradient in the foam along its length (x axis). This temperature distribution determines the amount of heat transfer occurring through the foam attached to an isothermal surface.

In order to derive the governing equation for the temperature differential between any point of the foam and the surrounding convective medium, the following simplifying assumptions have been made:

1. Open-cell foam is made of uniformly distributed, equal-sized cubic cells attached to a plate at T_1.
2. Fluid stream temperature T_∞ remains constant over the element of foam under consideration.
3. Heat-transfer coefficient remains constant over the foam filaments, and its variation with foam density and porosity has been neglected.

As long as the foam is attached to the plate at constant temperature T_1, all the strut intersections within element x and $(x+dx)$ are at the same temperature T_x on the y-z plane. For example, the temperature of the metallic struts at their point of intersections N_1, N_2, N_3, and N_4 around N_0 on the y-z plane is T_x. When fluid flows over a strut connected between two points at constant temperature, the fin has a hyperbolic temperature with an *extremum* at the middle of the fin, as shown in Fig. 4 [22]. Therefore, local temperature variation in T_x between N_0 and N_1 (or between N_0 and N_3) along the transverse direction (z axis) is possible (Fig. 4). Similarly, temperature T_x between N_0 and N_2 (or between N_0 and N_4) along the y axis can also vary locally. Since N_0 and N_1 are at the same temperatures, the existence of an extremum indicates the occurrence of adiabatic condition at the middle of the strut, so that direct flow of heat by conduction from N_0 to N_1 or in the reverse direction is prohibited. As a result, the strut between N_0 and N_1 is virtually partitioned into two sections

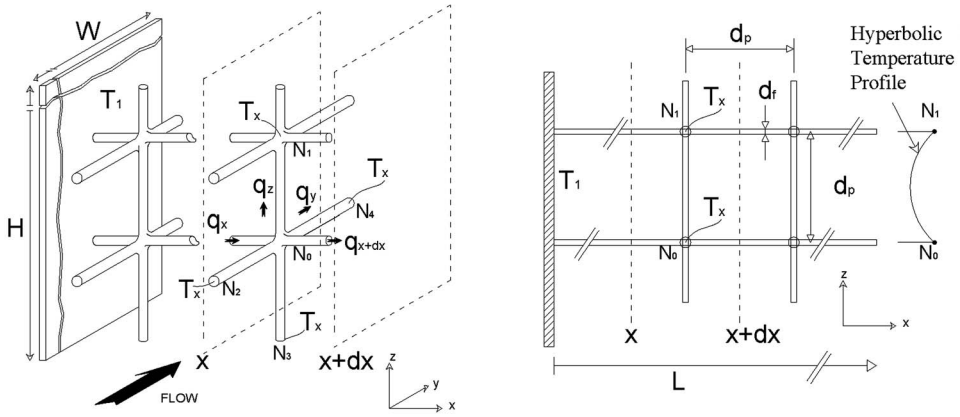

Fig. 4 Nomenclature of the differential element for deriving foam equation

with half of it being attached to N_0 while the other half is attached to N_1. Consequently, the heat transfer of each section can be treated independently. Following the same logic, the strut between N_0 and N_2 can be divided virtually into two parts, half of it being attached to N_0 with the rest being connected to N_2. Let q_z be the amount of heat flowing from N_0 to the middle of the N_0-N_1, and q_y is the amount of heat flowing from N_0 to the middle of N_0-N_2. The q_z and q_y are given by the following relation [22]:

$$q_z = q_y = \sqrt{hPk_fA_c}(T_x - T_\infty)\left[\frac{\cosh(md_p) - 1}{\sinh(md_p)}\right] = hPd_p(T_x - T_\infty)\eta_{1/2} \tag{4}$$

where

$$\eta_{1/2} = \frac{\tanh(md_p/2)}{md_p/2} \quad P = \pi d_f \quad A_c = \frac{\pi d_f^2}{4} m = \sqrt{\frac{4h}{k_f d_f}} \tag{5}$$

Now, applying a steady-state energy balance within the boundary volume around N_0 shown in Fig. 4,

$$q_x = q_{x+dx} + 2q_z\left(\frac{L}{d_p}\frac{1}{L}\right)dx + 2q_y\left(\frac{L}{d_p}\frac{1}{L}\right)dx + h(\pi d_f)dx(T_x - T_\infty) \tag{6}$$

where the fourth term in Eq. (6) is the convective heat transfer through the surface of the struts. Since $q_{x+dx}=q_x+(dq_x/dx)dx$, Eq. (6) can be written as

$$\frac{dq_x}{dx} + hP(T_x - T_\infty)(1 + 4\eta_{1/2}) = 0 \tag{7}$$

Substituting $q_x=-k_fA_c(dT_x/dx)$ and putting $\theta=(T_x-T_\infty)$ in Eq. (7), one can obtain

$$\frac{d^2\theta}{dx^2} - M^2\theta = 0 \tag{8}$$

where

$$M = \sqrt{\frac{hP}{k_fA_c}(1 + 4\eta_{1/2})} = m\sqrt{(1 + 4\eta_{1/2})} \tag{9}$$

Equation (8) is a second order, linear, homogeneous differential equation having constant coefficients with a general solution of the form

$$\theta = C_1e^{Mx} + C_2e^{-Mx} \tag{10}$$

where C_1 and C_2 are the constants to be evaluated from the boundary conditions.

Case I. The general boundary condition can be put in the form

$$\text{At } x = 0 \quad \theta = (T_1 - T_\infty) = \theta_1 \tag{11}$$

Substituting the condition of Eq. (11) in Eq. (10), one gets

$$\theta_1 = C_1 + C_2 \tag{12}$$

Another boundary condition can be set assuming negligible heat transfer from the tip of the foam struts, i.e.,

$$\text{At } x = L \quad \frac{d\theta}{dx} = 0 \tag{13}$$

This is also called the adiabatic condition, prevailing in most of the situations where foam is used as heat sink in electronic devices.

Applying the boundary condition of Eq. (13) in Eq. (10), another equation can be obtained to solve C_1 and C_2, and the resulting expression in Eq. (10) becomes

$$\frac{\theta}{\theta_1} = \frac{\cosh M(L - x)}{\cosh ML} \tag{14}$$

The amount of heat being transferred through the foam is thus

$$q_f = -\left(\frac{H}{d_p}\right)\left(\frac{W}{d_p}\right)kA_c \left.\frac{dT_x}{dx}\right|_{x=0} = \left(\frac{H}{d_p}\right)\left(\frac{W}{d_p}\right)\sqrt{hPk_fA_c(1 + 4\eta_{1/2})}\theta_1 \tanh(ML) \tag{15}$$

where the $(H/d_p)(W/d_p)$ factor stands for the total number of struts within height H and width W of the foam. Enhancement in heat transfer due to cross connections of struts is discernible from Eq. (15). Heat transfer has been increased by a factor of $\sqrt{(1+4\eta_{1/2})}$ in the nonhyperbolic part, while parameter M within the hyperbolic function contains a factor of $\sqrt{(1+4\eta_{1/2})}$ due to cross connections in the foam filaments.

Case II. Another set of boundary conditions other than the adiabatic one may exist, particularly in the case of plate and fin heat exchangers where foam can be used as an extended heat-transfer surface bounded between two separating plates at different temperatures, T_1 and T_2. While the boundary condition as expressed in Eq. (11) remains applicable at $x=0$, the boundary condition for the other end at $x=L$ becomes

$$\text{At } x = L \quad \theta = (T_2 - T_\infty) = \theta_2 \tag{16}$$

where T_2 is the temperature of the plate attached to the foam at the other end.

Applying boundary conditions of Eqs. (11) and (16), the resulting expression for the temperature differential between foam and fluid becomes

$$\frac{\theta}{\theta_1} = \frac{\sinh M(L - x) + (\theta_2/\theta_1)\sinh Mx}{\sinh ML} \tag{17}$$

The total amount of heat being transferred from the foam base at T_1 then becomes

$$q_f = \left(\frac{H}{d_p}\right)\left(\frac{W}{d_p}\right)\sqrt{hPk_fA_c(1 + 4\eta_{1/2})}\theta_1\left[\frac{\cosh(ML) - (\theta_2/\theta_1)}{\sinh ML}\right] \tag{18}$$

The resulting expressions for the foam temperature profile or the total heat transfer in Eqs. (14) and (15) and Eqs. (17) and (18) are similar to those of ordinary fins without any cross connections, except for the fact that the value of m has been increased by a factor of $\sqrt{1+4\eta_{1/2}}$.

Finally, the performance of foam as a fin or an extended heat-transfer surface can be defined in a way similar to that in a conventional fin where fin efficiency is defined as

$$\eta_f = \frac{q_{\max}}{q_f} \tag{19}$$

where $q_{\max}$ is the maximum heat transfer possible if the entire foam is at the fin base temperature. Therefore,

$$q_{\max} = \left(\frac{H}{d_p}\right)\left(\frac{W}{d_p}\right)[hPL\theta_1 + 4\eta_{1/2}hPL\theta_1] = \left(\frac{H}{d_p}\right)\left(\frac{W}{d_p}\right)[hPL(1 + 4\eta_{1/2})\theta_1] \tag{20}$$

Therefore, the efficiency of the foam as an extended heat-transfer surface with adiabatic condition at the tip of it becomes

$$\eta_f = \frac{\tanh(ML)}{ML} \tag{21}$$

However, for the situation where foam remains sandwiched between two different isothermal surfaces, the assumption of entire foam being at the fin base temperature (T_1) does not correspond to the maximum heat-transfer criterion, and the expression derived in Eq. (21) cannot be used to define foam efficiency for Case II. A different formalism as suggested in Ref. [22] may be adopted for this situation.

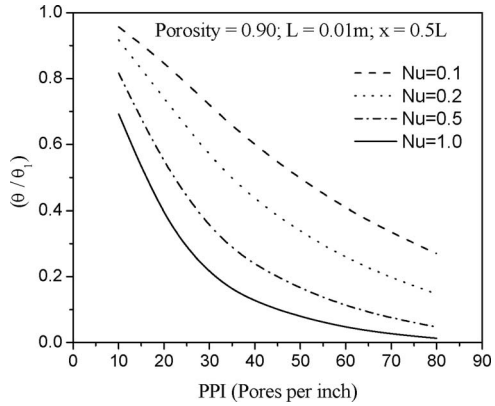

Fig. 5 Effect of pore density and Nusselt numbers on the temperature variation in aluminium foam

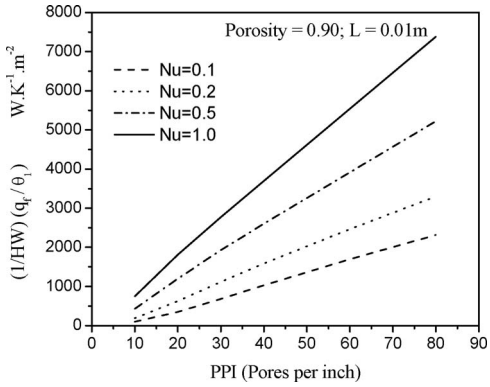

Fig. 6 Effect of pore density and Nusselt numbers on the total heat transfer

Results and Discussions

The parametric study of temperature variation in a metallic foam along its length or estimation of total heat transfer is possible with the closed-form solution obtained from the heat-transfer analysis of the metal foam. Variables for the parametric studies involve foam porosity (ε), pore density (in ppi), and the Nusselt number (Nu) based on the strut diameter d_f,

$$\mathrm{Nu} = \frac{h d_f}{k_\infty} \Rightarrow h = \frac{k_\infty \mathrm{Nu}}{d_f} \tag{22}$$

where k_∞ is the thermal conductivity of the convective fluid passing through the foam. Assuming ambient air as the convective fluid flowing through the foam matrix, k_∞ can be taken as 26.3×10^{-3} W/m K. The thermal conductivity of the foam struts has been taken as 216 W/m K, assuming that the foam is made of aluminium. It is apparent from Eqs. (14) and (15) and Eqs. (17) and (18) that the length of the foam (L) is an additional parameter necessary for the prediction of a foam temperature profile or the calculation of total heat transfer and hence for the study of the effect of porosity and pore density on them. Keeping the length of the foam (L) constant, heat-transfer analysis in metal foam is presented in the following section.

Case I. The effect of pore density on heat transfer has been analyzed, keeping the foam density and the length of the foam constant. Figure 5 shows the normalized temperature variation in foam matrix as a function of pore density (ppi), assuming that the length of the foam $L=0.01$ m, $x=L/2$, and foam density $\varepsilon=0.9$.

An increase in pore density (ppi) is characterized by a decrease in flow passage width (d_p), which otherwise means that the porous heat-transfer surface area is high. Therefore, an increase in pore density, keeping other parameters constant, is associated with a fall in normalized temperature difference θ/θ_1 or an enhancement in heat transfer, as shown in Fig. 6. A similar variation of temperature difference between the solid and the gas phase with pore density has been experimentally reported in Ref. [5]. Foam with pore density more than 60 ppi, has little change in temperature profile at the middle of the foam ($x=0.5$ L), particularly when the Nusselt number is high. It is also seen from Fig. 5 that θ/θ_1 decreases with increasing Nusselt number for a given pore density. It is for the obvious reason that an increase in Nusselt number enhances a convective heat-transfer coefficient and, consequently, a faster removal of heat from the isothermal surface takes place.

An estimation of the foam efficiency (η_f) as a function of pore density and Nusselt number are shown in Fig. 7. When the length (L) of the foam is kept constant, fin efficiency is a monotonically decreasing function of pore density and the efficiency also reduces with increasing Nusselt number.

The effect of porosity on heat transfer in metal foam has been analyzed, keeping pore density (ppi) constant at 10. The normalized temperature difference between the solid and the gas phases decreases with the increase of the porosity of the aluminium foam having a constant pore density (Fig. 8). A similar temperature variation in aluminium foam heat sinks with porosity has also been experimentally observed by Hsieh et al. [5].

When the pore density (ppi) remains constant, an increase in porosity ($\varepsilon=(1-\rho_{\mathrm{rel}})=1-(\rho_{\mathrm{foam}}/\rho_{\mathrm{solid}})$) implies a reduction in foam density (ρ_{foam}) and strut diameter (d_f). The reduction in strut diameter enhances the resistance to heat flow at the foam base so that the normalized temperature distribution reduces with higher porosity. However, the decrease in strut diameter lessens the heat-transfer surface area, and, as a result, there is a corresponding decrease in the total heat transfer (Fig. 9). When the convective flow is small, changes in temperature profile and heat transfer with porosity are not significant; the effect becomes more prominent with increasing Nusselt number. Figure 10 illustrates the effect of porosity and Nusselt number on fin efficiency. The fin efficiency η_f is found to decrease with increasing porosity, and the effect is more pronounced with increasing Nusselt number.

Case II. In order to analyze the heat transfer in metal foam enclosed between two isothermal surfaces, an additional parameter (θ_2/θ_1) needs to be specified. However, the nature of variation in temperature profile and total heat transfer with pore density (ppi) and porosity remains similar as in Case I.

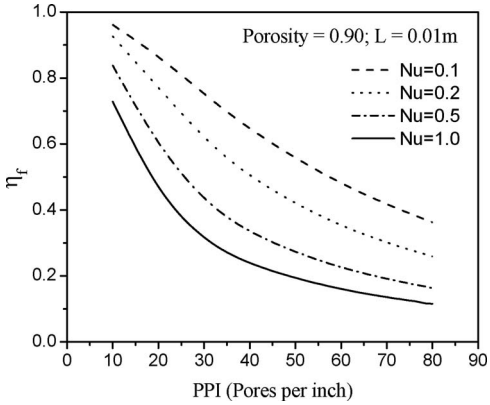

Fig. 7 Effect of pore density and Nusselt numbers on the fin efficiency of aluminium foam

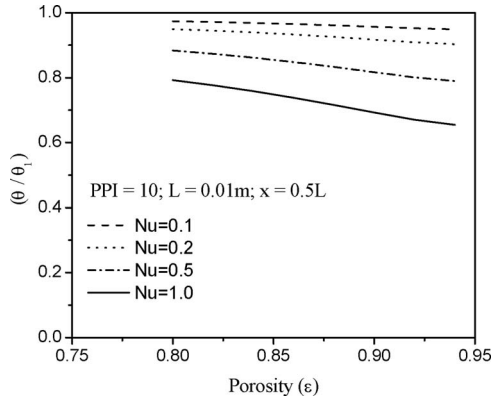

Fig. 8 Effect of porosity and Nusselt numbers on the temperature variation in aluminium foam

Conclusions

Since the complexity of foam microstructure renders the heat and fluid flow modeling difficult, a simplified cubic structure model of the foam has been assumed to analyze the forced convection heat transfer in high porosity metal foam. The microstructure based heat-transfer model takes account of the heat conduction through filaments of the foam in conjugation with convective heat flow over the foam struts. The model shows significant heat-transfer augmentation due to cross connections in the foam filaments.

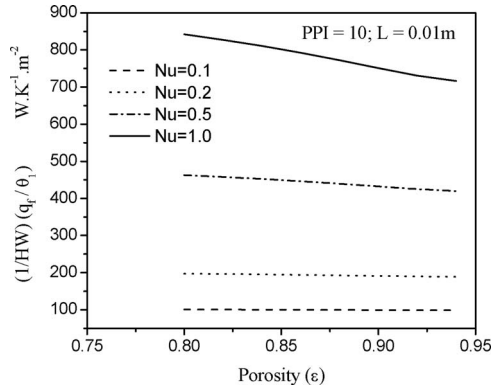

Fig. 9 Effect of porosity and Nusselt numbers on the total heat transfer

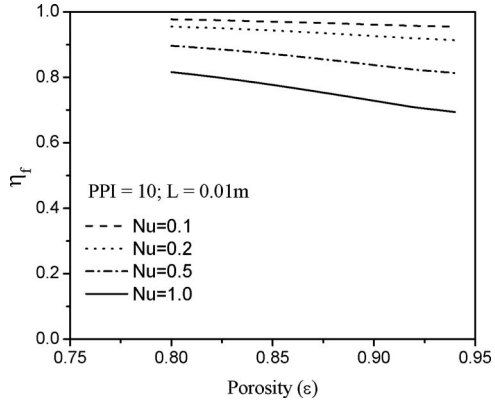

Fig. 10 Effect of porosity and Nusselt number on the fin efficiency of aluminium foam

A closed-form solution of the temperature differential between foam and convective fluid is able to calculate the total heat transfer from the isothermal surface(s) with which foam is attached to. Temperature difference between the solid and the gas phase has been found to decrease with pore density as well as porosity. A similar variation has been experimentally reported by Hsieh et al. [5]. An in-depth analysis of the effect of porosity and foam density has been made possible with the simplified heat-transfer model. The parametric study shows that the heat transfer increases sharply with the increase in pore density (ppi). Another foam parameter, porosity, results in a decrease of heat transfer with increasing porosity, and the effect is more pronounced in high Nusselt number application.

Nomenclature

A_{plate} = base plate surface area
A_c = cross-sectional area of strut
d_f = strut diameter
d_p = pore size
H = height of foam
h = heat-transfer coefficient
k_f = thermal conductivity of foam material
k_∞ = thermal conductivity of convective fluid
L = length of foam
m = factor defined in Eq. (5)
M = factor defined by Eq. (9)
Nu = Nusselt number
ppi = pores per inch
P = perimeter of strut
q_x, q_y, q_z = heat transfer through strut along x, y, and z directions, respectively
q_f = total heat transfer
Re = Reynolds number
T_1 = temperature of the base plate
T_∞ = temperature of the convective fluid

Greek Symbols

ε = porosity
η_f = foam efficiency
$\eta_{1/2}$ = efficiency of the half strut
θ = temperature differential between foam filament and convective fluid
ρ_{foam} = foam density
ρ_{rel} = relative foam density
ρ_{solid} = density of solid foam material

References

[1] Porvair: http://www.npl.co.uk/materials/metal_foams/pdf_files/spec_sheet.pdf
[2] Kaviany, M., 1991, *Principles of Heat Transfer in Porous Media*, Springer, New York.
[3] Lu, T. J., Stone, H. A., and Ashby, M. F., 1998, "Heat Transfer in Open-Cell Metal Foams," Acta Mater., **46**, pp. 3619–3635.
[4] Dukhan, N., Ramos, P. D., Cruz-Ruiz, E., Reyes, M. V., and Scott, E. P., 2005, "One-Dimensional Heat Transfer Analysis in Open-Cell 10-ppi Metal Foam," Int. J. Heat Mass Transfer, **48**, pp. 5112–5120.
[5] Hsieh, W. H., Wu, J. Y., Shih, W. H., and Chiu, W. C., 2004, "Experimental Investigation of Heat-Transfer Characteristics of Aluminum-Foam Heat Sinks," Int. J. Heat Mass Transfer, **47**, pp. 5149–5157.
[6] Zhang, H. Y., Pinjala, D., Joshi, Y. K., Wong, T. N., Toh, K. C., and Iyer, M. K., 2005, "Fluid Flow and Heat Transfer in Liquid Cooled Foam Heat Sinks for Electronic Packages," IEEE Trans. Compon. Packag. Technol., **28**(2), pp. 272–280.
[7] Kim, S. Y., Lee, M. H., and Lee, K. S., 2005, "Heat Removal by Aluminum-Foam Heat Sinks in a Multi-Air Jet Impingement," IEEE Trans. Compon. Packag. Technol., **28**(1), pp. 142–148.
[8] Perrot, C., Panneton, R., Olny, X., and Bouchard, R., 2003, "Mesostructural Approach for Characterising Macroscopic Parameters of Open Cell Foams With Computed Microtomography," Proc. Inst. Acoust., **25**(5), pp. 169–175.
[9] Paek, J. W., Kang, B. H., Kim, S. Y., and Hyun, J. M., (2000) "Effective Thermal Conductivity and Permeability of Aluminum Foam Materials," Int. J. Thermophys., **21**(2), pp. 453–464.
[10] Despois, J. F., and Mortensen, A., 2005, "Permeability of Open-Pore Microcellular Materials," Acta Mater., **53**, pp. 1381–1388.

[11] Bhattcharya, A., Calmidi, V. V., and Mahajan, R. L., 2002, "Thermophysical Properties of High Porosity Metal Foams," Int. J. Heat Mass Transfer, **45**, pp. 1017–1031.
[12] Tadrist, L., Miscevic, M., Rahli, O., and Topin, F., 2004, "About the Use of Fibrous Materials in Compact Heat Exchangers," Exp. Therm. Fluid Sci., **28**, pp. 193–199.
[13] Boomsma, K., Poulikakos, D., and Zwick, F., 2003, "Metal Foams as Compact High Performance Heat Exchangers," Mech. Mater., **35**, pp. 1161–1176.
[14] Kamiuto, K., and Yee, S. S., 2005, "Heat Transfer Correlations for Open-Cellular Porous Materials," Int. Commun. Heat Mass Transfer, **32**, pp. 947–953.
[15] Antohe, B. V., Lage, J. L., Price, D. C., and Weber, R. M., 1996, "Numerical Characterization Micro Heat Exchangers," Int. J. Heat Fluid Flow, **17**(6), pp. 594–603.
[16] Kiwan, S., and Al-Nimr, M. A., 2001, "Using Porous Fins for Heat Transfer Enhancement," ASME J. Heat Transfer, **123**, pp. 790–795.
[17] Alkam, M. K., Al-Nimr, M. A., and, Hamdan, M. O., 2001, "Enhancing Heat Transfer in Parallel-Plate Channels by Using Porous Inserts," Int. J. Heat Mass Transfer, **44**, pp. 931–938.
[18] Boomsma, K., Poulikakos, D., and Ventikos, Y., 2003, "Simulations of Flow Through Open Cell Metal Foams Using an Idealized Periodic Cell Structure," Int. J. Heat Fluid Flow, **24**, pp. 825–834.
[19] Kim, S. Y., Paek, J. W., and Kang, B. H., 2000, "Flow and Heat Transfer Correlations for Porous Fin in a Plate-Fin Heat Exchanger," ASME J. Heat Transfer, **122**, pp. 572–578.
[20] Giani, L., Groppi, G., and Tronconi, E., 2005, "Heat Transfer Characterization of Metallic Foams," Ind. Eng. Chem. Res., **44**, pp. 9078–9085.
[21] Fuller, A. J., Kim, T., Hodson, H. P., and Lu, T. J., 2005, "Measurement and Interpretation of the Heat Transfer Coefficients of Metal Foams," Proc. Inst. Mech. Eng., Part C: J. Mech. Eng. Sci., **219**, pp. 183–191.
[22] Prasad, B. S. V., 1997, "Fin Efficiency and Mechanisms of Heat Exchange Through Fins in Multistream Plate Fin Heat Exchangers: Development and Application of a Rating Algorithm," Int. J. Heat Mass Transfer, **40**, pp. 4279–4288.

Critical Analysis of the Available Ammonia Horizontal In-Tube Flow Boiling Heat Transfer Correlations for Liquid Overfeed Evaporators

N. Ablanque

J. Rigola

C. Oliet

J. Castro

Centre Tecnològic de Transferència de Calor (CTTC),
Universitat Politècnica de Catalunya (UPC),
Colom 11,
08222 Terrassa (Barcelona), Spain

The aim of this work is to present a critical examination of both the available experimental data and the performance of the available heat transfer correlations for oil-free ammonia horizontal in-tube boiling at fin-and-tube-type air-to-refrigerant liquid overfeed evaporation conditions. First, a selection and comparison of the experimental database found in the open literature at the mentioned working conditions is presented. Subsequently, after a short description of the most relevant heat transfer correlations, and in accordance with the selected data, a detailed analysis of the performance of each correlation is carried out. Results show an important divergence between the experimental data sets and conclude that the presently available correlations show considerable discrepancies in heat transfer coefficients within the selected conditions. [DOI: 10.1115/1.2804933]

Keywords: ammonia in-tube boiling, two-phase flow boiling correlations, heat transfer coefficient, liquid overfeed refrigeration systems

1 Introduction

The use of hydrofluorocarbons and other commercial refrigerants for in-tube evaporation has been widely reported in the technical literature. Thus, heat transfer correlations with acceptable level of accuracy have been reported and validated extensively. However, in the case of natural refrigerants, and specially ammonia, there is still an important lack of fundamental and empirical information. As shown by Cotter and Missenden [1], this problem is particularly noticeable at overfeed conditions: low mass velocities (namely, G lower than 150 kg/m^2 s), low vapor weight fractions (approximately, x_g lower than about 0.6), and low heat fluxes ($\dot{q}$ lower than approximately 8 kW/m^2).

A selection followed by a comparison of ammonia experimental data found in the open literature at liquid overfeed conditions is presented in the first section of this paper. The subsequent section includes a summary of the available heat transfer correlations for horizontal in-tube boiling and a detailed comparative study of their accuracy in predicting the data. Finally, concluding remarks are made regarding the improvement of available correlation experimental information.

Contributed by the Heat Transfer Division of ASME for publication in the JOURNAL OF HEAT TRANSFER. Manuscript received June 16, 2006; final manuscript received June 22, 2007; published online March 6, 2008. Review conducted by Ramendra P. Roy.

2 Ammonia Available Experimental Data

Several experimental studies on ammonia in-tube boiling heat transfer coefficients have been published in the open literature. Despite the scarcity of experimental works conducted at overfeed conditions, some relevant data at specific conditions were found in the literature.

Shah [2] reported experimental data for ammonia at overfeed conditions. Among the data set, 78 experimental measurements were found to be suitable for the scope of this study. Experiments for the selected data were carried out in a 26.2 mm inner diameter tube, with heat fluxes ranging from 1635 W/m^2 to 2520 W/m^2, mass velocities from 35.30 kg/m^3 s to 62.3 kg/m^2 s, and saturation temperatures from $-25.2°C$ to $-4.3°C$. Tests were performed using an electrically heated single-tube evaporator. A significant scatter in the tube wall temperature measurements was reported. In addition, the amount of oil in circulation was unknown because, apart from a standard oil separator, no specific devices for controlling the oil content were installed in the facility.

Kelly et al. [3] presented a study of pure ammonia evaporation in both smooth and microfin tubes. In the experiments, a double-tube heat exchanger with a 10.9 mm inner tube diameter was used. The researchers reported mean heat transfer coefficients with small vapor weight fraction change between the inlet and outlet sections of the inner tube. These coefficients were defined as sectional-average heat transfer coefficients and were calculated by means of the secondary fluid (R134a in these experiments) temperature drop between the inlet and the outlet positions of the test section annulus, considering a nominal vapor weight fraction for the refrigerant. Selected tests suitable for this study are defined by the following ranges: heat fluxes from 860 W/m^2 to 5430 W/m^2, mass velocities from 9 kg/m^2 s to 61 kg/m^2 s, and saturation temperatures from $-20°C$ to $5°C$. Data were obtained at precise overfeed conditions. However, significant uncertainties, due to high vapor weight fraction changes through test sections and to the difficulty of measuring low temperature differences, were reported.

Chaddock and Buzzard [4] reported experimental results for ammonia with different oil contents. The experiments were carried out in an electrically heated single-tube (13.39 mm inner diameter) evaporator. Some of the data were found to be appropriate for this study and correspond to mass velocities from 16 kg/m^2 s to 65 kg/m^2 s, saturation temperatures from $-34.4°C$ to $-21.8°C$, and heat fluxes from 6300 W/m^2 to 12,600 W/m^2.

Zurcher et al. [5,6] published some suitable data for ammonia in-tube evaporation and reported a mean uncertainty of $\pm 5\%$, which was significantly lower than the uncertainty values calculated by Kelly et al. [3] for the sectional-average heat transfer measurements. The experimental facility consisted of a double-tube heat exchanger with water flowing through the annulus. The heat fluxes at specific positions of the test section were calculated by means of a Lagrange polynomial method that approximated the water enthalpy distribution along the external tube. The inner tube diameter was 14 mm, and the selected measurements were within the following ranges: heat fluxes of 5400–12,200 W/m^2 mass velocities of 10–50 kg/m^2 s, and saturation temperature of 4°C.

In summary, 345 experimental heat transfer coefficient data were selected from the four works mentioned previously. Data with heat fluxes up to 13 kW/m^2 were included in order to assemble a reasonably large data set. The data reported by Shah [2] and Kelly et al. [3], although having large uncertainties, are valuable as the experiments conditions were clearly set for overfeed conditions. The other two data groups, Chaddock and Buzzard [4] and Zurcher et al. [5,6], did not report high experimental uncertainties, but were carried out at heat fluxes higher than those expected for typical overfeed conditions.

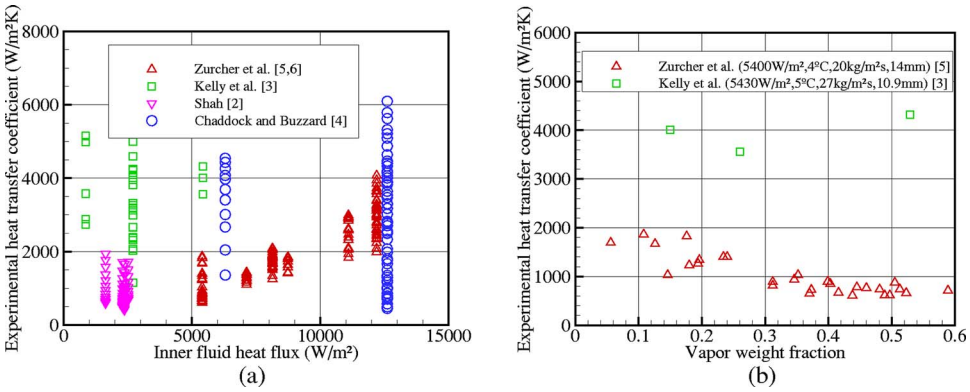

Fig. 1 (***a***) **Selected test measurements plotted against heat fluxes and** (***b***) **two specific tests plotted against vapor weight fraction**

2.1 Comparative Analysis Between the Selected Experimental Data. Figure 1(*a*) shows all of the experimental heat transfer coefficients of the selected tests detailed in the previous section. The conditions of the test by Zurcher et al. [5] obtained at $\dot{q}=5400\ \mathrm{W/m^2}$ are very similar to those of the test by Kelly et al. [3] carried out at $\dot{q}=5430\ \mathrm{W/m^2}$. However, the experimental heat transfer coefficients obtained by Kelly et al. [3] are three to four times larger, as depicted in Fig. 1(*b*).

These two tests do not have the same parameter values. The test by Kelly et al. [3] was carried out with a slightly larger mass velocity compared to that of Zurcher et al. [5], $G=27\ \mathrm{kg/m^2\,s}$ versus $G=20\ \mathrm{kg/m^2\,s}$, respectively. This may not explain the huge difference found in the experimental heat transfer coefficients, as at such low flow rates the convective contribution to heat transfer has little influence. The saturation temperatures are almost equal. Furthermore, the distribution of measurements along the studied vapor weight fraction range is not an explanation, as both tests include points along the range shown in Fig. 1(*b*). Although only three measurements were reported by Kelly et al. [3] for this specific case, small variations through the vapor weight fraction range are observed, while the data of Zurcher et al. [5] present a smooth and constant decreasing heat transfer coefficient with increasing vapor weight fraction.

Data comparison may be altered in a significant manner as the experimental data uncertainty of Kelly et al. [3] is much larger than that of Zurcher et al. [5,6]. Kelly et al. [3] reported high vapor weight fraction changes across sectional-average test sections—up to 60%—for their tests carried out at relatively low mass fluxes and relatively high heat fluxes such as that presented in Fig. 1(*b*).

Another important aspect in explaining the large difference found in the experimental heat transfer coefficients is the fluid flow pattern types in each test. Kelly et al. [3] reported that the predominant flow pattern observed in all their tests was stratified wavy with some periodic large waves passing through the tube. These waves have an important influence in heat transfer as they are constantly wetting the upper part of the inner tube. Zurcher et al. [5] reported the same type of flow regime for their specific test plotted in Fig. 1(*b*). The frequency and amplitude of the large waves may have a significant influence in the uncertainty and measurement of heat transfer coefficients in both works.

3 Ammonia Available Correlations and Comparison to Experimental Data

3.1 Available Correlations. Two different phenomena are observed during in-tube evaporation heat transfer: nucleate and convective boiling. Both types may coexist and contribute to the total heat transfer in similar or different proportions. Thus, correlations may be classified depending on the model used to relate these heat transfer modes: the enhancement model, the superposition model, or the asymptotic model. Alternatively, other two-phase correlations use a flow pattern map to predict the vapor and liquid distribution around the tube perimeter. In this case, the heat transfer contribution of the liquid phase (which may include nucleate and convective boiling phenomena) and the contribution of the vapor phase are related in order to calculate the global heat transfer coefficient. Those are the map-oriented correlations.

Shah [7] presented a set of equations that allow an easier implementation of a previously developed graphical method for heat transfer coefficient prediction. The result was an expression of the enhancement model type, $h_{tp}=Eh_{cb}$, where the two-phase heat transfer coefficient is equal to the liquid convective boiling heat transfer coefficient multiplied by a two-phase enhancement factor. The latter factor is deduced from three dimensionless parameters (the convective number, the boiling number, and the Froude number) depending on the flow boiling regime. The liquid convective heat transfer coefficient is obtained from the Dittus–Boelter correlation [8].

Gungor and Winterton [9] proposed a superposition model where the convective and nucleate boiling heat transfer coefficients are added: $h_{tp}=h_{cb}+h_{nb}$. The nucleate boiling contribution is calculated with the pool boiling correlation of Cooper [10], and, similarly, the convective contribution is obtained from the Dittus–Boelter correlation [8]. However, the nucleate boiling contribution term was suppressed, and a simpler expression was deduced. Both Shah and Gungor and Winterton correlations were tested on many fluids and at a wide range of conditions (ammonia was not included among the fluids used to develop those correlations).

The correlation of Kandlikar [11] for horizontal and vertical in-tube evaporation is also based on the additive mechanism, but with a different approach, somewhere between the enhancement model and the superposition model. In this case, no nucleate boiling heat transfer coefficient is calculated, but the enhancement factor is the total amount of a convective and a boiling term: $h_{tp}=(C+N)h_{cb}$. Here, h_{cb} is also calculated from the Dittus–Boelter expression [8], and the terms C and N are used to characterize the convective and nucleate contributions. This correlation was first calculated for water, but its applicability can be extended to other fluids by means of a fluid-dependent parameter F_{fl}. This parameter is included in the nucleate term and varies depending on the refrigerant. The correlation was tested against more than 5000 data points. No ammonia data were compared; consequently, no F_{fl} factor for this fluid was proposed by Kandlikar. In the present work, the procedure used to find this parameter consisted in calculating the mean prediction error (MPE) for all the database points at different fluid parameter values: $\mathrm{MPE}=\Sigma_{i=1}^{n}(|h_{exp}-h_{calc}|/h_{exp})_i/n$. The lower MPE was found at $F_{fl}\approx 0.0$, which is beyond the range stated by Kandlikar.

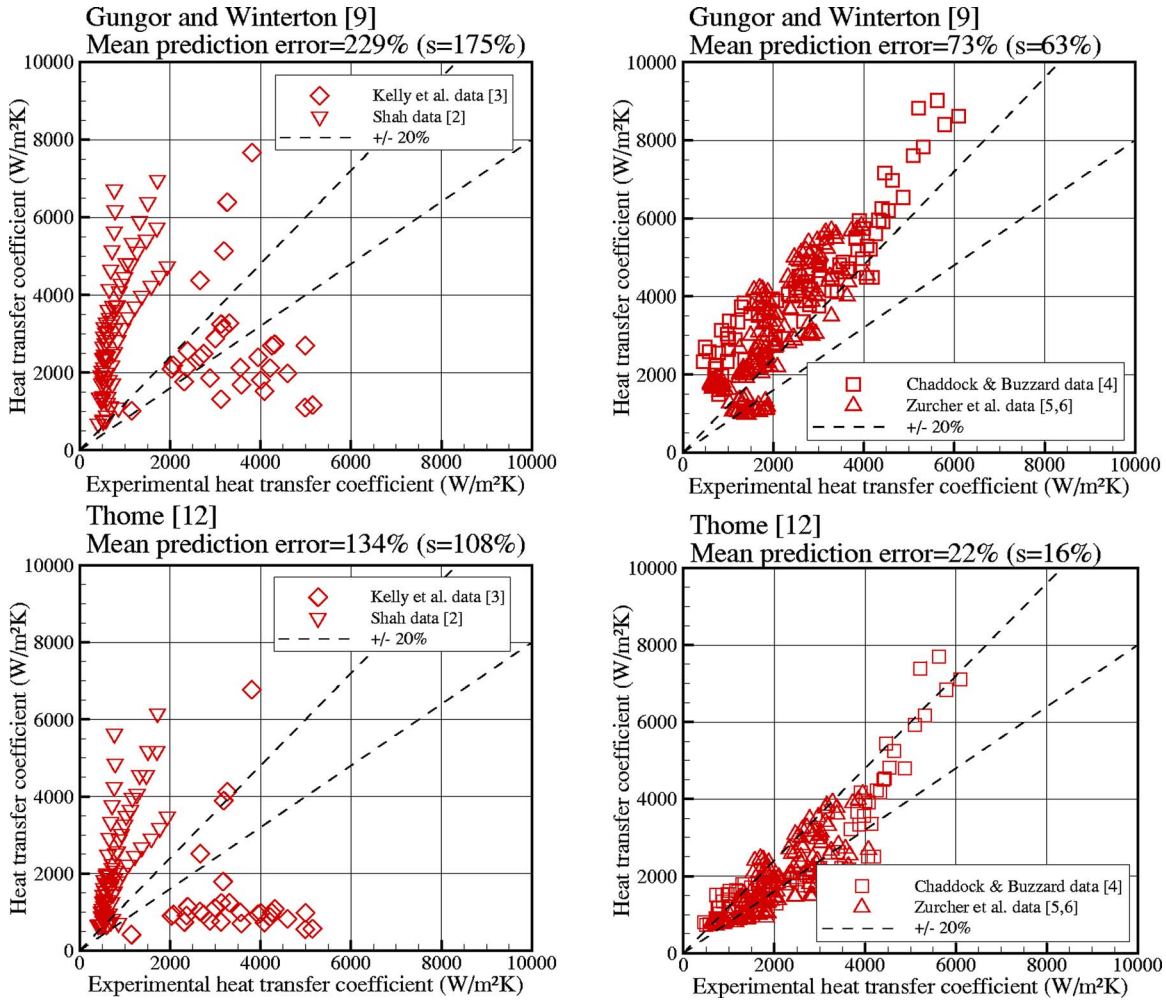

Fig. 2 Comparison of Gungor and Winterton [9] and Thome [12] correlations to experimental data

During in-tube saturated boiling conditions, the inner perimeter can be fully or partially wetted depending on the flow pattern type. The heat transfer coefficient prediction presented in Thome [12] evaluates both contributions: the heat transfer occurring through the portion of the tube inner perimeter, which is in contact with the liquid phase h_{wet}, and the vapor heat transfer coefficient through the dry part of the perimeter h_g, as follows: $h_{tp} = (\theta_{dry}/2\pi)h_g + (1-\theta_{dry}/2\pi)h_{wet}$. This equation represents the total heat transfer coefficient, where the angle θ_{dry} indicates the portion of the tube inner perimeter, which is in contact with the gas phase. The value of h_g is directly calculated with the Dittus–Boelter correlation [8], while h_{wet} is determined by means of the asymptotic model proposed by Steiner and Taborek [13]. This is a flow pattern dependent correlation as the angle θ_{dry} is calculated according to the flow pattern. A further version, including a more detailed map, was presented by Wojtan et al. [14,15].

3.2 Correlation Comparison Against Experimental Data. In the current section, a comparison of the performance of several correlations at overfeed conditions is presented. The thermodynamic properties of ammonia were taken from the NIST refrigerant database [16]. Five different correlations [7,9,11,12,15] are tested and compared directly against the selected data from four experimental databases [2–6].

Figure 2 shows predictions obtained with the correlations of Gungor and Winterton [9] and Thome [12]. The diagonal line across the graphics represents the zone of complete agreement and allows appreciation of data scatter. The heat transfer coefficient resulting from each correlation is plotted separately against different pairs of data sources. The data of Chaddock and Buzzard [4] and Zurcher et al. [5,6] correspond to data taken at higher heat fluxes, while the data of Shah [2] and Kelly et al. [3] correspond to data taken at conditions closer to those of overfeed air coolers.

As Fig. 2 shows, both correlations have large MPE and standard deviation values when predicting the two experimental data sets taken at low heat fluxes, 229% and 134%, respectively. It is seen that Shah's data are highly overpredicted by these correlations. In fact, all Shah's experimental heat transfer coefficients are below 2000 W/m^2 K, while both predictions reach values over 6000 W/m^2 K. This general overprediction occurs because the amount of oil circulating in those tests was large enough to significantly reduce the heat transfer coefficient (see Fig. 1). Thus, Shah's experimental data set is not appropriate for this study. A completely different behavior is observed in the predictions of the data of Kelly et al. [3]. In this case, data are mostly underpredicted except for the few experimental tests at high mass velocities of 47–61 kg/m^2 s, where data tend to be overpredicted. This general underprediction of the data of Kelly et al. [3] may be partly due to the high experimental uncertainties reported by Kelly et al. [3], but also by the absence of ammonia test data carried out at low heat fluxes used in the development of these two correlations. The discrepancies between the data of Kelly et al. [3] and Zurcher et al. [5,6] should be clarified with future tests. Furthermore, the other three correlations studied, Shah [7], Kandlikar [11], and Wojtan et al. [15], have similar prediction

Table 1 MPE and standard deviations of each correlation prediction for different data sets

	Zurcher et al. [5,6]		Chaddock and Buzzard [4]		Kelly et al. [3]		All data	
	MPE (%)	s (%)	MPE (%)	s (%)	MPE (%)	s (%)	MPE (%)	s (%)
Shah [7]	75	59	125	98	48	42	86	75
Gungor and Winterton [9]	62	43	97	90	38	30	69	61
Kandlikar [11]	52	37	63	66	45	34	54	47
Thome [12]	20	13	26	20	65	20	27	21
Wojtan et al. [14,15]	28	18	43	52	57	25	36	33

trends regarding the data of Shah [2] and Kelly et al. [3].

On the other hand, the data sets taken at higher heat fluxes, Chaddock and Buzzard [4] and Zurcher et al. [5,6], are predicted more accurately. As shown in Fig. 2, both correlations have appropriate diagonal trends. However, the MPE of the Gungor and Winterton correlation [9] is much greater than that of Thome [12], 73% versus 22%, respectively. The latter correlation has a higher accuracy, as it was developed using the ammonia database of Zurcher et al. [5]. However, the data of Chaddock and Buzzard are also well predicted by this correlation. This map-oriented correlation has a good adaptability to different parameter ranges and refrigerants because it includes more phenomenological aspects.

Table 1 presents the MPEs of each selected correlation against each selected data set (Shah's data [2] are not included because they contain an excessive amount of circulating oil). The best global MPE (27%) was obtained with the correlation of Thome [12]. Less accurate predictions (36%) were obtained with the correlation of Wojtan et al. [15], which has been developed using only two refrigerants, R22 and R410A. The other correlations, those by Shah, Gungor and Winterton, and Kandlikar, show even less accurate predictions for all data, 86%, 69%, and 54%, respectively. However, as regards only the data of Kelly et al., the lower MPE was obtained with the Gungor and Winterton correlation (38%). Thus, the data of Kelly et al. [3] are not accurately predicted by any of the correlations studied in this paper.

4 Concluding Remarks

The aim of this work was to examine the experimental data and the available correlations for ammonia evaporation inside tubes at liquid overfeed evaporation conditions.

It was noticed that not much experimental data were available in the open literature. In spite of this limitation, some useful data could be found to pursue the objective of this paper (Kelly et al. [3], Chaddock and Buzzard [4], and Zurcher et al. [5,6]). Among them, the data set of Kelly et al. [3] exhibited large uncertainty values, but is probably the most representative for overfeed conditions. The selected experimental data sets show significant discrepancies between each other at similar test conditions.

The performance of various two-phase correlations for ammonia evaporation inside tubes at liquid overfeed working conditions was studied. The selected data were compared against some of the well-known two-phase heat transfer correlations that were mainly developed for other refrigerants. From this comparison, none of the available correlations show a complete agreement when predicting data. The earlier correlations, i.e., such as those of Shah [7] and Gungor and Winterton [9], exhibit a considerable disagreement with the data. The Kandlikar correlation has been found unsuitable for being used with ammonia at the stated conditions. Better results were found with the correlations of Wojtan et al. [14,15] and Thome [12]. The latter shows a generally reasonable predictive capability, except for the data of Kelly et al. [3].

Based on the present study, it is suggested that further experimental works should be carried out in order to enlarge the present ammonia database at overfeed conditions. The experiments should be focused on low mass velocities of 10–150 kg/m^2, low heat fluxes, of 1–8 kW/m^2, and low vapor weight fractions, lower than 0.6. This will require a significant effort as these specific parameter ranges are difficult to set and measure accurately. The data will be essential in clarifying current data set discrepancies and in developing/modifying heat transfer coefficient correlations, which should preferably be of the map-oriented type.

Acknowledgment

This work has been partially funded by the European Commission, Cooperative Research Project "EFROST" (Contract No. COOP-CT-2004-513106) and by the Ministerio de Educación y Ciencia (Ref. no. ENE2005-08302).

Nomenclature

C = convective contribution factor
E = two-phase enhancement factor
F_{fl} = fluid parameter of Kandlikar correlation
G = mass velocity of liquid plus vapor, $kg/m^2\,s$
g = acceleration due to gravity, m/s^2
h = heat transfer coefficient, $W/m^2\,K$
MPE = mean prediction error, %
N = nucleate contribution factor
n = database measurements
$\dot{q}$ = heat flux, W/m^2
s = standard deviation
x_g = vapor weight fraction

Greek Symbols

θ = angle of tube perimeter, rad

Subscripts

calc = calculated
cb = convective boiling
dry = dry part of tube
exp = experimental
l = liquid
nb = nucleate boiling
tp = two phase
g = vapor
wet = wet part of tube

References

[1] Cotter, D., and Missenden, J., 2004, "In Search of Heat Transfer in Ammonia Air Coolers," *Proceedings of the Sixth IIR Gustav Lorentzen Natural Working Fluids Conference*.

[2] Shah, M., 1978, "Heat Transfer, Pressure Drop, Visual Observation, Test Data for Ammonia Evaporating Inside Pipes," ASHRAE Trans., **84**(1), pp. 38–59.

[3] Kelly, J., Eckels, S., and Fenton, D., 2002, "An Experimental Investigation of In-Tube Evaporation of Pure Ammonia in a Smooth and a Microfin Tube: Part I. Heat Transfer (RP-866)," HVAC&R Res., **8**(3), pp. 239–256.

[4] Chaddock, J., and Buzzard, G., 1986, "Film Coefficients for In-Tube Evaporation of Ammonia and R-502 With and Without Small Percentages of Mineral Oil," ASHRAE Trans., **92**(1A), pp. 22–40.

[5] Zurcher, O., Thome, J., and Favrat, D., 1999, "Evaporation of Ammonia in a Smooth Horizontal Tube: Heat Transfer Measurements and Predictions," ASME J. Heat Transfer, **121**(1), pp. 89–101.

[6] Zurcher, O., Favrat, D., and Thome, J., 2002, "Evaporation of Refrigerants in a Horizontal Tube: An Improved Flow Pattern Dependent Heat Transfer Model Compared to Ammonia Data," Int. J. Heat Mass Transfer, **45**(2), pp. 303–317.

[7] Shah, M., 1982, "Chart Correlation for Saturated Boiling Heat Transfer: Equations and Further Study," ASHRAE Trans., **88**(1), pp. 185–196.
[8] Dittus, F. W., and Boelter, L. M. K., 1930, *University of California Berkeley Publications on Engineering*, Vol. 2, University of California, Berkeley, CA, p. 443.
[9] Gungor, K., and Winterton, R., 1987, "Simplified General Correlation for Saturated Flow Boiling and Comparisons of Correlations With Data," Chem. Eng. Res. Des., **65**(2), pp. 148–156.
[10] Cooper, M., 1984, "Saturation Nucleate Pool Boiling: A Simple Correlation," Inst. Chem. Eng. Symp. Ser., **86**, pp. 785–793.
[11] Kandlikar, S., 1990, "A General Correlation for Saturated Two-Phase Flow Boiling Heat Transfer Inside Horizontal and Vertical Tubes," ASME J. Heat Transfer, **112**(1), pp. 219–228.
[12] Thome, J., 2005, "Update on Advances in Flow Pattern Based Two-Phase Heat Transfer Models," Exp. Therm. Fluid Sci., **29**(3), pp. 341–349.
[13] Steiner, D., and Taborek, J., 1992, "Flow Boiling Heat Transfer in Vertical Tubes Correlated by an Asymptotic Model," Heat Transfer Eng., **13**(2), pp. 43–69.
[14] Wojtan, L., Ursenbacher, T., and Thome, J., 2005, "Investigation of Flow Boiling in Horizontal Tubes: Part I. A New Diabatic Two-Phase Flow Pattern Map," Int. J. Heat Mass Transfer, **48**(14), pp. 2955–2969.
[15] Wojtan, L., Ursenbacher, T., and Thome, J., 2005, "Investigation of Flow Boiling in Horizontal Tubes: Part II. Development of a New Heat Transfer Model for Stratified-Wavy, Dryout and Mist Flow Regimes," Int. J. Heat Mass Transfer, **48**(14), pp. 2970–2985.
[16] REFPROP v7.0, 2002, "Reference Fluid Thermodynamic and Transport Properties," NIST Standard Reference Database 23, Gaithersburg, MD.

Experimental Study and Model on Critical Heat Flux of Refrigerant-123 and Water in Microchannels

Wai Keat Kuan[1]
Mem. ASME
Systems and Technology Group,
IBM Corporation,
Research Triangle Park,
NC 27709
e-mail: wkuan@us.ibm.com

Satish G. Kandlikar[2]
Fellow ASME
Thermal Analysis and Microfluidics Laboratory,
Mechanical Engineering Department,
Kate Gleason College of Engineering,
Rochester Institute of Technology,
Rochester, NY 14623
e-mail: sgkeme@rit.edu

The present work is aimed toward understanding the effect of flow boiling stability on critical heat flux (CHF) with Refrigerant 123 (R-123) and water in microchannel passages. Experimental data and theoretical model to predict the CHF are the focus of this work. The experimental test section has six parallel microchannels, with each having a cross-sectional area of $1054 \times 157\ \mu m^2$. *The effect of flow instabilities in microchannels is investigated using flow restrictors at the inlet of each microchannel to stabilize the flow boiling process and avoid the backflow phenomena. This technique resulted in successfully stabilizing the flow boiling process. The present experimental CHF results are found to correlate best with existing correlations to overall mean absolute errors (MAEs) of 33.9% and 14.3% with R-123 and water, respectively, when using a macroscale rectangular equation by Katto (1981, "General Features of CHF of Forced Convection Boiling in Uniformly Heated Rectangular Channels," Int. J. Heat Mass Transfer,* **24**, *pp. 1413–1419). A theoretical analysis of flow boiling phenomena revealed that the ratio of evaporation momentum to surface tension forces is an important parameter. A theoretical CHF model is proposed using these underlying forces to represent CHF mechanism in microchannels, and its correlation agrees with the experimental data with MAE of 2.5%.*
[DOI: 10.1115/1.2804936]

Keywords: critical heat flux, modeling critical heat flux, boiling, channel flow, heat transfer, microscale, two phase

Introduction

Advancements in microprocessors and other high power electronics have resulted in increased heat dissipation from those devices. In addition, to reduce cost, the functionality of microprocessor per unit area has been increasing. The increase in functionality accompanied by reduction in chip size has caused its thermal management to be challenging. In order to dissipate the increased heat generation, the size of conventional fin-type heat sinks has to be increased. As a result, the performance of these high heat flux generating electronics is often limited by the available cooling technology and space to accommodate the larger conventional air-cooled heat sinks.

One way to enhance heat transfer from electronics without sacrificing its performance is the use of heat sink with many microchannels and liquid passing through it. Because of the small size of microchannel heat sink, the performance of a computer system can also be increased by incorporating more microprocessors at a given space without the issue of overheated or burned-out chips. Flow boiling in microchannels is being studied worldwide because of its potential in high heat flux cooling. Compared to a single-phase flow, flow boiling is advantageous because it utilizes the heat of vaporization of a working fluid. Because of that, given a mass flow rate, the heat flux in flow boiling is much higher than that of single phase. In addition, flow boiling in microchannel heat sink can provide approximately uniform fluid and solid temperatures, and it can also be directly coupled with a refrigerant system to provide a lower coolant temperature.

In designing a two-phase microchannel heat sink, it is necessary to know its critical heat flux (CHF). This is because CHF determines the upper thermal limit on the microchannel operation, and the rapid rise in operating temperature after CHF is detrimental to electronics. That is why CHF data and a good understanding of CHF in microchannels are needed before the application of a two-phase microchannel heat sink can be implemented. Furthermore, very few experimental CHF data have been reported in microchannels. Hence, the objective of the present work is to experimentally investigate the CHF of saturated flow boiling in microchannels using R-123 and water as the working fluids. The present experiment involves the collection of CHF data over the ranges of mass flux and heat flux supplied to the microchannels.

A theoretical analysis of flow boiling phenomena revealed that the ratio of evaporation momentum to surface tension forces is an important parameter. A theoretical CHF model is proposed using these underlying forces to represent CHF mechanism in microchannels. The predicted results from the model are then compared to the present experimental CHF data. Similarly, the CHF model is also used to predict Qu and Mudawar's [1] water CHF data, and the predicted results are compared to their experimental CHF data. In their experiment, Qu and Mudawar obtained the CHF data using 21 parallel channels, with each channel having a cross-sectional area of $215 \times 821\ \mu m^2$. The operating conditions from Qu and Mudawar's experiments and the present experiments can be found in Table 1.

Literature Review

Because of the limited number of investigations on CHF in microchannels, experimental studies related to both minichannels and microchannels will be reviewed. Minichannels cover the range from 200 μm to 3 mm channel diameter.

Bowers and Mudawar [2] experimentally studied CHF in circular channels with diameters of 2.54 mm and 0.510 mm using R-113 as the working liquid. The heated length of the channels is 10 mm. In their experiment, CHF is found to be independent of the inlet subcooling at low flow rates due to fluid reaching the saturation temperature in a short distance into the heated channels.

Roach et al. [3] used uniformly heated channels to experimentally investigate CHF. The four different channels, all 160 mm in length, are two circular with 1.17 mm and 1.45 mm diameter, and two other flow channels in microrod bundle with a triangular array and 1.131 mm hydraulic diameter. One of the microrod bundles is uniformly heated over its entire surface, and the other is heated only over the surfaces of the surrounding rods. The authors found that the CHF occurs at high flow quality of 0.36 and higher, indicating dryout as the CHF mechanism. In addition, the CHF increases with increasing mass flux and pressure, and depends on channel diameter.

[1]Corresponding author.
[2]Co-Author.

Contributed by the Heat Transfer Division of ASME for publication in the JOURNAL OF HEAT TRANSFER. Manuscript received July 31, 2006; final manuscript received July 22, 2007; published online March 6, 2008. Review conducted by Chang Oh. Paper presented at the Fourth International Conference on Nanochemical, Microchannels and Minichannels (ICNMM2006), Limerick, Ireland, June 19–21, 2006.

Table 1 Operating conditions

CHF data by	Fluid	Operating conditions G (kg/m^2 s); q'' (kW/m^2); x; T_{in} (°C); P_{in} (kPa)
Qu and Mudawar [1]	Water	G=86–368 q''=264.2–542.0 x=0–0.56 T_{in}=30 P_{in}=121.3–139.8
Present work	R-123	G=410.5–533.8 q''=136.3–201.3 x=0.79–0.93 T_{in}=17.2 P_{in}=162.8–248.3
Present work	Water	G=50.4–231.7 q''=205.8–544.6 x=0.39–0.81 T_{in}=25.4 P_{in}=10.6–110.9

Jiang et al. [4] investigated the CHF condition in diamond-shaped channels with hydraulic diameter ranging from 0.04 mm to 0.08 mm using water as the working fluid. The authors suggested that the evolution of the phase change from liquid to vapor in microchannels is different from conventional channels. They found that the CHF condition depends on the flow rate and the channel size. The authors speculated that in such small channels, bubble formation may be suppressed, and they recommended flow visualization studies to determine the governing heat transfer mechanism.

Yu et al. [5] found that CHF occurs at high flow quality between 0.5 and 1.0 for water, and such qualities are higher than those found in larger diameter tubes at higher pressures and mass fluxes. The CHF quality was found to decrease with decreasing mass flux, and this trend is opposite to the one found in larger tubes. Their experiments were performed using a horizontal tube with 2.98 mm inside diameter and 910 mm heated length.

Qu and Mudawar [1] measured CHF for a water-cooled heat sink containing 21 parallel 0.215×0.821 mm^2 channels. The authors found that flow reversal caused by flow instabilities has resulted in a CHF independent of inlet temperature but which increases with increasing mass velocity. Koşar et al. [6] and Wojtan et al. [7] found that CHF increases with mass flux and decreases with vapor mass fraction at the exit.

Experimental Facility and Experimental Procedure

The experimental setup and experimental procedure developed by Kuan and Kandlikar [8,9] are used in the present work. The experimental setup is designed to provide R-123 at a constant flow rate and temperature to the test section. The experimental facility for water can be found in an earlier paper by Kuan and Kandlikar [10]. A common test section is used for both the R-123 and water experiments.

Modeling Critical Heat Flux

A new flow boiling CHF model is developed based on the forces shown in Fig. 1. The earlier CHF model by Kandlikar [11,12] for pool boiling CHF considered the forces per unit width of the contact line. The same concept is extended here to flow boiling by including additional forces due to fluid flow. The surface tension force per unit length is given by

$$F_S' = \sigma \cos\theta \tag{1}$$

In a nucleating bubble, the difference in the density of the two phases causes the vapor phase to leave the liquid-vapor interface at a much higher velocity than the corresponding liquid velocity

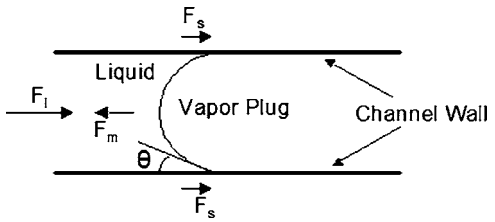

Fig. 1 Forces acting on a liquid-vapor interface

toward the receding interface. The change in momentum as result of evaporation introduces a force at the interface [11,12]. The magnitude of this force is the highest near the heater surface because of the higher evaporation rate in the contact line region near the heater surface. The equation for force per unit length due to momentum change is given by

$$F_M' = \frac{q''D}{h_{fg}}\frac{q''}{h_{fg}}\frac{1}{\rho_G} = \left(\frac{q''}{h_{fg}}\right)^2 \frac{D}{\rho_G} \tag{2}$$

where D is the characteristic dimension.

The stress resulting from inertia force is given by ρV^2. The force per unit length due to inertia is given by

$$F_I' = \frac{1}{2}\rho_L V^2 D = \frac{G^2 D}{2\rho_L} \tag{3}$$

The forces shown in Fig. 1 are used in the development of a new flow boiling CHF model. In the new CHF model, the forces are considered in per unit channel width, as shown in Eqs. (4)–(6),

$$F_S = 1\sigma\cos\theta \tag{4}$$

$$F_M = \frac{q''b}{h_{fg}}\frac{q''}{h_{fg}}\frac{1}{\rho_G} = \left(\frac{q''}{h_{fg}}\right)^2 \frac{b}{\rho_G} \tag{5}$$

$$F_I = \frac{1}{2}\bar{\rho}\bar{V}^2 b = \frac{1}{2}\frac{G^2 b}{\bar{\rho}} \tag{6}$$

where b is the channel height, and $\bar{\rho}$ is the average density given by Eq. (7). Note that the channel height is used instead of D in Eq. (5) since the CHF occurs on the lower wall and the channel height b is the relevant dimension at a particular section. The heat flux q'' is based on the liquid-vapor interfacial area,

$$\frac{1}{\bar{\rho}} = \frac{x}{\rho_g} + \frac{1-x}{\rho_f} \tag{7}$$

The x in Eq. (7) is the thermodynamic quality at the microchannel exit because CHF has been observed to occur first at the exit end of the microchannels. The range of x in the present CHF model is from 0 to 1.

A new flow boiling CHF model is developed based on a force balance, as shown in Eq. (8), which uses the forces, as shown in Fig. 1.

$$F_M = 2F_s + F_I \tag{8}$$

Substituting Eqs. (4)–(6) into Eq. (8), we get

$$q'' = h_{fg}\sqrt{\rho_g}\sqrt{\frac{2\sigma\cos\theta}{b} + \frac{G^2}{2\bar{\rho}}} \tag{9}$$

The interfacial-area-based q'' in the above equation is related to the CHF based on the channel wall. Since this relation is not explicitly known, a constant C is introduced to express the CHF based on the channel-wall surface area. The new flow boiling CHF model is shown in Eq. (10) with the constant C introduced into Eq. (9),

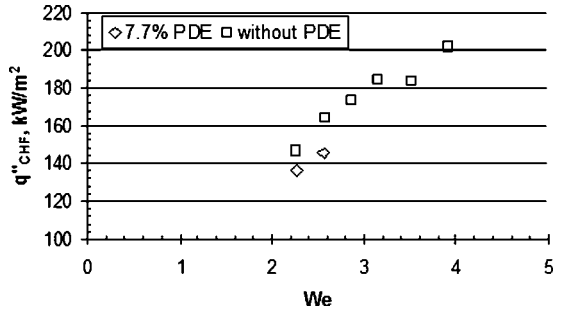

Fig. 2 CHF data from present experiment with and without the 7.7% PDEs in manifold plotted against the Weber number, R-123

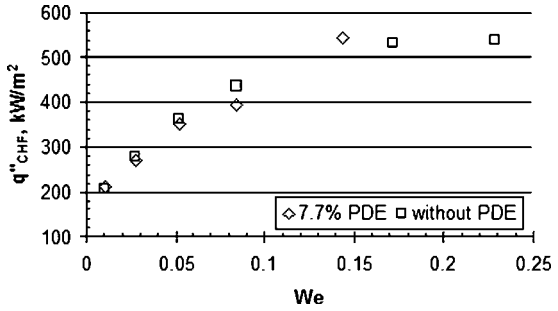

Fig. 3 CHF data from present experiment with and without the 7.7% PDEs in manifold plotted against the Weber number, water

$$q''_{\mathrm{CHF}} = Ch_{fg}\sqrt{\rho_g}\left(\sqrt{\frac{2\sigma\cos\theta}{b}+\frac{G^2}{2\bar{\rho}}}\right) \tag{10}$$

This new CHF model will be used to predict flow boiling CHF. The single constant C will be determined from the experimental data. Because of the complex liquid-vapor behavior at the interface, especially near the CHF condition, it is not possible at this stage to develop models to predict the constant C. It is expected that with the availability of a large number of data sets for different fluids, and with advanced numerical simulation of the interface, further insight will be obtained on the nature of the constant C in the future. The predicted CHF results will be compared to experimental CHF results. The receding contact angles θ for water/copper and R-123/copper systems are 45 deg and 5 deg, respectively [12].

Results

The effect of pressure drop elements (PDEs) on CHF is presented in this section. All tests in this section are conducted with microchannels in the horizontal orientation. The results from the case without PDEs are compared to those with 7.7% PDEs at the inlet of each channel. The latter case uses a manifold that incorporates inlet openings of 127 μm diameter at the inlet to each channel, giving an open area that is 7.7% of the cross-sectional area of a 1054×157 μm^2 microchannel. These pressure restrictors are expected to reduce the backflow by forcing an expanding vapor bubble in the downstream direction and not allowing the liquid-vapor mixture to enter the inlet manifold.

CHF has been observed to occur at the exit end of the microchannels for all runs conducted. The heater power is increased in steps of 1 W to 2 W increments, and the temperatures in the copper blocks are monitored. As the CHF is reached, the temperature of the last thermocouple near the exit end experiences a gradual temperature rise of around 0.5°C/min due to the thermal mass of the assembly. To prevent damage to the test section assembly, the heaters are shut off when the highest temperature in the block (near the exit end) reached 100°C and 160°C for R-123 and water, respectively. The temperature then overshoots by a few degrees before cooling down after shutting off the power. Again, the last thermocouple near the exit end leads the temperature rise during the CHF condition, thus indicating that the microchannel exit is where CHF first began.

After the CHF has been reached, the temperatures at all locations in the copper block start to go up, indicating that the CHF location was gradually moving upstream. Since the heater power was fixed, the local heat flux increased in the microchannels upstream, following the CHF condition toward the exit.

Figures 2 and 3 show the present experimental R-123 and water CHF data with and without the 7.7% PDEs in manifold plotted against the Weber number. As shown in the figures, CHF increases with the Weber number. This indicates that as the mass flux increased, the CHF increased, as one might expect.

Present experimental R-123 and water CHF data are compared to the correlations reported by previous researchers [1,13,14], and the results can be found in Tables 2 and 3. The experimental results with and without the 7.7% PDEs in manifold are compared to the predicted results using the CHF correlations by Bowring [13], Katto [14], and Qu and Mudawar [1]. The CHF correlations by Bowring, Katto, and Qu and Mudawar have better performance when predicting CHF using water as the working liquid rather than R-123. The experimental results with and without the 7.7% PDEs in manifold are compared to predicted results from various correlations using the mean absolute error (MAE) method, as shown in Eq. (11).

$$\mathrm{MAE} = \frac{1}{M}\sum\frac{|q''_{\mathrm{CHF,expt}} - q''_{\mathrm{CHF,pred}}|}{q''_{\mathrm{CHF,expt}}}\times 100\% \tag{11}$$

The macroscale equation by Katto [14] for rectangular channels has overall MAEs of 33.9% and 14.3% for R-123 and water, respectively. For a rectangular channel, this equation has the lowest MAEs for both the working fluids.

The present R-123 and water CHF data, and those reported by Qu and Mudawar [1], are compared to the predicted results using the new Kandlikar and Kuan CHF model (Eq. (10)) from the section on modeling CHF,

$$q''_{\mathrm{CHF}} = Ch_{fg}\sqrt{\rho_g}\left(\sqrt{\frac{2\sigma\cos\theta}{b}+\frac{G^2}{2\bar{\rho}}}\right)$$

A common value of C is used to predict CHF for both R-123 and water, and their respective MAEs are reported. In addition, individually optimized C values for R-123 and water will be used, which allow the model to correlate better to each R-123 and water data. Table 4 shows the summary of comparing the experimental CHF data to the predicted CHF results using the CHF model by Kandlikar and Kuan (Eq. (10)).

Table 2 CHF correlation results for R-123

Reference	Recommended channel geometry and size	MAE	
		(i)	With 7.7% PDEs
		(ii)	Without 7.7% PDEs
Bowring [13]	Circular conventional channels	(i)	66.2%
		(ii)	68.8%
Katto [14]	Rectangular conventional channels	(i)	29.4%
		(ii)	38.5%
Qu and Mudawar [1]	Rectangular, d_h=0.38–2.54 mm	(i)	519.4%
		(ii)	450.7%

Table 3 CHF correlation results for water

Reference	Recommended channel geometry and size	MAE	
		(i)	With 7.7% PDEs
		(ii)	Without 7.7% PDEs
Bowring [13]	Circular conventional channels	(i)	29.5%
		(ii)	26.2%
Katto [14]	Rectangular conventional channels	(i)	12.6%
		(ii)	16.0%
Qu and Mudawar [1]	Rectangular d_h=0.38–2.54 mm	(i)	62.0%
		(ii)	63.6%

Critical Heat Flux Correlation (Common C=0.002679 for Both Water and R-123). Qu and Mudawar's [1] water CHF data and the present R-123 and water CHF data are compared to the predicted values from the Kandlikar and Kuan CHF model. Using the C value of 0.002679, the correlation agrees with Qu and Mudawar's experimental data with a MAE of 13.0%. In addition, the correlation agrees with the present R-123 and water experimental data with MAEs of 16.3% and 8.2%, respectively.

Critical Heat Flux Correlation (C=0.002492 for Water Only). Using the individually optimized C value of 0.002492, Fig. 4 shows the CHF data from Qu and Mudawar [1] and the predicted CHF plotted against the Weber number. The correlation agrees with Qu and Mudawar's and present water experimental data with the MAEs of 6.8% and 3.9%, respectively.

Compared to using a common C value for both R-123 and water, the individually optimized C value of 0.002492 for water has resulted in a better agreement between the correlation and the experimental data.

Critical Heat Flux Correlation (C=0.003139 for R-123 Only). The correlation agrees with the experimental data with a MAE of 2.5% when using the individually optimized C value of 0.003139 for R-123. Figure 5 shows the present R-123 experimental CHF and the predicted CHF plotted against the Weber number.

Table 4 CHF data compared to the predicted results using the CHF model

CHF data by	Working fluid	C in the new CHF model	Microchannel geometry, $w \times b$; number of channels	MAE (%)
Using single value for C				
Qu and Mudawar [1]	Water	0.002679	215×821 μm^2; 21 parallel	13.0
Present work	R-123	0.002679	1054×157 μm^2; 6 parallel	16.4
Present work	Water	0.002679	1054×157 μm^2; 6 parallel	8.2
Using individually optimized values of C				
Qu and Mudawar [1]	Water	0.002492	215×821 μm^2; 21 parallel	6.8
Present work	R-123	0.003139	1054×157 μm^2; 6 parallel	2.5
Present work	Water	0.002492	1054×157 μm^2; 6 parallel	3.9

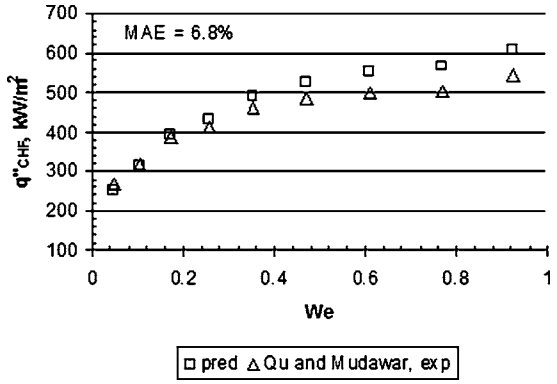

Fig. 4 Qu and Mudawar [1] CHF data compared to the present Kandlikar and Kuan CHF model (Eq. (10)), plotted against the Weber number, C=0.002492, water

Comparing the experimental CHF data to the model prediction, the ability of the model to predict the CHF for R-123 and water with remarkable accuracy is extremely encouraging. It indicates that the underlying mechanisms are well represented through the forces employed in the model development. A larger data set with different channel sizes and fluids and wider ranges of operating conditions will be helpful in refining this model further in the future work.

Conclusions

Experiments are conducted to obtain the CHF data using R-123 and water in microchannels. The present experimental CHF results are found to correlate best with existing correlations to overall MAEs of 33.9% and 14.3% with R-123 and water, respectively, when using a macroscale rectangular equation by Katto [14]. A theoretical analysis of flow boiling phenomena revealed that the ratio of evaporation momentum to surface tension forces is an important parameter. A new model is proposed using this parameter and the inertia force to represent the CHF mechanism in microchannels. The new theoretical model is able to predict correct parametric trends. CHF is found to increase with increasing mass flux. The results of the present work are summarized in the following.

- CHF is found to increase with increasing Weber number, which indicates that as the mass flux increased, the CHF increased.

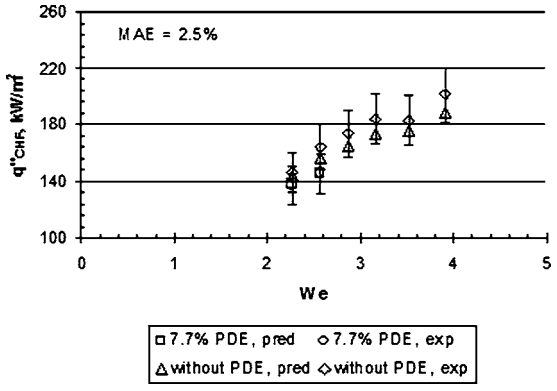

Fig. 5 Present R-123 CHF data with and without 7.7% PDE in manifold compared to the present Kandlikar and Kuan CHF model (Eq. (10)), plotted against the Weber number, C =0.003139

- The trend in CHF with mass flux is similar to those obtained by earlier investigators.
- CHF data are slightly lower when using the 7.7% PDEs with R-123. PDEs have negligible effect on CHF in the present water experiment.
- PDEs help in flow stabilization, but the CHF is somewhat reduced when using R-123. The ability of the restrictors to reduce localized dryout is, however, more important, and therefore PDEs are still recommended for use in the operating ranges, as shown in Table 1.
- The present R-123 and water experimental CHF results are found to correlate with overall MAEs of 33.9% and 14.3%, respectively, with the macroscale equation by Katto [14] for rectangular channels.
- A new theoretical model is developed to predict flow boiling CHF in microchannels. It is developed based on the surface tension, evaporation momentum, and inertia forces.
- The new model is able to correlate with present experimental R-123 and water CHF data to MAEs of 16.4% and 8.2%, respectively, when using a single constant C value of 0.002679. The best correlation seen is with the individually optimized C value of 0.003139 for R-123, which has an MAE of 2.5%.

Acknowledgment

The authors would like to thank the National Science Foundation for providing financial support (CTS Grant No. 0245642) for this research.

Nomenclature

b = height of microchannel, m
C = constant in the present CHF model
D = characteristic dimension, m
d = diameter of circular channel, m
F_I = force due to inertia, N
F_M = force due to momentum change, N
F_S = surface tension force, N
F' = force per unit length, N/m
G = mass flux, $\mathrm{kg/m^2\,s}$
I = electrical current, A
P = pressure, kPa
ΔP = pressure drop, kPa
q'' = heat flux, $\mathrm{kW/m^2}$
q''_{CHF} = critical heat flux, $\mathrm{kW/m^2}$
q_{in} = power input to the test section, W
q_{loss} = heat loss from the test section, W
T = temperature, °C
ΔT_{amb} = differential temperature for use in performing test section heat loss calibration, °C
T_s = surface temperature, °C
$\bar{V}$ = average velocity based on average density $\bar{\rho}$, m/s
We = Weber number, $(G^2D)/(\rho\sigma)$
x = thermodynamic quality

Greek Symbols

ρ = density, $\mathrm{kg/m^3}$
$\bar{\rho}$ = average density, $\mathrm{kg/m^3}$
θ = dynamic receding contact angle, deg.
σ = surface tension, N/m

Subscripts

amb = ambient
CHF = critical heat flux, $\mathrm{kW/m^2}$
expt = experimental
G,g = gas or vapor
I = inertia
in = inlet
L,f = liquid
loss = unrecoverable loss
M = due to momentum change
pred = predicted
s = microchannel surface
S = surface tension

References

[1] Qu, W., and Mudawar, I., 2004, "Measurement and Correlation of Critical Heat Flux in Two-Phase Micro-Channel Heat Sinks," Int. J. Heat Mass Transfer, **47**, pp. 2045–2059.
[2] Bowers, M. B., and Mudawar, I., 1994, "High Flux Boiling in Low Flow Rate, Low Pressure Drop Mini-Channel and Micro-Channel Heat Sinks," Int. J. Heat Mass Transfer, **37**, pp. 321–332.
[3] Roach, G. M., Jr., Abdel-Khalik, S. I., Ghiaasiaan, S. M., Dowling, M. F., and Jeter, S. M., 1999, "Low-Flow Critical Heat Flux in Heated Microchannels," Nucl. Sci. Eng., **131**, pp. 411–425.
[4] Jiang, L., Wong, M., and Zohar, Y., 1999, "Phase Change in Micro-Channel Heat Sinks With Integrated Temperature Sensors," J. Microelectromech. Syst., **8**(4), pp. 358–365.
[5] Yu, W., France, D. M., Wambsganss, M. W., and Hull, J. R., 2002, "Two-Phase Pressure Drop, Boiling Heat Transfer, and Critical Heat Flux to Water in a Small-Diameter Horizontal Tube," Int. J. Multiphase Flow, **28**, pp. 927–941.
[6] Koşar, A., Kuo, C., and Peles, Y., 2005, "Reduced Pressure Boiling Heat Transfer in Rectangular Microchannels With Interconnected Reentrant Cavities," ASME J. Heat Transfer, **127**, pp. 1106–1114.
[7] Wojtan, L., Revellin, R., and Thome, J. R., 2006, "Investigation of Saturated Critical Heat Flux in a Single, Uniformly Heated Microchannel," Exp. Therm. Fluid Sci., **30**, pp. 765–774.
[8] Kuan, W. K., and Kandlikar, S. G., 2005, "Development of an Experimental Facility for Investigating Critical Heat Flux of Saturated Flow Boiling of Refrigerant-123 in Microchannels," ASME International Mechanical Engineering Congress and Exposition, Orlando, FL, Nov. 5–11.
[9] Kuan, W. K., and Kandlikar, S. G., 2006, "Critical Heat Flux Measurement and Model for Refrigerant-123 and Water Under Stabilized Flow Conditions in Microchannels," ASME International Mechanical Engineering Congress and Exposition, Chicago, IL, Nov. 5–10.
[10] Kuan, W. K., and Kandlikar, S. G., 2006, "Experimental Study on Saturated Flow Boiling Critical Heat Flux in Microchannels," *Fourth International Conference on Microchannels and Minichannels, ASME*, Limerick, Ireland, June 19–21, pp. 1–7.
[11] Kandlikar, S. G., 2004, "Heat Transfer Mechanisms During Flow Boiling in Microchannels," ASME J. Heat Transfer, **126**, pp. 8–16.
[12] Kandlikar, S. G., 2001, "A Theoretical Model to Predict Pool Boiling CHF Incorporating Effects of Contact Angle and Orientation," ASME J. Heat Transfer, **123**, pp. 1071–1079.
[13] Bowring, R. W., 1972, "A Simple But Accurate Round Tube Uniform Heat Flux, Dryout Correlation Over the Pressure Range 0.7-17 MN/m2 (100–2500 psia)," United Kingdom Atomic Energy Authority, Report No. AEEW-R 789.
[14] Katto, Y., 1981, "General Features of CHF of Forced Convection Boiling in Uniformly Heated Rectangular Channels," Int. J. Heat Mass Transfer, **24**, pp. 1413–1419.

An Experimental Study of Effective Thermal Conductivity of High Temperature Insulations

Bo-ming Zhang

Wei-hua Xie

Shan-yi Du

Shu-yuan Zhao

Center for Composite Material,
Harbin Institute of Technology,
Harbin 150080, China

An experimental apparatus was designed and fabricated to measure the effective thermal conductivities and simulate the temperature and pressure history of reentry of a launch vehicle into a planetary atmosphere with a maximum temperature of 1600°C. An improved testing method was used to test the thermal conductivities of an alumina fibrous insulation at environmental pressures from 0.03 Pa to 10^5 Pa with the average temperature of the sample increased to 864°C and its density being 128 kg/m^3. A method based on temperature difference is used to compute the in-plane effective thermal conductivity, and the result shows that the in-plane thermal conductivity along the y axis is 1.47 times that along the x axis. The influences of temperature and pressure on the contribution of three heat transfer mechanisms to the effective thermal conductivities were compared.
[DOI: 10.1115/1.2804946]

Keywords: effective thermal conductivities, heat transfer, high temperature insulation, in-plane thermal conductivity

Introduction

To reduce the cost of delivering a pound of payload to low earth orbit, NASA is concentrating on the second generation of reusable launch vehicles (RLVs) [1]. The metallic thermal protection system is a key technology in achieving the goal of reducing the cost of space access and it is one of the most important parts of the new generation of RLV. The main function of thermal protection system is to prevent the vehicle inner structural temperature from exceeding a specified value during reentry, and the high temperature insulation is the main component of the thermal protection system. Up to now, there are two typical kinds of insulations: one is fibrous insulation and the other is multilayer insulation, which consists of thin ceramic/composite foils with high reflectance gold coatings separated by fibrous insulation spacers. Both kinds of insulations are based on the analysis of the insulation. Analysis and measurement of high temperature fibrous insulation for RLVs are indispensable for evaluating and designing thermal protection systems. The study of evaluation technology is one of the most important fundamental researches, and the lag of evaluation technology will greatly restrict the application of the materials.

The study on high temperature insulation is getting more and more important with its rapid development in some application fields especially in aerospace. In the past several decades, many researchers studied on heat transfer through fibrous insulation, but the majority of the work was limited to testing equipment and experimental methods, and failed to test the overall performance of the materials. Keller et al. [2] and Mathes et al. [3] studied on radiant heat transfer in insulations and provided a method of numerically predicting the performance of high temperature multilayer insulation. Williams and Curry [4] provided a theoretical formulation of heat transfer through rigid fibrous insulation. Petrov [5] modeled radiation and conduction in fiber thermal insulation at high temperatures, however, without experimental results. Lee and Cunnington [6,7] mainly modeled radiant heat transfer in high-porosity fiber thermal insulations and compared his theoretical predictions with experimental data of other investigators. Spinnler et al. [8,9] performed an experimental and theoretical study on effective thermal conductivities of multilayer thermal insulation with top temperatures of the material surface up to 1000°C at ambient pressure. Daryabeigi [10–14] modeled heat transfer through fibrous insulation and multilayer insulation, and compared the numerical results with experimental results at pressures from 1 Pa to 1.01×10^5 Pa with surface temperature up to 1000°C. The past studies only measured the thermal conductivity at low temperature in vacuum, or at high temperature and atmospheric pressure, and failed to provide the results at high temperature in vacuum, which represents the real reentry environment. In all studies, Daryabeigi reached the highest average temperature at only 506°C.

In this study, an experimental apparatus was designed and fabricated to measure the effective thermal conductivities. An improved testing method was also proposed to increase the average temperature of the testing sample greatly. The thermal conductivities of an alumina fibrous insulation were measured over a wide range of pressures with the minimum pressure at about 10^{-2} Pa and the maximum average temperature up to 864°C. The influences of temperature and pressure on heat transfer mechanisms were analyzed.

Experimental Apparatus

In general, there are three modes of heat transfer [10] through fibrous insulation, which are solid conduction through fibers, gas conduction between fibers and natural convection, and radiation interchange through participating media. The variation of temperatures and pressures during reentry, and the complex coupling of the heat transfer modes make the analysis and design of high temperature insulation difficult. While it is difficult to seek numerical resolutions, testing cannot only help to modify the theoretical model but also provide solid data support for evaluating the performance of the material.

For the testing apparatus mentioned in the references, the highest operating temperature is 1200°C, which is mentioned in Ref. [8]. It is an indirect method to heat a ceramic plate by means of a 24 kW infrared heater. To evaluate the performance of insulation at high temperatures, a high vacuum graphite heating chamber was designed and built to measure the effective thermal conductivities of insulation subject under large temperature grads representative of typical launch vehicle reentry conditions for experimental analysis. The radiant heater panel is on top of the graphite chamber; the temperature of 1600°C or even higher can be easily achieved. The water-cooled plate was instrumented at the bottom side. The pressure controlling system of the apparatus consisted of a vacuum production system, a vacuum monitoring system, and a vacuum corrector system. The measuring instruments consist of a vacuum measuring instrument, a heat flux gauge, and thermocouples. A photograph of the overall setup is shown in Fig. 1. This apparatus can be used to evaluate the performance of the insulations, even the typical thermal protection system samples. The size of the sample is up to 450×450 mm^2, the top surface can be heated up to 1600°C, and the pressure can be controlled between 6.67×10^{-3} and 10^5 Pa. Its schematic diagram is shown in Fig. 2.

Contributed by the Heat Transfer Division of ASME for publication in the JOURNAL OF HEAT TRANSFER. Manuscript received September 30, 2006; final manuscript received June 18, 2007; published online March 6, 2008. Review conducted by Louis C. Burmeister.

Fig. 1 Photograph of high vacuum graphite heating chamber

Improved Experimental Approach

During reentry, the heat transfer in the insulation can be simplified to a one-dimensional static heat transfer problem. For a given sample with the thickness being L, if the steady state is achieved, and the temperatures of the hot side and cool side and the heat flux through the sample are noted as T_{heat}, T_{cool}, and q, respectively, based on Fourier's theorem, the effective thermal conductivity is defined as

$$k_e = \frac{qL}{T_{heat} - T_{cool}} \tag{1}$$

There were two factors which limited the researches on the fibrous insulation in the past studies: one was the ability of the experimental apparatus and the other was the testing methods. In this study, an improved testing method of the effective thermal conductivities was proposed, which suggested use of multilayer insulations. The past studies found that for a given apparatus, the temperature of the cool surface is usually a constant, and from Eq. (1) it can be concluded that the only way to increase the average temperature of the sample is to increase the temperature of the hot surface whatever the thickness of the single insulation is. However, for most equipment, the highest temperature of the hot surface is about 1000°C, so the average temperature of the single insulation will be no higher than 600°C. However, the multilayer method can increase not only the overall thermal capacity but also the average temperature of the insulation, because the temperature of the lower surface of the top layer in multilayer insulation is much higher than that of the single layer insulation, and the heat flux q in the z direction through the sample is all the same in the steady-state condition

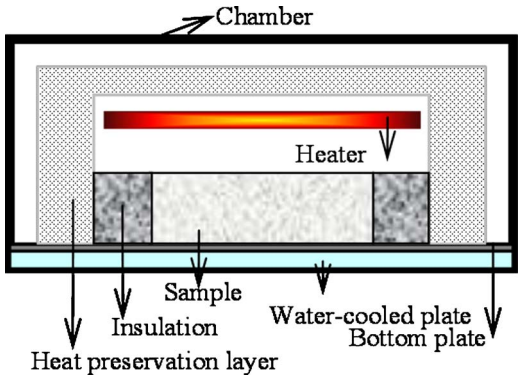

Fig. 2 Schematic diagram of the interior of heating

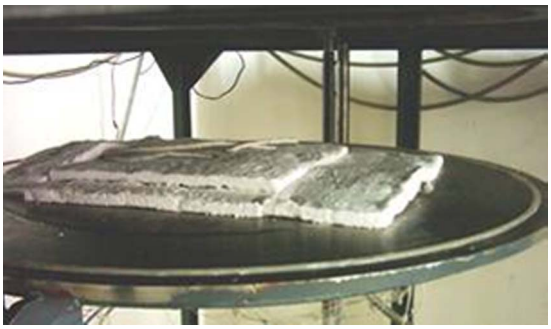

Fig. 3 Photograph of testing sample in chamber

The testing sample is high alumina fibrous insulation (designation: GXT-1200, ~98% $Al_2O_3+SiO_2$, ~0.25% Fe_2O_3, ~0.25% R_2O) with its thickness being 20 mm, which is supplied by SinoSteel Luoyang Institute of Refractories Research; its transverse dimensions of 450×450 mm^2 are bigger than the dimensions of those ever used. The density of the sample is 128 kg/m^3, and the density of the fiber parent material is 2600 kg/m^3. The average diameter of the fiber is about 2.4 μm. In order to increase the average temperature of the sample and reduce the errors, double-layer insulation samples were used. There are three heat flux gages, nine K type thermocouples between the water-cooled plate and the lower layer sample, nine K type thermocouples in the middle of the two layers, and three platinum-30% rhodium/platinum-6% rhodium thermocouples on the top surface. Some insulation is put around the sample to provide an adiabatic boundary condition and prevent horizontal heat loss. The sample and surroundings are shown in Fig. 3. Only the data from the central 270×270 mm section of the test setup, referred to as the metered region, are used for calculating the effective thermal conductivities.

Data acquisition is completed by the multichannel measurement instrument. The collecting program was developed by using LABVIEW™, and the recorded data versus time was plotted on the program window.

Experimental Data Analysis

In order to get corresponding effective thermal conductivities under different conditions, tests were conducted with the environmental pressure of nitrogen inside the chamber controlled at nominal values of 0.03 Pa, 4.5 Pa, 28 Pa, 1800 Pa, 3500 Pa, 6500 Pa, 50000 Pa, and 10^5 Pa and the temperature of the top surface of the sample set at nominal temperatures of 100°C, 200°C, 300°C, 400°C, 500°C, 600°C, 700°C, 800°C, 900°C, and 1000°C under each environmental pressure. To get the effective conductivity of the sample at high average temperature, the data of the insulation's upper layer were used. The average temperature of the top surface was used as the hot side temperature, the average temperature of middle surface layer was used as the cool side temperature, and the average of these two values was used as the average temperature of the upper layer sample, noted as T_{av}. For the steady state, the heat flux in the z direction through the sample is constant, so the value measured at the bottom can be used as that of the top. After substituting the heat flux, which is modified by the bottom temperature into Eq. (1), the corresponding effective thermal conductivity was ciphered out. The experimental results are shown in Fig. 4 where the effective thermal conductivity changes with average sample temperature with the environmental pressures at 0.03 Pa, 3500 Pa, and 10^5 Pa, respectively.

It is found in Fig. 4 that there are some abnormal points at low temperature. For instance, the values at 85°C at the pressures of 3500 Pa and 10^5 Pa are higher than those at 250°C. These singu-

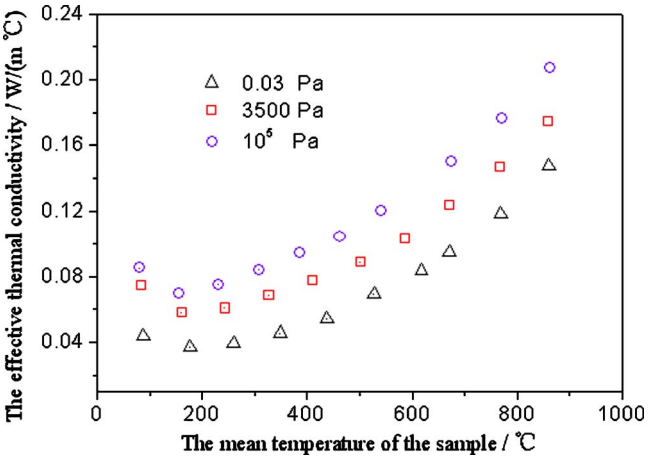

Fig. 4 The effective thermal conductivity versus average temperature at three environmental pressures

larities are mainly caused by the uncertainty of measured values. The total uncertainty in a measurement is the combination of uncertainty due to random errors and uncertainty due to systematic errors. There can be many sources of systematic errors in a measurement, such as the calibration process, instrument systematic errors, transducer errors, and fixed errors of method. Also, environmental effects, such as radiation effects in a temperature measurement, can cause systematic errors of the method. To estimate the expected conductivity uncertainty, the measurement errors associated with the heat flux, temperature, and geometry must be estimated. In Table 1 are the parameters at pressure of 3500 Pa and temperature of 85 °C, as an example, where the symbol N_i is the number of measurements of a parameter, and Table 2 shows the final results at different temperatures. Inspection of Table 1 lends insight into the magnitude of the contributions to the overall uncertainty. The uncertainty of heat flux becomes the dominant parameter, which controlled the systematic uncertainty at low temperature in the measurement. Therefore, in order to improve the precision of the measurement at low temperature, the high resolution heat flux gauge and thermocouples can be used in the future.

To understand the influence of pressure on heat conduction, the results of thermal conductivity versus pressure were plotted, as shown in Fig. 5. The corresponding temperatures are 165 °C, 592 °C, 772 °C, and 864 °C, respectively. It is found that the pressure has no influence on the effective conductivity when the pressure is below 200 Pa. A decrease in pressure is therefore accompanied by an increase in molecular mean free path, and the collision frequency decreases as the pressure decreases and mean free path increases. Gas conduction and convection will decrease greatly, which related to gas molecule. Gas conduction is negligible within this pressure range whatever the temperature is, because the pressure is only directly related to gas conduction, having no relationship with solid conduction and radiation. However, when the pressure ranges from 200 Pa to 10,000 Pa, thermal conductivity increases rapidly with the pressure, and then asymptotically approaches a constant when the pressure is above 10,000 Pa.

Table 2 Summary of test results at different temperatures

Temperature	Conductivity and expanded uncertainty in conductivity
84.1 °C	$K=0.075\pm0.021$ W/(m °C)
243.5 °C	$K=0.061\pm0.013$ W/(m °C)
327.0 °C	$K=0.078\pm0.007$ W/(m °C)
670.9 °C	$K=0.123\pm0.006$ W/(m °C)
864.0 °C	$K=0.175\pm0.005$ W/(m °C)

In-Plane Thermal Conductivity Analysis of the Insulation

During manufacturing, the fibers were not stacked up entirely randomly—more fibers were oriented to one direction than to the others, which make the thermal conductivities vary in different directions. The next relationship can be obtained based on Eq. (1):

$$\Delta T_x = \Delta T/L_x = q_x''/k_x$$

$$\Delta T_y = \Delta T/L_y = q_y''/k_y \tag{2}$$

where ΔT_x and ΔT_y are temperature differences along the x-axis and the y-axis direction, respectively, k_x and k_y are the thermal conductivities along the x-axis and the y-axis direction, respectively. Although most of the heat transfers through the insulation in the thickness (z) direction, a little heat transfers to the surroundings through the boundaries of the insulation. For the symmetry of the boundary conditions of the sample, it is assumed that $q_x''=q_y''$. So Eq. (3) can be obtained:

$$\Delta T_x/\Delta T_y = k_y/k_x \tag{3}$$

If the temperatures of four points in the middle plane of the sample are denoted separately as T_A, T_B, T_C, and T_D, assuming the temperature changes linearly in plane, the next equation set can be obtained:

$$T_A + L_{XAB}\Delta T_x + L_{YAB}\Delta T_y = T_B$$

$$T_C + L_{XCD}\Delta T_x + L_{YCD}\Delta T_y = T_D \tag{4}$$

where L_{XAB} is the distance between point A and point B in the x axis, and the meanings of the other symbols are similar to this one. The conductivity ratio of k_x and k_y can be calculated by substituting the temperature and distance values of the four points at different pressures and environment temperatures. The results show that the pressure and temperature have no impact on the ratio, and the final mean value of different conditions is 1.47. However, this value will be changed for the other insulations, because the manufacturing technologies may be different. However, the ratio can be obtained in this way.

$$k_y/k_x = \Delta T_x/\Delta T_y = 1.47 \tag{5}$$

Table 1 Uncertainties of independent parameters

Parameters	Nominal values	Standard deviation	N_i	Absolute systematic standard uncertainty	Absolute random standard uncertainty	Absolute sensitivity	Absolute systematic standard uncertainty contribution	Absolute random uncertainty contribution
q (W/m^2)	114.4	0.12	758	14.2	4.36E−03	6.64E−04	8.90E−05	8.38E−12
L (m)	0.0202	3.40E−03	20	6.0E−04	7.60E−04	3.76E+00	5.10E−06	8.18E−06
ΔT (°C)	30.5	0.0024	758	0.75	8.72E−05	−2.49E−03	3.49E−06	4.72E−14

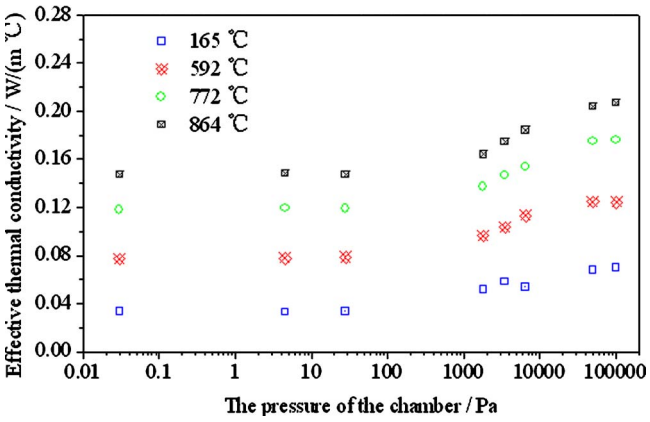

Fig. 5 The effective thermal conductivity versus pressure at four average temperatures

So the insulation works most effectively when the heat flux direction is perpendicular to the direction in which most fibers are stacked. If the thermal conductivity in the x-axis direction is not fully understood, a lot of trouble will be caused in practical application. For example, if heat resistance of x direction is less than that of y direction, x direction should be the one vertical to that of most fibers stacked.

Conclusion

In this study, an improved testing method was used to increase the average temperature of the samples, and the effective thermal conductivities of fibrous insulations at average temperatures up to 864°C were measured in a high vacuum graphite heating chamber. The influence of temperature and pressure on the contribution of three heat transfer mechanisms on the effective thermal conductivities was compared.

Results of the study show that gas conduction is almost negligible when the environmental pressure is below 200 Pa and, although increasing with increasing pressure, never exceeds 0.15. The results show that the in-plane thermal conductivity along the y axis is 1.47 times that along the x-axis direction. The results present singularity when the temperature is below 250°C because of the low resolution of the heat flux gauge.

References

[1] Blosser, M. L., Chen, R. R., Schmidt, I. H., Dorsey, J. T., Poteet, C. C., Bird, R. K., and Wurster, K. E., 2004, "Development of Advanced Metallic Thermal-Protection-System Prototype Hardware," J. Spacecr. Rockets, **41**(2), pp. 183–194.

[2] Keller, K., Hoffmann, M., Zorner, W., and Blumenberg, J., 1992, "Application of High Temperature Multilayer Insulations," Acta Astronaut., **26**(6), pp. 451–458.

[3] Mathes, R., Blumenberg, J., and Keller, K., 1990, "Radiative Heat Transfer in Insulations With Random Fibre Orientation," Int. J. Heat Mass Transfer, **33**(4), pp. 767–770.

[4] Williams, S. D., and Curry, D. M., 1993, "Prediction of Rigid Silica Based Insulation Conductivity Using Morphological Data," *Heat Transfer Measurements and Analysis*, American Society of Mechanical Engineers, New York, HTD-249, pp. 51–59.

[5] Petrov, V. A., 1997, "Combined Radiation and Conduction Heat Transfer in High Temperature Fiber Thermal Insulation," Int. J. Heat Mass Transfer, **40**(9), pp. 2241–2247.

[6] Lee, S. C., and Cunnington, G. R., 1998, "Fiber Orientation Effect on Radiative Heat Transfer Through Fiber Composites," Paper No. AIAA-1998-2840.

[7] Lee, S. C., and Cunnington, G. R., 2000, "Conduction and Radiation Heat Transfer in High-Porosity Fiber Thermal Insulation," J. Thermophys. Heat Transfer, **14**(2), pp. 121–136.

[8] Spinnler, M., Winter, E. R. F., Viskanta, R., and Sattelmayer, T., 2004, "Theoretical Studies of High-Temperature Multilayer Thermal Insulations Using Radiation Scaling," J. Quant. Spectrosc. Radiat. Transf., **84**(4), pp. 477–491.

[9] Spinnler, M., Winter, E. R. F., and Viskanta, R., 2004, "Studies on High-Temperature Multilayer Thermal Insulations," Int. J. Heat Mass Transfer, **47**(6–7), pp. 1305–1312.

[10] Daryabeigi, K., 1999, "Analysis and Testing of High Temperature Fibrous Insulation for Reusable Launch Vehicles," Paper No. AIAA-99-1044.

[11] Daryabeigi, K., 2000, "Design of High Temperature Multi-Layer Insulation for Reusable Launch Vehicles," Ph.D. thesis, University of Virginia.

[12] Daryabeigi, K., 1999, "Effective Thermal Conductivity of High Temperature Insulations for Reusable Launch Vehicles," NASA TM-199-208972.

[13] Daryabeigi, K., 2001, "Thermal Analysis and Design of Multi-layer Insulation for Re-entry Aerodynamic Heating," Paper No. AIAA-2001-2834.

[14] Daryabeigi, K., 2002, "Heat Transfer in High-Temperature Fibrous Insulation," Paper No. AIAA 2002-3332.

Studies on Optimum Distribution of Fins in Heat Sinks Filled With Phase Change Materials

S. K. Saha

K. Srinivasan

P. Dutta[1]
Mem. ASME
e-mail: pradip@mecheng.iisc.ernet.in

Department of Mechanical Engineering,
Indian Institute of Science,
Bangalore 560 012, India

This paper deals with phase change material (PCM), used in conjunction with thermal conductivity enhancer (TCE), as a means of thermal management of electronic systems. Eicosane is used as PCM, while aluminium pin or plate fins are used as TCE. The test section considered in all cases is a 42×42 mm^2 *base with a TCE height of* 25 mm. *An electrical heater at the heat sink base is used to simulate the heat generation in electronic chips. Various volumetric fractions of TCE in the conglomerate of PCM and TCE are considered. The case with 8% TCE volume fraction was found to have the best thermal performance. With this volume fraction of TCE, the effects of fin dimension and fin shape are also investigated. It is found that a large number of small cross-sectional area fins is preferable. A numerical model is also developed to enable an interpretation of experimental results.*
[DOI: 10.1115/1.2804948]

Keywords: heat sink, phase change material, thermal conductivity enhancer

1 Introduction

The dynamics of electronic packaging continues to demand a high level of performance from their thermal management systems. The race toward compactness and high reliability of electronic devices is also propelling innovations in the design of cooling systems. The border of conventional air cooled designs is already stretched too far. Novel cooling techniques, keeping in view the temporal functionality of electronic equipments, are emerging. In this context, the use of phase change materials (PCMs) is emerging as one of the sensible approaches as they can absorb a large amount of latent heat, hence limiting the rise in temperature of the component [1].

Most of the PCMs explored to date, though endowed with a high latent heat capacity, suffer from a low thermal conductivity. Hence, it becomes necessary to add some amount of aluminum or copper as thermal conductivity enhancers (TCEs) [2]. Then, it becomes important to identify an effective way of distributing this high thermal conductivity material in the body of PCM to achieve the best thermal management. The conglomerate of PCM and TCE will be referred to as thermal storage unit (TSU) [3].

There exist comprehensive descriptions of the experimental and computational assessment of PCM-based thermal management for different electronic systems. Among the studies regarding the enhancement of heat transfer through PCM using TCE, Pal and Joshi [3] investigated the melting of PCM inside honeycomb cores mounted such that the cells are vertical. A numerical simulation was performed for a single cell, considering the effect of natural convection in the PCM. Alawadhi and Amon [4] investigated the effectiveness of a TSU, made of PCM and aluminum fins, for portable electronic devices. Some recent experimental investigations on PCM-based heat sinks have also been reported. Mettawee and Assassa [5] investigated a method of enhancing the thermal conductivity of paraffin wax by dispersing aluminum powder in it. Kandasamy et al. [6] determined the effects of various input parameters on the performance of a PCM-based heat sink under cyclic loading.

The present work focuses on determining the optimal volume fraction of TCE in TSU to maintain a low component temperature. Two types of TCE distribution have been identified, namely, pin fins or plate fins. The effects of dimensions and fractions of TCE fins are investigated. The electronic component is simulated by a wire wound heater. In each case, the performance of TSU is evaluated from the transient heater temperature data. A computational model is also used to interpret some of the experimental observations.

2 Experiments

The TSU is composed of PCM and TCE. A schematic representation of a TSU, showing the arrangement of heater, plate fins, and PCM, is given in Fig. 1(*a*). The volumetric solid percentage of TCE, excluding the base, is considered to be the percentage of the volume of TCE present in the heat sink. The material used as PCM in the present experiments is eicosane ($C_{20}H_{42}$). Eicosane is a pure material with a constant melting temperature of 35 °C. Aluminum is used as the material for thermal conductivity enhancement because of its low density, high thermal conductivity, corrosion resistance, and wide acceptance in the electronic industry. In the present case, ease of manufacturing by electrodischarge machining (EDM) is another consideration. The thermophysical properties of eicosane and aluminum are summarized in Table 1.

In the present work, two types of TCE distribution have been studied. One method of distribution is to optimally distribute it as plate-type fins, and the second way is to arrange it as pin fins, as shown in Fig. 1(*b*). The fins are made by wire cut EDM from an aluminum block of overall dimensions of $42 \times 42 \times 30$ (height) mm^3. The heater receptacle of dimensions $36 \times 36 \times 3$ (height) mm^3 is milled at the base with a provision for connecting wires for the element. Several volumetric fractions of TCE are chosen. These are 0%, 2%, 8%, 18%, and 27% volumetric fractions of TCE in TSU, corresponding to 0, 9, 36, 81, and 121 pin fins, respectively. A common feature is the dimensions of pin fins, which are $2 \times 2 \times 25$ (height) mm^3. As it is shown later that the case of the 8% volumetric fraction of TCE is the best performing one, two additional types of arrangements are studied with the same volume fraction of TCE: (a) three plate fins ($1.14 \times 42 \times 25$ mm^3) and (b) nine pin fins ($4 \times 4 \times 25$ mm^3).

The four sidewalls of TSU are insulated. Mica sheets of 0.2 mm thickness are used as enclosures covered with a 10 mm thick glass wool as insulation. A constant power is applied to a heater from a dc power supply. The heater, of dimensions $36 \times 36 \times 3$ mm^3, is mounted in the recess at the bottom of the TSU. The 0.576 mm wire wound heater has a resistance of 4.3 Ω. The power densities used in the experiments are 4 W and 8 W, resulting in a flux of 3086 W/m^2 and 6173 W/m^2, respectively. The relevant thermophysical properties of the heater material are summarized in Table 1.

The temperature of the heater and the temperature at various points in TSU are measured by polytetrafluoroethylene (PTFE) 24 gauge coated *T*-type (Copper-Constantan) thermocouples. The

[1]Corresponding author.

Contributed by the Heat Transfer Division of ASME for publication in the JOURNAL OF HEAT TRANSFER. Manuscript received November 6, 2006; final manuscript received July 17, 2007; published online March 6, 2008. Review conducted by Ramendra P. Roy.

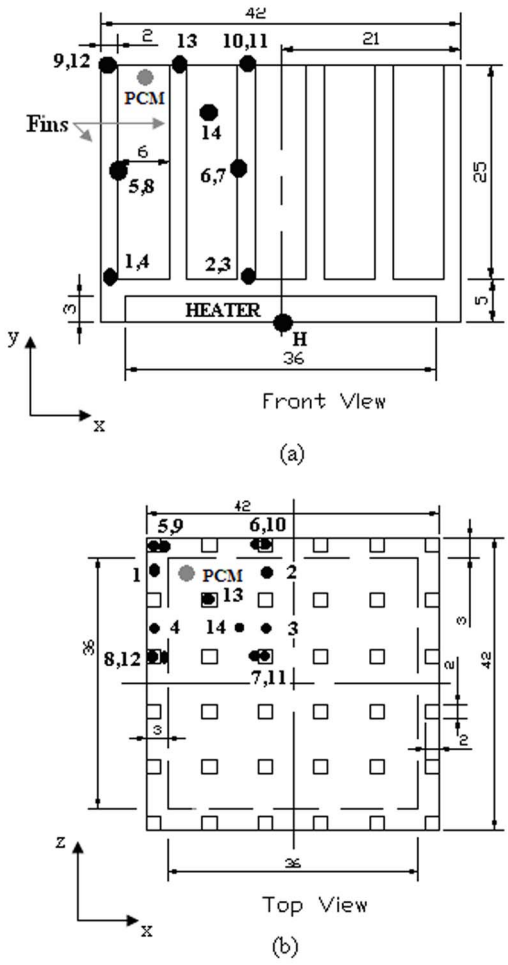

Fig. 1 Thermocouple locations within a TSU with 8% TCE

range of temperature measured by *T*-type thermocouples is 0–200°C. Figure 1 shows the location of thermocouples for TSU with 8% TCE with 36 pin fins.

3 Mathematical Model and Numerical Technique

The governing equations follow a single domain approach. Since the PCM undergoes melting by absorbing heat from the heater, both fluid flow and heat transfer equations are to be solved for the domain. The TCE, heater, and substrate materials are assigned very high viscosity ($\sim 10^{20}$ m^2/s) and melting point, which ensures that they remain solid and fixed in the domain. Conjugate heat transfer is considered in the analysis. Accordingly, a common set of governing conservation equations for both the solid and liquid regions are written, as described elaborately in Ref. [7], and are not repeated here for the sake of brevity. The thermal boundary conditions include insulated sidewalls and bottomwalls and free convection cooling from the top surface.

4 Results and Discussion

A typical temperature profile of the heater surface and the PCM is shown in Fig. 2(*a*). Zone A is the region of sensible heat gain in the solid phase of the PCM until it reaches the melting point. This is followed by a flat profile (zone B) resulting from the melting of PCM, which is the main region of interest. In zone C, the temperature rise is due to a sensible heating of the molten PCM. It is seen that the heater attains a fairly uniform temperature of about 80°C after 600 s of heating at 8 W. The melting period is about 1400 s through which the heater temperature varies marginally. This marginal temperature increases can be attributed to heat conduction by the TCE. A notable feature is the slope of the temperature profiles in zones A and C. A sharp increase of heater temperature in zone A is due to poor thermal diffusivity of the solid PCM. In zone C, heat transfer results in sensible heating, which depends on the thermal capacities and heat dissipation to the ambient. On the other hand, the temperature profiles of the PCM indicate a comparable slope governed by the thermal capacities of the solid and liquid phases.

Figures 2(*b*) and 2(*c*) show numerically determined velocity distribution and isotherms, respectively, within the TSU after 1700 s of heating. It is clear from Fig. 2(*c*) that there is thermal stratification within the heater section, while the region containing molten PCM has a fairly uniform temperature. Temperature uniformity within the molten PCM is caused by the presence of TCE fins as well as by buoyancy induced melt circulation. Natural convection of molten PCM promotes good mixing and reduces thermal stratification within the melt.

Comparison of cooling effects of all configurations of TSUs at 4 W. Figure 3 shows heater temperature variations for different TSU configurations for a power level of 4 W. It brings out the significant advantages of adding pin-type TCE fins in comparison to the baseline case (PCM without TCE). Due to low thermal diffusivity of the PCM, the heater is not able to dissipate heat, leading to its sharp temperature rise. The addition of TCE enhances the thermal energy dissipative process in general. However, the rate of enhancement is a strong function of the percentage of TCE in TSU. The duration of melting time is reduced by the addition of TCE fins because the PCM content decreases as a result. A notable feature among TSUs with TCE is that the duration of melting phase is large at a low volume fraction of the TCE fins (less than 27% TCE). This is to be attributed to convection cells in the molten region of the PCM. At a large volume fraction of the TCE, these cells are suppressed, and the entire heat transfer results in melting. Figure 3 also reveals that TSU with 8% TCE is associated with the lowest temperature of the heater surface. A good qualitative agreement between the experimental and numerical results is also observed.

Effect of fin distribution for 8% volumetric fraction of TCE. Since it emerges that about 8% volume fraction of TCE performs better than the other arrangements, a further investigation is carried out to explore the influence of fin geometries, maintaining the same TCE volume fraction. The cases considered are 36 pin fins (2×2 mm^2) and 9 pin fins (4×4 mm^2) at a power level of 4 W. Results for two cases of fin distribution are shown in Fig. 4. The heater temperature for the case with 36 pin fins is lower than that with 9 pin fins, keeping a constant TCE volumetric percentage of

Table 1 Thermophysical properties of materials used

Materials	Melting point (°C)	Density (kg/m^3)	Thermal conductivity (W/m K)	Specific heat (J/kg K)	Heat of fusion (kJ/kg)	Kinematic viscosity (m^2/s)
Eicosane	35	790.0	0.230	2050	241.0	4.6×10^{-6}
TCE/substrate	—	2712.9	179.6	960	—	—
Heater	—	740.0	0.145	1750	—	—

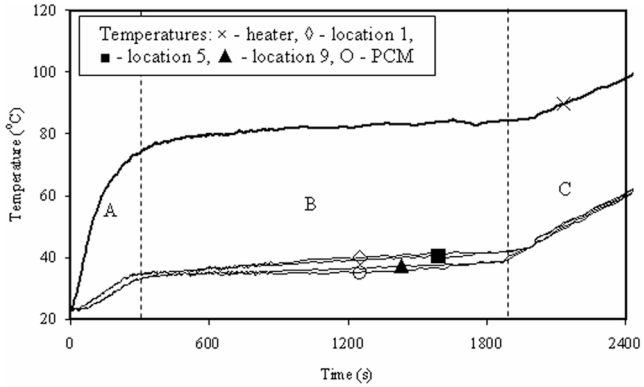

(*a*)

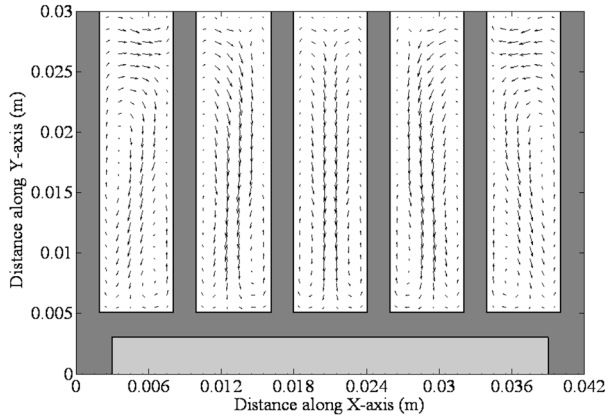

(*b*)

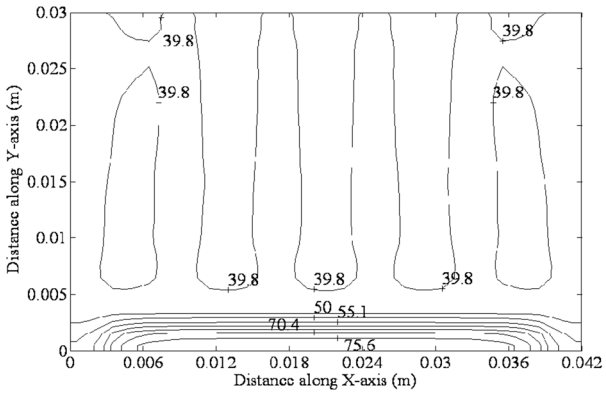

(*c*)

Fig. 2 (*a*) Different zones in the experimental temperature graph. Numerical (*b*) velocity vectors and (*c*) temperature contours in a sectional view of TSU with 8% (2×2 mm², 36 pin fins) TCE at 8 W at 1700 s.

8%. For the case with 36 pin fins, the availability of a larger contact area between the fins and PCM augments heat transfer from the fins, thus resulting in a lower heater temperature. A larger number of fins also permit a longer duration of phase change, as the convection cells will be smaller and weaker.

It is also evident from Fig. 4 that pin fin heat sinks lower the heater temperature more effectively than plate fin heat sinks, despite both having same volumetric percentage of TCE. In a pin fin configuration, a large number of uniformly distributed fins transfer heat more effectively to the PCM. This indicates that convective cells in a pin fin case communicate with each other, while this is

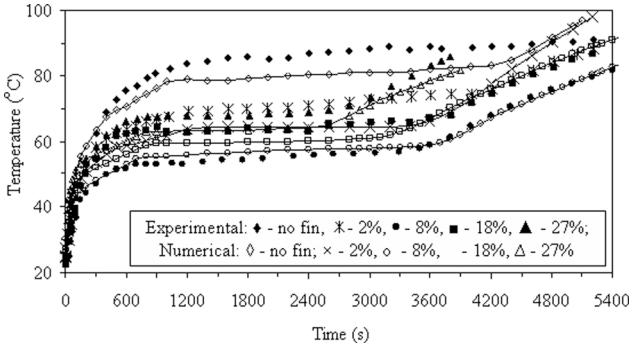

Fig. 3 Experimental and numerical temperature histories of the heat source at 4 W for pin-fin-type TSUs (fin dimensions: 2×2 mm²) having different volumetric fractions of TCE with eicosane as PCM

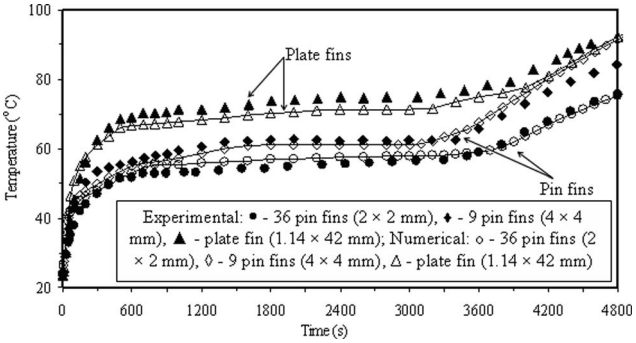

Fig. 4 Experimental and numerical temperature histories of the heat source at 4 W for pin-fin-type and plate-fin-type TSUs with 8% TCE with eicosane as PCM

not possible among cells locked in between plates. In all the cases described above, there is a good agreement between numerical and experimental results.

5 Conclusions

Experimental and numerical studies are performed to investigate the effectiveness and performance of a TSU as a thermal management device for electronic components. For the configuration studied, the lowest operating temperatures are attained with about 8% volume fraction of TCE and with a larger number of fins. It is found that the duration of constancy of temperature is directly related to the amount of PCM, but the value of that constant temperature depends on the volume fraction of TCE. After melting, the rise in the temperature of heat source follows an identical pattern in all cases.

Acknowledgment

The work reported in this paper is supported by a research grant from the Defence Research and Development Organisation, Government of India.

References

[1] Abhat, A., 1981, "Low Temperature Latent Heat Thermal Storage," *ISPRA Course on Energy Systems and Technology*, G. Beghi, ed., Reidel, Holland, pp. 33–91.

[2] Tong, X., Khan, J. A., and Amin, M. R., 1996, "Enhancement of Heat Transfer by Inserting a Metal Matrix Into a Phase Change Material," Numer. Heat Transfer, Part A, **30**, pp. 125–141.

[3] Pal, D., and Joshi, Y. K., 1998, "Thermal Management of an Avionics Module

Using Solid-Liquid Phase Materials," J. Thermophys. Heat Transfer, **12**(2), pp. 256–262.
[4] Alawadhi, E. M., and Amon, C. H., 2002, "Thermal Analysis of a PCM Thermal Control Unit for Portable Electronics Devices: Experimental and Numerical Analysis," Eighth Intersociety Conference on Thermal and Thermomechanical Phenomena in Electronic Systems, San Diego, CA.
[5] Mettawee, E. S., and Assassa, G. M. R., 2007, "Thermal Conductivity Enhancement in a Latent Heat Storage System," Sol. Energy, **81**, pp. 839–845.
[6] Kandasamy, R., Wang, X.-Q., and Mujumdar, A. S., 2007, "Application of Phase Change Materials in Thermal Management of Electronics," Appl. Therm. Eng., **27**, pp. 2822–2832.
[7] Nayak, K. C., Saha, S. K., Srinivasan, K., and Dutta, P., 2006, "A Numerical Model for Heat Sinks With Phase Change Materials and Thermal Conductivity Enhancers," Int. J. Heat Mass Transfer, **49**(11–12), pp. 1833–1844.